

**SEAMLESS DUAL-BRAKE TRANSMISSION
FOR ELECTRIC VEHICLES: DESIGN,
MODELING, ESTIMATION, AND CONTROL**

Mir Saman Rahimi Mousavi

Department of Electrical and Computer Engineering
McGill University, Montréal

January 2017

A Thesis submitted to the Faculty of Graduate Studies and Research
in partial fulfilment of the requirements for the degree of
Doctor of Philosophy

*This thesis is dedicated to my Mom and Dad for their encouragement,
support, and constant love throughout my life.*

Abstract

In automotive applications, a transmission is a mechanical device that delivers the power of the traction unit to the wheels in different combinations of torque and speed. Various transmissions have been suggested and developed for internal combustion engine vehicles (ICEVs) to meet the above-mentioned objective. Moreover, complex gear shift techniques have also been introduced in order to meet certain characteristics such as efficiency, drivability, and lifetime of the system. However, increasing fuel cost and environmental concerns have pushed the automotive industry to gradually replace ICEVs with hybrid electric vehicles (HEVs) and fully electric vehicles (EVs). The migration from ICEVs to EVs has a considerable number of hurdles. One of the main challenges is the lower energy density of electric batteries in comparison with fossil fuels. Thus, by changing the traction unit from internal combustion engines to electric motors, it is required to minimize losses in the driveline in order to maximize the range of EVs and more importantly make them competitive with ICEVs. Transmission, in particular, has a considerable impact not only on dynamic performance but also on the overall efficiency of the driveline, and therefore, its mechanical design and gear shift algorithms have to be revised. In recent years, multi-speed transmissions for EVs have been studied and developed in two different directions. In one direction, based on the characteristics of electric motors, transmissions initially designed for ICEVs were modified in order to be retrofitted to HEVs and EVs. In the other direction, novel transmissions have been developed for EVs from the ground up considering effective controllability of electric motors as well as their wide range of efficient operation.

ABSTRACT

In this thesis, a special attention is given to the second direction in which a novel seamless two-speed transmission particularly designed for EVs is proposed. In this system, clutches and torque converters are eliminated from the powertrain, and instead, the transmission is perpetually connected to the powertrain. This is done not only because of the high controllability of electric motors, but also for efficiency and drivability improvements. Further, the hydraulic gear shift actuators are replaced with electromechanical ones in order to improve efficiency and reliability and reduce the weight and volume of the overall system. Kinematic analysis of the introduced transmission is performed to provide achievable gear ratios of the system that are beneficial for gear ratio optimization purposes. Further, various modeling techniques are fused together in order to provide a detailed dynamical model of an EV powertrain equipped with the proposed transmission. The derived model is validated by means of a down-scaled proof-of-concept experimental prototype as well as simulation models built in MATLAB/Simulink® using SimDriveLineTM library. This model validation is performed through different test scenarios while the transmission system undergoes gear shift operations. Based on the dynamical model of the system, in order to reduce the number of sensors and transducers on the powertrain, a stochastic observer is designed to estimate the unmeasured state variables and the unknown input imparted on the system. The observer mitigates the process and measurement noises and provides a smooth estimation of unmeasured states and the unknown input. By considering all state variables and disturbances available for feedback, two optimal control problems minimizing shifting time and energy dissipation during the gear shift processes are solved using the Pontryagin minimum principle (PMP) while eliminating the power interruption at the output. The solutions to these optimal control problems shed light on novel gear shift algorithms in which conventional phases, namely the torque and inertia phases, are not necessary for the introduced transmission. Finally, a closed-loop controller is designed to track the optimal control inputs and trajectories while coping with actuators limitations. The performance of the designed observers and controllers are verified by experiments and simulation analyses.

Résumé

Dans les applications automobiles, une transmission est un dispositif mécanique qui fournit la puissance de l'unité de traction aux roues dans différentes combinaisons de couple et de vitesse. Diverses transmissions ont été proposées et développées pour les véhicules à moteur à combustion internes (VMCIs) afin d'atteindre l'objectif mentionné ci-dessus. De plus, des techniques de changement de vitesses complexes ont également été proposées afin de répondre à certaines caractéristiques telles que l'efficacité, la maniabilité et la durée de vie du système. Cependant, l'augmentation du coût du carburant et des préoccupations environnementales ont poussé l'industrie automobile à remplacer progressivement les VMCIs par des véhicules électriques hybrides (VÉHs) et des véhicules entièrement électriques (VÉs). La migration technologique des VMCIs aux VÉs présente un nombre considérable d'obstacles. L'un des principaux défis est la plus faible densité énergétique des batteries électriques par rapport aux combustibles fossiles. Ainsi, en changeant le moteur à combustion interne par un moteur électrique dans l'unité de traction, il est nécessaire de minimiser les pertes dans la transmission afin de maximiser l'autonomie des véhicules électriques et ainsi les rendre plus compétitifs. La transmission a donc un impact considérable non seulement sur la performance dynamique, mais aussi sur l'efficacité globale de la chaîne cinématique, et par conséquent, les algorithmes pour sa conception et ses changements de rapports de vitesse mécanique doivent être révisés. Au cours des dernières années, les transmissions multi-vitesses pour les véhicules électriques ont été étudiées et mises au point selon deux axes différents. Dans le premier axe, sur

RÉSUMÉ

la base des caractéristiques des moteurs électriques, des transmissions initialement conçues pour VMCI sont été modifiées afin d'être adaptées aux VÉHs et VÉs. Dans l'autre axe, de nouvelles transmissions ont été développées pour les véhicules électriques à partir de principes fondamentaux considérant l'excellente gouvernabilité des moteurs électriques ainsi que leur grande plage de fonctionnement efficace.

Dans cette thèse, une attention particulière est accordée aux deuxième axe dans lequel une nouvelle transmission à deux vitesses sans interruption de couple est conçue pour les véhicules électriques. Dans ce système, les embrayages et les convertisseurs de couple sont éliminés du groupe motopropulseur, et au lieu, la transmission est perpétuellement connectée au groupe motopropulseur. Cela se fait non seulement en raison de la grande gouvernabilité des moteurs électriques, mais aussi pour améliorer l'efficacité et l'agrément de conduite. En outre, les actionneurs de changement de vitesse hydrauliques sont remplacés par des actionneurs électromécaniques afin d'améliorer l'efficacité et la fiabilité et de réduire le poids et le volume de l'ensemble du système. L'analyse cinématique de la transmission est effectuée pour fournir des rapports de vitesse réalisables qui sont bénéfiques à des fins d'optimisation du rapport d'engrenage. En outre, diverses techniques de modélisation sont fusionnées afin de fournir un modèle dynamique du groupe motopropulseur détaillé d'un véhicule électrique équipé de la transmission proposée. Le modèle proposé est validé au moyen d'un prototype expérimental réduit à l'échelle, ainsi que de modèles de simulation créés dans MATLAB/Simulink® en utilisant la bibliothèque SimDrivelineTM. Cette validation du modèle est réalisée au moyen de différents scénarios de test alors que le système de transmission subit des opérations de changement de vitesse. Basé sur le modèle dynamique du système, et afin de réduire le nombre de capteurs et transducteurs sur le groupe motopropulseur, un observateur stochastique est conçu pour estimer les variables d'état non mesurées et l'entrée inconnue transmise dans le système. L'observateur atténue les bruits de processus et de mesure et fournit une estimation lisse des états non mesurés et de l'entrée inconnue. En tenant compte de toutes les variables d'état et des perturbations disponibles pour la rétroaction,

RÉSUMÉ

deux problèmes de contrôle optimal minimisant le temps et la dissipation d'énergie pendant les opérations de changement de vitesse sont résolus en utilisant le Principe du Minimum de Pontryagin (PMP), tout en éliminant l'interruption de couple à la sortie. Les solutions à ces problèmes de contrôle optimal offrent une nouvelle perspective pour des algorithmes de changement de vitesse dans lesquels les phases classiques de couple et d'inertie ne sont pas nécessaires pour la transmission proposée. Enfin, un contrôleur en boucle fermée est conçu pour asservir le système aux entrées et aux trajectoires de contrôle optimales tout en faisant face aux limitations des actionneurs. La performance des observateurs et des contrôleurs conçus est vérifiée par des expériences et des analyses de simulation.

Claims of Originality

- (i) This thesis develops a novel two-speed transmission called *dual brake transmission (DBT)* for electric vehicles characterized by seamless gear shifts. The proposed system is a departure from conventional transmissions developed for internal combustion engine vehicles (ICEVs) to innovative systems specifically designed for EVs. The DBT system allows improving the efficiency and drivability of the overall system by eliminating clutches, torque converters, and hydraulic actuators and replacing them with brakes and electromechanical actuators. Utility patents for this novel transmission are filed in Canada and the US.
- (ii) A detailed dynamical model of the powertrain of an electric vehicle equipped with the DBT system is derived to characterize the responses of the system to the control inputs and disturbances in different working phases, namely, the first gear ratio, the second gear ratio, and during gear shift operations. Various modeling techniques from classical and analytical dynamics used for this purpose. Given the fact that the transmission system exhibits both discrete and continuous behaviour due to transitions between different gear ratios, its dynamical model is formulated in the framework of hybrid dynamical systems. The derived dynamical model is verified by experimental and simulation analyses.
- (iii) A stochastic observer is designed in order to estimate the unmeasured state variables and disturbances applied on the EV powertrain equipped with the

CLAIMS OF ORIGINALITY

DBT system. Here, the method of modeling unknown inputs as fictitious state variables is combined with the Kalman-Bucy filter in order to provide a concurrent estimation of unmeasured states and the unknown input applied on the system. The observer estimates angular velocities of the off-going and on-coming gears and consequently the gear ratio, the input and output torques of the transmission, and the unknown torque exerted on the vehicle based on the speed measurements of the electric motor and wheels which are commonly available in commercial vehicles. The main reason behind designing such an observer is to provide an accurate real-time monitoring of unmeasured states and disturbances for exploitation in the closed-loop feedback control system to yield proper gear shifts, enhancing drivability.

- (iv) For the DBT system, first, the gear shift control problem is formulated in such a way that the output torque and output speed of the transmission system are kept constant during the gear shift process. Then, based on this formulation, optimal gear shift problems are solved using the Pontryagin minimum principle (PMP) to minimize the characterized cost functional optimizing shifting time and energy dissipation during these operations. In fact, the proposed gear shift strategy is an integrated technique wherein the traction motor is controlled simultaneously with the gear shift actuators. Based on the resulting optimal control laws and trajectories, a closed-loop controller using the Backstepping control technique is derived to provide a stabilizing feedback law while relaxing abrupt control commands from the optimal control.

Published Journal Papers

- (i) **Rahimi Mousavi, M. S.**, A. Pakniyat, T. Wang, and B. Boulet (2015). Seamless dual brake transmission for electric vehicles: Design, control and experiment. *Mechanism and Machine Theory* 94, 96–118.

Contribution of each author:

Mr. Mir Saman Rahimi Mousavi proposed the mechanical layout of the dual brake transmission (DBT). He performed the kinematical analysis of the DBT system and derived the dynamical model of the system. Based on the derived dynamical system. He also designed the closed-loop controller using Backstepping method to track the optimal trajectories and control inputs. He created simulation models in MATLAB/Simulink® to validate the performance of the designed controller. He also experimentally investigated the performance of this controller

Dr. Ali Pakniyat developed the ideal controller for the algebraic satisfaction of the constant output requirements, which form the basis for the controllers, such as the back-stepping controller, that satisfy this requirement asymptotically.

He also formulated optimal control problems for the minimization of the shifting duration and the energy wasted during the shifting period, and developed the optimal control results. Ali Pakniyat also worked in collaboration with Mir Saman Rahimi Mousavi on the integration of the optimal control results into the feasible controllers.

Dr. Ali Pakniyat's work forms the introduction of Chapter 5 and the formulation of the optimal control problem in Section 5.1 of this thesis.

Dr. Tao Wang collaborated with Mr. Mir Saman Rahimi Mousavi on the programming and implementation of the control algorithms on the experimental setup.

Prof. Benoit Boulet supervised the entire procedure and guided research team members.

The results of this paper are presented in Chapters 2, 3, 4, 5.

- (ii) **Rahimi Mousavi, M. S.**, Vahid Alizadeh, H., and B. Boulet (2016). Estimation of Synchromesh Frictional Torque and Output Torque in a Clutchless Automated Manual Transmission of a Parallel Hybrid Electric Vehicle. *IEEE Transactions on Vehicular Technology*.

CLAIMS OF ORIGINALITY

Contribution of each author:

Mr. Mir Saman Rahimi Mousavi designed and validated a stochastic observer for an automated manual transmission system.

Dr. Hossein Vahid Alizadeh performed the dynamical modeling of the system and he built the experimental prototype.

They collaborated on the programming and implementation of the estimation algorithms on MATLAB® and LABVIEW®.

Prof. Benoit Boulet conducted this study and led the group.

The conclusion of this study is used in the development of the stochastic observer designed in Chapter 4.

- (iii) **Rahimi Mousavi, M. S.** and B. Boulet (2016). Estimation of the state variables and unknown input of a two-speed electric vehicle driveline using fading-memory Kalman filter. *IEEE Transactions on Transportation Electrification* 2(2), 210-220.

Contribution of each author:

Mr. Mir Saman Rahimi Mousavi designed and validated a stochastic observer to estimate the unmeasured state variables and the unknown inputs imparted on the DBT system. He also experimentally validated the performance of the designed observer.

Prof. Benoit Boulet supervised and led this study.

The results of this paper are presented in Chapter 4.

Published Conference Papers

- (i) **Rahimi Mousavi, M. S.** and B. Boulet (2015). Modeling, simulation and control of a seamless two-speed automated transmission for electric vehicles. *In American Control Conference (ACC), 2014, pp. 3826–3831. IEEE.*

Contribution of each author:

Mr. Mir Saman Rahimi Mousavi introduced the DBT system for the first

time and developed the kinematic equations, dynamical modeling, and gear shift controller via torque and inertia phases.

Prof. Benoit Boulet supervised this study.

- (ii) **Rahimi Mousavi, M. S.**, A. Pakniyat, and B. Boulet (2014). Dynamic modeling and controller design for a seamless two-speed transmission for electric vehicles. *In Control Applications (CCA), 2014 IEEE Conference on*, pp. 635–640. IEEE.

Contribution of each author:

Mr. Mir Saman Rahimi Mousavi performed the kinematic analysis and dynamical modeling of an EV equipped with the DBT system. He also created the simulation environment of the entire powertrain to validate the control algorithm. He designed the feasible controller using the Backstepping method, based on the results of optimal control problem, and implemented it in the simulation environment to validate the performance of the designed controller.

Dr. Ali Pakniyat developed the ideal controller for the algebraic satisfaction of the constant output requirements, which form the basis for the controllers, such as the back-stepping controller, that satisfy this requirement asymptotically.

He also formulated optimal control problems for the minimization of the shifting duration and the energy wasted during the shifting period, and developed the optimal control results. Ali Pakniyat also worked in collaboration with Mir Saman Rahimi Mousavi on the integration of the optimal control results into the feasible controllers.

Prof. Benoit Boulet conducted this study and led the group.

This study is further developed in (Mousavi et al., 2015).

CLAIMS OF ORIGINALITY

- (iii) Tahmasebi, R., H. V. Alizadeh, **Rahimi Mousavi, M. S.** and B. Boulet (2016). Robust H_∞ force control of a solenoid actuator using experimental data and finite element method. *In Control Applications (CCA), 2014 IEEE Conference on*, pp. 1172–1177. IEEE.

Contribution of each author:

Ms. Rana Tahmasebi collaborated with Dr. Hossein Vahid Alizadeh on the development of an H_∞ controller for the solenoid actuator. The system identification together with the finite element method (FEM) are studied and uncertainties of the system are modeled. Furthermore, Ms. Rana Tahmasebi and Dr. Hossein Vahid Alizadeh derived the nonlinear algebraic model of the electromagnetic force versus current and air gap based on the experimental and FEM analysis.

Mr. Mir Saman Rahimi Mousavi performed the experimental tests and analysis for this study and collaborated with Ms. Rana Tahmasebi and Dr. Hossein Vahid Alizadeh on the derivation of the nonlinear model of the electromagnetic force versus current and air gap.

Prof. Benoit Boulet supervised this study.

The result of this study is used in Chapter 3.

- (iv) **Rahimi Mousavi, M. S.** and B. Boulet (2015). Dynamical modeling and optimal state estimation using kalman-bucy filter for a seamless two-speed transmission for electric vehicles. *In Control and Automation (MED), 2015 23th Mediterranean Conference on*, pp. 76–81. IEEE.

Contribution of each author:

Mr. Mir Saman Rahimi Mousavi designed and experimentally validated a stochastic observer and a deterministic observer to estimate the unmeasured state variables of the DBT system.

Prof. Benoit Boulet supervised and led this study.

This study is further developed in (Mousavi and Boulet, 2016).

- (v) Alizadeh, H. V., **Rahimi Mousavi, M. S.** and B. Boulet (2015). Synchromesh torque estimation in an electric vehicle's clutchless automated manual transmission using unknown input observer. *In Vehicle Power and Propulsion Conference (VPPC), 2015 IEEE, pp. 1–5. IEEE.*

Contribution of each author:

Mr. Mir Saman Rahimi Mousavi designed and validated a stochastic observer for an automated manual transmission system.

Dr. Hossein Vahid Alizadeh performed the dynamical modeling of the system and he built the experimental prototype.

They collaborated on the programming and implementation of the estimation algorithms on MATLAB® and LABVIEW®.

Prof. Benoit Boulet conducted this study and led the group.

- (vi) **Rahimi Mousavi, M. S.**, A. Pakniyat, M. K. Helwa, and B. Boulet, Observer-based backstepping controller design for gear shift control of a seamless clutchless two-speed transmission for electric vehicles. *In Vehicle Power and Propulsion Conference (VPPC), 2015 IEEE, pp. 1–6. IEEE.* Mr. Mir Saman Rahimi Mousavi performed the kinematic analysis and dynamical modeling of an EV equipped with the DBT system. He designed the observer-based controller for the DBT system and he validated this controller in a simulation environment.

Dr. Ali Pakniyat worked on the idea of minimum order observer design, and worked together with Mir Saman Rahimi Mousavi and Mohamed K. Helwa on the implementation of the ideas into the observer.

Dr. Mohamed K. Helwa verified the designed observer-based controller and provided the separation proof of the observer and controller.

Prof. Benoit Boulet supervised this study.

CLAIMS OF ORIGINALITY

Note

Examples of citation method in this thesis:

References with one author: Mousavi 2015

References with two authors: Mousavi and Boulet 2015

References with more than two authors: Mousavi et al., 2015

Acknowledgements

First, I would like to thank my supervisor, professor Benoit Boulet for his great guidance throughout this research. This work would not have been possible without his great encouragement and support.

I would like to thank Dr. Tao Wang for his amazing contribution with data logging, electric circuit design, and programming so that the experiments could be performed smoothly and successfully. I would also like to appreciate the help of Dr. Ali Pakniyat on the development of the optimal control algorithm in Chapter 5 and hybrid dynamical formulation in Chapter 3 in this thesis. He gave me a great insight into optimal control theories and hybrid systems.

I would like to thank Dr. Mohamed K. Helwa for his valuable advice and support in developing the observer-based controller. I am very grateful to you.

I would also like to thank Dr. Hossein Vahid Alizadeh and Ms. Rana Tahmasebi for their great work on the development of a nonlinear model for the solenoid actuator.

I would like to express my appreciation to my colleagues Dr. Yingxuan Duan, Dr. Alexei Morozov, Mr. Kieran Humphries, Mr. Diego Mascarella, and all the people who have contributed to the Automotive Partnerships Canada (APC) project at McGill University.

Finally, I would like to acknowledge the financial support of the Natural Sciences and Engineering Research Council of Canada (NSERC) and Automotive Partnerships Canada (APC) and the contribution of industrial partners: TM4, Linamar, and Infolytica.

TABLE OF CONTENTS

Abstract	i
Résumé	iii
Claims of Originality	vii
Published Journal Papers	viii
Published Conference Papers	x
Acknowledgements	xv
LIST OF FIGURES	xxi
LIST OF TABLES	xxvii
CHAPTER 1. INTRODUCTION	1
1.1. Background	1
1.1.1. Energy source/storage systems	3
1.1.2. Electric motors and power converters	5
1.1.3. Mechanical transmission and driveline	7
1.2. Literature Review	10
1.2.1. Adopted transmissions for EVs: challenges and obstacles	12
1.2.2. Powertrain Dynamical Model Approaches	15
1.2.3. Gear shift Control Criteria and Approaches	17
1.2.4. Powertrain State and Disturbance Estimation Methods	19
1.3. Scope and Objectives of the Thesis	20

TABLE OF CONTENTS

1.4. Thesis Outline	22
CHAPTER 2. Dual Brake Transmission: Mechanical Design and Kinematic Analysis	
2.1. Design of the Dual Brake Transmission	25
2.2. Kinematic Analysis	38
2.2.1. Kinematic Equations	38
2.2.2. Gear Ratios of the DBT	42
CHAPTER 3. Dynamical Model of the Powertrain	
3.1. Rotational Dynamics of the Electric Motor	47
3.2. Flexible Input and Output Shaft Models	47
3.3. Dynamical Model of the DBT System	49
3.3.1. Degrees of Freedom and Constraints	49
3.3.2. Hybrid Dynamical System Formulation for the DBT System	52
3.3.3. D'Alembert-Lagrange Principle	55
3.3.4. Determination of the Generalized Applied Torques	56
3.3.5. Hybrid Dynamical Model of the DBT System	61
3.4. Vehicle Dynamics	66
3.5. Electromechanical Gear shift Actuators	68
3.6. Validation of the Dynamical Model	72
3.6.1. Upshift during acceleration	74
3.6.2. Downshift during deceleration	76
CHAPTER 4. Observer Design	
4.1. Augmented State-Space Model of States and Disturbances	81
4.2. Observability Analysis	83
4.3. Observer Design	84
4.3.1. Deterministic Luenberger Observer	84
4.3.2. Stochastic Kalman-Bucy Filter	85
4.4. Experimental Validation of the Designed Observers	88

TABLE OF CONTENTS

CHAPTER 5. Controller Design	99
5.1. Optimal Controller Design	100
5.1.1. Definitions and Controllability Analysis	101
5.1.2. Preliminaries of the Optimal Controller Design	102
5.1.3. Optimal Control Problems	104
5.1.4. Backstepping Controller Design	108
5.2. Simulation and Experimental Results	112
CHAPTER 6. Conclusions	127
6.1. Summary of Results and Contributions	127
6.2. Recommendations for Future Work	130
BIBLIOGRAPHY	135
APPENDIX A. APPENDIX A	151
A.1. Planetary Gear Sets and Their Interconnections	151
A.2. Bearings and Supports	153
A.3. Motors and Brake Systems	155
A.4. Final 3D CAD Model and Implemented Design	159

LIST OF FIGURES

1.1	EV powertrain and control configuration (See (Ehsani et al., 2009))	2
1.2	Typical electric motor characteristic curve (See (Ehsani et al., 2009))	6
1.3	Transmission Synchronizer main elements (Alizadeh and Boulet, 2014; Alizadeh et al., 2014, 2015)	8
1.4	Schematic Diagram of a multi-speed dual clutch transmission	9
1.5	Tractive effort of a single speed powertrain versus a two-speed one (See (Ehsani et al., 2009))	11
2.1	Schematic diagram of the DBT core structure	29
2.2	Schematic diagram of an 8-speed transmission	30
2.3	Proof-of- concept prototype of the proposed transmission for EVs	30
2.4	Interconnections of the sun and ring gears.	31
2.5	Multi-plate brake mechanism for the sun gears (interior view)	32
2.6	Multi-plate brake mechanism for the sun gears (exterior view)	32
2.7	Band brake mechanism for the ring gears	33
2.8	Experimental prototype equipped with the traction and load motors .	34
2.9	Control enclosure and its components	36
2.10	Structure of the control, communication, data logging, and processing systems for the experimental test rig.	37
2.11	Planetary gear set and its major components	39

LIST OF FIGURES

2.12	Schematic view of the power transmission paths, (top): power transmission path in the first gear, (middle): power transmission paths during the gear shift, (bottom): power transmission path in the second gear	41
2.13	Achievable GR_1 and GR_2 by varying R_1 and R_2	43
3.1	Schematic diagram of the powertrain of an electric vehicle equipped with the proposed seamless clutchless two-speed transmission	46
3.2	Free-body diagram of the electric motor	48
3.3	Free-body diagram of the transmission's input and output shafts . . .	49
3.4	Free-body diagram of the dual brake transmission (DBT)	50
3.5	Hybrid dynamical model of the DBT system	54
3.6	Multi-plate brake assembly	58
3.7	Band brake assembly	58
3.8	Free-body diagram of the lumped parameter model of the vehicle, wheels, drive shafts, and the differential assembly	67
3.9	Main components of the solenoid actuator	69
3.10	Front and rear views of the solenoid assembly	70
3.11	Section view of conical and flat face solenoids	70
3.12	Force measurement apparatus	71
3.13	Fitted surface to the experimental electromagnetic force measurements of the solenoid actuator	72
3.14	Powertrain model in MATLAB/Simulink [®] built by SimDriveLine TM .	73
3.15	Motor speed (ω_M) before, during, and after the upshift process . . .	75
3.16	Output speed (ω_w) before, during, and after the upshift process . . .	75
3.17	Motor speed (ω_M) before, during, and after the downshift process . .	76
3.18	Output speed (ω_w) before, during, and after the downshift process .	77
4.1	Block diagram of the estimation using the Luenberger observer . . .	86

4.2	Block diagram of the estimation using the Kalman-Bucy filter	88
4.3	Probability distribution of the speed measurement sensor data.	91
4.4	Estimated and measured speed of the sun gear ω_S (upshift)	91
4.5	Estimated and measured speed of the ring gear ω_R (upshift)	92
4.6	Estimated and measured gear ratio of the transmission (upshift).	92
4.7	Estimated and measured torque of the input shaft T_d (upshift)	93
4.8	Estimated and measured torque of the output shaft T_o (upshift).	93
4.10	Estimated and measured speed of the sun gear ω_S (downshift)	94
4.9	Estimated and measured load torque T_v (upshift)	94
4.11	Estimated and measured speed of the ring gear ω_R (downshift)	95
4.12	Estimated and measured gear ratio of the transmission (downshift) . . .	95
4.14	Estimated and measured torque of the output shaft T_o (downshift) . .	96
4.13	Estimated and measured torque of the input shaft T_d (downshift) . . .	96
4.15	Estimated and measured load torque T_v (downshift).	97
5.1	Normalized brake force profiles applied to both experimental and simulation tests during the upshift and downshift operations	113
5.2	Block diagram of the observer-based backstepping controller	115
5.3	The motor (ω_M) and output (ω_w) speeds for the upshift operation .	116
5.4	The ring (ω_R) and sun (ω_S) speeds for the upshift operation	116
5.5	The variation of the gear ratio (GR) for the upshift operation	117
5.6	The output torque (T_o) for the upshift operation.	117
5.7	The motor (ω_M) and output (ω_w) speeds for the downshift operation .	118
5.8	The ring (ω_R) and sun (ω_S) speeds for the downshift operation	118
5.9	The variation of the gear ratio (GR) for the downshift operation . . .	119
5.10	The output torque (T_o) for the downshift operation	119
5.11	Simulated brake friction torque and motor torque (Upshift)	120
5.12	Simulated brake friction torque and motor torque (Downshift)	120

LIST OF FIGURES

5.13	Normalized brake forces of the ring and sun during the upshift	121
5.14	Normalized brake forces of the ring and sun during the downshift	122
5.15	The variation of the gear ratio during the upshift	122
5.16	The variation of the gear ratio during the downshift	123
5.17	The braking energy during the upshift	123
5.18	The braking energy during the downshift	124
6.1	Standard LFT diagram for H_∞ -optimal control design	131
A.1	Planetary gear sets and their interconnections	152
A.2	Isometric exploded and collapsed views of the DBT core structure . . .	152
A.3	3D CAD model and implemented design of the DBT core structure . .	152
A.4	Aligning bearings and output pulley of the DBT system	153
A.5	Isometric exploded and collapsed views of aligning bearings and out- put pulley	154
A.6	Major supports of the DBT system	154
A.7	Isometric exploded and collapsed views of the major supports of the DBT system	155
A.8	Multi-plate brake mechanism for the common sun gears	156
A.9	Isometric exploded and collapsed views of the multi-plate brake mechanism	
	156	
A.10	Traction motor installation	157
A.11	Isometric exploded and collapsed views of the traction motor installation	
	157	
A.12	Load motor installation	158
A.13	Isometric exploded and collapsed views of the load motor installation .	158
A.14	Band brake force actuator installation	159
A.15	Isometric exploded and collapsed views of the band brake force ac- tuator installation	159

LIST OF FIGURES

A.16	3D CAD model and the implemented prototype (front view)	160
A.17	3D CAD model and the implemented prototype (rear view)	160

LIST OF TABLES

3.1	Constraints classification of mechanical systems	51
3.2	Coefficients of the dynamical model of the transmission	63
3.3	Coefficients of the fitted surface (3.42) to the experimental results. . .	71
3.4	Parameters of the Experimental Apparatus	74
4.1	RMSE of states and the unknown input estimation (Upshift).	90
4.2	RMSE of states and the unknown input estimation (Downshift)	98
5.1	Parameters of the Backstepping Controller	112

CHAPTER 1

INTRODUCTION

1.1. Background

Increasing fuel cost and environmental issues have compelled the automotive industry to move toward the electrification of internal combustion engine vehicles (ICEVs) to provide a green, cost-effective, and sustainable transportation infrastructure (Husain, 2011). Electrical power generated from renewable sources such as hydro, wind, tidal, and solar resolves the dependency of the transportation system on oil as the exclusive source of energy and consequently could mitigate the economic issues related to limited and deteriorating fossil fuel resources (Ehsani et al., 2009; Husain, 2011; Khajepour et al., 2014).

Electric vehicles (EVs) were initially invented almost 60 years before the invention of ICEVs. However, their higher cost, lower range, and lower power in comparison with ICEVs caused them to disappear (Mi et al., 2011). Most of the efforts to commercialize electric vehicles failed until the time when the Toyota Prius was introduced for the first time (Mi et al., 2011). The flourishing market of this hybrid electric vehicle (HEV), which used electric machines and a downsized internal combustion engine, together with other HEVs such as the Honda Insight paved the way to the development of currently available EVs on the market. In fact, the integration of internal combustion engines with electric motors in HEVs has provided a unique opportunity for the automotive industry to establish a basis on top of which technologies of today's

CHAPTER 1. INTRODUCTION

high performance and zero-emission electric vehicles could be developed (Larminie and Lowry, 2004; Mi et al., 2011).

In electric vehicles, the driving torque is provided by electric motors. The primary components of an EV powertrain, which generate and deliver the power to the road, are an electric motor(s), a transmission, a final drive and differential assembly, driveshafts, and wheels (Ehsani et al., 2009; Mi et al., 2011; Khajepour et al., 2014; Husain, 2011). The vehicle supervisory controller collects acceleration and braking commands from the driver and transfers corresponding inputs to local controllers such as the energy management unit, the motor controller, and the transmission controller to track the driver's command while meeting certain predefined criteria such as efficiency, drivability, and performance. The schematic diagram of an EV powertrain together with its control configuration are conceptually depicted in Fig. 1.1 (Khajepour et al., 2014; Ehsani et al., 2009; Mi et al., 2011).

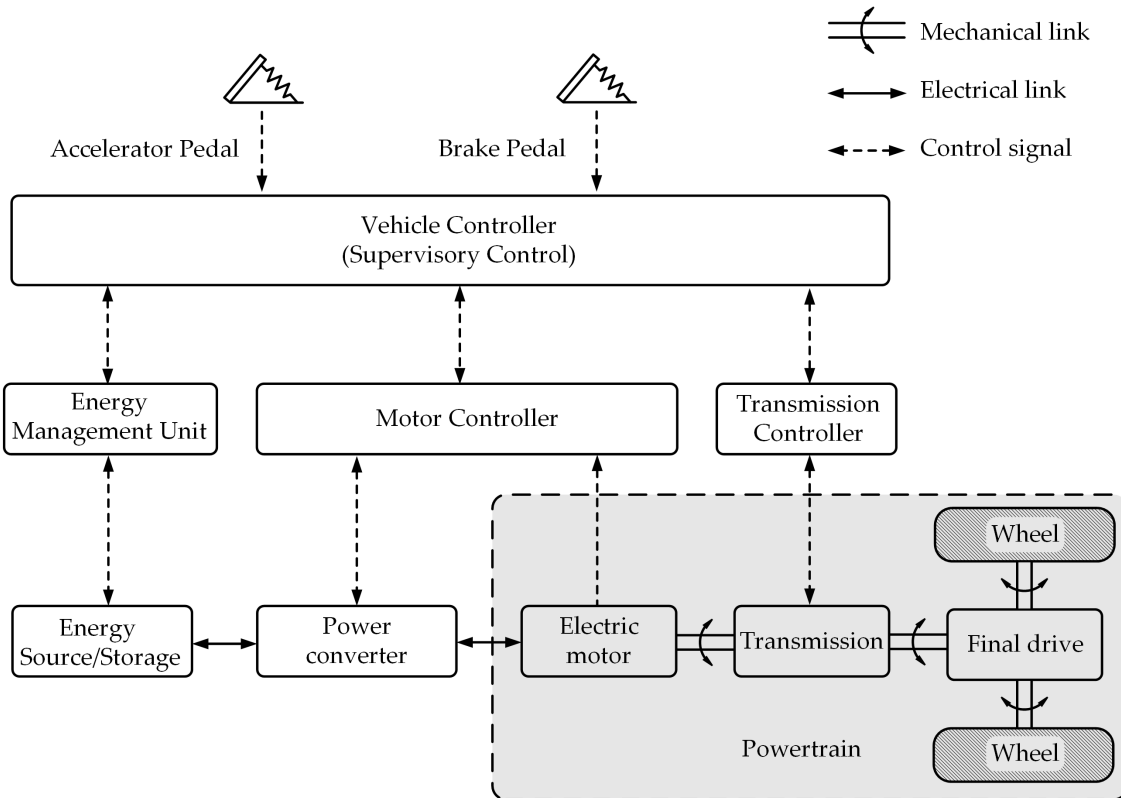


FIGURE 1.1. EV powertrain and control configuration (See (Ehsani et al., 2009))

The EV propulsion system is commonly studied in three main categories: 1) energy source/storage systems, 2) electric motors and power converters, and 3) mechanical transmission and driveline (Ehsani et al., 2009). Here, the term driveline is referred to the components of the powertrain excluding the motor and transmission.

1.1.1. Energy source/storage systems

The energy source/storage system in EVs provides the required energy for vehicle acceleration and stores the vehicle's energy during regenerative braking operation. An ideal energy source/storage system for EVs should satisfy two main criteria: 1) high energy density, 2) high power density (Khajepour et al., 2014). Currently available energy source/storage systems suffer from a well-known trade-off between energy storage capability and high-power deliverability (Khajepour et al., 2014). This trade-off is one of the main hurdles that affects the mass production of EVs due to its considerable impact on the vehicle range. This problem is tackled to a great extent by hybridization of various energy source/storage systems with different characteristics. Therefore, each energy source/storage system can boast its advantages while its disadvantages are being compensated by the others. Three major types of energy source/storage systems adopted for EVs are as follows (Husain, 2011; Ehsani et al., 2009; Lukic et al., 2008, 2006; Tie and Tan, 2013; Vazquez et al., 2010):

- Rechargeable batteries
- Ultracapacitors
- Ultra-High-Speed Flywheels

Batteries are the primary energy source/storage systems in EVs due to their outstanding characteristics regarding life, reliability, cost, specific power and energy (Tie and Tan, 2013; Khajepour et al., 2014). The five prevailing types of batteries on the market for transportation applications are (Khajepour et al., 2014; Catenacci et al., 2013):

- Nickel-Cadmium
- Nickel-metal hydride
- Nickel-Zinc

- Lead-acid
- Lithium-Ion

Although Li-Ion batteries suffer from high self-discharge rate and are costly, they have become the most dominant batteries since the time they were commercialized for the first time by Sony¹. This is due to their energy density and long lasting cycle life which make them a suitable solution for electric vehicles (Khajepour et al., 2014; Ehsani et al., 2009). Batteries are most commonly designed to provide a very high specific energy in order to maximize vehicle range. However, the maximum deliverable power of batteries is limited. In a typical drive cycle, the average power demand of cells is generally within their rated range. However, during abrupt acceleration this power request could go up to 5-10 times of the battery rated power. Similarly, during sudden deceleration, while the regenerative system is activated, the regenerated power to the battery can go much higher than the manageable power of the battery (Khajepour et al., 2014; Ehsani et al., 2009). These phenomena might considerably reduce the battery life and the life of the regenerative braking system. As previously mentioned, this problem can be tackled in EVs by hybridization of the batteries with other energy storage systems (Khajepour et al., 2014; Mi et al., 2011). A prevalent power storage hybridization is attained by combining primary batteries with ultracapacitors in order to provide an energy storage system with high energy density and high power deliverability.

In addition to ultracapacitors, flywheels can also be incorporated with batteries as mechanical energy storage systems to provide more power demands. Flywheels used to be made out of heavyweight rotors rotating at low speeds. However, nowadays, in order to reduce the overall weight of EVs and consequently to improve efficiency, flywheels are made of lightweight rotors spinning at very high speeds. A distinctive feature of interest in flywheels is their long cycle life, high specific power, and high specific energy density. However, their gyroscopic effect and abrupt energy release

¹<http://www.sonyenergy-devices.co.jp/en/keyword/>

due to vehicle accident are the main drawbacks of flywheels (Pena-Alzola et al., 2011; Khajepour et al., 2014).

1.1.2. Electric motors and power converters

Electric motors are the exclusive traction systems in the EVs powertrain which convert stored energy in the batteries to mechanical energy to provide the propulsion torque for the vehicle acceleration. These machines can also serve as generators to transform mechanical energy into electrical energy during regenerative braking and restore the electrical energy into the energy source/storage systems (Husain, 2011). This energy transformation is performed by a unit called power converter which is commonly made of high power and high frequency insulated-gate bipolar transistors (IGBTs). The electric motor controller generates switching commands for IGBTs in order to control the flow of power from energy source/storage systems to wheels and vice versa (Ehsani et al., 2009; Khajepour et al., 2014; Husain, 2011).

Electric motors adopted for EVs are mainly classified into direct current (DC) and alternating current (AC) motors. DC motors were of great interest on the primary prototypes of EVs. This was not only because of the great match between their torque-speed characteristics and the road load specifications but also due to their simplicity in terms of control. However, their high preserving cost and heavy weight made them to disappear (Husain, 2011). The prevailing DC motors used in EVs are:

- Shunt wound DC motors
- Series wound DC motors
- Separately excited DC motors

which are controlled via DC drives such as DC choppers, resonant converters, or isolated full-bridge converters (Husain, 2011; Ehsani et al., 2009; Lukic et al., 2008, 2006; Tie and Tan, 2013; Vazquez et al., 2010).

Despite the fact that the control of AC motors is more complex than DC ones, nowadays most electric vehicles on the market are equipped with AC motors. This is due to their higher efficiency, lighter weight, and lower maintenance cost in comparison

CHAPTER 1. INTRODUCTION

to DC motors. Three major types of AC motors currently available for electric vehicle applications are:

- Permanent magnet synchronous motors
- Induction motors
- Switch reluctance motors

which are typically controlled via six-switch inverters and unipolar converters (Husain, 2011).

Electric motors adopted for EVs have two regions of operation, namely constant torque and constant power. In the constant torque region, the electric motor provides a constant torque required for vehicle launching, acceleration, and hill climbing within the speed range from zero to the base speed. The motor enters the constant power region when the angular velocity of the motor passes the base speed wherein the available torque of the motor decreases with speed. This combination of constant torque and constant power regions with their corresponding speed range appropriately matches with the desired characteristics of EVs traction units (Ehsani et al., 2009).

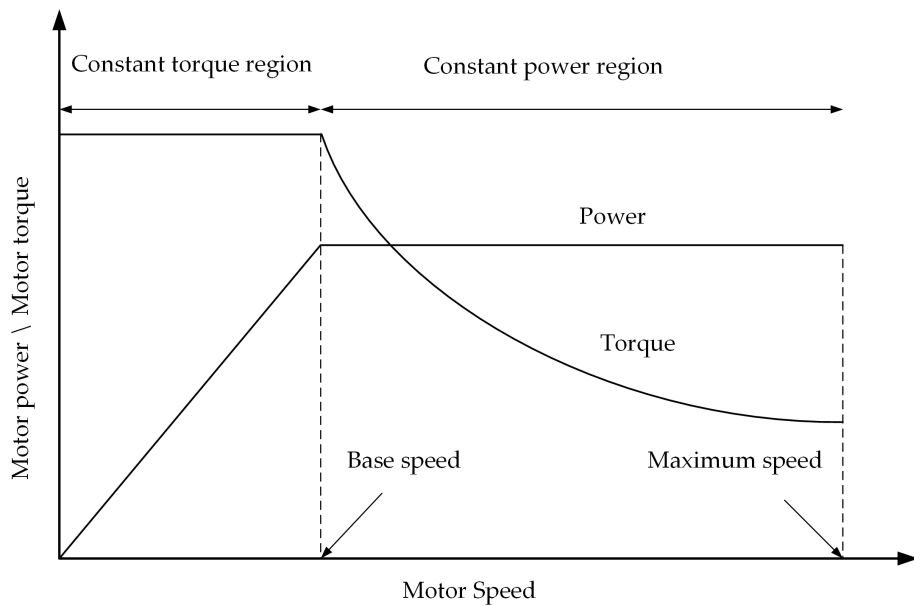


FIGURE 1.2. Typical electric motor characteristic curve (See (Ehsani et al., 2009))

Typical torque-speed and power-speed characteristic curves of electric motors adopted for EVs are illustrated in Fig. 1.2 (Ehsani et al., 2009; Husain, 2011).

1.1.3. Mechanical transmission and driveline

The mechanism that transfers the power from the engine or motor to the wheels in different combinations of torque and speed is called the transmission, and it has a crucial role to play on efficiency, dynamic performance, and drivability (Rahimi Mousavi and Boulet, 2014). The most well-known types of vehicle transmissions can be classified as follows:

- Manual Transmission (MT)
- Automated Manual Transmission (AMT)
- Automatic Transmission (AT)
- Dual Clutch Transmission (DCT)
- Continuously Variable Transmission (CVT)

Manual transmissions are those in which the driver performs gear selections and gear shift operations. This type of transmission is typically divided into two categories: 1) single-stage countershaft, 2) two-stage countershaft (Naunheimer et al., 2010). In the single-stage countershaft type, the input and output shafts of the transmission are on two parallel and non-coaxial axes. These types of transmissions are commonly adopted for the cases in which the traction unit is placed next to the wheels. For the sake of compactness, in this type of transmission, the final drive is integrated into the transmission. Two-stage countershaft MTs, are those in which the input and output shafts are coaxial and a drive shaft connects the transmission output shaft to the final drive and differential assembly (Naunheimer et al., 2010). In both types of MTs mentioned above, gear shifts are accomplished by a mechanical system called synchronizer which matches the speed of the gears and driveline by using the friction surfaces between the gear cone and the synchro ring of this mechanism (Alizadeh and Boulet, 2014; Alizadeh et al., 2014, 2015). The exploded view of the synchronizer mechanism is shown in Fig. 1.3.

CHAPTER 1. INTRODUCTION

The lack of automatically controlled gear shifts in MTs is addressed in automated manual transmissions (AMTs) in order to improve drivability, efficiency, and lifetime of the system. The mechanical layouts of AMTs are identical with those of MTs but instead of the driver, external actuators execute the gear selection, gear shift, and vehicle launch (Alizadeh and Boulet, 2014; Alizadeh et al., 2014, 2015). These actuators are typically controlled together with the traction unit in an integrated gear shift algorithm (Lucente et al., 2007; Zhang et al., 2002; Ge et al., 2000; Goetz, 2005).

Dual clutch transmissions (DCTs), regarding the mechanical design, were almost developed almost 75 years ago with the intention of providing seamless gear shifts. Porsche and Audi retrofitted this type of transmission to their racing cars. However, due to intricacies of controlling gear changes, they could not be commercialized until 2003 (Naunheimer et al., 2010). The mechanism of DCTs is made of two sub-gearboxes wherein the structure of each sub-gearbox is equivalent to that of the manual transmission. One of the sub-gearboxes provides the odd gears and the other one the even gears. Each sub-gearbox is coupled with a separated clutch to the traction unit and the output shaft of each sub-gearbox is connected to the drive-line (Naunheimer et al., 2010; Galvagno et al., 2011; Walker et al., 2011). Figure 1.4 conceptually illustrates the mechanical layout of DCTs.

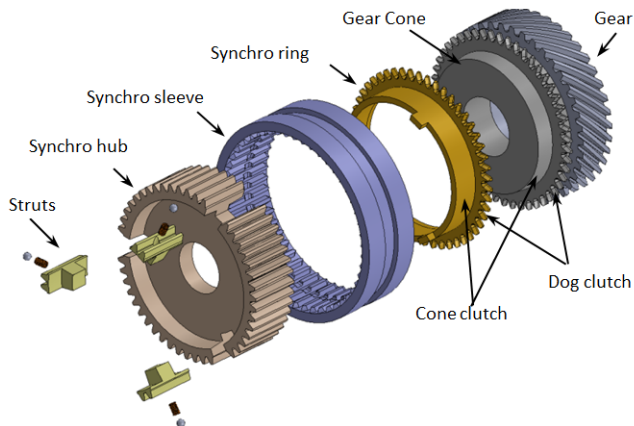


FIGURE 1.3. Transmission Synchronizer main elements (Alizadeh and Boulet, 2014; Alizadeh et al., 2014, 2015)

Continuously variable transmissions (CVTs) provide continuous and stepless gear ratios. The principle typically used by CVTs is to keep the traction unit in the most efficient point while changing the gear ratio in order to obtain different combinations of the torque and speed (Naunheimer et al., 2010). There are many types of CVTs with various characteristics such as belt, chain, toroidal, and spherical (Kim et al., 2002; Srivastava and Haque, 2008; Chen et al., 1998; Srivastava and Haque, 2009a; Tanaka, 2003), among which, chain and belt are the most common types in automotive applications. The most important mechanism in chain/belt CVTs is a variable diameter pulley (VDP). These variable diameter pulleys change the diameter of the belt/chain on the drive and driven sides by adjusting the gap between tapered disks which consequently changes the gear ratio of the transmission (Naunheimer et al., 2010).

Automatic transmissions (ATs) typically consist of multi-stage planetary gear sets, a torque converter, multi-plate clutches, and band brakes. Engaging and disengaging clutches and brakes provide different gear ratios. The torque converter is located between the traction unit and the transmission in order to improve drivability. Moreover, the torque converter releases the mechanical coupling between the traction unit and the transmission and allows the traction system to rotate independently from

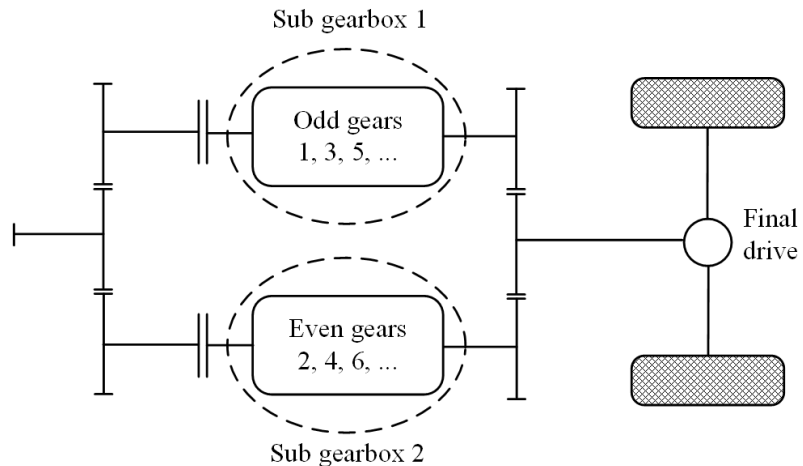


FIGURE 1.4. Schematic Diagram of a multi-speed dual clutch transmission

CHAPTER 1. INTRODUCTION

the transmission while transferring torque via a hydraulic coupling. Similar to DCTs, planetary-gear-based ATs have the ability to eliminate output torque interruptions during gear shift operations (Naunheimer et al., 2010; Jung et al., 2000; Haj-Fraj and Pfeiffer, 1999; Lazar et al., 2010; Asl et al., 2012).

The vehicle driveline, which transmits the transmission output power to the wheels, typically encompasses a final drive and differential assembly, half shafts, and wheels. The differential transfers the torque of the final drive to the wheels via the half shafts while providing independent rotation of the wheels. Therefore, the differential provides required speeds of the wheels for the vehicle maneuvers (Khajepour et al., 2014; Husain, 2011).

1.2. Literature Review

One of the main hurdles in the electrification of on-road vehicles is the lower energy density of electric batteries in comparison with fossil fuels. Therefore, optimization of efficiency plays a crucial role in the vehicle range and makes these vehicles competitive with ICEVs. However, in practice, this efficiency optimization is constrained to some performance criteria such as maximum speed, acceleration, and gradability. Research indicates that exploiting multi-speed transmissions for the EV powertrain provides an appropriate balance between efficiency and dynamic performance by enriching available combinations of torques and speeds (Hu et al., 2014; He et al., 2013; Sun et al., 2011; Pakniyat and Caines, 2014a, 2015, 2016a; Rahimi Mousavi and Boulet, 2014; Mousavi et al., 2014, 2015; Walker et al., 2013). Using multi-speed transmissions for EVs powertrain boosts the available torque at low speeds for vehicle launching, acceleration, and hill climbing and increases the vehicle top speed by increasing the area under the tractive effort-speed curve as illustrated in Fig. 1.5. More importantly, exploiting multiple speed transmissions for EVs provides a unique opportunity for the electric motors to operate close to their efficient points which may improve energy efficiency and range of this type of vehicles and reduce the overall cost of powertrain by reducing the size of electric motor.

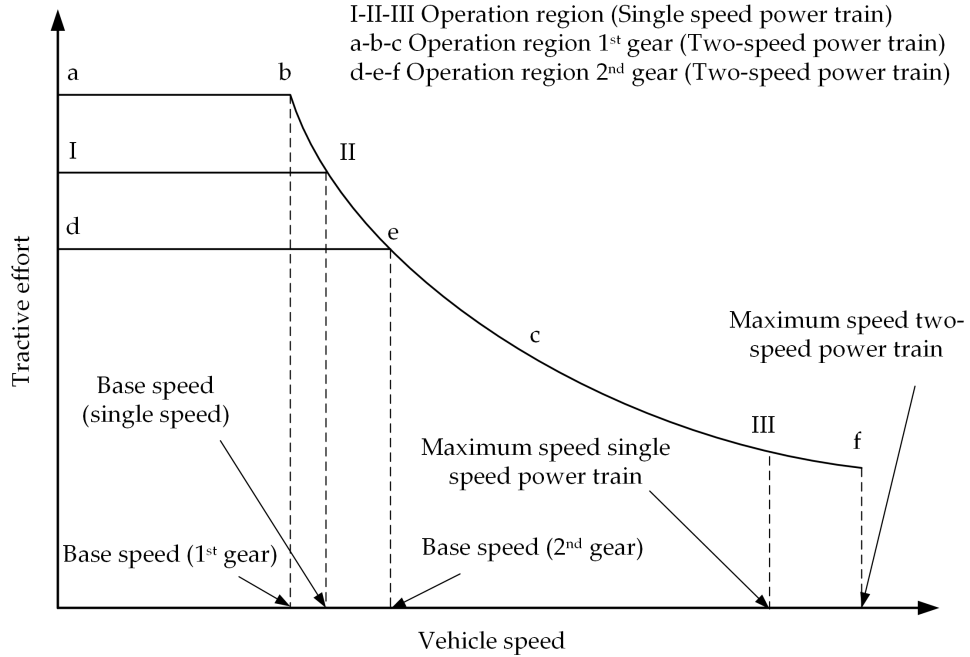


FIGURE 1.5. Tractive effort of a single speed powertrain versus a two-speed one (See (Ehsani et al., 2009))

In recent years, there has been considerable research devoted to retrofitting the transmissions designed for ICEVs such as AMTs (Alizadeh and Boulet, 2014; Lucente et al., 2007; Zhang et al., 2002; Ge et al., 2000), ATs (Huang et al., 2012; Yuan et al., 2012), DCTs (Zhou et al., 2014b,a), and CVTs (Gunji and Fujimoto, 2013; Hofman and Dai, 2010) into EVs. Unfortunately, these transmissions are not completely capable of providing the desired efficiency, performance, and drivability for EVs. This is due to the presence of clutches, torque converters, and hydraulic systems to cope with limitations of the internal combustion engines (Rahimi Mousavi and Boulet, 2014; Mousavi et al., 2014, 2015). This lack of an appropriate design was one of the main reasons for which early prototypes of EVs were equipped with single ratio transmissions with a trade-off between efficiency and dynamic performance (Walker et al., 2013). However, as mentioned earlier, research emphasizes that using properly designed multi-speed transmissions for EV's can reduce the size of the electric motor and provide a desired balance between efficiency and dynamic performance (Zhang

CHAPTER 1. INTRODUCTION

et al., 2013; Rahimi Mousavi and Boulet, 2014; Mousavi et al., 2014; Pakniyat and Caines, 2014a, 2015, 2016a; Walker et al., 2013; Zhou et al., 2014a; Gao et al., 2015). This, in fact, is one of the main reasons for which developing novel transmissions for EVs from the ground up has recently gained considerable momentum. This thesis aims at contributing to this topic by introducing a novel transmission specifically designed for EVs and developing its gear shift control technique. To this end, in this section, the main challenges are pinpointed in this context, namely the adopted transmission for EVs, dynamical modeling of the powertrain, state and disturbance estimation, and gear shift control strategies.

1.2.1. Adopted transmissions for EVs: challenges and obstacles

As mentioned in Section 1.1.3, there is an extensive literature on the application of ICEVs transmissions for EVs. Since these transmissions were initially designed for ICEVs, there are considerable challenges in retrofitting these transmissions into EVs which are briefly discussed in this subsection. Moreover, in this subsection, some of the transmissions specifically designed for EVs are introduced, and their advantages and drawbacks are discussed. The literature reviewed here constitutes a basis for proposing an innovative transmission for EVs.

Automated manual transmissions (AMTs) are of great interest for EVs because of their lower weight and higher efficiency in comparison with other types of transmissions such as ATs, CVTs, and DCTs (Lucente et al., 2007; Zhang et al., 2002; Ge et al., 2000). Specifically, clutchless automated manual transmissions (CLAMTs) wherein the clutch is eliminated from the powertrain to further improve efficiency. Although these transmissions are highly efficient, the torque interruption during the gear shift operation, which comes from the disengagement and re-engagement of the transmission synchronizer reduces passenger comfort (i.e., drivability) and the lifetime of the synchronizers. In fact, this type of transmissions suffers from the fundamental trade-off between efficiency and drivability (Gao et al., 2015; Liang et al., 2012).

In contrast to AMTs, DCTs have the special feature of eliminating the output torque interruption during gear shifts by controlling the pressure of the clutches together with the torque of traction unit. However, they have higher weight and lower efficiency, particularly DCTs with wet clutches (Naunheimer et al., 2010; Galvagno et al., 2011; Walker et al., 2011; Zhu et al., 2013; Zhou et al., 2014a).

As expressed in Section 1.1.3, the chain and belt CVTs are the most prevailing types of continuously variable transmissions adopted in the automotive industry. In chain/belt CVTs, the tension of the chain/belt plays a crucial role in the performance of the transmission. Excessive tension reduces the efficiency of the system and increases stress on the transmission. However, the tension should be adequate to avoid slippage (Naunheimer et al., 2010). In addition to these intricacies, the set of efficient operating points of electric motors is rich enough, and thus, the multiplicity of gear ratios or a continuously variable transmission may not be necessary for EVs (Mousavi et al., 2015; Srivastava and Haque, 2009b,a).

Similar to DCTs, planetary-gear-based ATs have the ability to eliminate the output torque interruption during the gear shift operation. However, due to the existence of torque converters and hydraulic systems in ATs, they have lower efficiency in comparison with other types of transmissions, and they are not of great interest for EVs. Furthermore, the provided power in the output of the transmission is decreased due to the power loss inside the torque converter when it is not completely engaged (Naunheimer et al., 2010; Jung et al., 2000; Haj-Fraj and Pfeiffer, 1999; Lazar et al., 2010; Asl et al., 2012).

There is no substantial literature supporting the application of manual transmissions (MTs) in EVs. This is due to the fact that in MTs the driver is the sole controller of the transmission system that performs the gear selection and gear shifts. Therefore, efficiency and driveability of the vehicle highly depend on the driver's skills. Consequently, there remains little opportunity for implementation of optimal control algorithms related to the transmission control. Hence, efficiency, drivability,

CHAPTER 1. INTRODUCTION

and lifetime improvements could not be addressed systematically (Kim et al., 2003; Kubur et al., 2004; Siriyapuraju et al., 2015; Gahagan et al., 2003; Li et al., 2015).

In addition to the above-mentioned systems, there has been a considerable research effort aimed at introducing transmissions specifically designed for EVs by considering the characteristics of electric motors and their advantages in comparison to ICEs. A novel two-speed layshaft type transmission for EVs is proposed by Sorniotti et al. (2012) in which the power is transferred via a one-way clutch in the first gear ratio and by a frictional clutch in the second one. A similar concept is adopted by Liang et al. (2012) in order to propose a novel AMT transmission for EVs called inverse automated manual transmission (I-AMT). In this system, the dry clutch is placed at the rear of the transmission in order to keep the tractive torque and eliminate the torque hole by means of a slipping sleeve. Further, a two-speed planetary gear-based transmission for EVs is patented by Wenthen (2013) in which the electric motor is connected to the sun gear of the first planetary gear set whose ring gear is grounded. The carrier of the first planetary gear set transfers the power to the transmission output shaft via either the sun or ring gears of the second planetary gear set depending on the state of the clutches. Similar patents have also been published by Weiss (1998); Bowen (2002); Zhang et al. (2016); Cavallino (2015).

Given the fact that ICEs cannot operate below a certain speed and controlling their speed is not an easy task, the presence of frictional and hydraulic couplings is inevitable for vehicle launching and gear shifting. This, however, is not the case for EVs as electric motors are speed controllable in terms of speed and torque in a wide range of operating. Therefore, the presence of clutches and torque converters is not necessary for the transmission designed for EVs (Mousavi et al., 2015). This has been addressed in novel designed proposed by Shin et al. (2014); Faid (2015) in which instead of clutches, brakes are used to seamlessly change the path of power flow and consequently the gear ratio.

In addition to the above-mentioned articles and patents, similar and relevant patents such as Rosemeier et al. (2013); Koser (1985); Holmes (2006); Mori and

Morikawa (1995); Ooyama et al. (1997); Hvolka et al. (2009); Matsuoka and Kitada (2013) have also been reviewed for development of the innovative system proposed in this thesis.

1.2.2. Powertrain Dynamical Model Approaches

A dynamical model of the vehicle powertrain is essential to design the control strategies and to implement the state estimation techniques. An accurate mathematical model of the powertrain provides an elaborate understanding of system responses to control inputs, the driver's command, and road disturbances. The powertrain mathematical model is typically derived by employing approaches such as the Newtonian method, Euler-Lagrange equations, the d'Alembert-Lagrange principle, the Hamilton principle, and graphical techniques (Greenwood, 2006; Goetz, 2005).

The Newtonian approach, which is also referred to as the vectorial dynamics, is established based on the free-body diagram of multi-body systems wherein the applied torques/forces on the isolated bodies are graphically visualized. In this method, the Newton-Euler equations are employed to determine the accelerations of isolated bodies for given applied torques/forces. This method is often adopted for modular modeling approaches due to the isolation of components. Moskwa et al. (1997); Ciesla and Jennings (1995) are the pioneers of the powertrain modeling using the modular technique (Goetz, 2005). They modeled the major components of powertrain as independent modules in simulation tools such as MATLAB/Simulink[®] wherein the powertrain model can be constructed by connecting these modules. This approach is then used by Lucente et al. (2007); Glielmo et al. (2006) in order to develop a dynamical model of the powertrains equipped with AMTs. Walker and Zhang (2013); Goetz (2005); Oh et al. (2014) employed the same method in order to derive a detailed dynamical model of the powertrain of an internal combustion engine vehicle retrofitted with a dual-clutch transmission. Walker and Zhang (2013) considered various degrees of freedom for the system and compared the responses of the derived models.

CHAPTER 1. INTRODUCTION

Although the Newtonian approach provides modeling flexibility and adaptability, for the multi-body systems with multiple constraints it may not be an appropriate option due to intricacies involved in the determination of the constraint forces/torques (Goetz, 2005).

In contrast to the Newtonian method, dynamical modeling of the system with constraints can be easily performed by exploiting approaches of analytical dynamics such as the Euler-Lagrange equations, the Hamilton principle, and the d'Alembert-Lagrange principle. These methods provide the dynamical model of multi-body systems by executing certain mathematical operations on a scalar function that contains the system's energies. This method is typically used when the overall dynamics of the system are sought rather than the dynamics of individual components. This method is of great interest for powertrains equipped with planetary gear-based transmissions wherein the overall dynamics of the transmission is required instead of the intermediate gears dynamics (Goetz, 2005).

The dynamical model of the vehicle powertrain can also be developed by exploiting graphical methods such as the bond-graph and lever analogy (Goetz, 2005). A key benefit of the bond-graph method is its ability to demonstrate the power flow in various fields identically (Goetz, 2005). This approach is used by Hubbard et al. (1997) wherein the transient and steady-state dynamical models of a hybrid electric vehicle powertrain are derived to develop control systems. This method is also adapted by Hrovat and Tobler (1991); Deur et al. (2006) in order to extract the dynamical model of the powertrain of an internal combustion engine vehicle equipped with an automatic transmission to design control strategies and to optimize simulation models. The lever analogy method is beneficial in the mathematical modeling of hybrid electric vehicle powertrains in which different power sources (e.g., electric motors and internal combustion engines) are coupled via planetary gear sets. In this method, torques and speeds are demonstrated on a lever. This method is adopted by Mashadi and Emadi (2010) wherein a novel dual-mode power split transmission for hybrid-electric vehicles is modeled.

1.2.3. Gear shift Control Criteria and Approaches

As mentioned earlier, the transmission system provides different combinations of torque and speed based on the selected gear ratio in order to meet the required efficiency and dynamic performance. Transitions among gear ratios are achieved through a so-called gear shift process. This operation needs to be performed and controlled systematically in order to meet a set of desired drivability and efficiency criteria.

Gear shift control strategies are typically classified into two main categories, namely the local and integrated control techniques (Goetz, 2005). Local control approaches are those in which gear shift processes are performed via an open-loop control of the motor or engine torque and independently from the transmission. However, in the integrated control techniques, the control of the motor or engine torque is concurrently carried out in a closed-loop control configuration together with the gear shift actuators (Goetz, 2005). Typically, the gear shift control problems are formulated in an optimal control framework in order to perform the state transitions from the initial values to the desired ones while optimizing certain performance measures such as maximizing gear shift quality, minimizing shifting time, and reducing energy dissipation during gear shift operations (Goetz, 2005; Mousavi et al., 2015, 2014; Pakniyat and Caines, 2014a, 2015, 2016a).

Different metrics have been introduced in order to measure the quality of gear shifts. Among these metrics, the longitudinal vehicle acceleration is identified to be one of the most important factors affecting passenger comfort and drivability of the vehicle (Goetz, 2005). The generated vibrations in the output of the transmission, which is originated from the motor and transmission vibrations, are reflected in the vehicle vibrations. Therefore, the transmission output torque can be monitored instead of the wheel torque in order to measure the quality of gear shifts. Studies demonstrate that the human body is sensitive to the aforementioned vibrations in the low frequencies (Goetz, 2005).

CHAPTER 1. INTRODUCTION

The gear shift process of the layshaft transmissions without powershift specification such as AMTs initiates by reducing the tractive torque to the vicinity of zero in order to facilitate the disengagement of the synchronizer and reduce oscillations in the driveline. This reduction of the tractive torque can be performed by either disconnecting the transmission clutch or controlling the torque of the traction unit in CLAMTs. After disengagement of the synchronizer from the off-coming gear, the motor/engine speed is matched with the speed of the target gear while the synchronizer is approaching the on-coming gear. The synchronization of the motor/engine speed with the speed of the target gear can be achieved either by controlling the clutch via the local or integrated powertrain approaches. In AMTs, during the gear shift operation, the motor/engine is disconnected from the driveline resulting in an interruption of the traction torque at the wheels which considerably affects passenger comfort. A considerable number of studies have been conducted on the improvement of the gear shift quality and drivability of the vehicles equipped with AMTs. The gear shift quality problem of AMTs is addressed in Gao et al. (2011) wherein an observer-based controller is designed to reduce the shock during the disengagement of the clutch. The controller entirely disengages the clutch while the estimated torque of the drive shaft reaches zero. The simulation results in AMESim demonstrated that the proposed controller improves the shifting time and quality while it is robust to parameter uncertainties and disturbances. In Gao et al. (2015), first, the gear ratios of the I-AMT is optimized by dynamic programming method in order to maximize the efficiency of the powertrain for urban and suburb drive cycles. Thereafter, for a two-speed transmission with optimal gear ratios, the control strategy is designed in order to eliminate the torque hole. The simulation results performed in AMESim environment confirm the claim of output torque interruption elimination. In recent years, CLAMTs for EVs have gained a lot of attentions. This is because of the accurate torque and speed controllability of the electric motor in comparison to the ICE. Reducing the gear shift time and improving the shift quality of an electric vehicle equipped with CLAMT are addressed in Yu et al. (2012). In this article, first, the

motor parameters are identified using the recursive least squares method. Thereafter, based on this parameter identification, a sliding control is designed for executing the speed synchronization process. A similar problem is tackled by Zhu et al. (2014) using a combination of state-feedback and H_∞ robust controllers to minimize the impact of disturbances on the speed synchronization.

The gear shift process in powershift transmission such as ATs and DCTs are different from AMTs wherein the former case the gear shift can be made seamless and without torque interruption. The gear shift control in ATs and DCTs is performed through two phases called the torque phase and the inertia phase. This method has been extensively employed in the literature (Goetz, 2005; Walker et al., 2011; Kulkarni et al., 2007; Zhu et al., 2013; Xiusheng et al., 2011).

In the torque phase, the motor/engine torque hands over from one clutch to the other one and in the inertia phase, the speed of the motor/engine is synchronized with the speed of the target gear. There are two types of powershift in ATs and DCTs namely, power-on and power-off shifts. In the power-on shift, the power is transferred from motor/engine to the vehicle. However, in the power-off shift, the vehicle drives the motor/engine and the vehicle energy can be restored in the batteries of EVs (Goetz, 2005).

The transmission proposed in this thesis is controlled via the torque and inertia phases in (Rahimi Mousavi and Boulet, 2014). However, as it is discussed in more detail throughout this thesis and also in Mousavi et al. (2015, 2014), due to the special design of the proposed transmission, torques and speeds are always dependent on each other through the transmitted power. Hence, the control strategy can be further improved such that it would not be required to be completely distinguished into the torque and inertia phases. This forms the basis for the controller design in this thesis and it is basically a significant departure from conventional methods.

1.2.4. Powertrain State and Disturbance Estimation Methods

A proper gear shifting process is typically achieved by optimization of certain measures such as the shifting time, the energy dissipation, and jerk (Oh and Choi,

CHAPTER 1. INTRODUCTION

2015; Oh et al., 2013, 2014; Mousavi et al., 2015, 2014; Rahimi Mousavi et al., 2015). Such a task is attainable only by means of an accurate real-time monitoring of the transferred torque through components of the powertrain and their angular velocities. However, using torque measurement devices and speed sensors other than currently available sensors on commercial vehicles such as the motor and wheels speed sensors is not desirable. This is because of the technical intricacies involved in the installation of these devices as well as their high cost and maintenance requirements. Therefore, an accurate estimation of these torques and speeds based on the readily available information from the powertrain, such as the speed of the motor and wheels as well as the electromagnetic torque of the motor, is required (Oh et al., 2013, 2014; Mousavi et al., 2015, 2014; Rahimi Mousavi et al., 2015).

There is an extensive literature on the torque and speed estimation of the vehicle powertrain equipped with multi-speed transmissions such as AMTs, DCTs, and ATs (Oh et al., 2013, 2014; Oh and Choi, 2015; Pettersson, 1997; Kim et al., 2006; Yi et al., 2000, 1999).

Given the fact that the case study transmission in this thesis incorporates different mechanical configuration and consequently different dynamical model, the currently available estimators mentioned above are not applicable to this design. In fact, the difference comes from the special design of the transmission proposed here and it is discussed in more detail in the subsequent chapters. Thus, an observer has to be designed from the ground up based on the dynamics of the new system.

1.3. Scope and Objectives of the Thesis

The goal of this thesis is to design a novel seamless two-speed transmission for EVs and to develop its state-of-the-art gear shift strategy. The design process is performed based on the models suggested by Pahl et al. (2007); French (1992); Angeles (2013). The mechanical layout is inspired from 4000 patents, journal articles, conference paper, and technical reports reviewed for this purpose. The design procedure, in fact, covers all the steps proposed by Pahl et al. (2007); French (1992); Angeles

1.3 SCOPE AND OBJECTIVES OF THE THESIS

(2013) spanning from the identification of need and problem analysis to the conceptual design and fabrication of a down-scaled proof-of-concept prototype. The proposed system consists of two planetary gear sets with common sun and common ring gears which consistently provides one overdrive and one underdrive ratios with a large step between these ratios. This is beneficial for EVs because electric motors are highly efficient throughout their speed range and having a large step between the first and second gear ratios considerably increases the area under the tractive effort-speed curve (Ehsani et al., 2009; Gao et al., 2015). Furthermore, the kinematic analysis of the transmission is performed using the vectorial method in order to characterize the achievable gear ratios as functions of the ratios of the planetary gear sets. Thus, the desired gear ratios can be obtained by appropriate selection of the ratios of the first and second planetary gear sets. This is beneficial for optimizing the overall gear ratios of the system based on the desired specifications and criteria.

A detailed dynamical model of the proposed transmission alongside other components such as the traction motor, flexible shafts, and final drive and wheels which generate and transfer the power to the road surface is derived using a combination of the Newtonian method and the d'Alembert-Lagrange principle. It is discussed in more detail in Chapter 3 that the dynamics of the proposed transmission is composed of continuous states and discrete states, and thus, its mathematical model is provided in the framework of hybrid dynamical systems. The derived dynamical model is verified by means of a simulation model built in MATLAB/Simulink® using SimDriveLineTM library and an experimental testbed designed and implemented for this purpose.

As mentioned earlier, using measurement devices in the powertrain to measure the state variables as well as the disturbances is not desirable in commercial vehicles. Instead, observers are commonly utilized in order to estimate these variables. Because the proposed transmission system has a different mechanical layout and consequently different dynamical model, the currently available estimators in the literature are not suitable for this design. To this end, based on the dynamical model of an EV equipped with the proposed transmission, the method of modeling unknown disturbances as

state variables of the a fictitious dynamical system is combined with the Kalman-Bucy filter (KBF) in order to design an observer to provide a concurrent estimation of unmeasured state variables and unknown disturbances. A set of experiments with distinct scenarios is performed to compare the performance of the designed stochastic observer with a deterministic one and to quantify by how much the KBF can improve the root mean square error (RMSE) of the estimation while mitigating the effect of the process and measurement noises.

Based on the dynamical model of the system and the established full-order observer, two optimal problems are solved using the Pontryagin minimum principle (PMP) to find the optimal control law minimizing the shifting time and the energy dissipation during the gear shift process while eliminating the torque hole at the transmission output. Further, in order to cope with the limitations of actuators, a feasible controller is designed by exploiting the Backstepping method. This is the main advantage of the proposed gear shift technique and it is discussed in more detail in Chapter 5.

1.4. Thesis Outline

This thesis includes six chapters and one appendix:

- Chapter 1 provides an overview of the major components of the EV powertrain. This review also encompasses the design of multi-speed transmissions for EVs as well as their dynamical modeling, gear shift control, and state estimation.
- Chapter 2 proposes a novel seamless clutchless two-speed transmission for EVs and its design procedure. Further, the kinematic analysis of the transmission and its achievable gear ratios are computed using the vectorial approach.
- Chapter 3 is devoted to the derivation of a dynamical model of the powertrain of an EV equipped with the proposed transmission. The derived dynamical model is verified by simulation and experimental analyses.

- Chapter 4 is dedicated to the design and validation of a stochastic observer to estimate the unmeasured state variables and imparted disturbances on the powertrain in the presence of process and measurement noises.
- Chapter 5 starts by solving two open-loop optimal control problems minimizing the shifting time and energy dissipation during the gear shift process to generate the desired state and output trajectories. Then, based on the solutions of these optimal control problems, a closed-loop controller is designed to track the optimal control law and its corresponding trajectories while coping with actuator limitations.
- Chapter 6 concludes the topic presented in this thesis and highlights the contributions and the areas for future research work.
- Appendix A provides the assembly drawings for the down-scaled prototype of the transmission designed and developed in this thesis.

CHAPTER 2

Dual Brake Transmission: Mechanical Design and Kinematic Analysis

This chapter is devoted to the mechanical design and kinematic analysis of a novel seamless, clutchless, compact transmission for electric vehicles called the *dual-brake transmission*¹. This thesis scrutinizes a two-speed transmission, however, the core structure of the proposed system has the ability to be stacked in series to provide a higher number of gear ratios, if required. The chapter starts off by explaining major steps performed in the design procedure of the proposed transmission from the identification of need and problem analysis to the conceptual design and fabrication of a down-scaled proof-of-concept prototype in Section 2.1. Thereafter, in Section 2.2, the kinematic analysis of the transmission and its achievable gear ratios are studied in order to be exploited in the dynamical modeling and control system design. Furthermore, it is described how desired overall gear ratios, such as optimal ones suggested in the literature (Walker et al., 2013; Gao et al., 2015), can be obtained by appropriate selection of the transmission and the final drive ratios.

In order to perform the kinematic analysis of the proposed transmission, existing methods in this realm are studied. Drawing from the literature review, the kinematic analysis of gear trains are typically performed via five principal methods: 1) signal

¹The utility patent for this invention is filed in the US (US20160091059) and Canada.

flow graphs, 2) tabular, 3) train value, 4) lever analogy, and 5) vector analysis (Tsai et al., 2010; Penaud and Alazard, 2010).

Wojnarowski and Lidwin (1975) were pioneers of the application of signal flow graphs in the kinematic analysis of gear trains informed by Mason's rule (Mason, 1953; Tsai et al., 2010). The manual procedure of converting the mechanism into the signal flow graphs is the main drawback of this method (Tsai et al., 2010; Penaud and Alazard, 2010). The tabular and train value methods are of great interest due to their simplicity. The tabular method, wherein the angular velocities are considered as scalar quantities, requires an extensive amount of calculation and may not be appropriate for complex mechanisms. The train value method is usually simpler than other methods, however, it is commonly used when the overall speed ratios of the mechanism are of interest (Tsai et al., 2010; Penaud and Alazard, 2010).

The lever analogy was initially introduced by Benford and Leising (1981) to analyse the kinematics of planetary gear-based mechanisms. In this method, each planetary gear set is presented by a single lever and the angular velocities of its sun gear, ring gear, and carrier are visualized on this lever. Due to the simplicity of this method, it has been widely used in the automotive technology and particularly electric vehicles and hybrid electric vehicles (Liu and Peng, 2008; Kim et al., 2011). However, in this method, the angular velocities of the planet gears are not typically demonstrated on the lever and consequently need to be calculated separately. Moreover, the entire procedure from sketching the levers to calculations of the angular velocities has to be performed manually (Kahraman et al., 2004).

The vector analysis method is relatively the most complicated method of kinematic analysis of gear trains but at the same time the most accurate one. This method provides the angular velocities of the internal components as well as the overall speed ratio (Penaud and Alazard, 2010). This method is adopted in this chapter to derive the kinematic equations of the proposed system.

2.1. Design of the Dual Brake Transmission

Design is an iterative process which undoubtedly involves creativity and requires systematic approaches (Angeles, 2013). Various models of design have been introduced in the literature among which the models suggested by Pahl et al. (2007); French (1992); Angeles (2013) are the most widely-used ones; particularly in the field of engineering design. The aforementioned models consist of four major steps: 1) analysis of the problem, 2) conceptual design, 3) embodiment design, and 4) detailing. In what follows, the design procedure of a proof-of-concept prototype of a novel transmission is explained aiming at creating an innovative system particularly designed for electric vehicles from the ground up (Angeles, 2013). This design can be easily retrofitted and scaled-up to the actual vehicle size after necessary modifications.

1) Problem analysis: The need for multi-speed and particularly two-speed transmissions for electric vehicles is identified throughout an extensive literature review presented in Chapter 1. Based on the identification of this need, a seamless, compact, two-speed transmission for electric vehicles is introduced while keeping in mind the possibility of its expansion to a multi-speed transmission. In fact, a multiplicity of gear ratios can be easily obtained by stacking a certain number of transmission core structures in series in a common housing. In other words, if each structure—a.k.a module—provides m_t numbers of gear ratios, stacking n_t number of them side-by-side provides $m_t^{n_t}$ speed ratios.

In order to come up with an appropriate structure, various gear train configurations are studied (Crolla, 2009; Naunheimer et al., 2010; Mashadi and Crolla, 2012). Among existing gear train configurations adopted in the automotive industry, planetary gear sets are selected as the building block of the transmission core structure. The rated torque and rated speed of these planetary gears have to be matched with the rated torque and rated speed of the traction motor(s) as well as the characteristics of the load. Moreover, as opposed to ICEs, electric motors are effectively operational and accurately

controllable throughout their speed range, and therefore, the presence of clutches or torque converters is not required in EVs powertrains. Thus, the transmission can be connected perpetually to the traction motor(s) from the input side and to the final drive via the output shaft. Finally, in order to improve efficiency and provide a compact design, the gear shift actuation systems can be selected to be electromechanical rather than hydraulic and pneumatic systems (Chopra, 2014; Jo et al., 2010; Furlani, 2001; Treder and Woernle, 2004).

- 2) **Conceptual design:** Based on the requirements stated in the previous step and an in-depth literature review carried out on the existing mechanisms, free-hand sketches are created with a rich set of alternatives. Thereafter, an extensive and iterative simulation analysis are performed based on the free-hand sketches. Ultimately, the scheme illustrated in Fig. 2.1 is selected due to its compactness, ease of implementation, and design simplicity which make it easy to scale to any desired size and application. Moreover, as it will be further discussed in the kinematic analysis section, the proposed system consistently provides an overdrive and an underdrive speed ratio which is beneficial for EVs due to the resultant large step between the first and second gear ratios (Pakniyat and Caines, 2014a; Walker et al., 2013; Gao et al., 2015; Morozov et al., 2014). The selected scheme illustrated in Fig. 2.1 is comprised of a dual-stage planetary gear set with common sun and common ring gears. The ratios of the pitch diameter of the ring gear to the sun gear in the first and second planetary gear sets are different in order to provide two distinct gear ratios. Moreover, two brake mechanisms are connected to the common sun and common ring gears in order to control the path of power flow and consequently the gear ratio. The input and output of the transmission are, respectively, the carriers of the first and second stages of the dual-stage planetary gear sets which are perpetually connected to

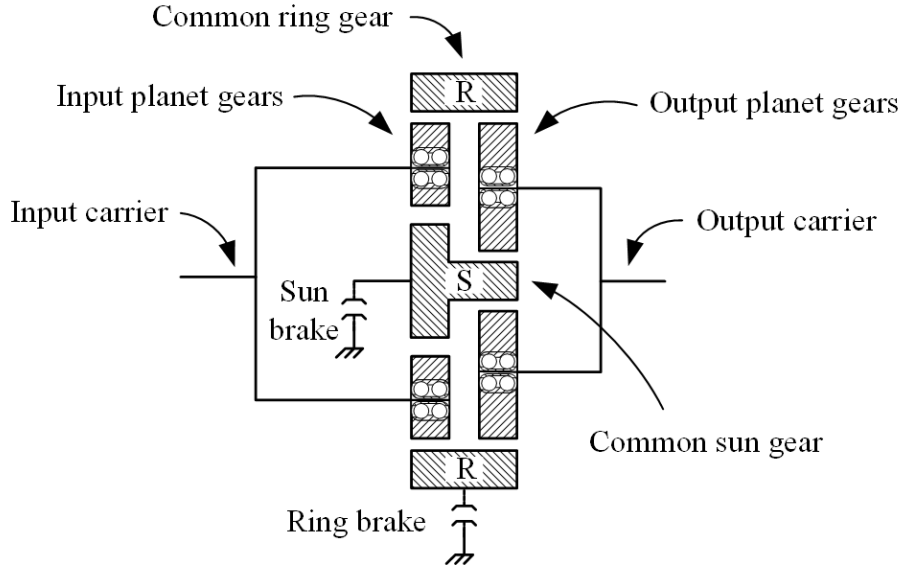


FIGURE 2.1. Schematic diagram of the DBT core structure

powertrain and there is no clutch or torque converter to disconnect this mechanical coupling.

As mentioned above, the proposed transmission in this thesis provides two distinct ratios and the kinematics analysis, dynamical modeling, and control systems design are performed for this two-speed transmission. A multiplicity of gear ratios can be achieved by connecting two or more cores of this transmission. Figure 2.2 illustrates how three modules can be connected in series in order to provide an 8-speed transmission.

- 3) **Embodiment of schemes:** Based on the selected scheme in the previous stage, preliminary design drawings for the proposed two-speed transmission are created using SolidWorksTM as the computer-aided design (CAD) software. The CAD drawings are initiated based on the preliminary dimensions obtained from off-the-shelf components selected based on the rated torque and speed of electric motors and rated force of the actuators.
- 4) **Detailed:** In this phase, detailed drawings of the custom made components are prepared for the manufacturing process considering required tolerances and fits.

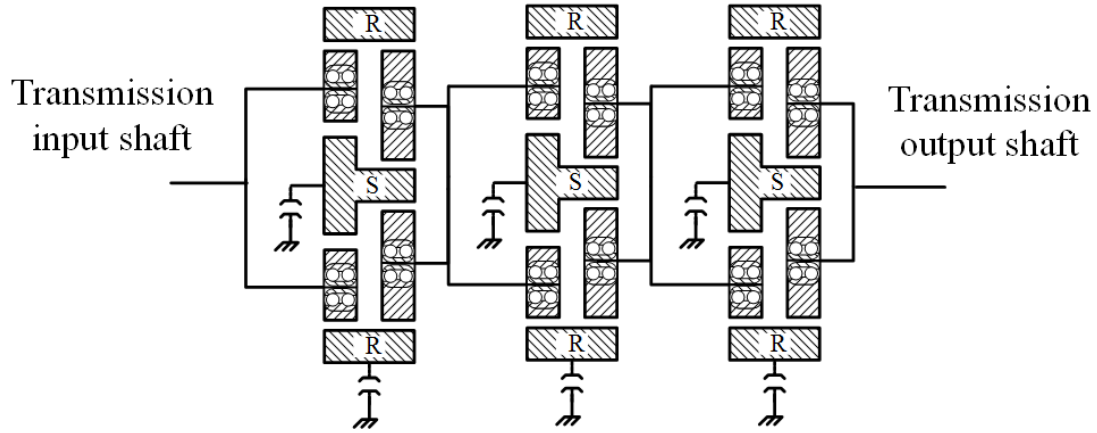


FIGURE 2.2. Schematic diagram of an 8-speed transmission

Finally, the proof-of-concept prototype of the proposed two-speed transmission shown in Fig. 2.3 is built and equipped with the required sensors and actuators for experimental analysis throughout this thesis.

The major components of the transmission, namely the dual-stage planetary gear set, the brake mechanism for sun gear, and the brake mechanism for the ring gear are illustrated in Fig. 2.4-2.7.

Figure 2.4 demonstrates the interconnections of the sun and ring gears of two planetary gear sets. These planetary gear sets have various input-output speed ratios in order to provide two distinct gear ratios when either the common sun gear or the common ring gear is grounded.

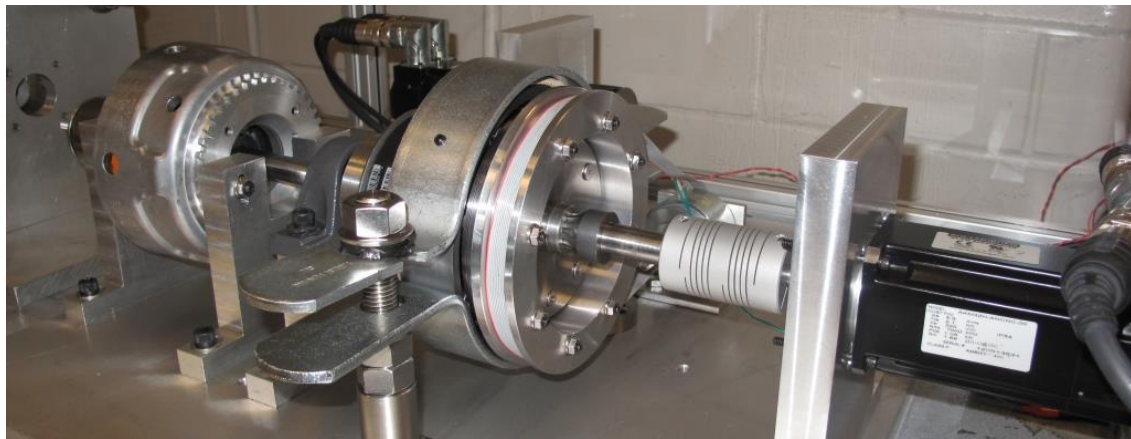


FIGURE 2.3. Proof-of- concept prototype of the proposed transmission for EVs

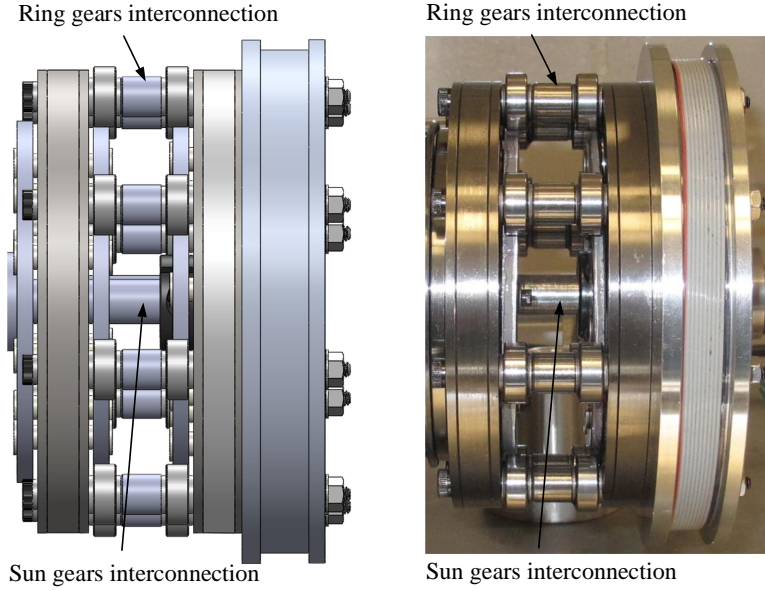


FIGURE 2.4. Interconnections of the sun and ring gears

The brake mechanisms of the sun and ring gears are selected to be the multi-plate brake and the band brake, respectively. Figure 2.5 and 2.6 illustrate the multi-brake mechanism for the common sun gears which mainly consists of an inner hub, an outer hub, an apply-plate, a force actuator, and a number of alternating friction and separator plates. Figure 2.7 depicts the band brake mechanism for the common ring gears which is composed of a drum, a band, and a force actuator. The friction models of these brake systems (i.e., force-torque relationship) are discussed in more detail in the next chapter.

In order to eliminate energy dissipation resulting from the sliding shear stress of wet brakes, the brake systems are designed to be of the dry type, and hence, would not encounter such an undesirable effect (Jibin et al., 2012; Zhou et al., 2014a; Iqbal et al., 2014).

It should be noted that the mentioned brakes in the proposed transmission could be of any type depending on the design of the transmission without any loss of seamless property. The band brake incorporates fewer components and is typically more efficient than the multi-plate brakes. However, the latter system has the benefit

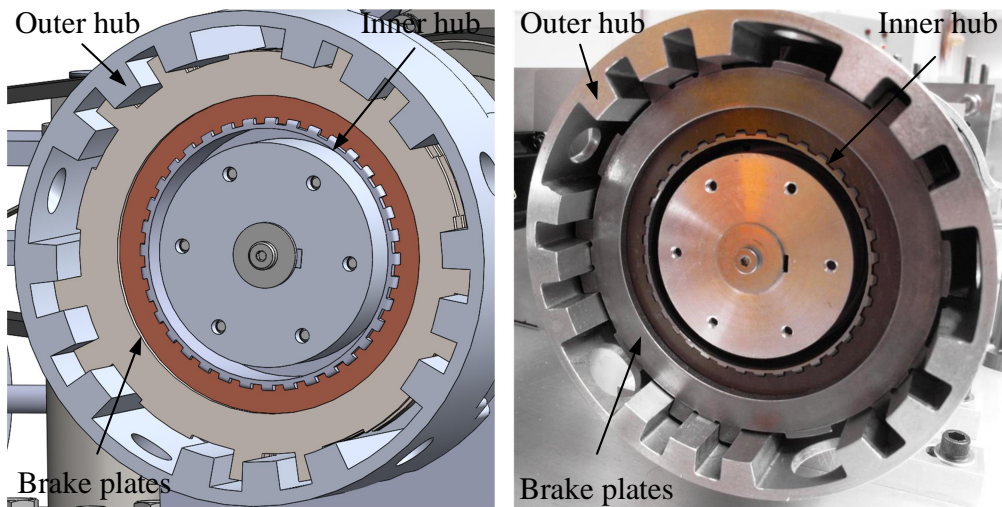


FIGURE 2.5. Multi-plate brake mechanism for the sun gears (interior view)

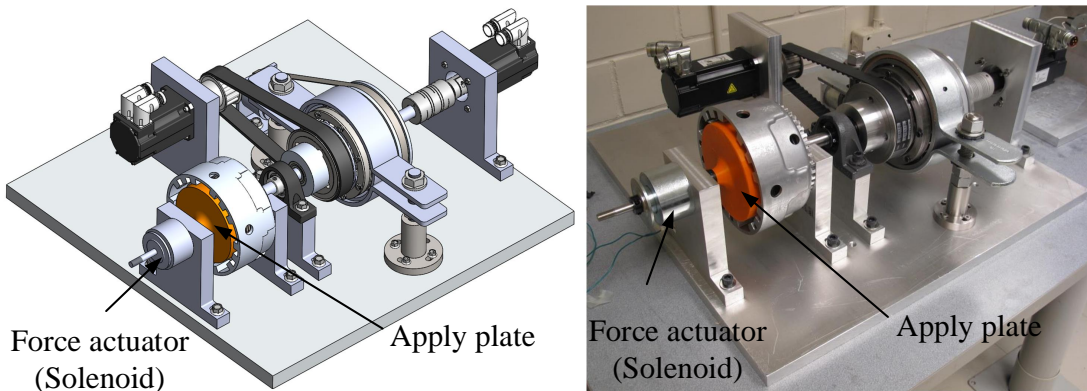


FIGURE 2.6. Multi-plate brake mechanism for the sun gears (exterior view)

of reducing the inertia of the rotating components and eliminating the inevitable radial force caused by the exerted force at the end of the band. Therefore, each brake system has its own advantages and disadvantages and they have to be selected based on desired criteria. The main reasons behind using multi-plate brake for sun gear and band brake for the ring gear in the design of the first prototype, which is, in fact, a proof-of-concept model, can be summed up into the following two factors: 1) ease of design and 2) fabrication cost (Mousavi et al., 2015).

2.1 DESIGN OF THE DUAL BRAKE TRANSMISSION

As illustrated in Fig. 2.8, the experimental test rig is equipped with two identical Kollmorgen AKM® 32H-ANCNC-00 AC synchronous servo motors as traction and load motors with the rated torque 1.45 Nm, the rated speed 314 rad/s, the maximum torque 7.26 Nm, and the moment of inertia 5.9×10^{-5} Kg.m². The motor drivers for the AKM® motors are Kollmorgen AKD®-P00606-NBAN-0000 analog servo drives. The motor drives provide speed measurement data of the motors as well as the imparted electromagnetic torques on the system ².

Two linear solenoids are adopted as the actuators for the brake mechanisms as shown in Fig. 2.6 and Fig. 2.7. These actuators are controlled by means of the Pulse Width Modulation (PWM) voltage controlled drivers which map the power supply input voltage to the solenoid based on the voltage command varying from 0 to 5 V³.

The electrical control system is designed based on the requirements of the prototype and the available power. For security purposes, all the electrical components are placed inside the enclosure shown in Fig. 2.9. The power for the motors drivers is taken from a NEMA 6-20R receptacle. This power passes through the circuit

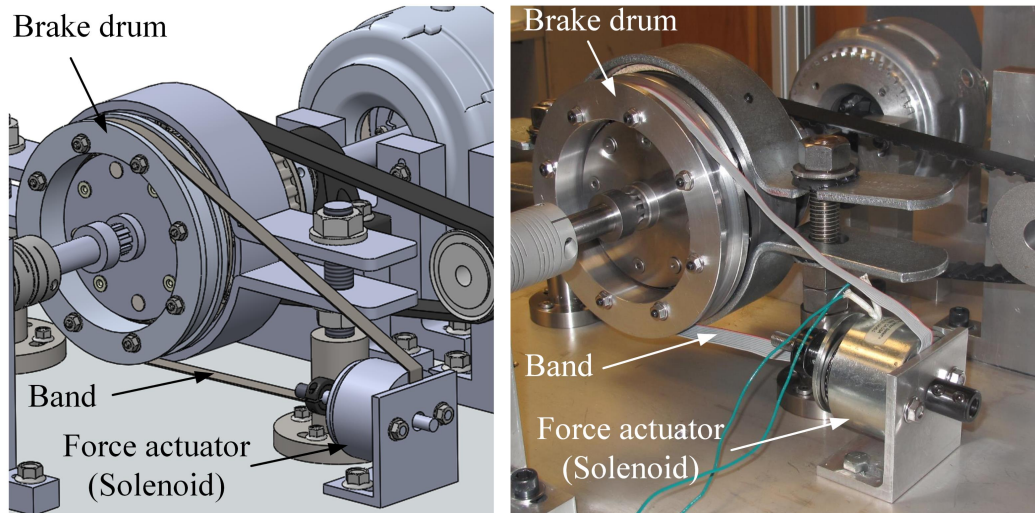


FIGURE 2.7. Band brake mechanism for the ring gears

²<http://www.kollmorgen.com/en-us/products/motors/servo/akm-series/>

³<http://www.magneticsensorsystems.com/>

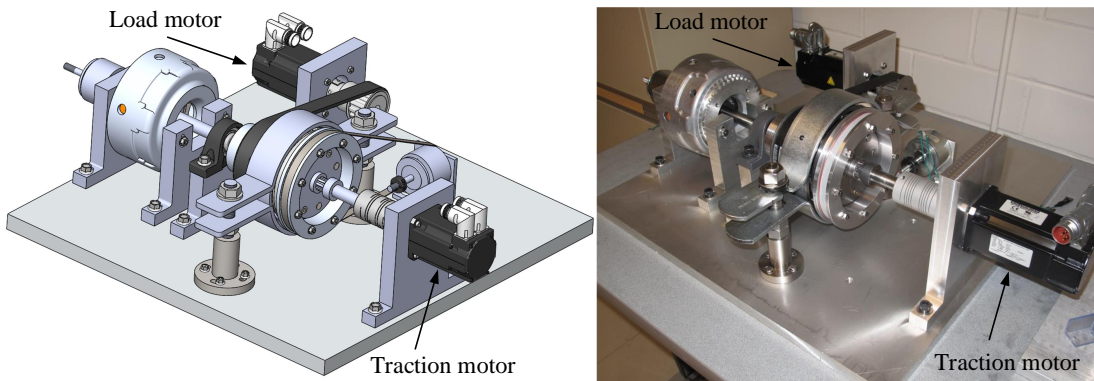


FIGURE 2.8. Experimental prototype equipped with the traction and load motors

breaker to prevent damage caused by overcurrent more than 20 A. Further, two separate starters are used to launch the servo motors separately and a pilot light is associated with each starter indicating whether the motor is powered or not. Two electromagnetic interference (EMI) filters are considered for each motor driver in order to mitigate conducted interference that is present on the power line. Moreover, an emergency stop mushroom push button is considered for safety purposes.

The National Instruments' CompactRIO®, which is an industrial control system, is chosen for communication, processing, data logging, and control purposes. This system is mainly comprised of a real-time embedded controller, reconfigurable digital and analog modules, a chassis with an embedded FPGA (Field-programmable gate array). The LabVIEW® software is used for Windows®, real-time, and FPGA programming.

Figure 2.10 illustrates the architecture of the control, data logging, and processing systems. In this structure, a multi-tiered programming technique is adopted wherein the FPGA of the CompactRIO® is operating at the frequency of 0.5 MHz as the target and the real-time controller of the CompactRIO® is processing at the frequency of 1 kHz as the host. The FPGA module interacts with the digital and analog modules on the chassis at the former frequency at which the control commands and feedback data are transferred. The real-time controller, as the host, receives the feedback data from

2.1 DESIGN OF THE DUAL BRAKE TRANSMISSION

the FPGA target and sends corresponding control commands while logging required data at 1 kHz. This architecture is adopted due to the following reasons ⁴:

- 1) Complex data processing and control strategies cannot fit on the FPGA.
- 2) Some operations such as double- or extended-precision are not available on the FPGA.
- 3) To avoid buffer overflow and control the sequence of data transfer.

The LabVIEW® software runs on the local PC in order to provide a user-interface to set the initial values, tune parameters, and monitor the entire process of control and data logging. The motor drives, which are powered by 230 VAC, transfer torque and speed data to the CompactRIO® and servo motors. The solenoid drivers, which are connected to 30 VDC power supply, transmit current/voltage data and command signals to the CompactRIO® and solenoid actuators.

⁴http://zone.ni.com/reference/en-XX/help/371599H-01/lvfgaconcepts/pfi_comm/

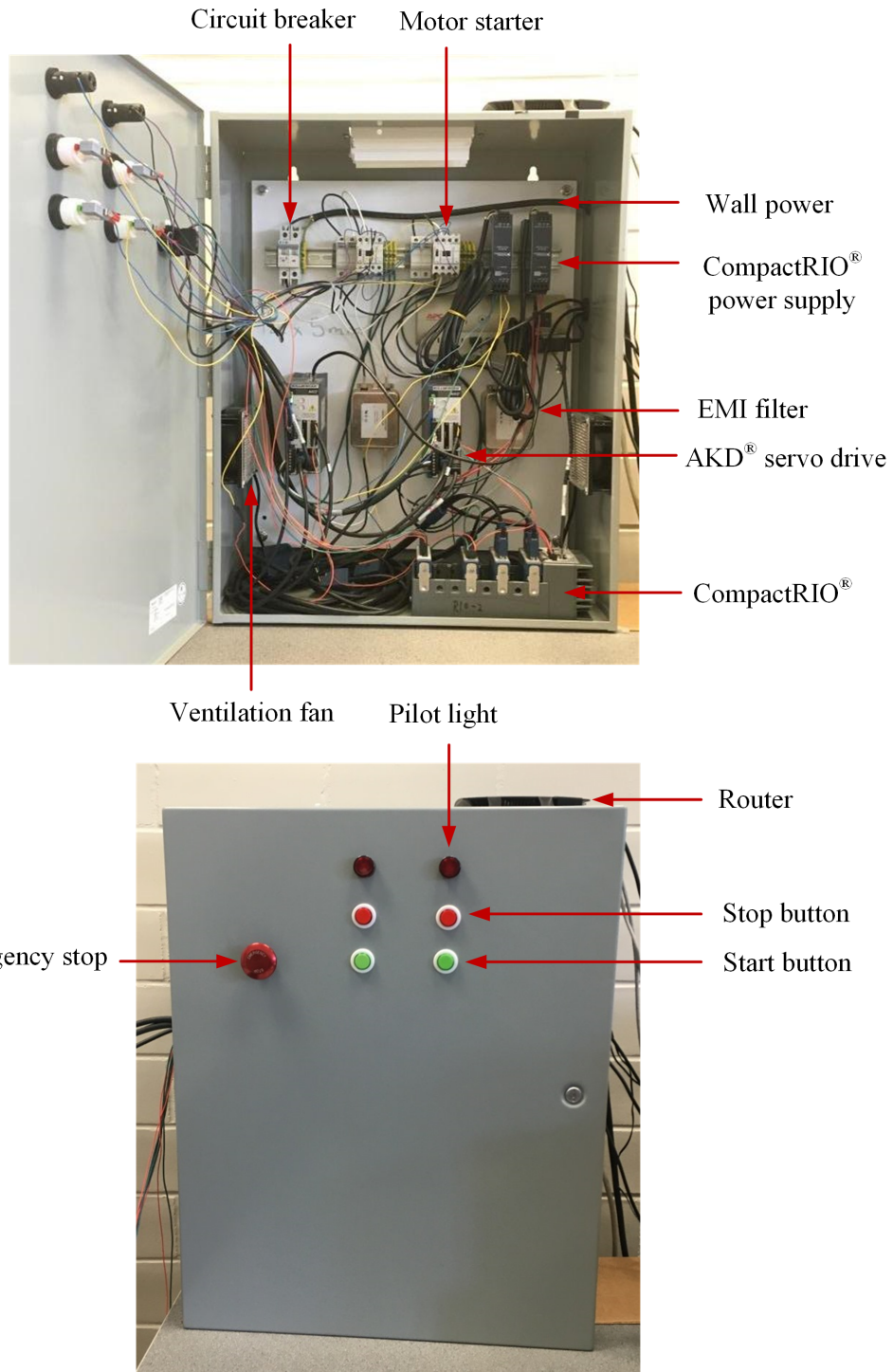


FIGURE 2.9. Control enclosure and its components

2.1 DESIGN OF THE DUAL BRAKE TRANSMISSION

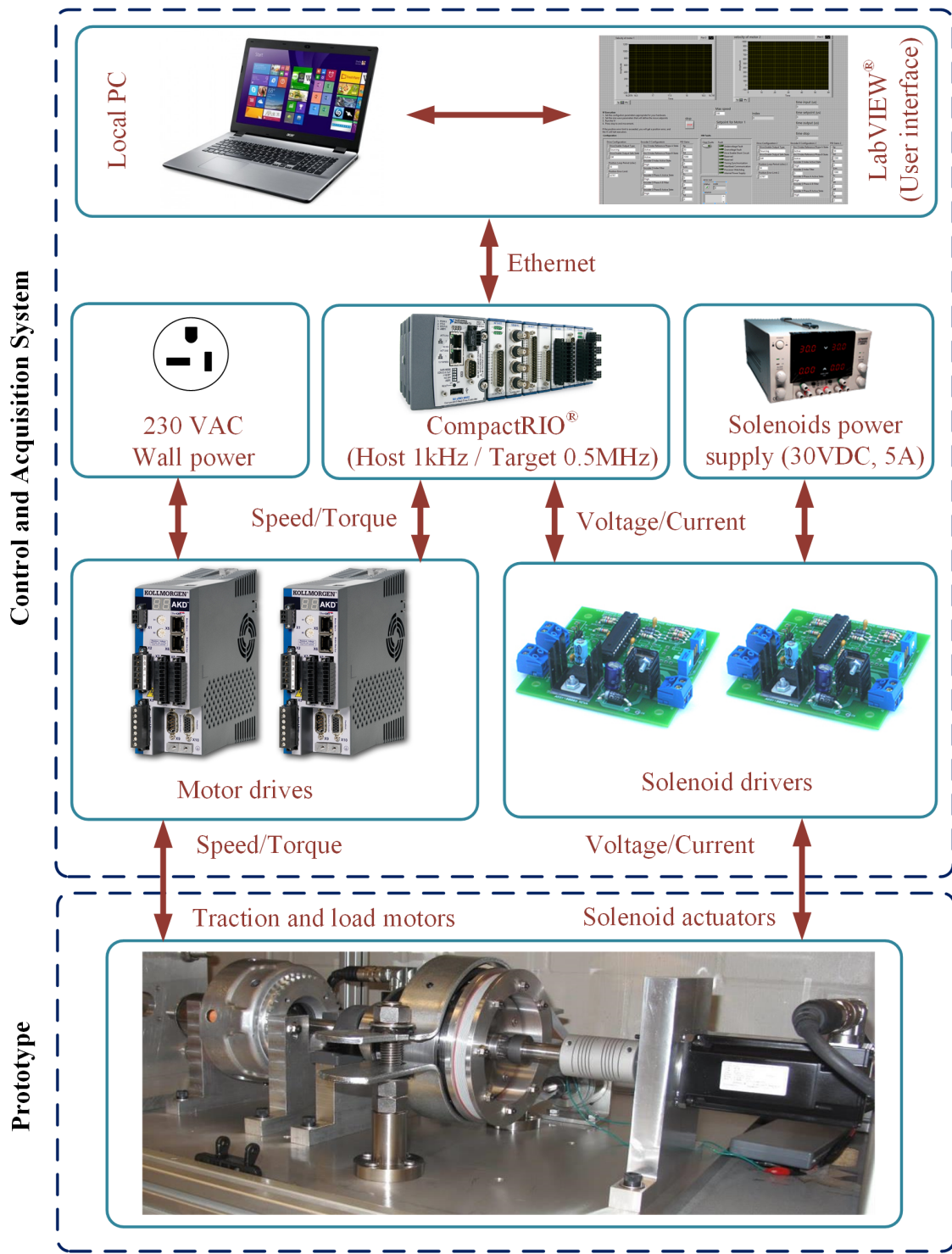


FIGURE 2.10. Structure of the control, communication, data logging, and processing systems for the experimental test rig

2.2. Kinematic Analysis

In this section, the kinematic relations among the components of a planetary gear set, namely carrier (C), sun (S), planets (P), and ring (R), and consequently among the components of the dual-stage planetary gear set shown in Fig. 2.1 are determined. Thereafter, based on the kinematic equations, the paths of power flow are described and the achievable gear ratios of the proposed transmission are investigated in order to be utilized throughout this thesis.

2.2.1. Kinematic Equations

Using the vector analysis method for the planetary gear shown in Fig 2.11, velocity relations among points A_1 , A_2 , and A_3 are expressed by:

$$\vec{v}_{A_1} = \vec{v}_{A_2} + \vec{\omega}_P \times \vec{r}_{A_1 A_2}; \quad \vec{r}_{A_1 A_2} = \vec{r}_{A_1} - \vec{r}_{A_2}, \quad (2.1a)$$

$$\vec{v}_{A_2} = \vec{v}_{A_3} + \vec{\omega}_P \times \vec{r}_{A_2 A_3}; \quad \vec{r}_{A_2 A_3} = \vec{r}_{A_2} - \vec{r}_{A_3}, \quad (2.1b)$$

where $\vec{\omega}_P$ is the angular velocity of the planet gears; \vec{r}_{A_1} , \vec{r}_{A_2} , \vec{r}_{A_3} are the position vectors of points A_1 , A_2 , A_3 , respectively. Given the fact that the planet gears mesh with ring and sun gears, $\vec{v}_{A_{1,R}} = \vec{v}_{A_{1,P}}$ and $\vec{v}_{A_{3,S}} = \vec{v}_{A_{3,P}}$. Therefore, Equation (2.1) can be rewritten as follows:

$$\vec{\omega}_R \times \vec{r}_{A_1} = \vec{\omega}_C \times \vec{r}_{A_2} + \vec{\omega}_P \times \vec{r}_{A_1 A_2}, \quad (2.2a)$$

$$\vec{\omega}_C \times \vec{r}_{A_2} = \vec{\omega}_S \times \vec{r}_{A_3} + \vec{\omega}_P \times \vec{r}_{A_2 A_3}, \quad (2.2b)$$

where $\vec{\omega}_R$, $\vec{\omega}_C$, $\vec{\omega}_S$ are the angular velocities of the ring gear, the carrier, and the sun gear, respectively. Decomposing Equation (2.2) in the inertial coordinate frame and considering the fact that the angular velocities of components of the planetary gear set in x and y directions are zero, Equations 2.2 can be further simplified and expressed by the following scalar equations:

$$r_R \omega_R = r_P \omega_P + r_C \omega_C; \quad r_R = r_P + r_C, \quad (2.3a)$$

$$r_C \omega_C = r_P \omega_P + r_S \omega_S; \quad r_C = r_P + r_S, \quad (2.3b)$$

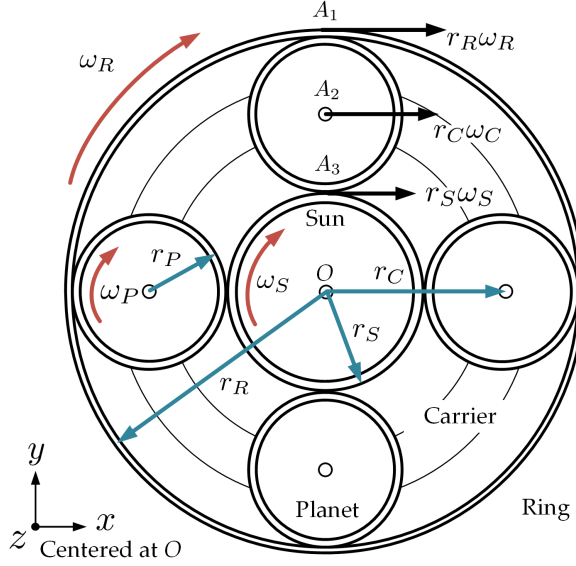


FIGURE 2.11. Planetary gear set and its major components

where r_S , r_P , and r_R are the pitch radii of the sun, planet, and ring gears, respectively. The parameter r_C is the radius of the circle on which the planets are mounted. The variables ω_S , ω_P , ω_R , and ω_C are the angular velocities of the sun gear, planet gears, ring gear, and carrier around the z axis, respectively. From (2.3a) and (2.3b), the kinematic relation between the ring, the sun, and the carrier is presented as follows wherein ω_P and r_P are eliminated:

$$(r_R + r_S)\omega_C = r_S\omega_S + r_R\omega_R. \quad (2.4)$$

To simplify notation, the ratio of the pitch radius of the ring (r_R) to the sun (r_S) for the first and second stages of the planetary gear sets are defined as:

$$R_1 := \left(\frac{r_R}{r_S} \right)_{1^{st} \text{ stage}}, \quad (2.5a)$$

$$R_2 := \left(\frac{r_R}{r_S} \right)_{2^{nd} \text{ stage}}. \quad (2.5b)$$

Given the fact that in planetary gear sets the ring diameter is generally greater than the sun's, from (2.5) it is concluded that:

$$R_1 > 1, \text{ and } R_2 > 1. \quad (2.6)$$

From (2.3)-(2.5) the angular velocities of the input carrier ($\omega_{C,in}$), the output carrier ($\omega_{C,out}$), the input planets ($\omega_{P,in}$), and the output planets ($\omega_{P,out}$) of the dual-stage planetary gear set of the DBT shown in Fig. 2.1 can be expressed as angular velocities of the sun (ω_S) and the ring (ω_R) as follows:

$$\omega_{C,in} = \frac{R_1\omega_R + \omega_S}{(R_1 + 1)}, \quad (2.7a)$$

$$\omega_{C,out} = \frac{R_2\omega_R + \omega_S}{(R_2 + 1)}, \quad (2.7b)$$

$$\omega_{P,in} = \frac{R_1\omega_R - \omega_S}{(R_1 - 1)}, \quad (2.7c)$$

$$\omega_{P,out} = \frac{R_2\omega_R - \omega_S}{(R_2 - 1)}. \quad (2.7d)$$

Expressing all angular velocities as functions of the angular velocities of the sun and ring gears (ω_S & ω_R) in (2.7) is not only beneficial for the analysis of the achievable gear ratios in the next subsection but also it is advantageous in the derivation of equations of motion. This will be explained in more detail in the next chapter wherein the generalized coordinates for the derivation of the system dynamics are chosen to be $q = [\theta_S \ \theta_R]^T$, where θ_S and θ_R are the angular displacements of the sun and ring.

In order to provide a better understanding of how the proposed transmission provides two distinct gear ratios, the powertrain of an electric vehicle equipped with such a transmission is conceptually illustrated in Fig. 2.12. The input and output carriers of the DBT are connected to the electric motor and the final drive, respectively, via flexible shafts modeled by spring-damper systems. This structure is discussed and modeled in more detail in the next chapter. In Fig. 2.12, the paths of power flow in the first gear ratio, in the second gear ratio, and during the gear shift process are highlighted. The first gear ratio corresponds to the case in which the ring gear is grounded and the power is transferred via the sun gear, whereas for the second gear ratio the sun gear is grounded and ring gear transmits the power to the wheels. During the transition between the first and second gear ratios, the power is transferred through both sun and ring gears.

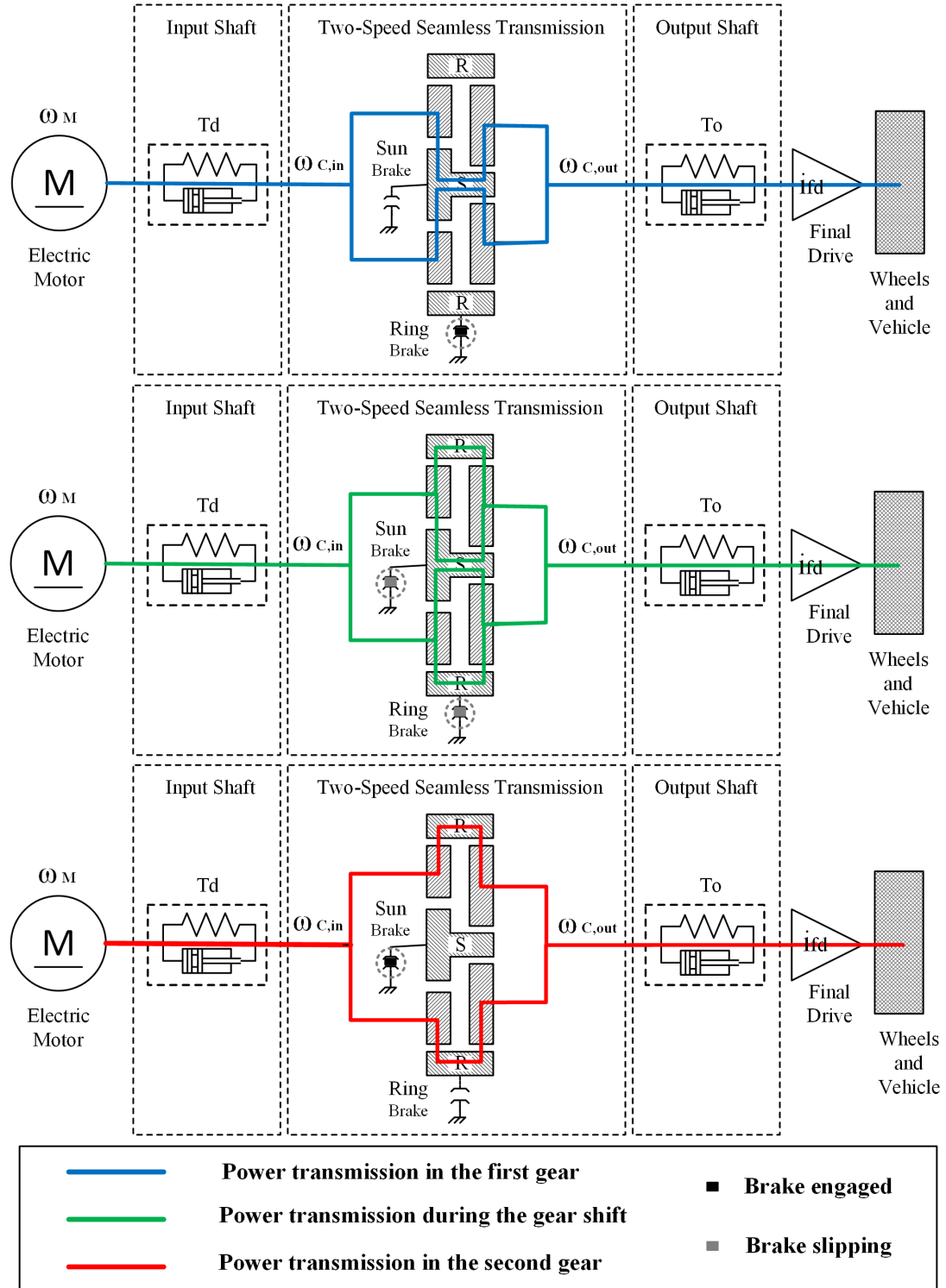


FIGURE 2.12. Schematic view of the power transmission paths, (top): power transmission path in the first gear, (middle): power transmission paths during the gear shift, (bottom): power transmission path in the second gear.

2.2.2. Gear Ratios of the DBT

According to Equations (2.7), the overall gear ratio of the transmission (the ratio of the input speed to the output speed) can be expressed as follows:

$$\frac{\omega_{C,in}}{\omega_{C,out}} = \frac{(R_2 + 1)(\omega_S + R_1\omega_R)}{(R_1 + 1)(\omega_S + R_2\omega_R)}. \quad (2.8)$$

From equation (2.8), the following gear ratios are achievable from the proposed transmission:

- (i) If the ring gear is completely grounded ($\omega_R = 0$):

$$GR_1 \triangleq \frac{\omega_{C,in}}{\omega_{C,out}} = \frac{(R_2 + 1)}{(R_1 + 1)} \quad (2.9)$$

- (ii) If the sun gears is completely grounded ($\omega_S = 0$):

$$GR_2 \triangleq \frac{\omega_{C,in}}{\omega_{C,out}} = \frac{(R_2 + 1)R_1}{(R_1 + 1)R_2} \quad (2.10)$$

- (iii) If neither the sun gear nor the ring gear is grounded ($\omega_R \neq 0$ and $\omega_S \neq 0$):

$$GR_T \triangleq \frac{\omega_{C,in}}{\omega_{C,out}} = \frac{(R_2 + 1)(\omega_S + R_1\omega_R)}{(R_1 + 1)(\omega_S + R_2\omega_R)} \quad (2.11)$$

Here, GR_1 and GR_2 are considered to be the two fixed gear ratios of the transmission, while GR_T is the transient gear ratio from one gear ratio to the other during the gear shift process. Although the gear ratios are dependent, the equations (2.9) and (2.10) can be solved for R_1 and R_2 in order to obtain the desired GR_1 and GR_2 . It can be proven that choosing the desired values for GR_1 and GR_2 such that one of the following two sets of conditions holds

$$C_1 : \begin{cases} GR_1 + GR_2 > 2 \\ GR_1 + GR_2 < 2 GR_1 GR_2 \end{cases} \quad (2.12a)$$

$$C_2 : \begin{cases} GR_1 + GR_2 < 2 \\ GR_1 + GR_2 > 2 GR_1 GR_2 \end{cases} \quad (2.12b)$$

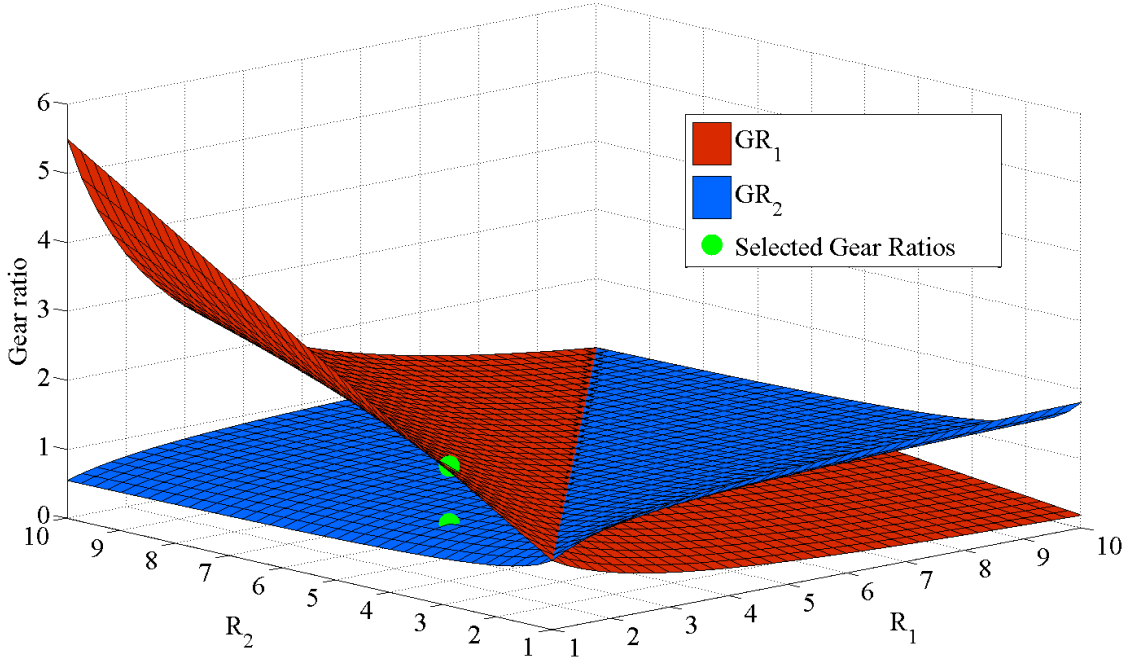


FIGURE 2.13. Achievable GR_1 and GR_2 by varying R_1 and R_2

results in such R_1 and R_2 that satisfy the physical constraints expressed by (2.6).

The achievable gear ratios of the proposed two-speed transmission are illustrated in Fig. 2.13 as functions of R_1 and R_2 . As it can be seen in Fig. 2.13, the proposed transmission with the gear ratios given in (2.9) and (2.10) consistently features one underdrive ($GR < 1$) and one overdrive ($GR > 1$) gear ratios.

The effect of gear ratio selection on the efficiency and dynamic performance is studied in Walker et al. (2013) wherein genetic algorithms are used in order to determine the optimal range of gear ratios for a pure electric vehicle permanent magnet AC motor and equipped with a two-speed transmission. The results show that the dynamic performance is highly dependent on the gear ratio selection while efficiency is not considerably affected by the transmission gear ratios. Thus, the possibility of improving the dynamic performance of EVs is an advantage of multi-speed transmissions compared to single speed ones. For the DBT system, the optimal overall gear ratios can be obtained by appropriate selection of R_1 , R_2 , and the final drive ratio (i_{fd}). For instance, by selecting $R_1 = 2$ and $R_2 = 4$, which results in $GR_1 = 1.667$

and $GR_2 = 0.833$, and taking the final drive ratio $i_{fd} = 5$, the overall gear ratios 8.333 and 4.167 are achievable. These gear ratios lie within the optimal ranges for the two-speed electric vehicle reported in Walker et al. (2013).

The aforementioned gear ratios $GR_1 = 1.667$ and $GR_2 = 0.833$ are chosen in this thesis. A large gap between the first and the second gear ratios has been recommended in the literature for two-speed electric vehicles (Pakniyat and Caines, 2014a; Walker et al., 2013; Gao et al., 2015; Morozov et al., 2014). This large step size, in fact, makes the gear shift a challenging task and this is what the remainder of this thesis is about.

CHAPTER 3

Dynamical Model of the Powertrain

In this chapter, the dynamical model of an electric vehicle powertrain equipped with the transmission proposed in Chapter 2 is derived, constituting the basis for designing gear shift controllers and states/disturbances estimators in subsequent chapters. This dynamical model yields system responses to the inputs. In order to analyse drivability of the vehicle, these responses are typically studied in low-frequency ranges and most commonly within the range 0-15 Hz. Powertrain vibrations in this frequency range—*a.k.a* shuffle oscillations—have various sources such as abrupt changes in the traction torque and gear shift operations and would noticeably degrade vehicle drivability if not systematically controlled. High-frequency vibrations, which affect the noise behaviour of the powertrain, are typically filtered out by backlashes and are not the subject of this study (Goetz, 2005; Fredriksson et al., 2002; Berriri et al., 2008).

The structure of the electric vehicle powertrain equipped with the proposed transmission is schematically illustrated in Fig. 3.1. The powertrain is mainly comprised of a traction motor, the proposed two-speed transmission, wheels and the vehicle frame which are connected together via steel shafts whose torsional compliances are taken into consideration and modeled by spring-damper systems as shown in Fig. 3.1. This four-degree of freedom model of the powertrain considered here has also been suggested by Walker et al. (2011); Zhu et al. (2013); Oh and Choi (2015) wherein powertrains equipped with DCTs are modeled.

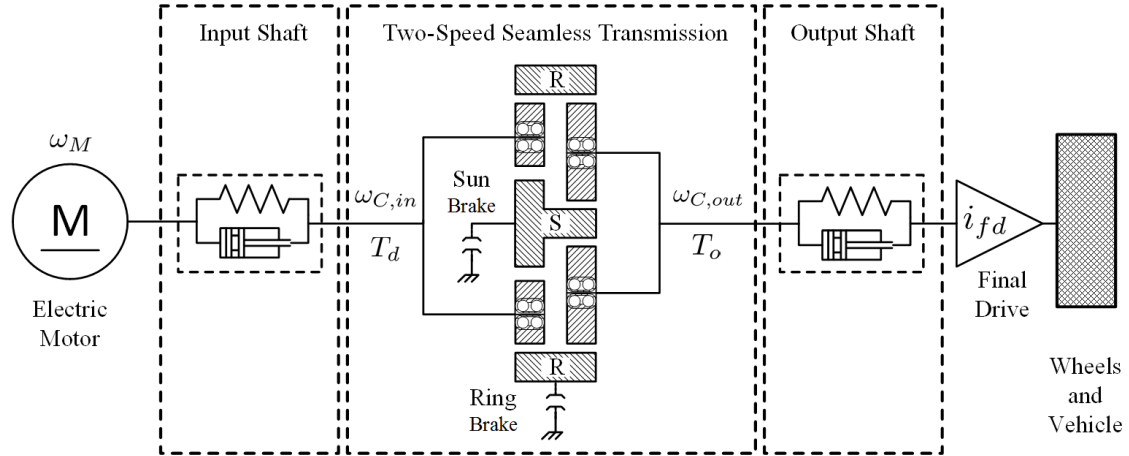


FIGURE 3.1. Schematic diagram of the powertrain of an electric vehicle equipped with the proposed seamless clutchless two-speed transmission

For the sake of computational efficiency and simplification of the driveline illustration, it is assumed that the half shafts and wheels are identical. It is also considered that vehicle cornering does not occur and the final drive and differential assembly exerts equal torques on the half shafts with no tire slippage. Thus, the half shafts and driven wheels are integrated together and considered as one half shaft and wheel structure as depicted in Fig. 3.1. Moreover, the backlash in the gears and flexibility of components with high stiffness are not taken into account in order to reduce computational complexities. The above-mentioned assumptions have been proposed and discussed in detail by Oh et al. (2013); Oh and Choi (2015); Goetz (2005); Walker and Zhang (2013). As expressed in Chapter 1, powertrain modeling using the Newtonian method is typically adopted for modular approaches and it is of great interest due to its flexibility and adaptability. Here, the dynamical model of the traction motor, wheels, and vehicle are derived using this method. However, due to intricacies involved in determining constraint forces/torques of the transmission system and since the dynamics of the transmission as a whole is desired rather than the dynamics of gears as individual bodies, its dynamical model is provided by exploiting one of the principles of analytical dynamics, namely, the d'Alembert-Lagrange principle (Angelles, 2002; Greenwood, 2006; Ginsberg, 1998).

This chapter starts off with the presentation of the rotational dynamics of the traction motor via the Newtonian method in Section 3.1. This is followed by the derivation of the flexible shafts models in Section 3.2 wherein the shaft compliances are taken into consideration. Section 3.3 begins by elaborating on the transmission's degrees of freedom and constraints, constituting the basis for developing a detailed dynamical model of the transmission. The DBT dynamical model is derived by exploiting the d'Alembert-Lagrange principle together with friction models in the framework of a hybrid dynamical system. In Section 3.4, the longitudinal vehicle dynamics expressing external longitudinal forces acting on the vehicle such as the tractive force, aerodynamic drag forces, gravitational forces, and rolling resistance, are discussed. Therefore, the linear solenoid as electromechanical gear shift actuator is introduced in Section 3.5 and its current-force relation is experimentally characterized for accurate control of the gear shifts. Ultimately, in Section 3.6, the derived dynamical model of the powertrain is validated through various sample drive cycles. This model validation is performed by means of a simulation model built in MATLAB/*Simulink*[®] and the experimental apparatus described in Chapter 2.

3.1. Rotational Dynamics of the Electric Motor

The rotational dynamics of the electric motor determine the angular acceleration of the rotor. According to the free-body diagram of the electric motor shown in Fig. 3.2, the dynamics of the rotor are obtained by using Euler's equation:

$$\dot{\omega}_M = \frac{T_M - T_d}{J_M}, \quad (3.1)$$

where J_M , T_M , and ω_M are the inertia, the electromagnetic torque, and the angular velocity of the motor, respectively. Here, T_d is the torque applied to the transmission.

3.2. Flexible Input and Output Shaft Models

As shown in Fig. 3.1, flexibilities of the input and output shafts of the transmission, and more precisely their torsional compliances, are taken into consideration

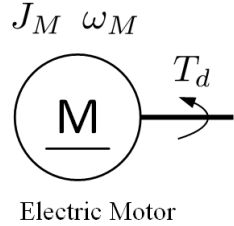


FIGURE 3.2. Free-body diagram of the electric motor

in the dynamical modeling of the powertrain. The input shaft transmits the power between the electric motor and the transmission and the output shaft transfers the power from the transmission to the wheels and vice versa.

The flexible input shaft is modeled with two distributed inertias which are connected together with a spring-damper system. One-half of the shaft inertia (including the inertias of the drive shaft and differential if present) is lumped to the inertia of the motor and the other half is integrated into the inertia of the transmission input carrier. Drawing from the free-body diagram of the input shaft illustrated in Fig. 3.3(a), the transmitted torque T_d can be obtained based on the angular positions and velocities of the electric motor and the input carrier of the DBT as follows:

$$T_d = K_d(\theta_M - \theta_{C,in}) + B_d(\omega_M - \omega_{C,in}), \quad (3.2)$$

where K_d and B_d are the equivalent torsional stiffness and damping constants of the flexible input shaft; θ_M and $\theta_{C,in}$ are the angular displacements of the motor and the input carrier, respectively. By taking the derivative of (3.2) with respect to time and neglecting the damping term (Oh et al., 2013; Oh and Choi, 2015), the torque rate of the input shaft can be approximated as follows:

$$\dot{T}_d = K_d(\omega_M - \omega_{C,in}). \quad (3.3)$$

In like manner, the output shaft is modeled with two distributed inertias which are connected together with a spring-damper system. One-half of the shaft inertia is lumped to the output carrier of the DBT and the other half is integrated into the inertia of wheels. As illustrated in Fig. 3.3(b), the output shaft torque of the

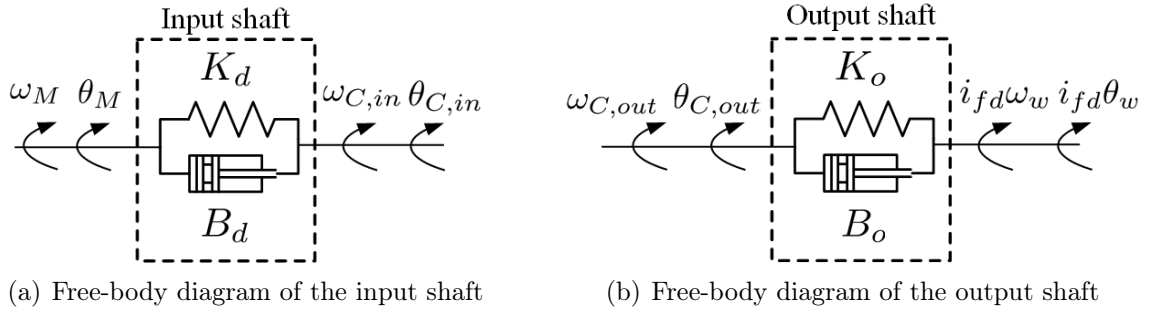


FIGURE 3.3. Free-body diagram of the transmission's input and output shafts

transmission can be computed based on the angular positions and velocities of the transmission output carrier and final drive as follows:

$$T_o = K_o(\theta_{C,out} - i_{fd}\theta_w) + B_o(\omega_{C,out} - i_{fd}\omega_w), \quad (3.4)$$

where K_o and B_o are the equivalent torsional stiffness and damping constants of the flexible output shaft; $\theta_{C,out}$ and θ_w are the angular displacements of the output carrier and the wheels, respectively. In Equation (3.4), ω_w stands for the angular velocity of the wheels. By taking the derivative of (3.4) with respect to time and neglecting the damping term (Oh et al., 2013; Oh and Choi, 2015), the torque rate of the output shaft can be approximated as follows:

$$\dot{T}_o = K_o(\omega_{C,out} - i_{fd}\omega_w). \quad (3.5)$$

3.3. Dynamical Model of the DBT System

3.3.1. Degrees of Freedom and Constraints

As explained earlier in Chapter 2 and based on the free-body diagram of the transmission system depicted in Fig. 3.4, the system is comprised of two planetary gear sets with common sun and common ring gears and offers two-speed ratios. The ratio of the pitch diameter of the ring gear to the sun gear in the first and second sets are different in order to provide two distinct gear ratios. The brake mechanisms connected to the common sun and common ring gears specify the path of power flow

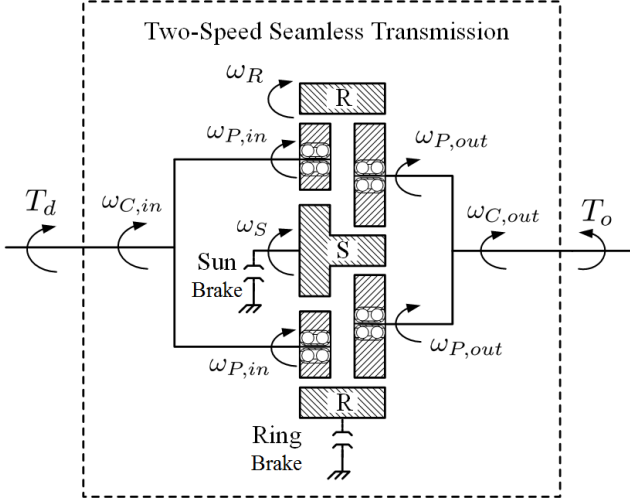


FIGURE 3.4. Free-body diagram of the dual brake transmission (DBT)

and consequently the overall gear ratios of the transmission. The traction motor is connected to the carrier of the first planetary gear set and the final drive is linked to the carrier of the second one. The transmission is perpetually linked to the powertrain and there is no clutch or torque converter to disconnect this mechanical coupling.

Deducing from the kinematic analysis given by Equations (2.7)-(2.11) and the assumptions about the rigidity of the gears expressed in the beginning of this chapter, the transmission system has one degree of freedom when it is operating in either the first or the second gear ratio. In these cases, angular velocities of transmission components can be expressed by the angular velocity of either the sun gear (ω_s) or the ring gear (ω_R). However, the mechanism is transformed to a system with two degrees of freedom when the power transfers through both sun and ring gears ($\omega_s \neq 0 \wedge \omega_R \neq 0$). The latter case happens during the gear shift operations when the off-coming brake is disengaging and the on-coming one is engaging in order to change the path of power flow and consequently the gear ratio. It should be noted that when both brakes are released the transmission system still has two degrees of freedom, however, the power could be trapped inside the system resulting in rotating the sun and ring gears in reverse directions and consequently no or low power transmission would occur. Therefore, the brakes should not be completely released simultaneously.

TABLE 3.1. Constraints classification of mechanical systems

Constraint	Description
Holonomic	Constraints can be expressed as functions of positions in the form $f(\theta_1, \theta_2, \dots, \theta_n, t) = 0$
Nonholonomic	Constraints are expressed as non-integrable relations among positions and velocities in the form $f(\theta_1, \theta_2, \dots, \theta_n, \dot{\theta}_1, \dot{\theta}_2, \dots, \dot{\theta}_n, t) = 0$
Scleronomic	Constraints are not time dependent
Rheonomic	Constraints are time dependent

The first step in deriving the dynamical model of the system is to investigate the class of mechanical system to which the case study system belongs. Mechanical systems are mostly classified based on their constraints into holonomic or nonholonomic and scleronomous or rheonomous systems (Angeles, 2002; Greenwood, 2006). A brief description of this categorization and corresponding constraints are listed in Table 3.1 wherein $\{\theta_1, \theta_2, \dots, \theta_n\}$ are the system coordinates (Angeles, 2002; Greenwood, 2006). According to the Equation (2.7) and Table 3.1, the dual brake transmission is a holonomic and scleronomous mechanical system. In the holonomic systems, the minimum number of coordinates required to define the system configuration is equal to the number of degrees of freedom. These coordinates are most commonly called minimum or independent generalized coordinates and they are denoted by ξ_k in this thesis. As mentioned earlier, the transmission system has one degree of freedom in the first gear ratio or the second gear ratio but the number of degrees of freedom increases to two during the gear shift operation (Angeles, 2002; Greenwood, 2006; Mousavi et al., 2015; Pakniyat and Caines, 2015, 2016a; Mousavi et al., 2014). This is because of transitions between the stiction and sliding phases of the friction surfaces which affect the number of degrees of freedom (Pfeiffer and Glocker, 1996). Thus, the selected coordinates during the gear shift process are a set of descriptor variables in the first gear ratio and the second gear ratio rather than the generalized coordinates. There are two ways to derive the dynamics of the system which have the aforementioned transition between different phases with various degrees of freedom. The first

method, which looks the straightforward one, is to define different sets of generalized coordinates for each phase of operation and derive the equation of the motion for each phase, independently. This method is not of great interest because dynamics of the system have to be derived from the ground up for different combinations of constraints. More importantly, for systems that involve Coulomb friction, in which frictional torques depend on phases of the Coulomb friction (slip/stick), the derivation of the system dynamics using this method would be more intricate (Pfeiffer and Glocker, 1996). The other technique, which is adopted in this thesis, is to fuse the unilateral constraints along with the dynamics of the system in the framework of a hybrid dynamical system (Pakniyat and Caines, 2015, 2016a). This hybrid dynamical model is composed of continuous states which describes the evolution of the system in each mode and discrete states that indicate in which mode the system is operating. The unilateral constraints specify the transition between the discrete states.

3.3.2. Hybrid Dynamical System Formulation for the DBT System

In order to provide the hybrid dynamical model of the DBT system (Pakniyat and Caines, 2015, 2016a), the nomenclature of hybrid systems are presented.

Definition 3.1 A hybrid dynamical system possessing both continuous and discrete behaviours is a tuple $H = (\mathcal{Q}, \mathcal{X}, \mathbf{f}, Init, Dom, \mathcal{E}, \mathcal{G}, \mathcal{R})$ where (Lygeros, 2004; Pakniyat and Caines, 2015; Goebel et al., 2012, 2009; Van Der Schaft and Schumacher, 2000; Khalil and Grizzle, 1996; Shaikh and Caines, 2007; Taringoo and Caines, 2013; Pakniyat and Caines, 2016b):

- $\mathcal{Q} = \{q_1, q_2, \dots, q_{|\mathcal{Q}|}\}$ is a finite set of discrete states ($|\mathcal{Q}| < \infty$);
- $\mathcal{X} \subseteq \mathbb{R}^n$ is a finite dimensional manifold of continuous states;
- $\mathbf{f}(\cdot, \cdot, \cdot) : \mathcal{Q} \times \mathcal{X} \times \mathcal{U} \rightarrow \mathbb{R}^n$ is a vector field satisfying the Lipschitz condition.

$$\exists L_f < \infty : \|f(q_i, \mathbf{x}_1, \mathbf{u}) - f(q_i, \mathbf{x}_2, \mathbf{u})\| \leq L_f \|\mathbf{x}_1 - \mathbf{x}_2\|, \forall \mathbf{x}_1, \mathbf{x}_2 \in \mathbb{R}^n, \mathbf{u} \in \mathcal{U}, q_i \in \mathcal{Q};$$

where $\mathcal{U} \subset \mathbb{R}^l$ is a set of l -dimensional input vectors;

- $Init \subseteq \mathcal{Q} \times \mathcal{X}$ is a set of initial conditions of the states;

- $\text{Dom}(\cdot) : \mathcal{Q} \rightarrow \mathcal{P}(\mathcal{X} \times \mathcal{U})$ is a domain associated to each $q_i \in \mathcal{Q}$ wherein a continuous evolution proceeds;
- $\mathcal{E} \subseteq \mathcal{Q} \times \mathcal{Q}$ is a set of edges indicating transitions among discrete events;
- $\mathcal{G}(\cdot) : \mathcal{E} \rightarrow \mathcal{P}(\mathcal{X} \times \mathcal{U})$ is a guard condition assigned to each edge satisfaction of which results in a transition from one edge to the other;
- $\mathcal{R}(\cdot, \cdot, \cdot) : \mathcal{E} \times \mathcal{X} \times \mathcal{U} \rightarrow \mathcal{P}(\mathcal{X})$ is a reset map updating continuous states when the aforementioned transition occurs;

$\mathcal{P}(\mathcal{X})$ is the power set of \mathcal{X} and (q_i, \mathbf{x}) is the state of the hybrid system $\mathcal{H} := \mathcal{Q} \times \mathcal{X}$.

The hybrid dynamical system starts off with an initial state $(q_1, \mathbf{x}_0) \in \text{Init}$ and the continuous state \mathbf{x} evolves based on the following vector field:

$$\dot{\mathbf{x}} = \mathbf{f}(q_1, \mathbf{x}, \mathbf{u}), \quad \mathbf{x}(0) = \mathbf{x}_0, \quad (3.6)$$

while the discrete event q_1 remains unaltered $q(t) = q_1$ and $\mathbf{x} \in \text{Dom}(q_1)$. Upon satisfaction of the guard condition $\mathcal{G}(q_1, q_2)$ of the edge $(q_1, q_2) \in \mathcal{E}$, the discrete event jumps from q_1 to q_2 and consequently the continuous states are updated based on the reset map $\mathcal{R}(q_1, q_2, \mathbf{x}, \mathbf{u})$. Thereafter, the continuous state flows according to the vector field $\mathbf{f}(q_2, \mathbf{x}, \mathbf{u})$ before meeting the guard condition of the next transition (Lygeros, 2004; Goebel et al., 2012, 2009).

The case study transmission has three discrete states q_1 , q_2 , and q_3 corresponding to the system dynamics in the first gear $\mathbf{f}(q_1, \mathbf{x}, \mathbf{u})$, the second gear $\mathbf{f}(q_2, \mathbf{x}, \mathbf{u})$, and during the gear shift process $\mathbf{f}(q_3, \mathbf{x}, \mathbf{u})$, respectively. Therefore,

$$\mathcal{Q} = \{q_1, q_2, q_3\}. \quad (3.7)$$

These discrete states are correlated with the combinations of phases of the friction model which are explained subsequently. The continuous states associated with the system dynamics are chosen to be the angular velocities of the sun and ring gears:

$$\mathbf{x} = \begin{bmatrix} \omega_S & \omega_R \end{bmatrix}^T, \quad \mathbf{x} \in \mathcal{X} = \mathbb{R}^2. \quad (3.8)$$

The control inputs to the transmission system are the frictional torque of the sun and ring brakes ($\mathcal{U} = \mathbb{R}^2$). Moreover, it is assumed that the system is always launched from stationary initial conditions in the first gear (q_1). Hence $Init = (q_1, \mathbf{0})$.

The domain of q_1 , q_2 , and q_3 are considered as:

$$Dom(q_1) = Dom(q_2) = Dom(q_3) = \mathcal{P}(\mathbb{R}^2 \times \mathbb{R}^2). \quad (3.9)$$

Transitions from first gear (q_1) to the second gear (q_2) and vice versa are required to traverse through the gear shift state (q_3). Thus, the set of edges describing all possible transitions between the discrete states of the system is expressed by:

$$\mathcal{E} = \{(q_1, q_3), (q_3, q_1), (q_2, q_3), (q_3, q_2)\}. \quad (3.10)$$

Each edge is associated with a guard condition and a reset map. As explained earlier, the guard conditions specify whether a transition from a discrete state to the other one occurs or not, and when a guard condition is satisfied, the reset map updates the values of the continuous states. In this thesis, continuous states do not change after discrete transitions and hence the reset map is the identity function. Thus,

$$\mathcal{R}(q_i, q_j, \mathbf{x}, \mathbf{u}) = \mathbf{x}, \forall (q_i, q_j) \in \mathcal{E}. \quad (3.11)$$

Figure 3.5 depicts a directed graph $(\mathcal{Q}, \mathcal{E})$ representing the hybrid dynamical system of the transmission. Each vertex is associated with a vector field and a domain; a guard condition and a reset map are assigned to each edge (Lygeros, 2004).

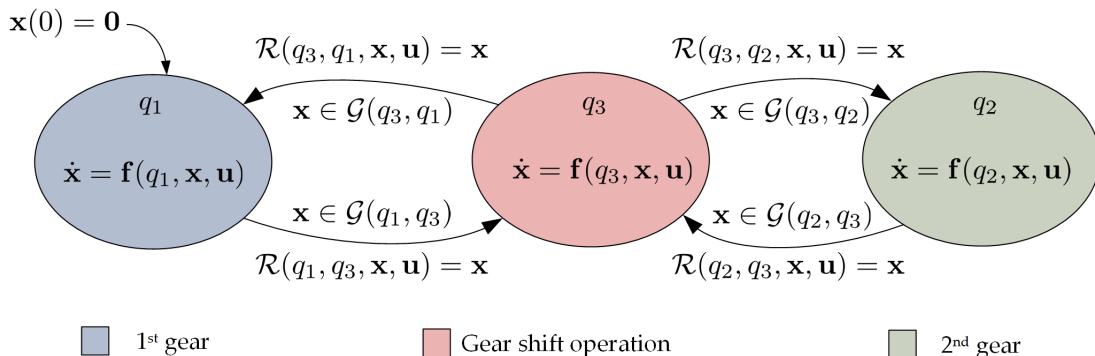


FIGURE 3.5. Hybrid dynamical model of the DBT system

In order to establish of the hybrid dynamical model of the system, the vector fields, and the guard conditions are required to be determined. To this end, the d'Alembert-Lagrange principle is applied to obtain the vector fields and the friction models are exploited in order to specify the guard conditions.

3.3.3. D'Alembert-Lagrange Principle

The d'Alembert-Lagrange principle—*a.k.a* extended principle of virtual work—states that the summation of the virtual work of the non-conservative applied torques and the inertia torques is zero for all virtual displacements fulfilling system constraints. This principle can be formulated as follows for a system with m generalized coordinates ξ_k , $k \in \{1, \dots, m\}$ (Kovacs, 2012; Greenwood, 2006; Lanczos, 1970; Ginsberg, 1998; Angeles, 2002; Goldstein et al., 2001):

$$\sum_{k=1}^m \left[\Xi_k^{appl,nc} - \frac{d}{dt} \left(\frac{\partial L}{\partial \dot{\xi}_k} \right) + \frac{\partial L}{\partial \xi_k} \right] \delta \xi_k = 0, \quad (3.12)$$

where $L = K - V$ is the Lagrangian and K and V are the kinetic energy and potential energy of the system, respectively. In Equation (3.12), the term $\delta \xi_k$ is virtual displacements of the generalized coordinates and $\Xi_k^{appl,nc}$ denotes the generalized applied torque and it is computed as follows:

$$\Xi_k^{appl,nc} = \sum_{i=1}^n T_i \frac{\partial \theta_i}{\partial \xi_k} = \sum_{i=1}^n T_i \frac{\partial \dot{\theta}_i}{\partial \dot{\xi}_k}, \quad (3.13)$$

where the terms n , T_i , and θ_i respectively denote the number of system components, applied torques on these components, and their virtual displacements.

Given the fact that the constraints of the system provided by (2.7) are holonomic and all the angular velocities of the DBT components are stated as functions of the angular velocities of the sun and ring gears, the generalized coordinates are selected to be the angular positions of these gears $\boldsymbol{\xi} = [\theta_S \ \theta_R]^T$.

The centre of mass of the system is considered as the reference point for the gravitational potential energy and it is assumed that all the mechanical components are rigid. Therefore, the potential energy of the entire system is kept constant and

equal to zero ($V = 0$). The kinetic energy of the system consists of the kinetic energy of the input and output carriers, the common ring gears, the common sun gears, and the four input and four output planet gears and it is expressed as follows:

$$K = \frac{1}{2}J_S\omega_S^2 + \frac{1}{2}J_{C,in}\omega_{C,in}^2 + 4\left(\frac{1}{2}J_{P,in}\omega_{P,in}^2 + \frac{1}{2}m_{P,in}r_{C,in}^2\omega_{C,in}^2\right) \\ + \frac{1}{2}J_R\omega_R^2 + \frac{1}{2}J_{C,out}\omega_{C,out}^2 + 4\left(\frac{1}{2}J_{P,out}\omega_{P,out}^2 + \frac{1}{2}m_{P,out}r_{C,out}^2\omega_{C,out}^2\right), \quad (3.14)$$

where $J_{C,in}$, $J_{C,out}$, J_S , J_R , $J_{P,in}$, and $J_{P,out}$ are moments of inertia of the input carrier, the output carrier, the sun gear, the ring gear, input planets, and output planets about the principal axis parallel to their axis of rotation, respectively. The terms $m_{P,in}$ and $m_{P,out}$ are the masses of the input and output planets. By substituting terms $\omega_{C,in}$, $\omega_{C,out}$, $\omega_{P,in}$, and $\omega_{P,out}$ from (2.7) the kinetic energy is expressed as a function of generalized velocities $\dot{\xi} = [\omega_S \ \omega_R]^T$:

$$K = 4\left(\frac{1}{2}J_{P,in}\frac{\omega_S^2 + R_1^2\omega_R^2 - 2R_1\omega_R\omega_S}{(R_1 - 1)^2}\right) + 4\left(\frac{1}{2}J_{P,out}\frac{\omega_S^2 + R_2^2\omega_R^2 - 2R_2\omega_R\omega_S}{(R_2 - 1)^2}\right) \\ + \frac{1}{2}J_S\omega_S^2 + \frac{1}{2}(J_{C,in} + 4m_{P,in}r_{C,in}^2)\frac{\omega_S^2 + R_1^2\omega_R^2 + 2R_1\omega_R\omega_S}{(R_1 + 1)^2} \\ + \frac{1}{2}J_R\omega_R^2 + \frac{1}{2}(J_{C,out} + 4m_{P,out}r_{C,out}^2)\frac{\omega_S^2 + R_2^2\omega_R^2 + 2R_2\omega_R\omega_S}{(R_2 + 1)^2}. \quad (3.15)$$

According to Equation (3.12) and (3.13), the generalized applied torques on the system are required to be computed as functions of generalized coordinates in order to extract the equations of motion using d'Alembert-Lagrange principal and consequently to determine the vector fields $\mathbf{f}(q_1, \mathbf{x}, \mathbf{u})$, $\mathbf{f}(q_2, \mathbf{x}, \mathbf{u})$, and $\mathbf{f}(q_3, \mathbf{x}, \mathbf{u})$. This is the topic of the following subsection.

3.3.4. Determination of the Generalized Applied Torques

The generalized applied torque ($\Xi_k^{appl,nc}$) is computed based on Equation (3.13) knowing all the external torques imparted on the system. For the DBT system, the applied torques are categorized into the following three groups: 1) transmission input torque, 2) transmission output torque, and 3) frictional torques and spin losses.

3.3.4.1. *Transmission input torque.* The transmission input torque denoted by T_d is applied to the carrier of the first planetary gear set via the flexible input shaft connecting the electric motor to the transmission.

3.3.4.2. *Transmission output torque.* The transmission output torque denoted by T_o is applied to the carrier of the second planetary gear set through the flexible output shaft linking the transmission to the final drive.

3.3.4.3. *Frictional torques and spin losses.* The frictional torques exerted on the transmission are classified into two main categories, namely controllable and uncontrollable frictional torques. The controllable frictional torques are basically the control inputs applied to the sun and ring gears via the brake mechanisms in order to control the flow of power and consequently the gear ratio. These frictional torques are modeled by Coulomb friction law.

In this thesis, the brake of the sun is designed to be of the multi-plate type as illustrated in Fig. 3.6. The multi-plate brake pack is composed of an inner hub, an outer hub, an apply-plate, a force actuator, and a number of alternating friction and separator plates. The contact area of the friction and separator plates is an annulus with the inner radius R_i and the outer radius R_o as marked in Fig. 3.6(a). The outer teeth of the inner hub mesh with the inner teeth of friction plates and the inner teeth of the outer hub are engaged with the outer teeth of separator plates as depicted in Fig. 3.6(b). Here, the inner hub of the brake mechanism is connected to the common shaft of the sun gears and the outer hub is grounded. Moreover, the apply-plate as shown in Fig. 3.6(c), imparts the resultant force of the linear solenoid actuator to the friction and separator plates and consequently changes the frictional brake torque applied to the common sun gears. In this thesis, this frictional torque is denoted by T_{BS} .

As illustrated in Fig. 3.7, the brake of the ring is designed to be of the band brake type comprising of a drum, a band, and a force actuator. The band is wrapped around the drum brake with the radius R_D and the wrap angle θ_D as illustrated in Fig. 3.7. The force actuator tightens the band around the rotating drum and it brings

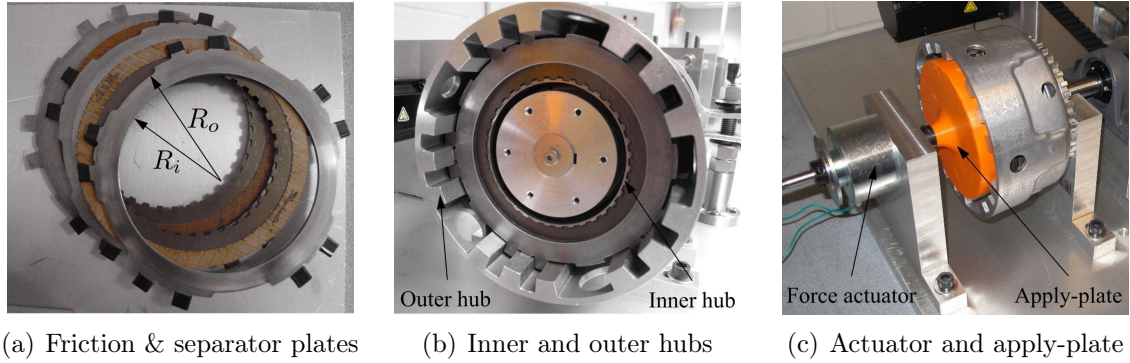


FIGURE 3.6. Multi-plate brake assembly

the friction surfaces in contact. The frictional torque of the band brake, which in this thesis is denoted by T_{BR} , can be controlled by means of the force actuator connected to the free end of the band as shown in Fig. 3.7(a).

As mentioned in Chapter 2, the brakes are selected to be of the dry type in order to avoid the undesirable drag torque in the brakes, particularly in the multi-plate brake (Zhou et al., 2014a; Jibin et al., 2012; Iqbal et al., 2014).

The uncontrollable frictional torques and spin losses, which are modeled by the combination of the Coulomb friction and viscous damping, are originated from ball bearings and the lubricated gears (Seetharaman et al., 2009; Kahraman et al., 2015). Here, the Coulomb friction components of the bearings other than that of the sun's and ring's are neglected. This is due to the fact that the largest portion of the

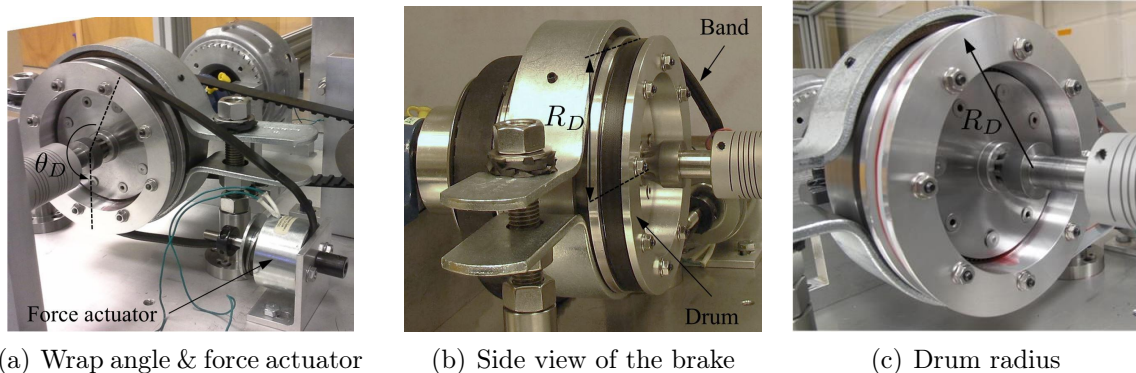


FIGURE 3.7. Band brake assembly

axial and radial loads on the system are supported by the bearings on which the sun and ring gears are mounted. The Coulomb friction components of the sun and ring bearings are denoted by T_{Sf} and T_{Rf} , respectively. The Coulomb friction model adopted in this thesis has been extensively utilized in the literature to model the frictional behaviour of the brakes and clutches of transmission systems (Oh et al., 2014; Walker et al., 2011; Zhu et al., 2013).

Since the summation of both controllable and uncontrollable frictional torques are exerted on the sun gear ($T_{BS} + T_{Sf}$) and the ring gear ($T_{BR} + T_{Rf}$), these frictional torques are modeled as a whole rather than individually. In fact, studying the Coulomb models of the controllable and uncontrollable frictional torques independently is not beneficial in this context.

The Coulomb model of the frictional torque applied to the sun gear is expressed as follows (Armstrong-Hélouvy et al., 1994; Olsson et al., 1998; Pfeiffer and Glocker, 2000):

$$T_{BS} + T_{Sf} = \begin{cases} -T_{C,S} \operatorname{sgn}(\omega_S) & \text{if } \omega_S \neq 0, \\ -T_{C,S} \operatorname{sgn}(T_{ext,S}) & \text{if } \omega_S = 0 \wedge |T_{ext,S}| > T_{C,S}, \\ -T_{ext,S} & \text{if } \omega_S = 0 \wedge |T_{ext,S}| \leq T_{C,S}, \end{cases} \quad (3.16)$$

where

$$T_{C,S} = (N_{BS}K_S + T_{Sf,C}). \quad (3.17)$$

In Equations (3.16) and (3.17), N_{BS} , $T_{Sf,C}$, and $T_{ext,S}$ denote the force applied to the friction plates, the Coulomb friction component of the sun bearings, and the external torque applied to the sun gear. The term K_S stands for the friction constant of the multi-plate brake which is function of the plates geometry and the coefficient of friction as follows (Bundynas and Nisbett, 2009):

$$K_S = n\mu_P \left(\frac{2}{3} \right) \left(\frac{R_o^3 - R_i^3}{R_o^2 - R_i^2} \right), \quad (3.18)$$

In Equation (3.18), μ_P and n stand for the coefficient of friction between the plates and the number of friction surfaces.

Similarly, the Coulomb model of the frictional torques imparted on the ring gear can be expressed as follows (Armstrong-Hélouvy et al., 1994; Olsson et al., 1998):

$$T_{BR} + T_{Rf} = \begin{cases} -T_{C,R} \operatorname{sgn}(\omega_R) & \text{if } \omega_R \neq 0, \\ -T_{C,R} \operatorname{sgn}(T_{ext,R}) & \text{if } \omega_R = 0 \wedge |T_{ext,R}| > T_{C,R}, \\ -T_{ext,R} & \text{if } \omega_R = 0 \wedge |T_{ext,R}| \leq T_{C,R}, \end{cases} \quad (3.19)$$

where

$$T_{C,R} = (N_{BR}K_R + T_{Rf,C}). \quad (3.20)$$

In Equations (3.19) and (3.20), the terms N_{BR} , $T_{Rf,C}$, and $T_{ext,R}$ are the actuation force applied at one end of the band, the Coulomb friction component of the ring bearing, and the external torque applied to the ring gear. The term K_R stands for the friction constant of the band brake which is function of the drum geometry and the coefficient of friction as follows (Bundynas and Nisbett, 2009):

$$K_R = R_D(e^{\mu_D \theta_D} - 1), \quad (3.21)$$

In Equation (3.21), R_D , μ_D , and θ_D denote the drum radius, the coefficient of friction, and the wrap angle of the band.

The spin losses inside the DBT systems are originated from the viscous damping in the bearings and the gears. Here, it is assumed that the bearing lubricant and the automatic transmission fluid (ATF) are Newtonian fluids and the viscous friction prevents rotation with the torque proportional to the angular velocity and in the reverse direction (Batchelor, 2000; Panton, 2006).

Considering the linear model for the viscous friction of the bearings and gears and from Equation (2.7), all the spin losses of the transmission can be superimposed and expressed as functions of generalized coordinates by $-C_S\omega_S$ and $-C_R\omega_R$ where C_S and C_R are equivalent coefficients of viscous damping (Munson et al., 1990).

Substituting the input torque (T_d), the output torque (T_o), Coulomb friction components ($T_{BS} + T_{Rf}$, $T_{BS} + T_{Sf}$), and spin losses ($-C_S\omega_S$, $-C_R\omega_R$) in (3.13), the

generalized applied torque is obtained as follows:

$$\begin{aligned}\Xi_1^{appl,nc} &= T_d \frac{\partial \omega_{C,in}}{\partial \omega_S} + (T_{BR} + T_{Rf} - C_R \omega_R) \frac{\partial \omega_R}{\partial \omega_S} \\ &\quad - T_o \frac{\partial \omega_{C,out}}{\partial \omega_S} + (T_{BS} + T_{Sf} - C_S \omega_S) \frac{\partial \omega_S}{\partial \omega_S},\end{aligned}\tag{3.22}$$

$$\begin{aligned}\Xi_2^{appl,nc} &= T_{C,in} \frac{\partial \omega_{C,in}}{\partial \omega_R} + (T_{BR} + T_{Rf} - C_R \omega_R) \frac{\partial \omega_R}{\partial \omega_R} \\ &\quad - T_o \frac{\partial \omega_{C,out}}{\partial \omega_R} + (T_{BS} + T_{Sf} - C_S \omega_S) \frac{\partial \omega_S}{\partial \omega_R}.\end{aligned}\tag{3.23}$$

3.3.5. Hybrid Dynamical Model of the DBT System

In this subsection, first, based on the kinetic energy, the potential energy, and the generalized applied torque determined in the previous subsections, the unconstrained dynamical model of the DBT system is developed by exploiting the D'Alembert-Lagrange principle. Thereafter, this dynamical model is fused with the constraints of Coulomb friction models expressed by (3.16) and (3.19) in order to specify the vector fields $\mathbf{f}(q_1, \mathbf{x}, \mathbf{u})$, $\mathbf{f}(q_2, \mathbf{x}, \mathbf{u})$, and $\mathbf{f}(q_3, \mathbf{x}, \mathbf{u})$ and consequently the hybrid dynamical model of the DBT system in all working modes (Pakniyat and Caines, 2015, 2016a; Lygeros, 2004).

Substituting Equations (2.7), (3.15), (3.22), and (3.23) in (3.12) results in:

$$\begin{aligned}&\left[\frac{T_d}{R_1 + 1} + T_{BS} + T_{Sf} - C_S \omega_S - \frac{T_o}{R_2 + 1} - (J_{C,in} + 4m_{P,in}r_{C,in}^2) \left(\frac{\dot{\omega}_S + R_1 \dot{\omega}_R}{(R_1 + 1)^2} \right) \right. \\ &\quad \left. - (J_{C,out} + 4m_{P,out}r_{C,out}^2) \left(\frac{\dot{\omega}_S + R_2 \dot{\omega}_R}{(R_2 + 1)^2} \right) - 4\{J_{P,in} \left(\frac{\dot{\omega}_S - R_1 \dot{\omega}_R}{(R_1 - 1)^2} \right)\} - J_S \dot{\omega}_S \right. \\ &\quad \left. - 4\{J_{P,out} \left(\frac{\dot{\omega}_S + R_2^2 \dot{\omega}_R - R_2 \dot{\omega}_R}{(R_2 - 1)^2} \right)\} \right] \delta \omega_S + \left[\frac{T_d R_1}{R_1 + 1} + T_{BR} + T_{Rf} - C_R \omega_R - \frac{T_o R_2}{R_2 + 1} \right. \\ &\quad \left. - (J_{C,in} + 4m_{P,in}r_{C,in}^2) \left(\frac{R_1^2 \dot{\omega}_R + R_1 \dot{\omega}_S}{(R_1 + 1)^2} \right) - (J_{C,out} + 4m_{P,out}r_{C,out}^2) \left(\frac{R_2^2 \dot{\omega}_R + R_2 \dot{\omega}_S}{(R_2 + 1)^2} \right) \right. \\ &\quad \left. - 4\{J_{P,in} \left(\frac{R_1^2 \dot{\omega}_R - R_1 \dot{\omega}_S}{(R_1 - 1)^2} \right)\} - 4\{J_{P,out} \left(\frac{R_2^2 \dot{\omega}_R - R_2 \dot{\omega}_S}{(R_2 - 1)^2} \right)\} - J_R \dot{\omega}_R \right] \delta \omega_R = 0.\end{aligned}\tag{3.24}$$

According to the D'Alembert-Lagrange principle, Equation (3.24) holds for all $\delta\xi_k$ satisfying the system constraints. This requires the factors multiplying $\delta\omega_S$ and $\delta\omega_R$ to be set to zero. Therefore,

$$\begin{aligned} \frac{T_d}{R_1 + 1} + T_{BS} + T_{Sf} - C_S\omega_S - \frac{T_o}{R_2 + 1} - (J_{C,in} + 4m_{P,in}r_{C,in}^2)\left(\frac{\dot{\omega}_S + R_1\dot{\omega}_R}{(R_1 + 1)^2}\right) \\ - (J_{C,out} + 4m_{P,out}r_{C,out}^2)\left(\frac{\dot{\omega}_S + R_2\dot{\omega}_R}{(R_2 + 1)^2}\right) - 4\{J_{P,in}\left(\frac{\dot{\omega}_S - R_1\dot{\omega}_R}{(R_1 - 1)^2}\right)\} - J_S\dot{\omega}_S \\ - 4\{J_{P,out}\left(\frac{\dot{\omega}_S + R_2^2\dot{\omega}_R - R_2\dot{\omega}_R}{(R_2 - 1)^2}\right)\} = 0, \end{aligned} \quad (3.25)$$

and

$$\begin{aligned} \frac{T_d R_1}{R_1 + 1} + T_{BR} + T_{Rf} - C_R\omega_R - \frac{T_o R_2}{R_2 + 1} - (J_{C,in} + 4m_{P,in}r_{C,in}^2)\left(\frac{R_1^2\dot{\omega}_R + R_1\dot{\omega}_S}{(R_1 + 1)^2}\right) \\ - (J_{C,out} + 4m_{P,out}r_{C,out}^2)\left(\frac{R_2^2\dot{\omega}_R + R_2\dot{\omega}_S}{(R_2 + 1)^2}\right) - 4\{J_{P,in}\left(\frac{R_1^2\dot{\omega}_R - R_1\dot{\omega}_S}{(R_1 - 1)^2}\right)\} \\ - 4\{J_{P,out}\left(\frac{R_2^2\dot{\omega}_R - R_2\dot{\omega}_S}{(R_2 - 1)^2}\right)\} - J_R\dot{\omega}_R = 0. \end{aligned} \quad (3.26)$$

Then, by keeping the derivatives of the generalized coordinates ($\dot{\omega}_S$, $\dot{\omega}_R$) in the left hand side of the equation (3.25) and (3.26) and bringing the rest of the terms to the right hand side, the equations of motion are obtained as follows:

$$\begin{aligned} \dot{\omega}_S &= \frac{1}{a}(T_{BS}\tau - T_{BR}\lambda - \omega_S C_S\tau + \omega_R C_R\lambda + cT_d - dT_o + T_{Sf}\tau - T_{Rf}\lambda) \\ \dot{\omega}_R &= \frac{1}{a}(T_{BR}\gamma - T_{BS}\lambda + \omega_S C_S\lambda - \omega_R C_R\gamma + eT_d - fT_o + T_{Rf}\gamma - T_{Sf}\lambda). \end{aligned} \quad (3.27)$$

where the coefficients α , β , γ , τ , λ , ϕ , ψ , a , c , d , e , f in Equation (3.27) are listed in Table 3.2.

As mentioned earlier and also expressed by (3.27), the continuous-time states associated with the dynamics of the system are the angular velocities of the sun and ring gear $\mathbf{x} = [\omega_S \ \omega_R]^T$ and the discrete-time states corresponding to the modes of operations of the system are the first gear ratio q_1 , the second gear ratio q_2 , and during the gear shift operation q_3 . Therefore, according to the equations (3.16), (3.19), and

3.3 DYNAMICAL MODEL OF THE DBT SYSTEM

TABLE 3.2. Coefficients of the dynamical model of the transmission

$\alpha = \frac{(J_{C,in} + 4m_{P,in}r_{C,in}^2)}{(R_1+1)^2}$	$\psi = \frac{4J_{P,out}}{(R_2-1)^2}$
$\beta = \frac{(J_{C,out} + 4m_{P,out}r_{C,out}^2)}{(R_2+1)^2}$	$a = (\gamma\tau - \lambda^2)$
$\gamma = [J_S + \alpha + \beta + \phi + \psi]$	$c = \frac{\tau - R_1\lambda}{R_1+1}$
$\tau = [J_R + (\alpha + \phi)R_1^2 + (\beta + \psi)R_2^2]$	$d = \frac{\tau - R_2\lambda}{R_2+1}$
$\lambda = [(\alpha - \phi)R_1 + (\beta - \psi)R_2]$	$e = \frac{\gamma R_1 - \lambda}{R_1+1}$
$\phi = \frac{4J_{P,in}}{(R_1-1)^2}$	$f = \frac{\gamma R_2 - \lambda}{R_2+1}$

(3.27) the hybrid dynamical model of the DBT system in three discrete-time working modes is expressed as follows:

- First gear (q_1): This mode of operation is associated with the dynamics of the system in the first gear wherein the power is entirely transferred through the sun gear and the ring gear is grounded. According to (3.27), the vector field $\mathbf{f}(q_1, \mathbf{x}, \mathbf{u})$ is expressed by

$$\mathbf{f}(q_1, \mathbf{x}, \mathbf{u}) = \begin{bmatrix} \frac{1}{a}(T_{BS}\tau - T_{BR}\lambda - \omega_S C_S \tau + \omega_R C_R \lambda + cT_d - dT_o + T_{Sf}\tau - T_{Rf}\lambda) \\ 0 \end{bmatrix}. \quad (3.28)$$

Further, from (3.16) and (3.19) the friction model corresponding to this operation mode is expressed as follows:

$$T_{BS} + T_{Sf} = -T_{CS} \operatorname{sgn}(\omega_S) \quad (3.29a)$$

$$T_{BR} + T_{Rf} = -T_{ext,R}, \quad (3.29b)$$

where $T_{ext,R}$ is computed from (3.27):

$$T_{ext,R} = \frac{1}{\gamma}(-T_{BS}\lambda + \omega_S C_S \lambda + eT_d - fT_o - T_{Sf}\lambda). \quad (3.30)$$

The guard condition associated with this mode is given by the following condition wherein the transition from the stiction phase to the slipping one takes place between the friction surfaces of the band brake:

$$\mathcal{G}(q_1, q_3) = \{(\mathbf{x}, \mathbf{u}) \in \mathbb{R}^2 \times \mathbb{R}^2 \mid \omega_R = 0 \wedge |T_{ext,R}| > T_{C,R}\}. \quad (3.31)$$

- Second gear (q_2): This mode of operation is related with the dynamics of the transmission in the second gear in which the power is solely transferred through the ring gear and the sun gear is grounded. According to (3.27), the vector field associated with this mode $\mathbf{f}(q_2, \mathbf{x}, \mathbf{u})$ is expressed by:

$$\mathbf{f}(q_2, \mathbf{x}, \mathbf{u}) = \begin{bmatrix} 0 \\ \frac{1}{a}(T_{BR}\gamma - T_{BS}\lambda + \omega_S C_S \lambda - \omega_R C_R \gamma + eT_d - fT_o + T_{Rf}\gamma - T_{Sf}\lambda) \end{bmatrix}. \quad (3.32)$$

Moreover, from (3.16) and (3.19) the friction model corresponding to this operation mode is expressed by:

$$T_{BR} + T_{Rf} = -T_{C,R} \operatorname{sgn}(\omega_R) \quad (3.33a)$$

$$T_{BS} + T_{Sf} = -T_{ext,S} \quad (3.33b)$$

where $T_{ext,S}$ is computed from (3.27) as follows:

$$T_{ext,S} = \frac{1}{\tau}(-T_{BR}\lambda + \omega_R C_R \lambda + cT_d - dT_o - T_{Rf}\lambda). \quad (3.34)$$

The guard condition related to this mode is given by the following condition wherein the transitions from stiction phase to slipping one takes place between the friction surfaces of the multi-plate brake:

$$\mathcal{G}(q_2, q_3) = \{(\mathbf{x}, \mathbf{u}) \in \mathbb{R}^2 \times \mathbb{R}^2 \mid \omega_S = 0 \wedge |T_{ext,S}| > T_{C,S}\}. \quad (3.35)$$

- Gear shifts (q_3): This mode is associated with the dynamics of the system during the gear shift operation wherein the power is transferred through both sun and

ring gears. According to (3.27), the vector field which corresponds to this mode $\mathbf{f}(q_3, \mathbf{x}, \mathbf{u})$ is expressed as follows:

$$\mathbf{f}(q_3, \mathbf{x}, \mathbf{u}) = \begin{bmatrix} \frac{1}{a}(T_{BS}\tau - T_{BR}\lambda - \omega_S C_S \tau + \omega_R C_R \lambda + cT_d - dT_o + T_{Sf}\tau - T_{Rf}\lambda) \\ \frac{1}{a}(T_{BR}\gamma - T_{BS}\lambda + \omega_S C_S \lambda - \omega_R C_R \gamma + eT_d - fT_o + T_{Rf}\gamma - T_{Sf}\lambda) \end{bmatrix} \quad (3.36)$$

Further, the sun and ring brakes are both slipping and thus, from (3.16) and (3.19), their corresponding torque friction model is expressed as follows:

$$T_{BS} + T_{Sf} = \begin{cases} -T_{C,S} \operatorname{sgn}(\omega_S) & \text{if } \omega_S \neq 0, \\ -T_{C,S} \operatorname{sgn}(T_{ext,S}) & \text{if } \omega_S = 0 \wedge |T_{ext,S}| > T_{C,S}, \end{cases} \quad (3.37a)$$

and (3.37b)

$$T_{BR} + T_{Rf} = \begin{cases} -T_{C,R} \operatorname{sgn}(\omega_R) & \text{if } \omega_R \neq 0, \\ -T_{C,R} & \text{if } \omega_R = 0 \wedge |T_{ext,R}| > T_{C,R}. \end{cases}$$

The guard conditions related to this mode are the transition to the first gear or the second gear. The transition from the gear shift operation mode to the first gear takes place when the guard condition $\mathcal{G}(q_3, q_1)$ is fulfilled. In this case, the equivalent external torque applied to the ring gear becomes less than the Coulomb friction at zero velocity wherein the ring gear becomes grounded. Mathematically, this statement can be expressed by:

$$\mathcal{G}(q_3, q_1) = \{(\mathbf{x}, \mathbf{u}) \in \mathbb{R}^2 \times \mathbb{R}^2 \mid \omega_R = 0 \wedge |T_{ext,R}| < T_{C,R}\}. \quad (3.38)$$

The transition from the gear shift operation mode to the second gear occurs if the equivalent external torque applied to the sun gear becomes less than the Coulomb friction at zero velocity which happens when the sun gear is grounded. This condition can be articulated as follows:

$$\mathcal{G}(q_3, q_2) = \{(\mathbf{x}, \mathbf{u}) \in \mathbb{R}^2 \times \mathbb{R}^2 \mid \omega_S = 0 \wedge |T_{ext,S}| < T_{C,S}\}. \quad (3.39)$$

Here, rotations of the sun and ring gears are considered in the positive direction and their rotations in the negative direction are prevented by means of the brake mechanisms. Thus, from equation (3.37) and (3.36) it is concluded that during the upshift operation the engagement of the sun brake exerts a positive torque on the ring gear and a negative torque on the sun gear and the disengagement of the ring brake reduces the negative torque imparted on the ring gear and the positive torque applied to the sun gear. Therefore, the engagement of the sun brake and the disengagement of the ring brake during the upshift process accelerate the ring gear and increase the angular velocity of this gear from zero to a certain value while the sun gear is decelerated and its angular velocity is reduced and brought to zero. This results in the change of power transmission path and consequently the gear ratio. This trend is conceptually similar for the downshift operation wherein the engagement of the ring brake applies a positive torque on the sun gear and a negative torque on the ring gear and the disengagement of the sun brake decreases the negative torque applied to the sun gear and the positive torque exerted to the ring gear. This procedure accelerates the sun gear and increases the angular velocity of this gear from zero to a certain value while the ring gear is decelerated and ultimately grounded. Accordingly, the path of power transmission is changed from the second gear ratio to the first one.

In conclusion, the engagement and disengagement of the brakes facilitate the gear shift operation by accelerating the on-coming gear and decelerating the off-going one and consequently changing the path of power flow and the gear ratio.

3.4. Vehicle Dynamics

As discussed in the beginning of this chapter, by using the lumped mass method and the torque balance equation, the dynamics of the vehicle can be expressed as:

$$\dot{\omega}_w = \frac{T_o i_{fd} - T_v}{J_v} \quad (3.40)$$

where J_v is the effective inertia of the vehicle, wheels, drive shafts, and the differential assembly as seen by the wheels. The term i_{fd} is the final drive ratio and T_v is the sum

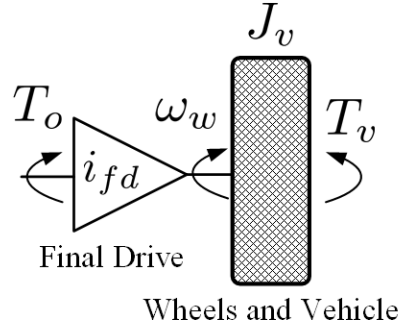


FIGURE 3.8. Free-body diagram of the lumped parameter model of the vehicle, wheels, drive shafts, and the differential assembly

of resisting torques imparted on the lumped system. The resisting torques applied on the system, i.e., road loads—are typically originated from the longitudinal force applied on the vehicle, namely the aerodynamic drag force, gravitational force, and tire rolling resistance as well as the brake torque applied by the driver. These resisting torques are generally formulated as follows (Andrzejewski and Awrejcewicz, 2006; Oh et al., 2013, 2014):

$$T_v = R_w \left(\frac{1}{2} \rho v_{rel}^2 C_d A_f + m_v g \sin(\theta_{road}) + K_r m_v g \cos(\theta_{road}) \right) + T_{Brake} \quad (3.41)$$

where R_w , θ_{road} , K_r , m_v , v_{rel} , ρ , C_d and A_f stand for wheel radius, road angle, tire rolling resistance, vehicle mass, relative velocity of the vehicle with respect to wind, air density, aerodynamic drag coefficient, and vehicle frontal area and the term T_{Brake} denotes the brake torque applied by the driver.

Relying on Equation (3.40) in order to measure the amount of resting load on the vehicle may not be an appropriate approach in practice. This is not only due to the considerable amount of uncertainties involved in the parameters and variables of this equation but also because of the hurdles in the measurement of the wind speed, road grade, variations of the vehicle frontal area and drag coefficient due to the vehicle configuration, and the brake torque exerted on the vehicle. This problem is tackled in the next chapter by estimating the sum of the resisting torques T_v together with the unmeasured states in the framework of stochastic systems.

3.5. Electromechanical Gear shift Actuators

In this section, the force-current relation of the solenoids adopted as gear shift actuators are experimentally obtained for accurate control of the brake torques.

In the past few decades, replacement of the hydraulic and pneumatic actuators of the brake/clutch systems with electromechanical ones has gained a considerable momentum in automotive applications and more importantly in the electric vehicle industry. This is not only due to the low efficiency of hydraulic and pneumatic systems due to the power loss in the pumps and corresponding components, but also because of the compactness, quick response, ease of control, high efficiency, low cost, low weight, and environmentally friendly specifications of the electromechanical systems (Chopra, 2014; Neelakantan et al., 2008; Jo et al., 2010). Various electromechanical actuators designed and introduced in the literature among, which the piezoelectric actuators, electric motors, and solenoids, are commonly used in automotive applications (Boldea and Nasar, 1997; Boldea, 2004). Piezoelectric actuators provide high amount of force; however, their working stroke is very limited (King, 1991; Neelakantan et al., 2008). Electric motors with linear mechanisms typically produce high normal forces but the presence of friction and backlash in these mechanism reduces their controllability and response time (Farris and Goldfarb, 2011; Yue et al., 2013; Gao et al., 2014; Chopra, 2014; Chopra et al., 2013). Given the fact that the gear shift operation is typically performed within a very short period of time, the response time of the actuator plays an important role in the quality of the gear shift. Solenoid actuators provide less normal force in comparison with piezoelectric actuators and linear motors; however, in addition to having fast response time, their working strokes match well with the required strokes of the brake/clutch systems in automotive applications (Mahajan et al., 2012; Neelakantan et al., 2008; Boldea, 2004). Due to the aforementioned advantages of the solenoid actuators, which have a direct impact on the gear shift time and quality, they are adopted as the gear shift actuators for the DBT system in this thesis.

A linear solenoid actuator, as illustrated in Fig. 3.9, is mainly comprised of a coil, a shield, a plunger, a linear bearing, a shaft, and a return spring (Tahmasebi et al., 2014). The solenoid magnetic circuit generated by the applied current to the coil, develops opposing poles across the solenoid air gap which results in an attractive force between the shield and the plunger. The resultant electromagnetic force is applied to a designated spot by means of the press-fitted shaft to the plunger sliding on the linear bearing as depicted in Fig. 3.9(a). The return spring leads the plunger back to its initial position when the current is cut off (Boldea, 2013; Tahmasebi et al., 2014; Coey, 2010; Lyshevski, 2008). Figure 3.10 demonstrates the solenoid actuator assembly.

Solenoid actuators are typically classified into the conical pole face and flat pole face as illustrated and compared in Fig. 3.11 (Tahmasebi et al., 2014). The conical pole face type, wherein the plunger and shield faces have cone shapes, provides lower normal force but it has longer displacement in comparison to the flat face type in which the plunger and shield faces are flat. The latter type is most commonly used in applications in which the maximum normal force for short displacement is of interest. In fact, in flat face solenoid actuators, increasing the main air gap considerably decreases the resultant force of the actuator. Thus, there is always a trade-off between

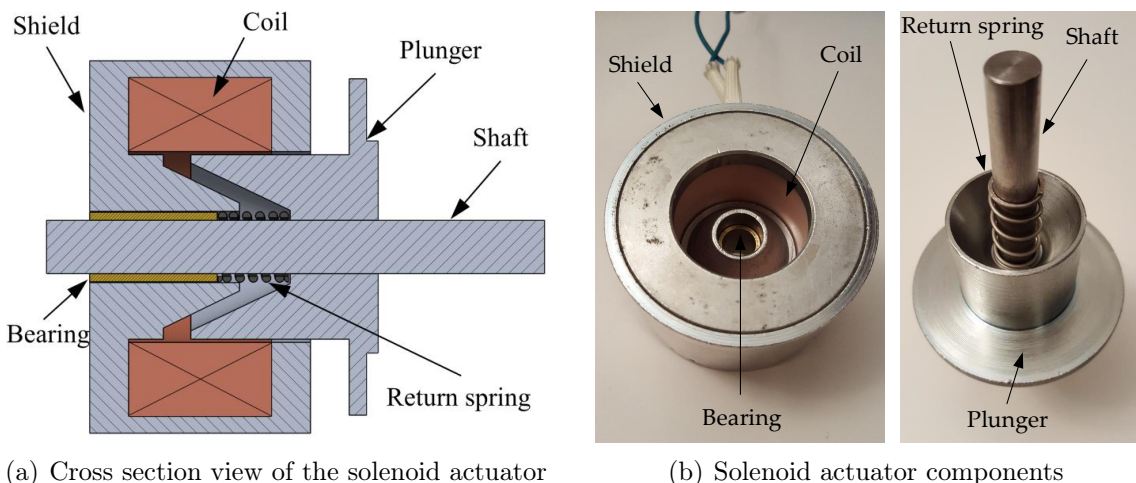


FIGURE 3.9. Main components of the solenoid actuator

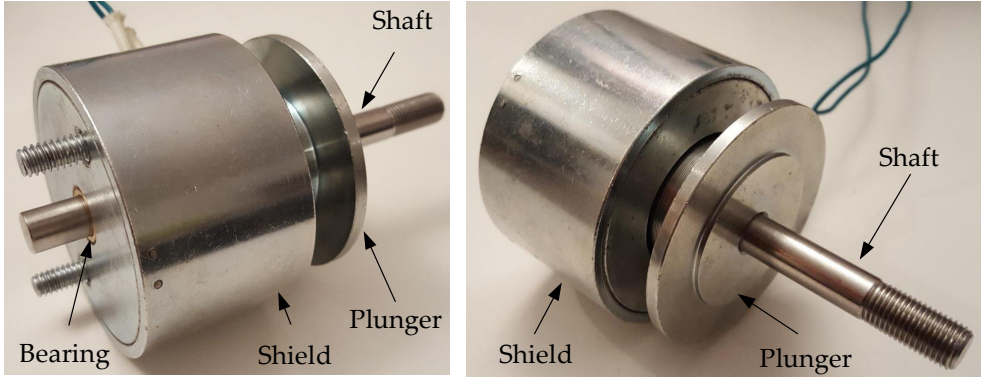


FIGURE 3.10. Front and rear views of the solenoid assembly

the available normal force and the maximum displacement (Tahmasebi et al., 2014; Underhill, 1914). A special feature of the conical face solenoids, which makes them easy to control, is their lower force sensitivity to the air gap in comparison to the flat face types^{1,2}. This is, in fact, the main reason for which conical face solenoids are adopted as gear shift actuators in this thesis.

For the solenoid actuator shown in Fig. 3.10, the resultant electromagnetic force is measured experimentally by means of the load cell shown in Fig. 3.12. In this experiment, the coil current is increased from 0 to 3.25 A and the plunger displacement

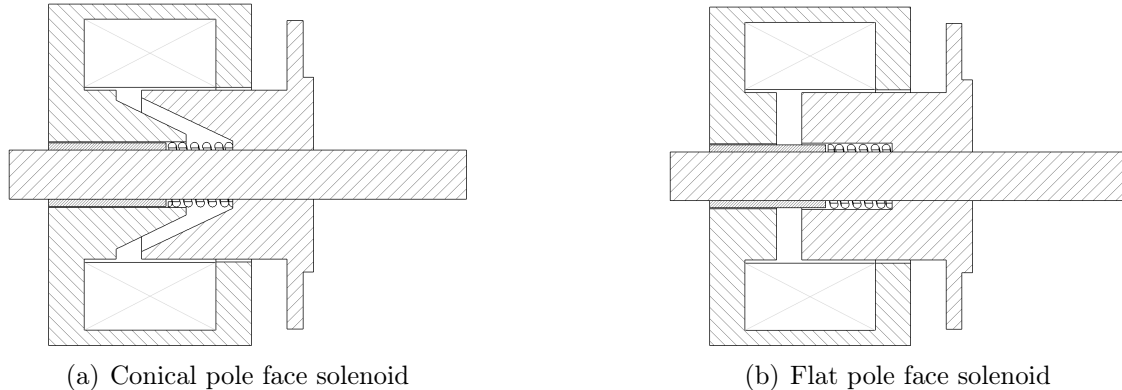


FIGURE 3.11. Section view of conical and flat face solenoids

¹http://www.contact-evolution.ch/files/LEDEX_Solenoids_G.pdf

²http://www.solen.com.tw/products/specs_dc_pushpull.asp

3.5 ELECTROMECHANICAL GEAR SHIFT ACTUATORS

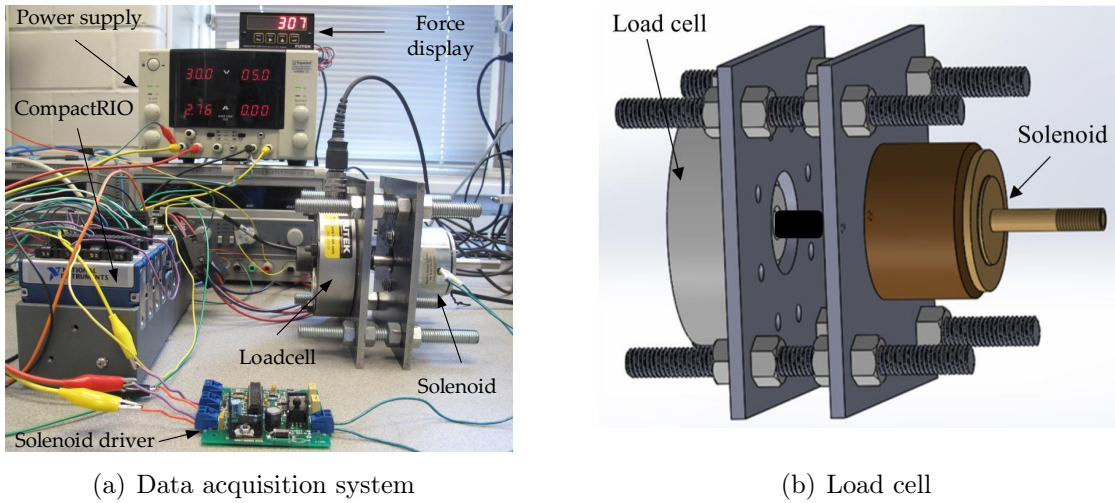


FIGURE 3.12. Force measurement apparatus

is varied from 1 mm to 9 mm with step of 1 mm. The relation among force-current-displacement of solenoid is studied in (Tahmasebi et al., 2014). Based on this study, the mentioned relation can be expressed by the following equation:

$$F_a(x_a, i) = \frac{h}{(kx_a + l)^2} (mi^2 + m'i^3), \quad (3.42)$$

where i , x_a , and F_a are the coil current in Amperes, plunger displacement in millimeters, and the electromagnetic force in Newtons, respectively. Based this equation a surface is fitted to the experimental data in order to find the coefficient of the above-mentioned equation, as illustrated in Fig 3.13. These coefficients (h , k , l , m , and m') are listed in Table 3.3. See (Tahmasebi et al., 2014) for more detail.

TABLE 3.3. Coefficients of the fitted surface (3.42) to the experimental results

h	k	l	m	m'
51483.61	40.14	226.9	226.9	-55.23

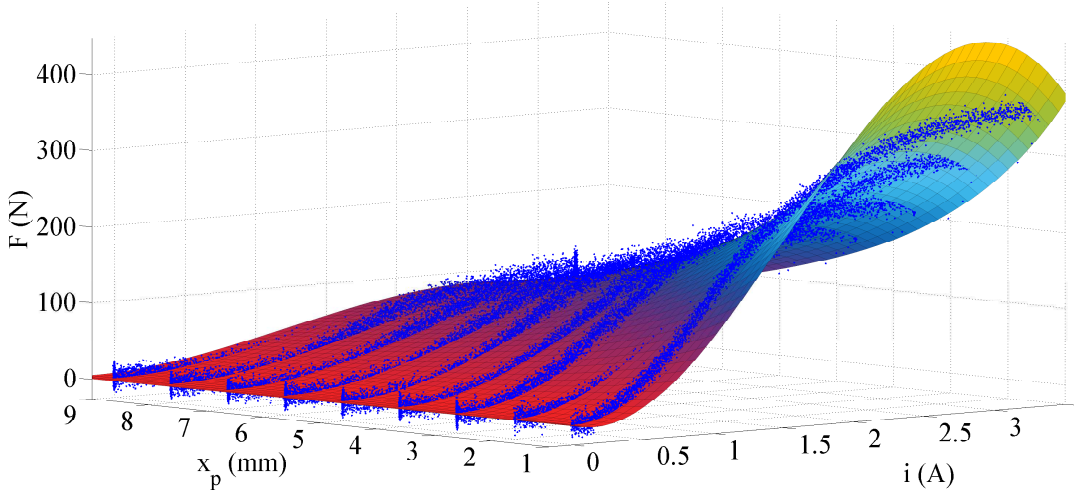


FIGURE 3.13. Fitted surface to the experimental electromagnetic force measurements of the solenoid actuator

3.6. Validation of the Dynamical Model

In this section, the derived dynamical model of the EV powertrain equipped with the DBT system is validated by means of a simulation model and the experimental apparatus. For the simulation analysis, the aforementioned system is modeled in MATLAB/Simulink[®] by utilizing the SimDriveLineTM library. The simulation model is depicted in Fig. 3.14. The experimental analysis is performed on the apparatus introduced in the previous chapter.

The values of the mass and moment of inertia of the components, the Coulomb, and viscous friction models and the coefficient of the friction of the brakes of the experimental apparatus are identified based on the time domain input-output data in MATLAB[®] System Identification Toolbox. The stiffness and damping parameters of the input and output shafts are collected from the datasheets and the radii of the drum of the band brake, the brake plates, and the gears are obtained by direct measurements. The mass and moment of inertia of the components are verified with their 3D CAD models. The obtained parameters are listed in Table 3.4.

In order to validate the mathematical model of the system presented in this chapter, the measured outputs of the dynamical model, which are ω_M and ω_w , are

3.6 VALIDATION OF THE DYNAMICAL MODEL

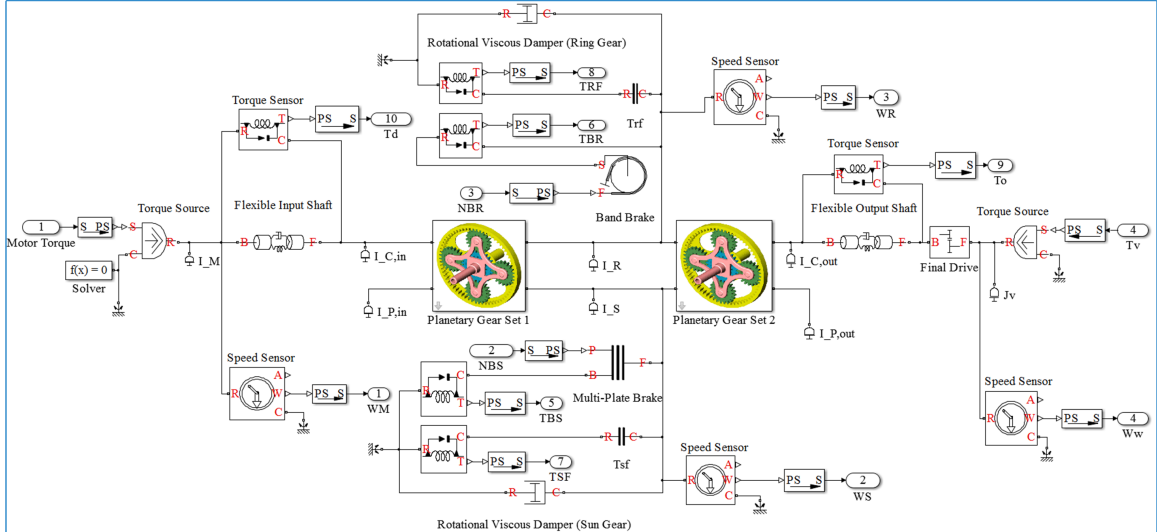


FIGURE 3.14. Powertrain model in MATLAB/Simulink[®] built by SimDriveLineTM

compared to those of the experimental test rig and the simulation model built in MATLAB/*Simulink*[®] for the identical control inputs (T_M , T_{BS} , T_{BR} , T_v) and system parameters given in the Table 3.4. A rich set of model validation tests has been performed among which the upshift during acceleration and downshift during deceleration, which are typical in practice, are illustrated in this thesis. This comparison, which is indeed an entirely open-loop model verification, is performed through a sample drive cycle with the duration of 50 s. No additional sensor other than currently available speed sensors (wheels and motor) in commercial vehicles is used for this analysis. The data acquisition system is performed at the frequency 1 kHz with National Instruments' CompactRIO[®] by programming in LabVIEW[®] FPGA/RealTime. In this experiment, the traction motor is controlled in such a way that the angular velocity ω_w tracks constant ramp commands while the DBT system undergoes upshift and downshift operations wherein the brakes of the sun and ring are engaged and disengaged depending on the gear shift scenario.

During the experimental test, the resisting torque of the load motor is set to be a quadratic function of the angular velocity with the equation $T_v = 0.0004\omega_w^2$ Nm in

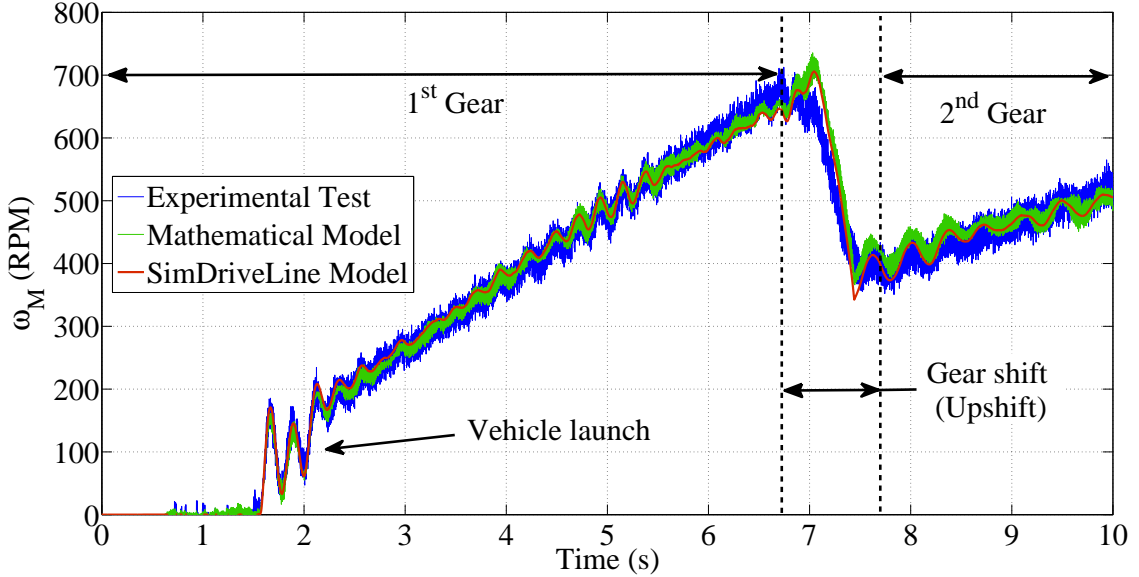
order to emulate the aerodynamic drag torque on the vehicle which is the dominant resisting load at high speeds Kadijk and Ligterink (2012).

3.6.1. Upshift during acceleration

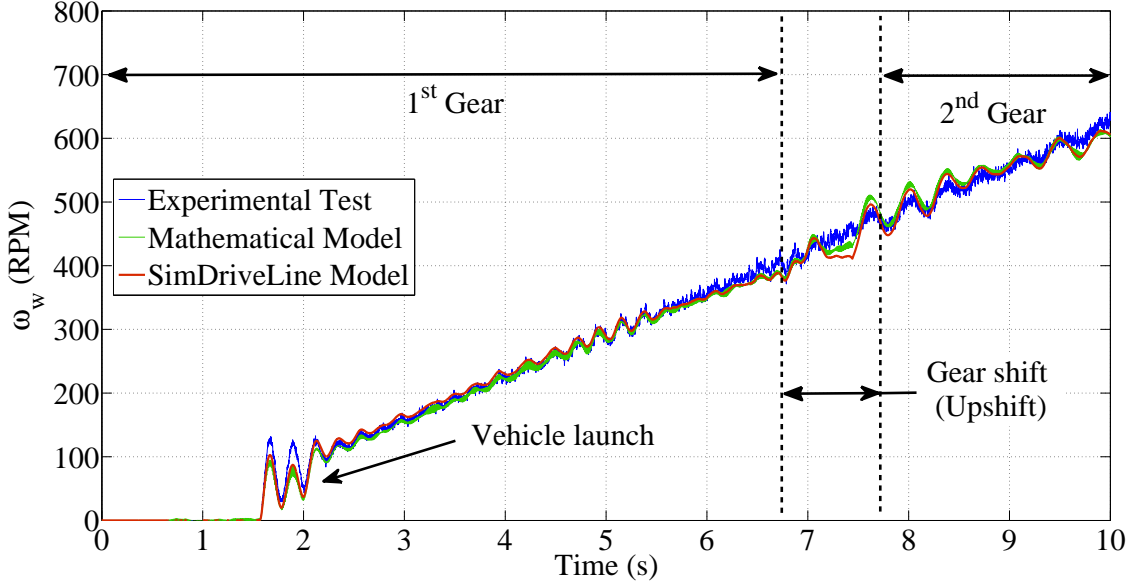
In this scenario, the system is launched from the first gear and it undergoes an upshift operation at $t = 6.7$ s. Throughout this scenario, the traction motor controls the output speed of the powertrain (ω_w) via a PID controller to track the desired ramp command. The dynamics of the electric motor, the flexible input and output shafts, and the vehicle follow those given by Equation (3.1), (3.3), (3.5), and (3.40).

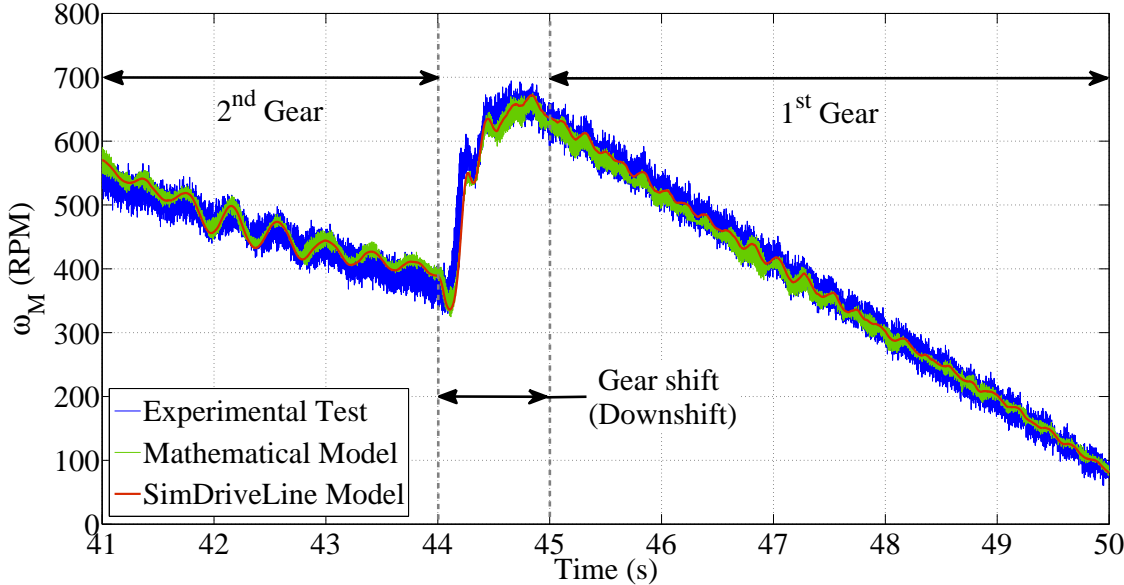
TABLE 3.4. Parameters of the Experimental Apparatus

Parameter	Value	Parameter	Value
$r_{R,in}$ (m)	6×10^{-2}	I_R (kg.m ²)	3×10^{-3}
$r_{R,out}$ (m)	6×10^{-2}	I_S (kg.m ²)	8×10^{-4}
$r_{S,in}$ (m)	3×10^{-2}	$I_{C,in}$ (kg.m ²)	1.4×10^{-3}
$r_{S,out}$ (m)	15×10^{-3}	$I_{C,out}$ (kg.m ²)	6×10^{-3}
$r_{P,in}$ (m)	15×10^{-3}	$I_{P,in}$ (kg.m ²)	6×10^{-6}
$r_{P,out}$ (m)	22.5×10^{-3}	$I_{P,out}$ (kg.m ²)	3.1×10^{-5}
C_R (Nm.s/rad)	3×10^{-3}	$m_{P,in}$ (kg)	5.1×10^{-2}
C_S (Nm.s/rad)	1×10^{-3}	$m_{P,out}$ (kg)	1.21×10^{-1}
K_d (Nm/rad)	162	K_o (Nm/rad)	150
J_M (kg.m ²)	5.9×10^{-5}	J_v (kg.m ²)	3.17×10^{-4}
μ_P	1.4×10^{-1}	μ_D	1.8×10^{-1}
n	2	θ_D (rad)	4.014
R_i (m)	5.4×10^{-2}	R_o (m)	6.75×10^{-2}
R_D (m)	7.55×10^{-2}	i_{fd}	1
T_{Rf} (Nm)	3.3×10^{-1}	T_{Sf} (Nm)	1.2×10^{-1}

FIGURE 3.15. Motor speed (ω_M) before, during, and after the upshift process

Since the system is launched from the first gear, the hybrid dynamics of the DBT system starts from the discrete state q_1 and it follows the corresponding vector field expressed by (3.28) before initiation of the gear shift operation. At $t = 6.7$ s when the gear shift takes place, the transition of discrete states from q_1 to q_3 occurs and the

FIGURE 3.16. Output speed (ω_w) before, during, and after the upshift process

FIGURE 3.17. Motor speed (ω_M) before, during, and after the downshift process

dynamics of the DBT follows the vector field given by (3.36) until the termination of the gear shift process. Then, at the end of the gear shift operation, another jump in the discrete states from q_3 to q_2 happens and the dynamics of the DBT system follows the vector field provided by (3.36). The measured outputs of the experimental test rig and simulation model together with those of the mathematical model are illustrated in Fig. 3.15-3.16. Provided that no feedback control of the speed was applied for this model validation, the results demonstrate that the output of the mathematical model effectively follows that of the experimental apparatus and the simulation model. Particularly, the superimposed oscillations of the outputs during the start-up and abrupt gear shifts indicate that the model of the system presented here indeed reflects the dynamics of the experimental apparatus.

3.6.2. Downshift during deceleration

In this scenario, the system undergoes a downshift operation at $t = 44$ sec during the deceleration. Similar to the previous test, in this scenario, the traction motor controls the output speed of the powertrain (ω_w) via a PID controller to track the desired ramp command. The dynamics of the electric motor, the flexible input and

3.6 VALIDATION OF THE DYNAMICAL MODEL

output shafts, and the vehicle follow those given by Equation (3.1), (3.3), (3.5), and (3.40). The dynamics of the DBT system starts from the discrete state q_2 and it follows the corresponding vector field expressed by (3.32) before the gear shift operation. At $t = 44$ s when the gear shift takes place, the transition of discrete states from q_2 to q_3 occurs and the dynamics of the DBT follows the vector field given by (3.36) until the termination of the gear shift process. Then, at the end of the gear shift operation, the discrete state jumps from q_3 to q_1 and the dynamics of the DBT system follows the associated vector field given by (3.36).

The measured outputs of the experimental test rig and simulation model together with those of the mathematical model are illustrated in Fig. 3.17-3.18. Similar to the previous test, no feedback control of the speed was applied for this model validation. The results demonstrate that the outputs of the mathematical model effectively follow those of the experimental apparatus and the simulation model. Particularly, the superimposition of outputs oscillations during the gear shift indicate that the dynamical model presented here, in fact, reflects the benchtop testing.

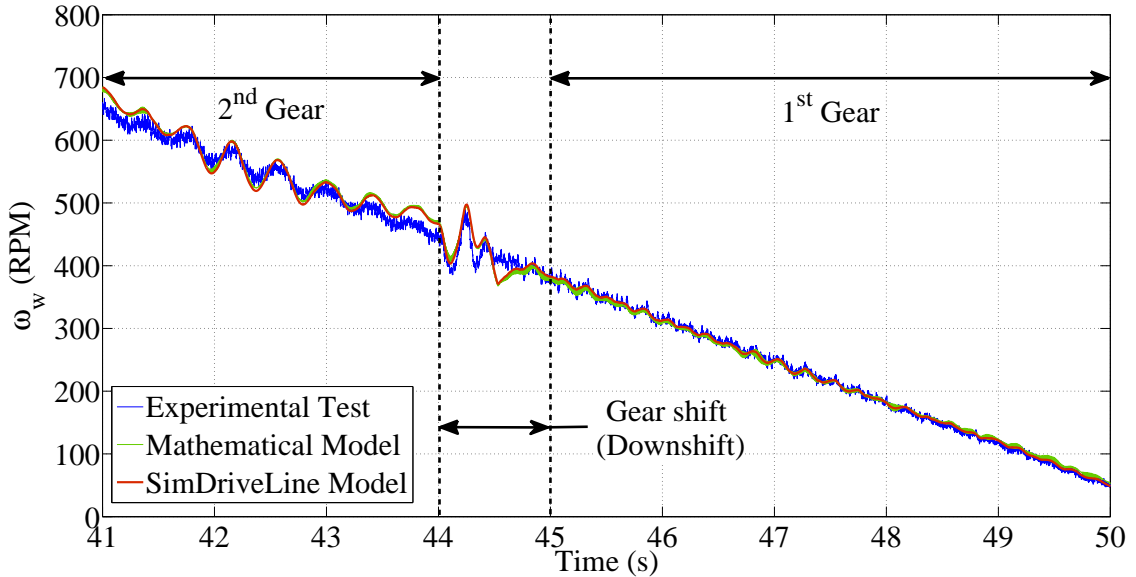


FIGURE 3.18. Output speed (ω_w) before, during, and after the downshift process

CHAPTER 4

Observer Design

In Chapter 3, the dynamical model of the electric vehicle powertrain equipped with the DBT system is derived to investigate the response of the system to the inputs and to constitute a basis for the gear shift controller design. Designing these controllers to achieve certain criteria during the gear shift operation, which are commonly the minimization of the shifting time, jerk, and energy dissipation, typically requires a real-time access to state variables and imparted disturbances on the system and to exploit them in a closed-loop feedback configuration (Oh et al., 2014, 2013; Mousavi et al., 2014). For the case study powertrain, these state variables are the angular velocities of the on-coming and off-going gears and consequently the gear ratio, the input and output torques of the transmission, angular velocities of the motor and wheels, and the imparted disturbances are the road loads. Among these state variables and disturbances, the angular velocities of the motor and wheels are easily measurable and conventionally available in commercial vehicles (Rahimi Mousavi et al., 2015). However, using torque transducers to measure the above-mentioned torques as well as the speed measurement sensors to obtain the angular velocities of the gears inside the transmission is not desirable for commercial vehicles. This is not only due to the technical intricacies involved in the installation and calibration of these devices but also because of the high cost and maintenance requirements of these sensors. Therefore, an accurate estimation of unmeasured state variables and disturbances based

on the available information from the powertrain is crucial for gear shift controller design purposes (Oh et al., 2014, 2013; Rahimi Mousavi et al., 2015). Estimation of these variables and disturbances is typically called observation and the device which performs such a task is known as an observer (Ogata, 2009).

Despite an extensive literature on the torque and speed estimation of vehicle powertrains equipped with multi-speed transmissions, the designed observers are not applicable to the case study system. This is because the electric vehicle powertrain equipped with the DBT system incorporates different mechanical configuration and consequently different dynamical model. Thus, the design of an observer that estimates the unmeasured state variables and disturbances for this system has to be performed from the ground up. In (Rahimi Mousavi et al., 2015), a minimum order observer is designed for an EV equipped with the DBT system to estimate the input and output torques of the transmission and the angular velocities of the sun and ring gears. In this paper, the nonlinear dynamics of the vehicle, such as the longitudinal vehicle dynamics, are considered in the designing of the observer. Then, an observer-based controller is designed to follow the optimal control law. The performance of the observer-based controller is validated by means of simulation analysis. In (Mousavi and Boulet, 2015), a deterministic Luenberger observer and a stochastic Kalman-Bucy filter are designed to estimate the same state variables of the DBT system while considering the process and measurement noises. The experimental results confirm the effectiveness of the Kalman-Bucy filter in mitigating the effect of the aforementioned noises on the estimation results. The goal here is to further develop these studies and estimate the angular velocities of the on-coming and off-going gears and the gear ratio, the input and output torques of the transmission, and the disturbances on the system considering the process and measurement noises.

To this end, in Section 4.1, first, the dynamical model of the powertrain derived in Chapter 3 is represented in state-space form. Then, the method of modeling the disturbances as unknown inputs is exploited in order to provide an augmented state-space model of the state variables and disturbances. This method is commonly

used for concurrent estimation of the system states and disturbances (Schrijver and Van Dijk, 2002; Söffker et al., 1995; Radke and Gao, 2006; Oh et al., 2013, 2014). Thereafter, in Section 4.2, the observability of the augmented system is parametrically investigated. Further, in Section 4.3, for the augmented system of the actual and fictitious state variables, a deterministic Luenberger observer (DLO) and a stochastic Kalman-Bucy filter (KBF) are designed to estimate the angular velocities of the on-coming and off-going gears and the gear ratio, the input and output torques of the transmission, and the disturbances on the system. The estimation is based on measuring angular velocities of the electric motor and wheels together with the imparted known torques on the system. Ultimately, in Section 4.4, a set of experiments with distinct scenarios are performed to compare the performance of the designed observers and to quantify by how much the KBF can improve the root mean square error (RMSE) of the estimation by mitigating the effect of the process and measurement noises.

4.1. Augmented State-Space Model of States and Disturbances

The state-space representation of a dynamical system constitutes an appropriate platform for systematic design of controllers/observers, and controllability/observability analysis. Thus, the dynamical model of the powertrain is represented in the following state-space form:

$$\begin{aligned}\dot{\mathbf{x}}(t) &= \mathbf{Ax}(t) + \mathbf{Bu}_k(t) + \mathbf{Eu}_d(t) \\ \mathbf{y}(t) &= \mathbf{Cx}(t) + \mathbf{Du}_k(t)\end{aligned}\tag{4.1}$$

where $\mathbf{x}(t)$, $\mathbf{u}_k(t)$, $\mathbf{u}_d(t)$, and $\mathbf{y}(t)$ are the state vector, the known input vector, the disturbance vector, and the measurement vector, respectively, and \mathbf{A} , \mathbf{B} , \mathbf{C} , \mathbf{D} , and \mathbf{E} are constant matrices with appropriate dimensions. Considering the angular velocities of the wheels ω_w and motor ω_M as the outputs of the system, T_M , $(T_{BS} + T_{Sf})$, $(T_{BR} + T_{Rf})$ as known inputs, and T_v as the disturbance, from (3.1), (3.3), (3.5), (3.36), and (3.40), vectors $\mathbf{x}(t) \in \mathbb{R}^6$, $\mathbf{y}(t) \in \mathbb{R}^2$, $\mathbf{u}_k(t) \in \mathbb{R}^3$, and $\mathbf{u}_d(t) \in \mathbb{R}$ are

defined as:

$$\begin{aligned}\mathbf{x}(t) &\triangleq \left[\omega_M(t) \quad T_d(t) \quad \omega_S(t) \quad \omega_R(t) \quad T_o(t) \quad \omega_w(t) \right]^T, \quad \mathbf{y}(t) \triangleq \left[\omega_M(t) \quad \omega_w(t) \right]^T, \\ \mathbf{u}_k(t) &\triangleq \left[T_M \quad T_{BS} + T_{Sf} \quad T_{BR} + T_{Rf} \right]^T, \quad \mathbf{u}_d(t) \triangleq T_v\end{aligned}\tag{4.2}$$

and the matrices **A**, **B**, **C**, **D**, and **E** are given by:

$$\mathbf{A} = \begin{bmatrix} 0 & \frac{-1}{J_M} & 0 & 0 & 0 & 0 \\ K_d & 0 & \frac{-K_d}{R_1+1} & \frac{-K_d R_1}{R_1+1} & 0 & 0 \\ 0 & \frac{c}{a} & \frac{-C_S \tau}{a} & \frac{C_R \lambda}{a} & \frac{-d}{a} & 0 \\ 0 & \frac{e}{a} & \frac{C_S \lambda}{a} & \frac{-C_R \gamma}{a} & \frac{-f}{a} & 0 \\ 0 & 0 & \frac{K_o}{R_2+1} & \frac{K_o R_2}{R_2+1} & 0 & -i_{fd} K_o \\ 0 & 0 & 0 & 0 & \frac{i_{fd}}{J_v} & 0 \end{bmatrix}, \quad \mathbf{B} = \begin{bmatrix} \frac{1}{J_M} & 0 & 0 \\ 0 & 0 & 0 \\ 0 & \frac{\tau}{a} & \frac{-\lambda}{a} \\ 0 & \frac{-\lambda}{a} & \frac{\gamma}{a} \\ 0 & 0 & 0 \\ 0 & 0 & 0 \end{bmatrix}, \quad \mathbf{C} = \begin{bmatrix} 1 & 0 & 0 & 0 & 0 & 0 \\ 0 & 0 & 0 & 0 & 0 & 1 \end{bmatrix}, \quad \mathbf{D} = \mathbf{0}_{2 \times 3}, \quad \mathbf{E} = \left[0 \quad 0 \quad 0 \quad 0 \quad 0 \quad \frac{-1}{J_v} \right]^T.\tag{4.3}$$

One of the commonly used methods in practical application to provide a concurrent estimation of unmeasured states and unknown inputs, and specifically in automotive and mechatronic systems (Oh and Choi, 2015; Han and Yoon, 2013; Oh et al., 2013, 2014), is to model unknown inputs by a fictitious unforced linear time-invariant dynamical system and augment this fictitious system with the plant (Radke and Gao, 2006). Mathematically, modeling the unknown input $\mathbf{u}_d(t)$ by a fictitious dynamical model is expressed as follows:

$$\begin{aligned}\dot{\mathbf{z}}(t) &= \mathbf{A}_f \mathbf{z}(t) \\ \mathbf{u}_d(t) &= \mathbf{C}_f \mathbf{z}(t)\end{aligned}\tag{4.4}$$

where $\mathbf{z}(t)$ is the fictitious state variable that generates the unknown input $\mathbf{u}_d(t)$ (Radke and Gao, 2006). The terms \mathbf{A}_f and \mathbf{C}_f are the state and output matrices of the dynamical system (4.4). Here, it is assumed the road angle, the brake torque applied by the driver, and relative velocity of the vehicle with respect to wind are constant

during the gear shift operation, and therefore, $\mathbf{A}_f = \mathbf{0}$ and $\mathbf{C}_f = \mathbf{I}$. As expressed by Cao et al. (2006); Kim et al. (2000, 2006), this is a reasonable assumption given the fact that the vehicle dynamics is relatively slow and the gear shift process takes place in a very short period of time. More importantly, for the cases that the exact dynamical model of unknown inputs is not available, which is typical in practice, selecting $\mathbf{A}_f = \mathbf{0}$ and $\mathbf{C}_f = \mathbf{I}$ is experimentally shown to be an acceptable approach in the estimation of the unknown inputs even though the unknown input is not perfectly constant (Söffker et al., 1995; Radke and Gao, 2006; Schrijver and Van Dijk, 2002). This, in fact, is verified in the experimental analysis section of this chapter as well. Therefore, by including this fictitious unknown input generator in the dynamical model, the augmented state-space model of the system is expressed as:

$$\begin{aligned}\dot{\mathbf{x}}_{aug}(t) &= \mathbf{A}_{aug}\mathbf{x}_{aug}(t) + \mathbf{B}_{aug}\mathbf{u}_k(t) \\ \mathbf{y}_{aug}(t) &= \mathbf{C}_{aug}\mathbf{x}_{aug}(t)\end{aligned}\tag{4.5}$$

where $\mathbf{x}_{aug}(t) = [\mathbf{x}(t)^T \quad \mathbf{z}(t)^T]^T$, $\mathbf{y}_{aug}(t) = [\omega_M(t) \quad \omega_w(t)]^T$, and

$$\mathbf{A}_{aug} = \begin{bmatrix} \mathbf{A} & \mathbf{E} \\ \mathbf{0}_{1 \times 6} & 0 \end{bmatrix}, \quad \mathbf{B}_{aug} = \begin{bmatrix} \mathbf{B} \\ \mathbf{0}_{1 \times 3} \end{bmatrix}, \quad \mathbf{C}_{aug} = \begin{bmatrix} \mathbf{C} & \mathbf{0}_{2 \times 1} \end{bmatrix}\tag{4.6}$$

4.2. Observability Analysis

The system (4.5) is observable if the initial state $\mathbf{x}_{aug}(t_0)$ can be completely determined from knowledge of present and future system input $\mathbf{u}_k(t)$ and output $\mathbf{y}_{aug}(t)$ over the time interval $t \in [t_0, t_1]$ (Boulet, 2003). In this case, the state response of the system can be computed as follows:

$$\mathbf{x}_{aug}(t) = e^{\mathbf{A}_{aug}(t-t_0)}\mathbf{x}_{aug}(t_0) + \int_{t_0}^t e^{\mathbf{A}_{aug}(t-\tau)}\mathbf{B}_{aug}\mathbf{u}_k(\tau)d\tau\tag{4.7}$$

and the output response is expressed by:

$$\mathbf{y}_{aug}(t) = \mathbf{C}_{aug}e^{\mathbf{A}_{aug}(t-t_0)}\mathbf{x}_{aug}(t_0) + \mathbf{C}_{aug}\int_{t_0}^t e^{\mathbf{A}_{aug}(t-\tau)}\mathbf{B}_{aug}\mathbf{u}_k(\tau)d\tau\tag{4.8}$$

Given the fact that the zero-state response of the system is known from the imparted inputs to the system, the observability of the system is specified based on the zero-input response and more precisely from the pair $(\mathbf{A}_{aug}, \mathbf{C}_{aug})$ (Ogata, 2009; Lin, 2007). It is proven that the linear time invariant system (4.5) with the matrices given in (4.3) and (4.6) is observable if and only if the observability matrix (\mathcal{O}_7) given by:

$$\mathcal{O}_7 = \begin{bmatrix} \mathbf{C}_{aug}^T & \vdots & \mathbf{A}_{aug}^T \mathbf{C}_{aug}^T & \vdots & \dots & \vdots & (\mathbf{A}_{aug}^T)^6 \mathbf{C}_{aug}^T \end{bmatrix} \quad (4.9)$$

has full column rank, e.g., $\text{Rank}\{\mathcal{O}_7\} = 7$ (Kailath, 1980; Ogata, 2009). Provided that all the parameters of the driveline are non-zero, the Gauss-Jordan elimination method transforms the observability matrix \mathcal{O}_7 of the system (4.1) into the reduced-row echelon of the form $\mathcal{O}_7 = \begin{bmatrix} \mathbf{I}_{7 \times 7} & \mathbf{0}_{7 \times 7} \end{bmatrix}$, which clearly demonstrates the observability of the system (4.1) for any combination of parameters. The aforementioned condition is the complete observability condition which is, in fact, the necessary and sufficient condition for the observation of the state variables of the system (4.5).

4.3. Observer Design

In this section, based on the augmented state-space representation (4.5), a deterministic Luenberger observer and a stochastic Kalman-Bucy filter are designed in order to provide a concurrent estimation of unmeasured state variables and the disturbance imparted on the system. In the next section, the performance of these observers are compared in order to demonstrate the necessity of considering the effect of process and measurement noises on the estimation result and to quantify by how much the KBF can improve the root mean square error (RMSE) of the estimation in comparison with the DLO by mitigating the effect of these noises.

4.3.1. Deterministic Luenberger Observer

For the system (4.5), the Luenberger observer is given by (Ogata, 2009):

$$\dot{\hat{\mathbf{x}}}_{aug}(t) = \mathbf{A}_{aug} \hat{\mathbf{x}}_{aug}(t) + \mathbf{B}_{aug} \mathbf{u}_k(t) + \mathbf{L}_d(\mathbf{y}_{aug}(t) - \hat{\mathbf{y}}_{aug}(t)), \quad (4.10)$$

where the $\hat{\mathbf{x}}_{aug}(t)$ represents the estimated value of the state variable $\mathbf{x}_{aug}(t)$ and the term \mathbf{L}_d represents the observer gain. Let $\mathbf{e}(t) = \mathbf{x}_{aug}(t) - \hat{\mathbf{x}}_{aug}(t)$ denote the error in the estimated states. From (4.5) and (4.10) the error dynamics can be written as follows:

$$\dot{\mathbf{e}}(t) = (\mathbf{A}_{aug} - \mathbf{L}_d \mathbf{C}_{aug})\mathbf{e}(t), \quad (4.11)$$

which is asymptotically stable if the matrix $\mathbf{A}_{aug} - \mathbf{L}_d \mathbf{C}_{aug}$ has all its eigenvalues in the open left half plane (Ogata, 2009). A sufficient condition for the existence of such \mathbf{L}_d is that the matrix pair $(\mathbf{A}_{aug}, \mathbf{C}_{aug})$ is observable (Ogata, 2009). The observability of this pair is verified in the previous section, and thus, the observer gain can be calculated using Ackermann's formula as follows:

$$\mathbf{L}_d = \phi_c(\mathbf{A}_{aug}) \begin{bmatrix} \mathbf{C}_{aug} \\ \mathbf{C}_{aug}\mathbf{A}_{aug} \\ \vdots \\ \mathbf{C}_{aug}\mathbf{A}_{aug}^6 \end{bmatrix}^{-1} \begin{bmatrix} 0 \\ 0 \\ \vdots \\ 1 \end{bmatrix}. \quad (4.12)$$

where ϕ_c is the desired characteristic polynomial expressed by (Ogata, 2009; Lin, 2007):

$$\phi_c = (s - p_1)(s - p_2) \cdots (s - p_n). \quad (4.13)$$

In Equation 4.13, p_1, p_2, \dots, p_n are the desired poles of the observer.

The block diagram of the estimation using the Luenberger observer is shown in Fig. 4.1.

4.3.2. Stochastic Kalman-Bucy Filter

Considering the dynamical system (4.5) in the frameworks of a deterministic system and neglecting the effect of process and measurement noises are mathematical assumptions which may not be accurate in practice and could impact the performance of the estimation. This problem is tackled in this subsection by expressing the aforementioned system in the framework of a stochastic system wherein the stochastic process and measurement noises are taken into consideration. To this end, the

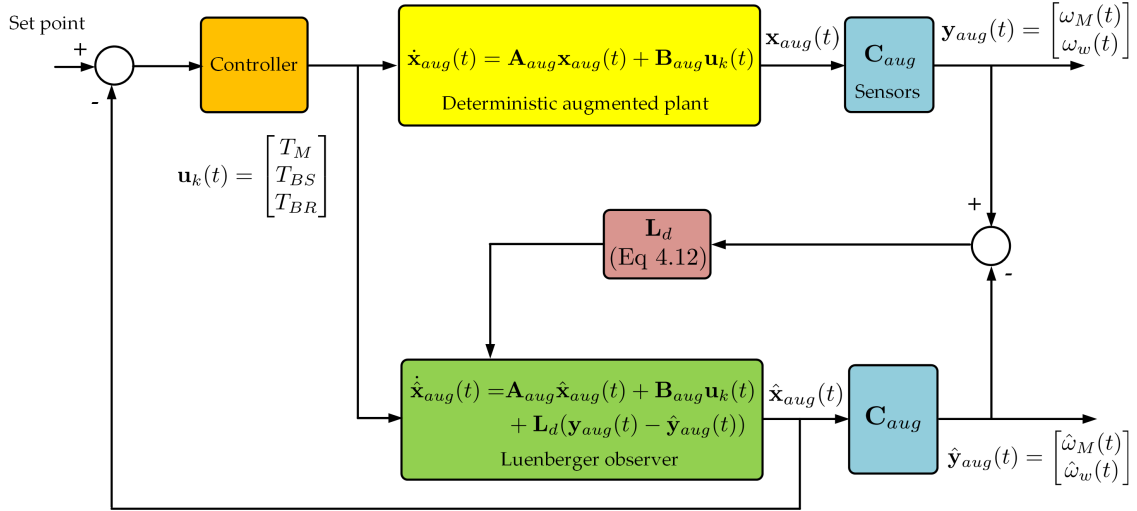


FIGURE 4.1. Block diagram of the estimation using the Luenberger observer

stochastic presentation of the dynamical model (4.5) is written as follows wherein the process and measurement noises are denoted by $\mathbf{w}(t)$ and $\mathbf{v}(t)$:

$$\begin{aligned} \dot{\mathbf{x}}_{aug}(t) &= \mathbf{A}_{aug}\mathbf{x}_{aug}(t) + \mathbf{B}_{aug}\mathbf{u}_k(t) + \mathbf{w}(t), \\ \mathbf{y}_{aug}(t) &= \mathbf{C}_{aug}\mathbf{x}_{aug}(t) + \mathbf{v}(t). \end{aligned} \quad (4.14)$$

Further, it is assumed that $\mathbf{w}(t)$ and $\mathbf{v}(t)$ are uncorrelated, zero-mean, and Gaussian white-noise stochastic processes as follows (Simon, 2006):

$$\begin{aligned} \mathcal{E}[\mathbf{w}(t)\mathbf{v}^T(\tau)] &= \mathbf{0}, \quad \forall t, \tau \\ \mathcal{E}[\mathbf{w}(t)] &= \mathbf{0}, \quad \mathcal{E}[\mathbf{v}(t)] = \mathbf{0}, \\ \mathcal{E}[\mathbf{w}(t)\mathbf{w}^T(\tau)] &= \mathbf{Q}_c\delta(t-\tau), \quad \mathbf{Q}_c = \mathbf{Q}_c^T > 0, \\ \mathcal{E}[\mathbf{v}(t)\mathbf{v}^T(\tau)] &= \mathbf{R}_c\delta(t-\tau), \quad \mathbf{R}_c = \mathbf{R}_c^T > 0, \end{aligned} \quad (4.15)$$

where $\mathcal{E}[x]$ is the expected value of the random variable x and it is defined by (Simon, 2006):

$$\mathcal{E}[x] \triangleq \int_{-\infty}^{+\infty} x f_x(x) dx. \quad (4.16)$$

In Equation (4.16), the term f_x stands for the probability density function of the random variable x . The expected value of a random vector $\mathbf{x} = [x_1 \ x_2 \ \dots \ x_p]^T$ is

the vector of expected values of the elements $\mathcal{E}[\mathbf{x}] = [\mathcal{E}[x_1] \ \mathcal{E}[x_2] \ \cdots \ \mathcal{E}[x_p]]^T$. Similarly, the expected value of a random matrix $\mathbf{X}_{p \times q}$ is $\mathcal{E}[\mathbf{X}] = [\mathcal{E}[x_{ij}]]$, $\forall i = 1, \dots, p$ and $j = 1, \dots, q$ (Ugarte et al., 2008). In Equation (4.15), the term \mathbf{Q}_c denotes the strength of the plant noise, \mathbf{R}_c stands for the strength of the measurement noise, and δ is the Dirac delta function (Lin, 2007; Simon, 2006). The goal of the optimal observer is to minimize the expected estimation error by knowing the stochastic behaviour of the plant and measurement noises. To this end, the Kalman-Bucy filter for the augmented stochastic system (4.14) is considered as follows (Simon, 2006):

$$\begin{aligned}\dot{\hat{\mathbf{x}}}_{aug}(t) &= \mathbf{A}_{aug}\hat{\mathbf{x}}_{aug}(t) + \mathbf{B}_{aug}\mathbf{u}_k(t) + \mathbf{L}_k(\mathbf{y}_{aug}(t) - \hat{\mathbf{y}}_{aug}(t)), \\ \hat{\mathbf{y}}_{aug}(t) &= \mathbf{C}_{aug}\hat{\mathbf{x}}_{aug}(t).\end{aligned}\quad (4.17)$$

Defining the estimation error as the difference between the actual value of the states and the estimates from (4.17), results in the following error dynamics ($\tilde{\mathbf{x}}_{aug}(t) = \mathbf{x}_{aug}(t) - \hat{\mathbf{x}}_{aug}(t)$) (Simon, 2006):

$$\dot{\tilde{\mathbf{x}}}_{aug}(t) = (\mathbf{A}_{aug} - \mathbf{L}_k\mathbf{C}_{aug})\tilde{\mathbf{x}}_{aug}(t) + \mathbf{w}(t) - \mathbf{L}_k\mathbf{v}(t). \quad (4.18)$$

It is proven that considering the gain \mathbf{L}_k for the Kalman-Bucy filter (4.17) as follows (Simon, 2006):

$$\mathbf{L}_k = \mathbf{P}(t)\mathbf{C}_{aug}^T\mathbf{R}_c^{-1}, \quad (4.19)$$

where $\mathbf{P}(t)$ is the solution of the following differential Riccati Equation,

$$\dot{\mathbf{P}}(t) = \mathbf{A}_{aug}\mathbf{P}(t) + \mathbf{P}(t)\mathbf{A}_{aug}^T - \mathbf{P}(t)\mathbf{C}_{aug}^T\mathbf{R}_c^{-1}\mathbf{C}_{aug}\mathbf{P}(t) + \mathbf{Q}_c, \quad (4.20)$$

minimizes the root mean-square error (RMSE) of the estimation (Ramachandra, 2000; Simon, 2006). Notice that the term $\mathbf{P}(t)$ is the estimated error covariance (Lin, 2007; Simon, 2006; Ramachandra, 2000):

$$\mathbf{P}(t) = \mathcal{E}[(\mathbf{x}_{aug}(t) - \hat{\mathbf{x}}_{aug}(t))(\mathbf{x}_{aug}(t) - \hat{\mathbf{x}}_{aug}(t))^T]. \quad (4.21)$$

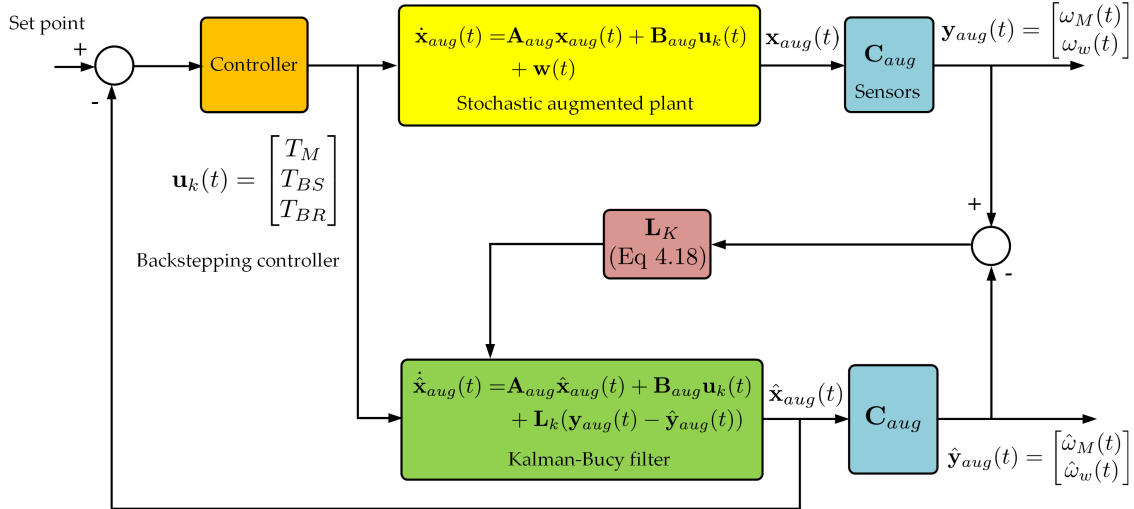


FIGURE 4.2. Block diagram of the estimation using the Kalman-Bucy filter

In practical applications, in order to reduce the computational intricacies of the filter, the steady-state value of \mathbf{P} is commonly utilized. This slightly reduces the performance of the filter before the convergence of \mathbf{P} to its steady-state value but significantly improve the efficiency of the filter by decreasing the required time and memory to perform the estimation (Simon, 2006).

The block diagram of the estimation using the Kalman-Bucy filter is shown in Fig. 4.2.

4.4. Experimental Validation of the Designed Observers

The performance of the proposed observers is verified by means of the experimental test rig introduced in Chapter 2. Here, a sample drive cycle with the duration of 50 s which involves an upshift operation at $t = 6.6$ s during the acceleration and a downshift operation at $t = 44$ sec during the deceleration is utilized for this performance verification. Moreover, the estimation results of the KBF are compared to those of the deterministic Luenberger observer (DLO) in terms of root-mean-square error (RMSE). The data acquisition system is performed at the frequency 1 kHz with National Instruments' CompactRIO® by programming in LabVIEW® FPGA/RealTime.

The determination of the process noise covariance, the measurement noise covariance, and the poles of the DLO have a great impact on the performance of these estimators, and hence, they should be selected thoughtfully. Determining the measurement error covariance is typically feasible. This is because the sensors measurement data are available for assessing the variance of the measurement noise. Generally, this step is performed prior to operation of the filter by using the off-line sample measurement data. This procedure is used in this thesis as shown in Fig. 4.3 wherein the frequency distribution of the speed measurement data together with the fitted normal distribution function are illustrated (Simon, 2006; Bishop and Welch, 2001). However, the process noise covariance is generally more difficult than the measurement noise covariance to be determined. This is due to the inaccessibility of the process which is subject to estimation. The determination of the process noise covariance is generally performed through a so-called tuning process which is a trial-and-error procedure (Simon, 2006; Bishop and Welch, 2001; Lewis et al., 2007). As a rule of thumb, the poles of Luenberger observers are typically selected to be 5 to 10 times farther from the imaginary axis than the poles of the control system in order to achieve fast and accurate state estimation (Ogata, 2009; Jeon and Tomizuka, 2007). On one hand, in practice, due to the presence of process and measurement noises, selecting these poles very far from the imaginary axis can degrade the performance of the observer and in the worst case may result in the divergence of the estimator. On the other hand, considering the poles of the DLO close to the imaginary axis reduces the convergence speed. Thus, the determination of the DLO poles in order to achieve desired performance criteria for the system that encounters process and measurement noise is not trivial. This is because the characteristics of the process and measurement noises are not taken into account when the observer poles are selected. Here, numerous trial-and-error attempts are performed in order to determine proper poles of the DLO which are $p = [-380 \ -290 \ -390 \ -460 \ -150 \ -310 \ -120]^T$. Moreover,

for the KBF, the obtained matrices \mathbf{R}_c and \mathbf{Q}_c are:

$$\begin{aligned}\mathbf{R}_c &= \text{diag}\{3.15 \text{ (rad/s)}^2, 3.15 \text{ (rad/s)}^2\} \times 10^{-3}, \\ \mathbf{Q}_c &= \text{diag}\{51.22 \text{ (rad/s}^2)^2, 1.1 \text{ (N.m/s)}^2, 50.2 \text{ (rad/s}^2)^2, 50.5 \text{ (rad/s}^2)^2, \\ &\quad 1.07 \text{ (N.m/s)}^2, 48.27 \text{ (rad/s}^2)^2, 0.91 \text{ (N.m/s)}^2\}.\end{aligned}\quad (4.22)$$

The estimation results of the unmeasured state variables and the unknown input are shown in Fig. 4.4-4.9 for the upshift operation and in Fig. 4.10-4.15 for the downshift process. The corresponding root-mean-square error of the estimation results is given in Table 4.1 and Table 4.2 for the quantitative comparison between the estimation results. The measurement of angular velocities of the ring and sun gears are performed via a Hall effect sensor with maximum speed detection of 15 kHz. Due to the technical difficulties in the installation of the torque transducer on the input and output shaft of the transmission, indirect measurements of the input and output torque of the transmission from (3.1) and (3.40) are used. From Fig. 4.4-4.6 and Fig. 4.10-4.12 it is observed that the deterministic and stochastic observers effectively estimate the angular velocities of the sun and ring gears and the corresponding gear ratios.

The estimated torque of the input and output shaft and the unknown resisting torque illustrated in Fig. 4.7-4.9 and Fig. 4.13-4.15 reveal that DLO fails to provide an accurate estimation of these state variables. In fact, the existence of the process and measurement noises dramatically affects the RMSE of estimation. However, the KBF provides higher estimation accuracy in terms of RMSE.

TABLE 4.1. RMSE of states and the unknown input estimation (Upshift)

RMS errors	ω_s (rad/s)	ω_r (rad/s)	GR	T_d (Nm)	T_o (Nm)	T_v (Nm)
DLO	13.25	4.55	0.0573	0.433	0.155	0.147
KF	12.14	4.31	0.0501	0.162	0.059	0.051

4.4 EXPERIMENTAL VALIDATION OF THE DESIGNED OBSERVERS

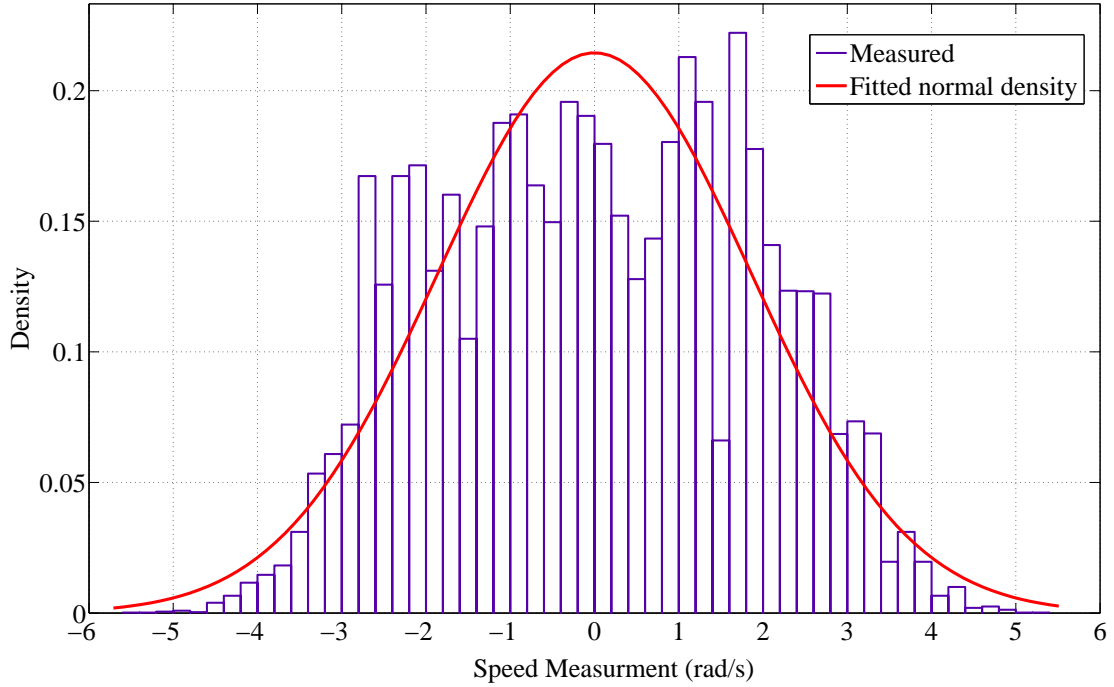


FIGURE 4.3. Probability distribution of the speed measurement sensor data

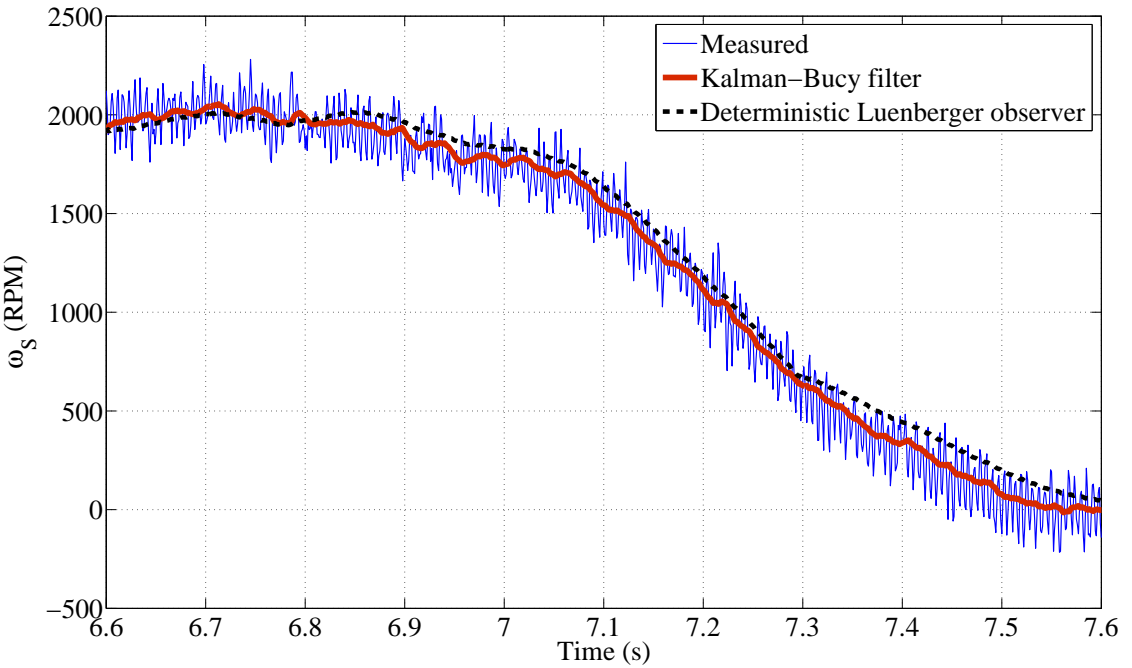


FIGURE 4.4. Estimated and measured speed of the sun gear ω_S (upshift)

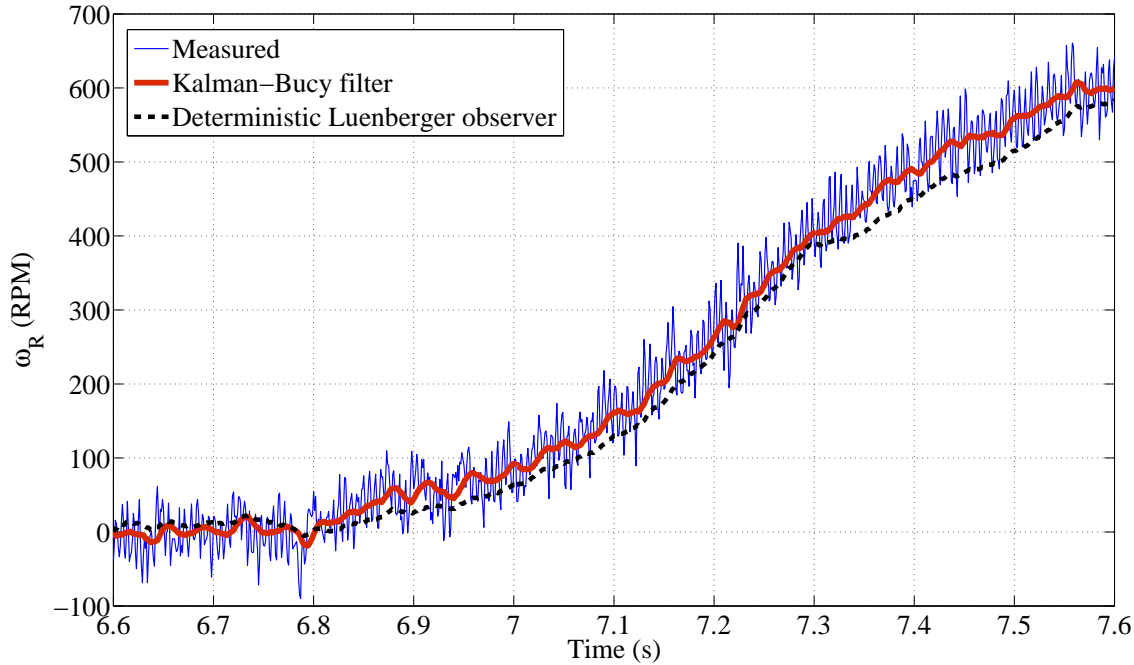
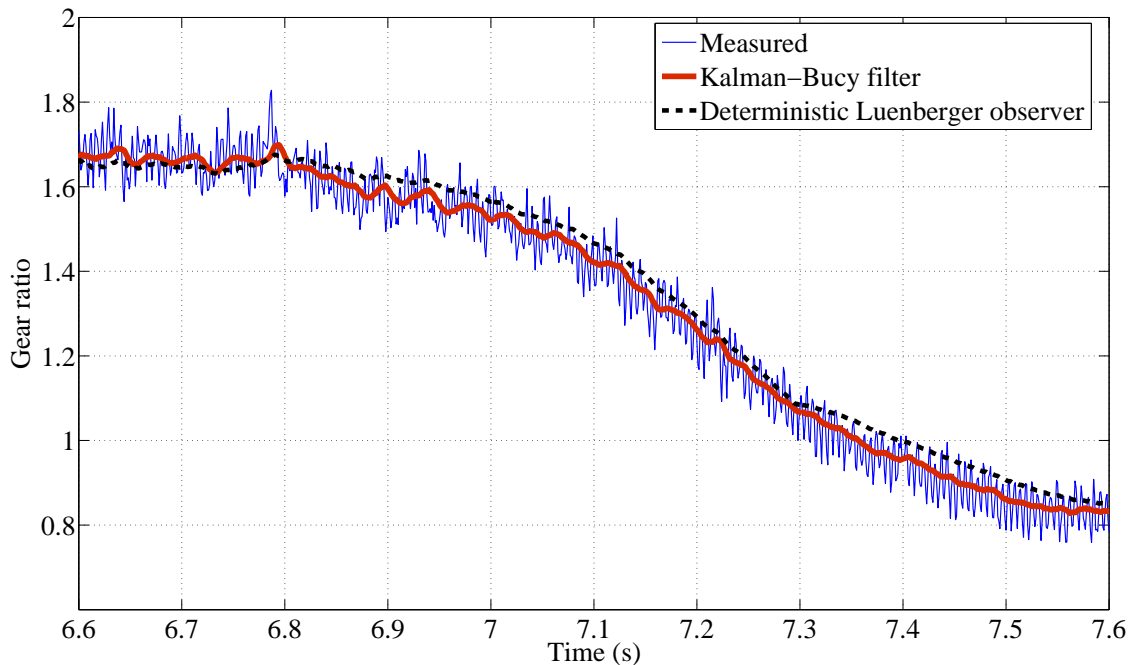
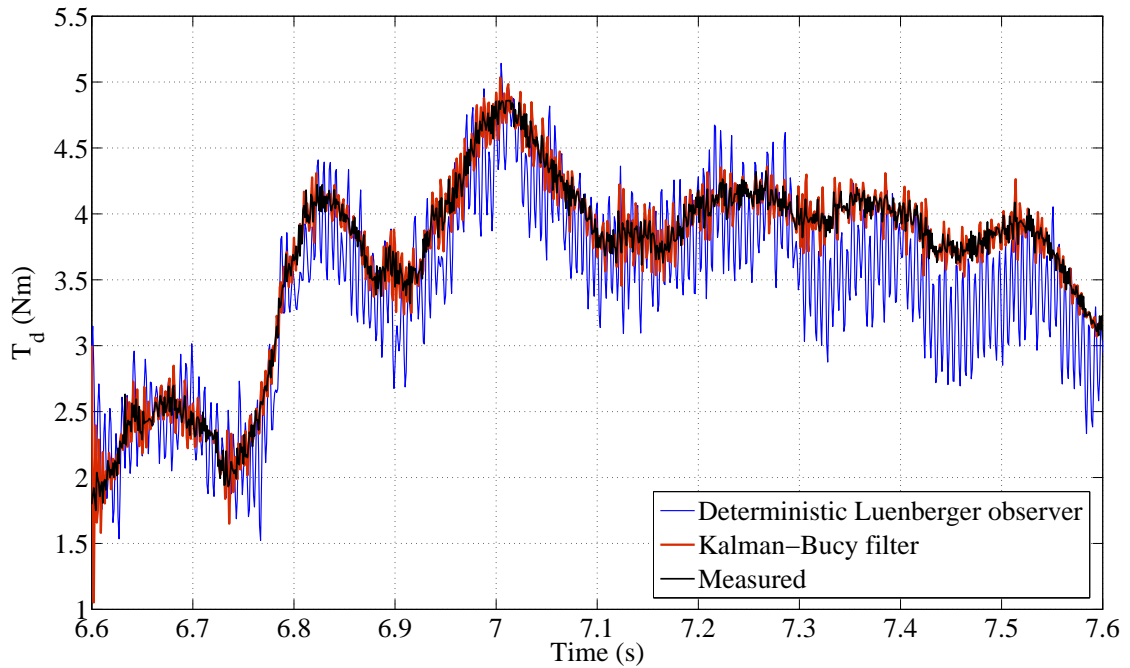
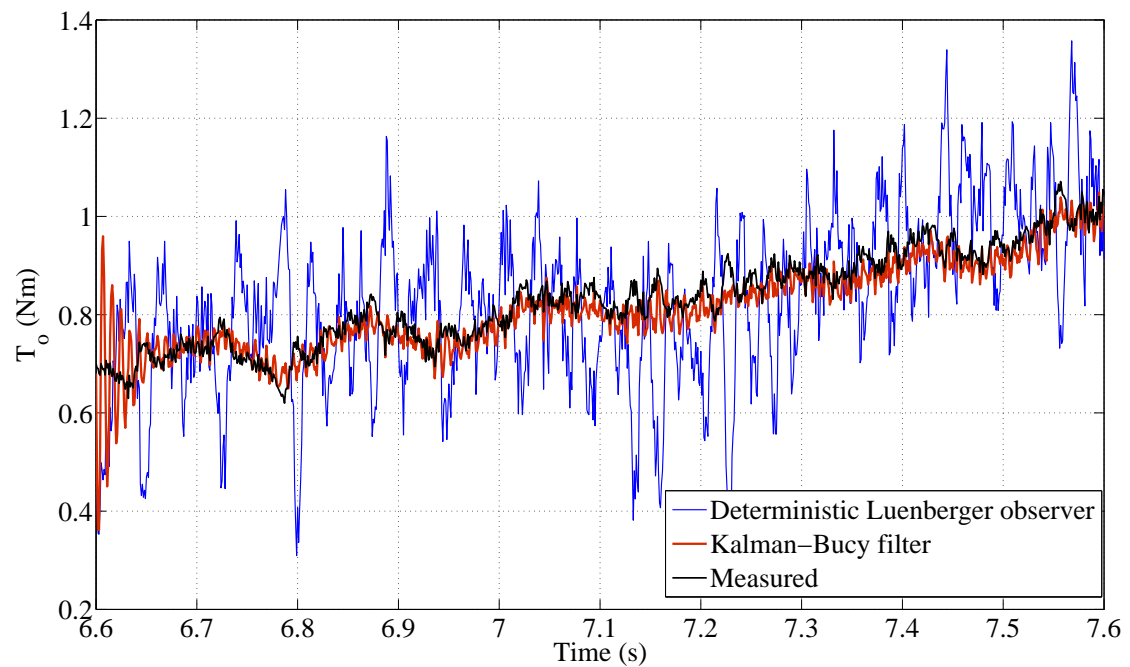
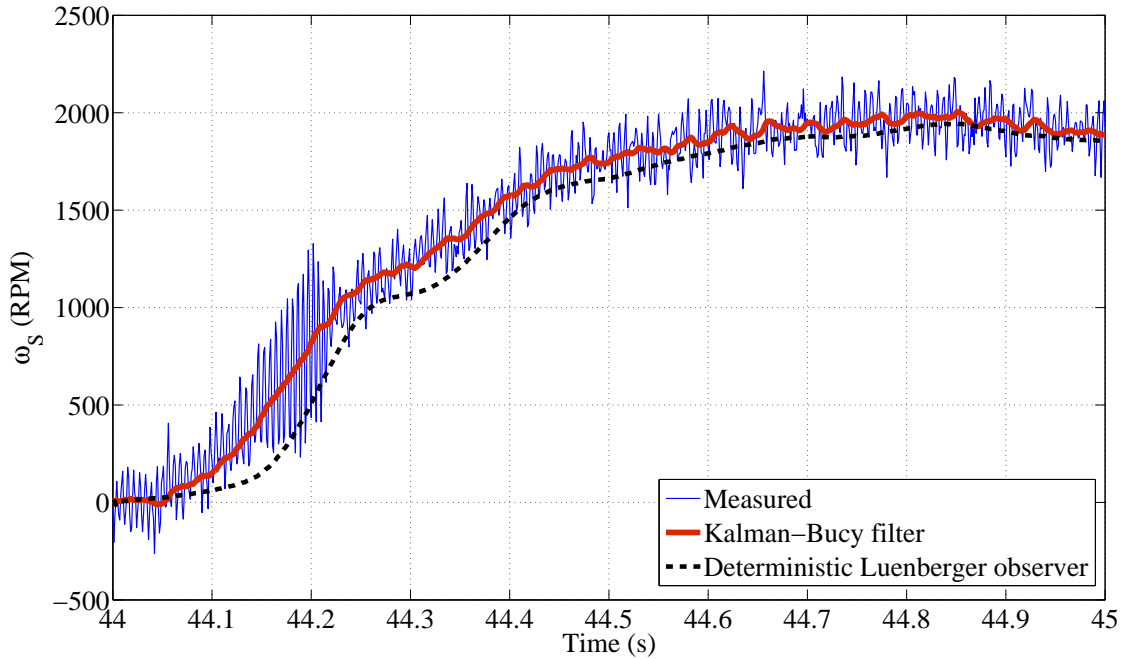
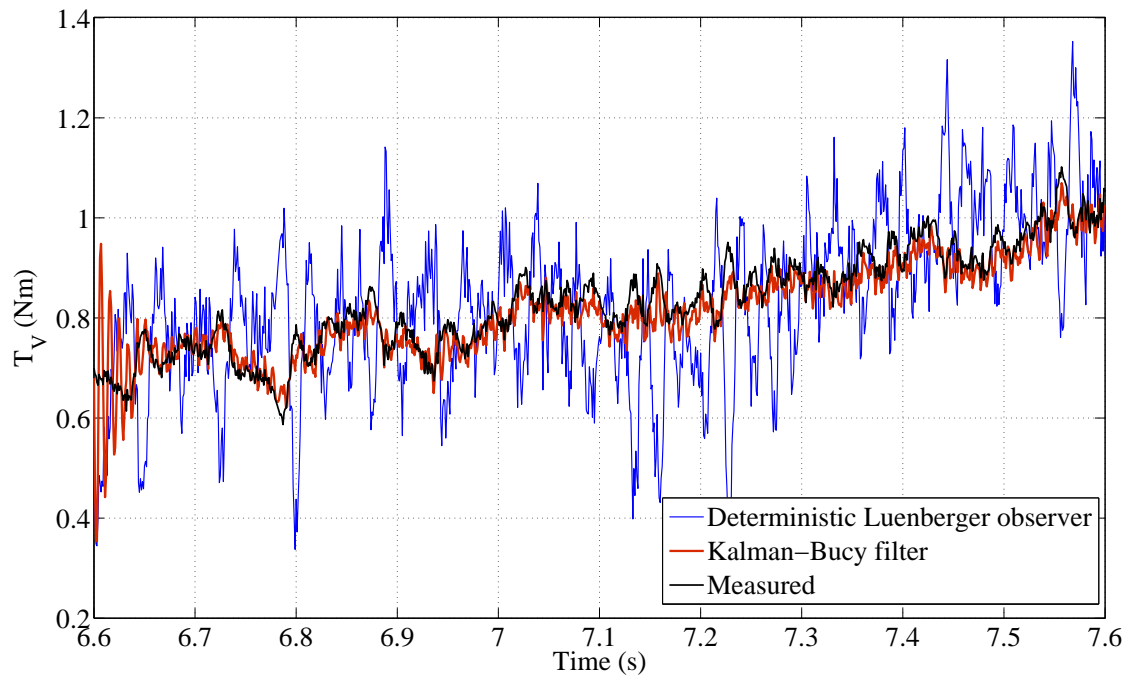
FIGURE 4.5. Estimated and measured speed of the ring gear ω_R (upshift)

FIGURE 4.6. Estimated and measured gear ratio of the transmission (upshift)


 FIGURE 4.7. Estimated and measured torque of the input shaft T_d (upshift)

 FIGURE 4.8. Estimated and measured torque of the output shaft T_o (upshift)

FIGURE 4.10. Estimated and measured speed of the sun gear ω_S (downshift)FIGURE 4.9. Estimated and measured load torque T_v (upshift)

4.4 EXPERIMENTAL VALIDATION OF THE DESIGNED OBSERVERS

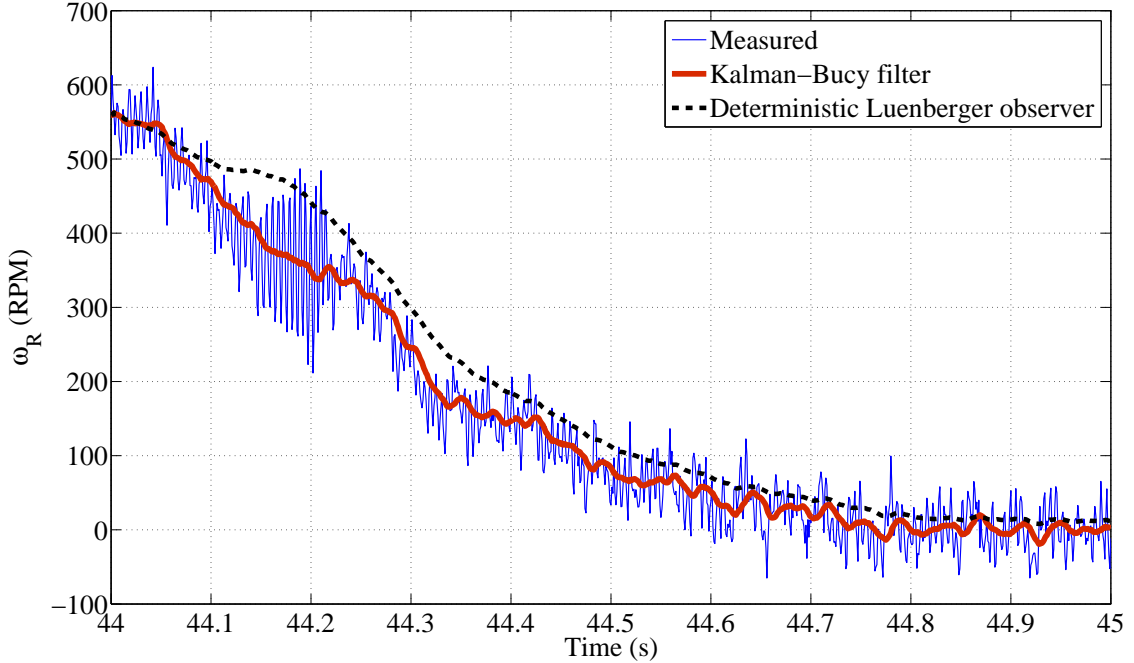


FIGURE 4.11. Estimated and measured speed of the ring gear ω_R (downshift)

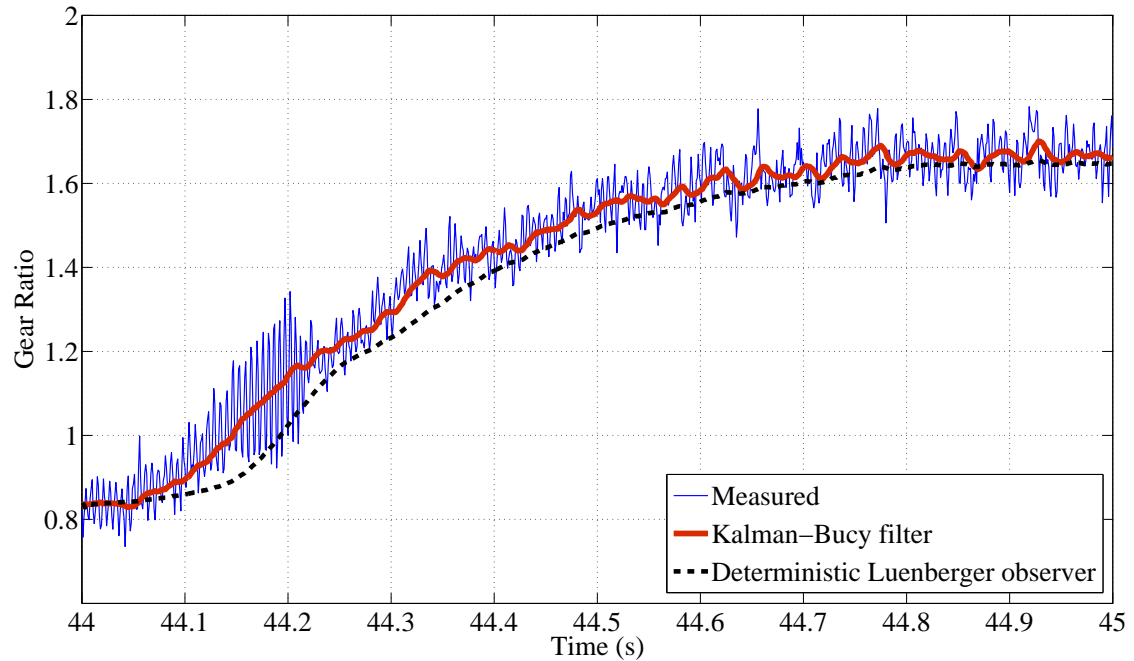
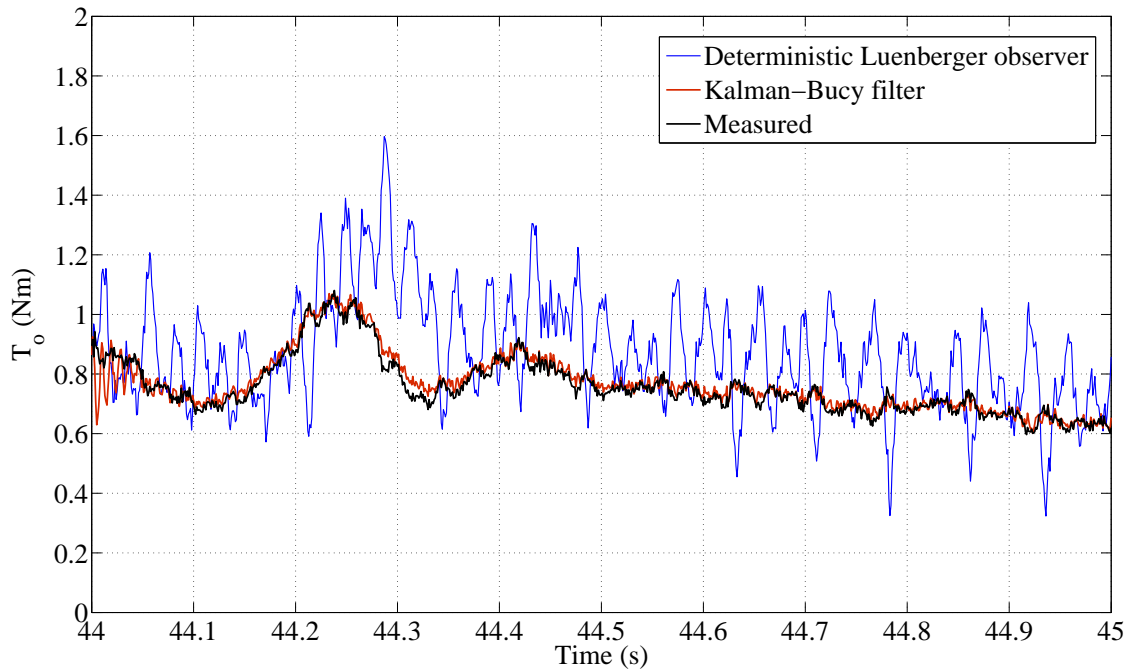
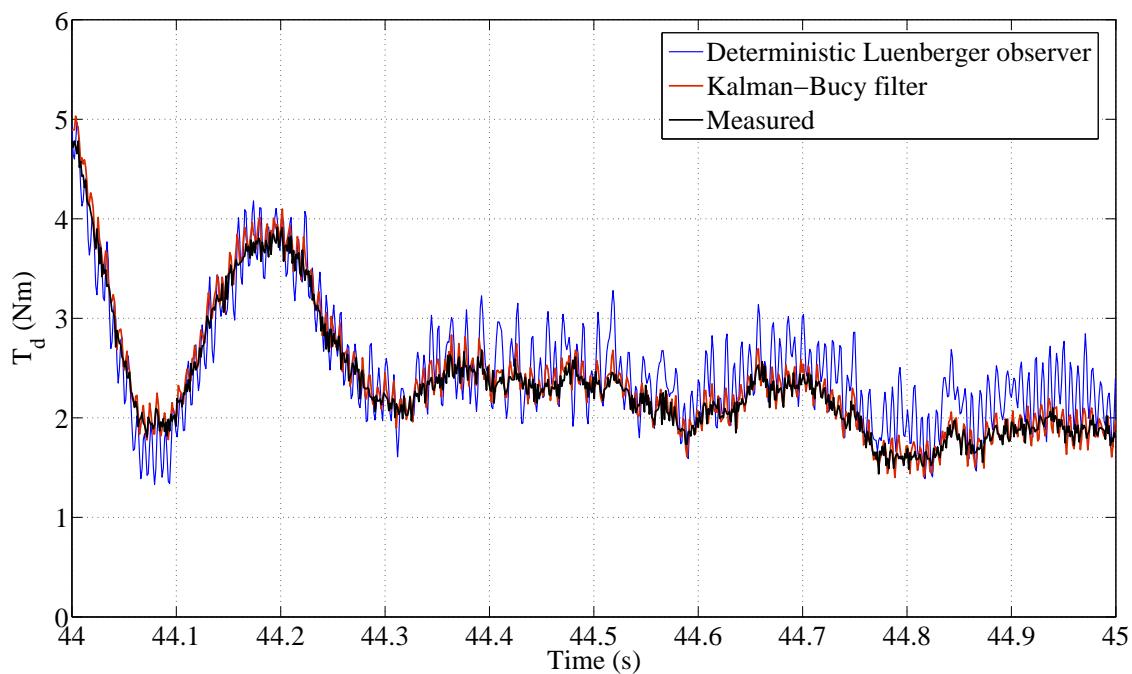
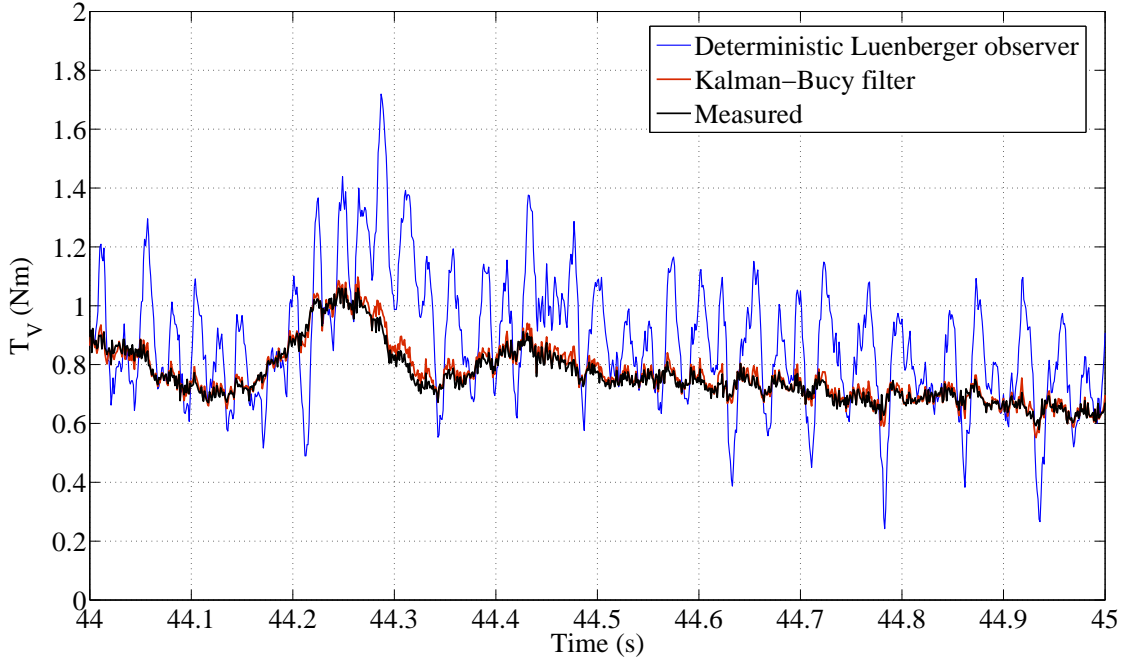


FIGURE 4.12. Estimated and measured gear ratio of the transmission (downshift)

FIGURE 4.14. Estimated and measured torque of the output shaft T_o (downshift)FIGURE 4.13. Estimated and measured torque of the input shaft T_d (downshift)

FIGURE 4.15. Estimated and measured load torque T_v (downshift)

The estimation results illustrate that deterministic observers may not be an appropriate choice in practice due to the existence of the measurement and process noise. Moreover, the experiments demonstrate that selecting the eigenvalues of the Luenberger observer further than those adopted here from the imaginary axis results in an extensive amount of noise on the estimates and selecting these eigenvalues closer to the imaginary axis considerably affects the convergence speed of the observer. The estimation results confirm the KBF improves the accuracy of the estimation in comparison to DLO by alleviating the effect of measurement and process noises on the observation. It is worth mentioning that the estimation of the angular velocities of the sun and ring gear not only can be employed for gear shift control but also to monitor and to avoid internal circulation of the power inside the transmission.

TABLE 4.2. RMSE of states and the unknown input estimation (Downshift)

RMS errors	ω_s (rad/s)	ω_R (rad/s)	GR	T_d (Nm)	T_o (Nm)	T_v (Nm)
DLO	18.47	5.88	0.077	0.345	0.195	0.201
KF	14.95	4.05	0.061	0.148	0.039	0.032

CHAPTER 5

Controller Design

This chapter is devoted to the gear shift controller design for the dual brake transmission (DBT) system aiming at eliminating the power interruption at the wheels while minimizing the shifting time and energy dissipation during the gear shift operation.

As described in more detail in Chapter 1, the gear shift control technique through the torque and inertia phases is the conventional strategy employed for powershift transmissions such as ATs and DCTs (Zhang et al., 2003; Goetz, 2005). The gear shift control of the DBT system via these phases is carried out in Rahimi Mousavi and Boulet (2014). In ATs and DCTs, the clutches and torque converters are designed to transfer the power from the engine/motor to the wheels and vehicle. However, the proposed transmission is completely clutchless and both power transmission paths, as illustrated in Fig. 3.1, are perpetually connected to the electric motor from the input side of the transmission and to the vehicle wheels from the output side. In fact, the application of the brakes in the DBT system is to change the path of power transmission by preventing the transmission of power from one path and redirecting it to the other one. Moreover, the minimization of the energy dissipation during this power redirection maximizes the transmitted power from the electric motor to the vehicle and consequently, improves the efficiency of the vehicle. Furthermore, because of the perpetual connectedness of the power transmission paths in the current

design, torques and speeds are always dependent to each other through the transmitted power. Thus, the control strategy does not require to be distinctly separated into the torque and inertia phases and a more advanced gear shift control strategy specifically designed for the DBT system can be developed from the ground up. Here, the main goals of the controller are to eliminate the output power interruption while minimizing the shifting time and energy dissipation. To this end, in Section 5.1, first, the optimal control definitions are briefly introduced and then the controllability of the case study system is parametrically investigated. Thereafter, the optimal control problem is formulated to eliminate the output power interruption while minimizing the shifting time and energy dissipation to maximize efficiency and drivability of the vehicle. In order to solve these optimal control problems, available techniques are reviewed. In this thesis, Pontryagin minimum principle (PMP) is used in order to solve optimal control problem. The relation between Pontryagin minimum principle (PMP) and Dynamic Programming (DP), which are two important methods in optimal control, is studied in more detail in (Pakniyat and Caines, 2016b, 2014b) wherein their advantages and necessary and sufficient conditions for optimality are discussed. In order to cope with actuators limitations in practice due to the sudden variations of the input commands obtained from the optimal control, the backstepping approach is utilized to design a closed-loop controller to track the optimal law and its corresponding trajectories. The proposed backstepping controller provides a stabilizing feedback law and proof of stability (Khalil and Grizzle, 1996). Finally, the performance of the developed controller is validated by experimental and simulation analyses in Section 5.2 through various gear shift scenarios.

5.1. Optimal Controller Design

As explained in previous chapters, the proposed DBT system has the ability to change the gear ratio without any power interruption in the output. This goal together with the minimization of the shifting time and the energy dissipation caused

by internal brakes of the transmission during the gear shift process is formulated in the optimal control framework in this section (Mousavi et al., 2015).

5.1.1. Definitions and Controllability Analysis

The main goal of the optimal control is to find an optimal control input law \mathbf{u}^* for the system

$$\dot{\mathbf{x}} = \mathbf{f}(\mathbf{x}(t), \mathbf{u}(t), t), \quad (5.1)$$

that minimizes the following performance measure (Kirk, 2012)

$$J = h(\mathbf{x}(t_f), t_f) + \int_{t_0}^{t_f} g(\mathbf{x}(t), \mathbf{u}(t), t) dt. \quad (5.2)$$

In this performance measure, the terms t_0 , t_f , h , and g are the initial time, the final time, the performance measure associated to the final state, and the scalar function specifying the performance measure from the initial time to the final time, respectively. The goal of the optimal control can be mathematically expressed as follows (Kirk, 2012):

$$J^* \triangleq h(\mathbf{x}^*(t_f), t_f) + \int_{t_0}^{t_f} g(\mathbf{x}^*(t), \mathbf{u}^*(t), t) dt \leq h(\mathbf{x}(t_f), t_f) + \int_{t_0}^{t_f} g(\mathbf{x}(t), \mathbf{u}(t), t) dt, \quad (5.3)$$

for all $\mathbf{u} \in \mathcal{U}$ and $\mathbf{x} \in \mathcal{X}$, where \mathbf{x}^* stands for the optimal trajectory. Here, \mathcal{U} and \mathcal{X} are the set of admissible inputs and the set of admissible trajectories, respectively (Kirk, 2012; Ogata, 2009).

Given the fact that the controllability of the system is required to compute the control law, this condition is verified (Kirk, 2012). According to the Kalman controllability rank condition, the linear time-invariant system (4.1) is completely controllable if and only if the 6×16 matrix

$$\mathcal{C} \triangleq [\mathbf{B} \vdots \mathbf{AB} \vdots \dots \vdots \mathbf{A}^5\mathbf{B}], \quad (5.4)$$

has rank 6. The Gauss-Jordan elimination method transforms the matrix \mathcal{C} into the following form which clearly confirms the complete controllability of the case study

system for any non-zero combination of parameters (Kirk, 2012; Ogata, 2009).

$$\tilde{\mathcal{C}} = \left[\begin{array}{cccc|cccc} 1 & 0 & \cdots & 0 & * & * & \cdots & * \\ 0 & 1 & \cdots & 0 & * & * & \cdots & * \\ \vdots & \vdots & \ddots & \vdots & \vdots & \vdots & \ddots & \vdots \\ 0 & 0 & \cdots & 1 & * & * & \cdots & * \end{array} \right] = \left[\mathbf{I}_{6 \times 6} \quad [*]_{6 \times 12} \right] (* \text{ could be anything}). \quad (5.5)$$

5.1.2. Preliminaries of the Optimal Controller Design

In this thesis, the optimal control is formulated for the case that the output torque and output speed of the driveline are desired to remain constant during the gear shift operations. These desired criteria are mathematically interpreted as:

$$\dot{\omega}_w = 0, \quad (5.6)$$

and

$$\dot{T}_o = 0. \quad (5.7)$$

Moreover, as expressed in Section 4.1, the resisting torque from the road (T_v) on the vehicle is assumed to be constant during the gear shift process. Hence, from Equations (2.7), (3.40), (5.6), and (5.7) it is concluded that:

$$T_o = \frac{1}{i_{fd}} T_v, \quad (5.8)$$

and

$$\omega_{C,out} = i_{fd} \omega_w. \quad (5.9)$$

The constant value for $\omega_{C,out}$ in (5.9) necessarily requires that (see (2.7)):

$$\omega_R = \left(\frac{R_2 + 1}{R_2} \right) i_{fd} \omega_w - \frac{1}{R_2} \omega_S, \quad (5.10)$$

as well as:

$$\dot{\omega}_{C,out} = 0 \Rightarrow \dot{\omega}_R = \frac{-1}{R_2} \dot{\omega}_S. \quad (5.11)$$

The objective of the control is to go from the initial gear ratio into the target one (i.e., from (2.9) to (2.10) through (2.11) and vice versa) by means of engaging and

disengaging the brakes of the DBT system. For the states ω_S and ω_R in (3.36), the initial and terminal conditions of the upshift process can be expressed by:

$$\begin{bmatrix} \omega_S(t_0) \\ \omega_R(t_0) \end{bmatrix} = \begin{bmatrix} (R_2 + 1)\omega_{c,out}(t_0) \\ 0 \end{bmatrix} \xrightarrow{\text{upshift}} \begin{bmatrix} \omega_S(t_f) \\ \omega_R(t_f) \end{bmatrix} = \begin{bmatrix} 0 \\ \frac{(R_2+1)}{R_2}\omega_{c,out}(t_f) \end{bmatrix}, \quad (5.12)$$

and for the downshift operation is specified by:

$$\begin{bmatrix} \omega_S(t_0) \\ \omega_R(t_0) \end{bmatrix} = \begin{bmatrix} 0 \\ \frac{(R_2+1)}{R_2}\omega_{c,out}(t_0) \end{bmatrix} \xrightarrow{\text{downshift}} \begin{bmatrix} \omega_S(t_f) \\ \omega_R(t_f) \end{bmatrix} = \begin{bmatrix} (R_2 + 1)\omega_{c,out}(t_f) \\ 0 \end{bmatrix}, \quad (5.13)$$

Substituting (5.11) in (3.36) yields:

$$\begin{aligned} & (\lambda R_2 - \tau) (C_S \omega_S - T_{BS}) - (\gamma R_2 - \lambda) (C_R \omega_R - T_{BR}) + (c + e R_2) T_d \\ & - (\lambda R_2 - \tau) T_{Sf} + (\gamma R_2 - \lambda) T_{Rf} - (d + f R_2) T_o = 0. \end{aligned} \quad (5.14)$$

Rearranging Equation (5.14) results in the following equation for T_d :

$$\begin{aligned} T_d = \frac{1}{c + e R_2} & \left((\lambda R_2 - \tau) T_{BS} + (\lambda - \gamma R_2) T_{BR} + (\tau - \lambda R_2) C_S \omega_S \right. \\ & \left. + (\gamma R_2 - \lambda) C_R \omega_R + (\lambda R_2 - \tau) T_{Sf} - (\gamma R_2 - \lambda) T_{Rf} + (d + f R_2) T_o \right). \end{aligned} \quad (5.15)$$

The controllability of the system implies that there exists a motor torque T_M such that Equation (5.15) is satisfied for all instants (see Mousavi et al. (2014) and also Equation (5.65)). Thus, among the control inputs, the motor torque T_M is reserved for satisfying equation (5.15), and hence, the number of independent control inputs is reduced to two, which are the brakes of the sun and ring T_{BS} and T_{BR} .

Substituting (5.15) and (2.7) into the equation for $\dot{\omega}_S$ in (3.36) results in:

$$\begin{aligned} \dot{\omega}_S = \frac{1}{a(c + e R_2)} & \left(- [(e\tau + c\lambda) C_S R_2 + (e\lambda + c\gamma) C_R] \omega_S - (de - cf) R_2 T_o \right. \\ & + (1 + R_2) (e\lambda + c\gamma) C_R \omega_{c,out} + (e\tau + c\lambda) R_2 T_{BS} - (e\lambda + c\gamma) R_2 T_{BR} \\ & \left. + (e\tau + c\lambda) R_2 T_{Sf} - (e\lambda + c\gamma) R_2 T_{Rf} \right). \end{aligned} \quad (5.16)$$

For ease of notation, the coefficients in (5.16) are defined as follows

$$A_S \triangleq \frac{(e\tau + c\lambda) C_S R_2 + (e\lambda + c\gamma) C_R}{a(c + eR_2)}, \quad (5.17a)$$

$$B_{S1} \triangleq \frac{(e\tau + c\lambda) R_2}{a(c + eR_2)}, \quad (5.17b)$$

$$B_{S2} \triangleq \frac{(e\lambda + c\gamma) R_2}{a(c + eR_2)}, \quad (5.17c)$$

$$G_S \triangleq \frac{1}{a(c + eR_2)} \left((1 + R_2)(e\lambda + c\gamma) C_R \omega_{C,out} - (de - cf) R_2 T_o + (e\tau + c\lambda) R_2 T_{Sf} - (e\lambda + c\gamma) R_2 T_{Rf} \right). \quad (5.17d)$$

Thus, from (5.17), Equation (5.16) is represented by:

$$\dot{\omega}_S = -A_S \omega_S + B_{S1} T_{BS} - B_{S2} T_{BR} + G_S, \quad (5.18)$$

with the following initial and terminal conditions from (5.13):

$$\begin{aligned} \text{Upshift: } & \omega_S(t_0) = (R_2 + 1)\omega_{c,out}(t_0); \quad \omega_S(t_f) = 0, \\ \text{Downshift: } & \omega_S(t_0) = 0; \quad \omega_S(t_f) = (R_2 + 1)\omega_{c,out}(t_f). \end{aligned} \quad (5.19)$$

As pointed out in Section 3.3.5, during the gear changing process the ring and the sun are rotating in the positive directions and hence according to (3.16) and (3.19) it can be concluded that:

$$-|T_{BS}^{max}| \leq T_{BS} \leq 0, \quad -|T_{BR}^{max}| \leq T_{BR} \leq 0. \quad (5.20)$$

5.1.3. Optimal Control Problems

In this subsection, first, the Pontryagin Minimum Principle (PMP), a powerful tool for computation of the optimal control, is presented. Thereafter, two problems: 1) the minimum gear shifting time, and 2) the minimum energy dissipation during the gear shifts, are solved based on the PMP in order to determine the optimal control laws. The Pontryagin Minimum Principle states that for the system (5.1) with the performance measure (5.2), there exists an adjoint process $\mathbf{p}^*(t)$ for the optimal control input $\mathbf{u}^*(t)$ and along the corresponding optimal trajectory $\mathbf{x}^*(t)$,

such that (Kirk, 2012):

$$\begin{cases} \dot{\mathbf{x}}^*(t) = \frac{\partial \mathcal{H}}{\partial \mathbf{p}}(\mathbf{x}^*(t), \mathbf{u}^*(t), \mathbf{p}^*(t), t), \\ \dot{\mathbf{p}}^*(t) = -\frac{\partial \mathcal{H}}{\partial \mathbf{x}}(\mathbf{x}^*(t), \mathbf{u}^*(t), \mathbf{p}^*(t), t), \\ \mathcal{H}(\mathbf{x}^*(t), \mathbf{u}^*(t), \mathbf{p}^*(t), t) \leq \mathcal{H}(\mathbf{x}^*(t), \mathbf{u}(t), \mathbf{p}^*(t), t), \end{cases} \quad (5.21)$$

for all admissible $\mathbf{u}(t)$ and $t \in [t_0, t_f]$, where the Hamiltonian \mathcal{H} is defined by (Kirk, 2012):

$$\mathcal{H}(\mathbf{x}(t), \mathbf{u}(t), \mathbf{p}(t), t) \triangleq g(\mathbf{x}(t), \mathbf{u}(t), t) + \mathbf{p}^T(t)\mathbf{f}(\mathbf{x}(t), \mathbf{u}(t), t), \quad (5.22)$$

The terminal boundary condition associated with this principle is (Kirk, 2012):

$$\begin{aligned} & \left[\mathcal{H}(\mathbf{x}^*(t_f), \mathbf{u}^*(t_f), \mathbf{p}^*(t_f), t_f) + \frac{\partial h}{\partial t}(\mathbf{x}^*(t_f), t_f) \right] \delta t_f \\ & + \left[\frac{\partial h}{\partial \mathbf{x}}(\mathbf{x}^*(t_f), t_f) - \mathbf{p}^*(t_f) \right]^T \delta \mathbf{x}_f = 0. \end{aligned} \quad (5.23)$$

5.1.3.1. The Minimum Shifting Time Problem. The performance measure for the minimum time control problem is:

$$J(\mathbf{u}) = \int_{t_0}^{t_f} 1 dt, \quad (5.24)$$

with t_f being the first time after t_0 that the terminal condition in (5.19) occurs. According to the equations (5.18) and (5.22), the Hamiltonian is formed as:

$$\mathcal{H}(\omega_S, p, T_{BS}, T_{BR}) = 1 + p(-A_S \omega_S + B_{S1} T_{BS} - B_{S2} T_{BR} + G_S). \quad (5.25)$$

Based on the Pontryagin Minimum Principle, the dynamics of the adjoint process p^* are governed by the following equation:

$$\dot{p}^* = -\frac{\partial \mathcal{H}(\omega_S, p^*, T_{BS}, T_{BR})}{\partial \omega_S} = p^* A_S, \quad (5.26)$$

and the Hamiltonian minimization condition results in:

$$\mathcal{H}(\omega_S^*, p^*, T_{BS}^*, T_{BR}^*) \leq \mathcal{H}(\omega_S^*, p^*, T_{BS}, T_{BR}^*), \quad (5.27)$$

for all $-|T_{BS}^{max}| \leq T_{BS} \leq 0$, and

$$\mathcal{H}(\omega_S^*, p^*, T_{BS}^*, T_{BR}^*) \leq \mathcal{H}(\omega_S^*, p^*, T_{BS}, T_{BR}), \quad (5.28)$$

for all $-|T_{BR}^{max}| \leq T_{BR} \leq 0$. Since this is a fixed terminal value problem, it is concluded that (Shaikh and Caines, 2007; Kirk, 2012):

$$\mathcal{H}(\omega_S^*(t), p^*(t), T_{BS}^*(t), T_{BR}^*(t)) = 0, \quad \text{for all } t \in [t_0, t_f]. \quad (5.29)$$

Hence, From Equation (5.25):

$$p^*(-A_S\omega_S^* + B_{S1}T_{BS}^* - B_{S2}T_{BR}^* + G_S) = -1, \quad (5.30)$$

for all $t \in [t_0, t_f]$. Solving (5.26) results in

$$p^*(t) = p^*(t_0) e^{A_s t}. \quad (5.31)$$

Since the angular velocity of the sun is decreasing in the upshift process ($\dot{\omega}_S \leq 0$), equation (5.30) requires that $p^*(t_0) > 0$ and hence $p^*(t) > 0$ for all $t \in [t_0, t_f]$. Thus the Hamiltonian minimization (5.27) and (5.28) give $T_{BS}^* = -|T_{BS}^{max}|$ and $T_{BR}^* = 0$, respectively. In a similar way it can be argued that the Hamiltonian minimization (5.27) and (5.28) give $T_{BS}^* = 0$ and $T_{BR}^* = -|T_{BR}^{max}|$ for the downshift process.

Given the fact that an optimal control law exists, the satisfaction of the Pontryagin minimum principle provides both necessary and sufficient condition of optimality for the minimum gear shift time problem (Kirk, 2012).

5.1.3.2. Minimum Energy Dissipation Controller. For the minimum energy dissipation problem the performance measure is expressed by:

$$J(\mathbf{u}) = \int_{t_0}^{t_f} -(T_{BS} + T_{Sf})\omega_S - (T_{BR} + T_{Rf})\omega_R dt, \quad (5.32)$$

with the initial and terminal conditions (5.19). Replacing ω_R from (2.7) into (5.32) results in the following performance measure:

$$J(\mathbf{u}) \int_{t_0}^{t_f} \left(- \left(T_{BS} + T_{Sf} - \frac{1}{R_2} (T_{BR} + T_{Rf}) \right) \omega_S - \left(1 + \frac{1}{R_2} \right) (T_{BR} + T_{Rf}) \omega_{C,out} \right) dt. \quad (5.33)$$

Therefore, the Hamiltonian can be formed as follows:

$$\begin{aligned} \mathcal{H}(\omega_S, p, T_{BS}, T_{BR}) &= p(-A_S \omega_S + B_{S1} T_{BS} - B_{S2} T_{BR} + G_S) \\ &\quad - \left(T_{BS} + T_{Sf} - \frac{1}{R_2} (T_{BR} + T_{Rf}) \right) \omega_S - \left(1 + \frac{1}{R_2} \right) (T_{BR} + T_{Rf}) \omega_{C,out}. \end{aligned} \quad (5.34)$$

Based on the Minimum Principle, the dynamics of the optimal adjoint process p^* is given by:

$$\dot{p}^* = -\frac{\partial \mathcal{H}(\omega_S, p^*, T_{BS}, T_{BR})}{\partial \omega_S} = p^* A_S + \left(T_{BS} + T_{Sf} - \frac{1}{R_2} (T_{BR} + T_{Rf}) \right). \quad (5.35)$$

The Hamiltonian minimization condition with respect to T_{BS} states that

$$(p^* B_{S1} - \omega_S^*) T_{BS}^* \leq (p^* B_{S1} - \omega_S^*) T_{BS}, \quad (5.36)$$

for all $-|T_{BS}^{max}| \leq T_{BS} \leq 0$, and the Hamiltonian minimization with respect to T_{BR} gives

$$\left(-p^* B_{S2} + \frac{\omega_S^*}{R_2} - \left(1 + \frac{1}{R_2} \right) \omega_{C,out} \right) T_{BR}^* \leq \left(-p^* B_{S2} + \frac{\omega_S^*}{R_2} - \left(1 + \frac{1}{R_2} \right) \omega_{C,out} \right) T_{BR}, \quad (5.37)$$

for all $-|T_{BR}^{max}| \leq T_{BR} \leq 0$. With the fixed terminal values specified in (5.19), the terminal condition (5.23) results in:

$$\mathcal{H}(\omega_S^*, p^*, T_{BS}^*, T_{BR}^*) = 0, \text{ for all } t \in [t_0, t_f], \quad (5.38)$$

which is similar to the minimum shifting time case. Noting that $\omega_S^* \geq 0$ and $\omega_R^* \geq 0$ for all $t \in [t_0, t_f]$, and consequently

$$\frac{\omega_S^*}{R_2} - \left(1 + \frac{1}{R_2} \right) \omega_{C,out} \equiv -\omega_R^* \leq 0. \quad (5.39)$$

Therefore, the optimality conditions (5.36) and (5.37) result in $T_{BS}^* = -|T_{BS}^{max}|$, $T_{BR}^* = 0$ when $p^* \geq \frac{\omega_S^*}{B_{S1}}$ for the upshift operation and $T_{BS}^* = 0$, $T_{BR}^* = -|T_{BR}^{max}|$ when $p^* \leq -\frac{\omega_R^*}{B_{S2}}$ for the downshift process. The existence of an adjoint process satisfying equation (5.35) and lying within the region determined by $p^* \geq \frac{\omega_S^*}{B_{S1}}$ for the upshift process and $p^* \leq -\frac{\omega_R^*}{B_{S2}}$ for the downshift operation verifies that the minimum energy dissipation controller is equivalent to the minimum shifting time controller.

5.1.4. Backstepping Controller Design

Implementation of the optimal control law computed in the previous section is rigorous in practice due to the sudden engagement and disengagement of the brakes which cause in abrupt variations of the motor torque. In order to tackle this problem, based on the results of the optimal controller, a feasible controller is designed in this section by replacing the sudden engagement and disengagement of the brakes with smooth commands that can be provided by the actuators. The backstepping approach is utilized due to the cascade structure of dynamical equations of the system. The proposed backstepping controller provides a stabilizing feedback law with the simultaneous proof of the stability. The backstepping approach is applied due to the cascade structure of dynamical equations of the system.

To start the recursive procedure of the backstepping, the dynamic equations of T_o and ω_w from (3.5) and (3.40) are rewritten as follows (Khalil and Grizzle, 1996):

$$\begin{aligned}\dot{\omega}_w &= \frac{-1}{J_v} T_v + \frac{i_{fd}}{J_v} T_o, \\ \dot{T}_o &= -i_{fd} K_o \omega_w + K_o \omega_{C,out}.\end{aligned}\tag{5.40}$$

Choosing the first control Lyapunov function (CLF) as:

$$V_1(\omega_w) = \frac{1}{2} (\omega_w - \omega_{w,des})^2,\tag{5.41}$$

and defining the virtual control input as:

$$\Phi(\omega_w) \triangleq T_{o,des} = \frac{J_v}{i_{fd}} \left(\frac{1}{J_v} T_v - K_I (\omega_w - \omega_{w,des}) \right),\tag{5.42}$$

result in:

$$\dot{V}_1(\omega_w) = -K_I(\omega_w - \omega_{w,des})^2. \quad (5.43)$$

Therefore, the system $\dot{\omega}_w = -K_I(\omega_w - \omega_{w,des})$ is globally exponentially stable. To backstep, the first change of variables is considered as follows (the backstepping variables appear in higher order terms by exploiting the modularity of the method):

$$\varpi = T_o - T_{o,des} = T_o - \Phi(\omega_w) \Rightarrow \dot{\varpi} = \dot{T}_o - \dot{\Phi}, \quad (5.44)$$

in order to transform the system (5.40) into the following form

$$\begin{aligned} \dot{\omega}_w &= -K_I(\omega_w - \omega_{w,des}) + \frac{i_{fd}}{J_v}\varpi, \\ \dot{\varpi} &= -i_{fd}K_o\omega_w + K_o\omega_{C,out} - \dot{\Phi}. \end{aligned} \quad (5.45)$$

Taking

$$V_2(\omega_w, \varpi) = \frac{1}{2}(\omega_w - \omega_{w,des})^2 + \frac{1}{2}(\varpi)^2, \quad (5.46)$$

and considering this CLF for the second order systems (5.45):

$$\Upsilon(\omega_w, \varpi) \triangleq \omega_{C,out,des} = -\frac{i_{fd}}{K_o J_v}(\omega_w - \omega_{w,des}) + i_{fd}\omega_w + \frac{1}{K_o}\dot{\Phi} - \frac{K_{II}}{K_o}\varpi, \quad (5.47)$$

yields

$$\dot{V}_2(\omega_w, \varpi) = -K_I(\omega_w - \omega_{w,des})^2 - K_{II}\varpi^2. \quad (5.48)$$

Therefore, the system is globally asymptotically stable around $(\omega_w, \varpi) = (\omega_{w,des}, 0)$.

In order to proceed with the second backstep, the second change of variable is considered as follows:

$$\sigma = \omega_{C,out} - \omega_{C,out,des} = \omega_{C,out} - \Upsilon \Rightarrow \dot{\sigma} = \dot{\omega}_{C,out} - \dot{\Upsilon}. \quad (5.49)$$

From system dynamics presented in Chapter 3 and Equations (5.45) and (5.47) it can be concluded that:

$$\begin{aligned}\dot{\omega}_w &= -K_I(\omega_w - \omega_{w,des}) + \frac{i_{fd}}{J_v}\varpi, \\ \dot{\varpi} &= -K_{II}\varpi - \frac{i_{fd}}{J_v}(\omega_w - \omega_{w,des}) + K_o\sigma, \\ \dot{\sigma} &= A_\sigma + B_\sigma T_d + C_\sigma(\varpi + \Phi) - \dot{\Upsilon},\end{aligned}\tag{5.50}$$

with

$$\begin{aligned}A_\sigma &= \frac{1}{a(R_2 + 1)} \left((R_2\gamma - \lambda)T_{BR} + (\tau - R_2\lambda)T_{BS} + (R_2\lambda - \tau)C_S\omega_S \right. \\ &\quad \left. + (\lambda - R_2\gamma)C_R\omega_R + (R_2\gamma - \lambda)T_{RF} + (\tau - R_2\lambda)T_{SF} \right), \\ B_\sigma &= \frac{R_2e + c}{a(R_2 + 1)}, \\ C_\sigma &= -\frac{R_2f + d}{a(R_2 + 1)}.\end{aligned}\tag{5.51}$$

Considering the following Lyapunov function:

$$V_3(\omega_w, \varpi, \sigma) = \frac{1}{2}(\omega_w - \omega_{w,des})^2 + \frac{1}{2}(\varpi)^2 + \frac{1}{2}(\sigma)^2,\tag{5.52}$$

and applying the virtual control law:

$$\Psi(\omega_w, \varpi, \sigma) \triangleq T_{d,des} = \frac{1}{B_\sigma}(-A_\sigma - K_o\varpi - C_\sigma(\varpi + \Phi) + \dot{\Upsilon} - K_{III}\sigma),\tag{5.53}$$

make the Lyapunov function's derivative negative definite:

$$\dot{V}_3(\omega_w, \varpi, \sigma) = -K_I(\omega_w - \omega_{w,des})^2 - K_{II}(\varpi)^2 - k_{III}(\sigma)^2.\tag{5.54}$$

This clearly ensures that the system (5.50) is globally asymptotically stable around the point $(\omega_w, \varpi, \sigma) = (\omega_{w,des}, 0, 0)$.

Considering the next backstepping change of variables as:

$$\zeta = T_d - T_{d,des} = T_d - \Psi \Rightarrow \dot{\zeta} = \dot{T}_d - \dot{\Psi},\tag{5.55}$$

transforms the system (5.50) and (3.3) to:

$$\begin{aligned}
\dot{\omega}_w &= -K_I(\omega_w - \omega_{w,des}) + \frac{i_{fd}}{J_v}\varpi, \\
\dot{\varpi} &= -K_{II}\varpi - \frac{i_{fd}}{J_v}(\omega_w - \omega_{w,des}) + K_o\sigma, \\
\dot{\sigma} &= -K_{III}\sigma - K_o\varpi + B_\sigma\zeta, \\
\dot{\zeta} &= K_d\omega_M - K_d\omega_{C,in} - \dot{\Psi}.
\end{aligned} \tag{5.56}$$

Choosing the CLF as follows:

$$\Gamma(\omega_w, \varpi, \sigma, \zeta) \triangleq \omega_{M,des} = \frac{1}{K_d}(K_d\omega_{C,in} + \dot{\Psi} - B_\sigma\sigma - K_{IV}\zeta), \tag{5.57}$$

for the candidate Lyapunov function:

$$V_4(\omega_w, \varpi, \sigma, \zeta) = \frac{1}{2}(\omega_w - \omega_{w,des})^2 + \frac{1}{2}(\varpi)^2 + \frac{1}{2}(\sigma)^2 + \frac{1}{2}(\zeta)^2, \tag{5.58}$$

ensures the asymptotic stability of the system (5.56) by making the derivative of the Lyapunov function (5.58) negative definite:

$$\dot{V}_4(\omega_w, \varpi, \sigma, \zeta) = -K_I(\omega_w - \omega_{w,des})^2 - K_{II}(\varpi)^2 - k_{III}(\sigma)^2 - K_{IV}\zeta^2. \tag{5.59}$$

The last backstepping change of variable is considered as:

$$\xi = \omega_M - \omega_{M,des} = \omega_M - \Gamma \Rightarrow \dot{\xi} = \dot{\omega}_M - \dot{\Gamma}, \tag{5.60}$$

which transforms the system dynamics presented in Chapter 3 and Equation (5.56)

$$\begin{aligned}
\dot{\omega}_w &= -K_I(\omega_w - \omega_{w,des}) + \frac{i_{fd}}{J_v}\varpi, \\
\dot{\varpi} &= -K_{II}\varpi - \frac{i_{fd}}{J_v}(\omega_w - \omega_{w,des}) + K_o\sigma, \\
\dot{\sigma} &= -K_{III}\sigma - K_o\varpi + B_\sigma\zeta, \\
\dot{\zeta} &= -K_{IV}\zeta - B_\sigma\sigma + K_d\xi, \\
\dot{\xi} &= \frac{1}{J_M}(T_M - (\Psi + \zeta)) - \dot{\Gamma}.
\end{aligned} \tag{5.61}$$

Thus, considering the motor torque as:

$$T_M(\omega_w, \varpi, \sigma, \zeta, \xi) = (\Psi + \zeta) + J_M(-K_d\zeta + \dot{\Gamma} - K_V\xi), \quad (5.62)$$

makes the derivative of the candidate Lyapunov function:

$$V_5(\omega_w, \varpi, \sigma, \zeta, \xi) = \frac{1}{2}(\omega_w - \omega_{w,des})^2 + \frac{1}{2}(\varpi)^2 + \frac{1}{2}(\sigma)^2 + \frac{1}{2}(\zeta)^2 + \frac{1}{2}(\xi)^2, \quad (5.63)$$

negative definite as follows:

$$\dot{V}_5(\omega_w, \varpi, \sigma, \zeta, \xi) = -K_I(\omega_w - \omega_{w,des})^2 - K_{II}(\varpi)^2 - k_{III}(\sigma)^2 - K_{IV}\zeta^2 - K_V\xi^2. \quad (5.64)$$

This clearly ensures the asymptotic stability of the dynamical system (5.61) as:

$$(\omega_w, \varpi, \sigma, \zeta, \xi) \rightarrow (\omega_{w,des}, 0, 0, 0, 0) \text{ when } t \rightarrow \infty.$$

The motor torque in equation (5.62) is equivalent to:

$$T_M = T_d + J_M \left(-K_d(T_d - T_{d,des}) + \dot{\omega}_{M,des} - K_V(\omega_M - \omega_{M,des}) \right). \quad (5.65)$$

5.2. Simulation and Experimental Results

In this section, the simulation and experimental results are provided for the designed gear shift controller. The tests are carried out for a sample drive cycle with a duration of 50 seconds which has one upshift at $t = 16$ s and one downshift at $t = 26$ s. The resisting torque of the load motor is set to be $T_v = 1 \pm 0.05$ Nm.

The designed backstepping controller with the parameters given in Table 5.1 is applied to both experimental and simulation tests to maintain the output torque and the output speed constant. The applied brake forces for both experimental and simulation tests are shown in Fig. 5.1 with $N_{BS,max} = 110$ N and $N_{BR,max} = 30$ N.

TABLE 5.1. Parameters of the Backstepping Controller

K_I	K_{II}	K_{III}	K_{IV}	K_V
900	1300	1200	2000	3400

5.2 SIMULATION AND EXPERIMENTAL RESULTS

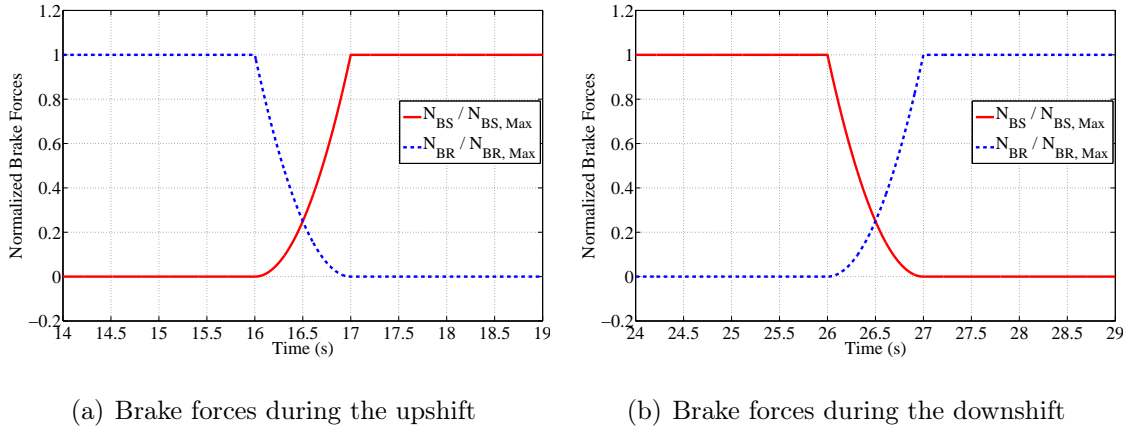


FIGURE 5.1. Normalized brake force profiles applied to both experimental and simulation tests during the upshift and downshift operations

For practical reasons, instead of direct measurement of the torques on the input and the output shafts, the stochastic observer designed in Chapter 4 is employed in order to estimate T_d , T_o , ω_S , ω_R , and T_v using the measured values of the states ω_M and ω_w and the known values of the input torques T_M , T_{BS} and T_{BR} . Figure 5.2 illustrates the block diagram of the observer-based backstepping controller.

For clarity of the figures, the results of the mathematical model are not shown because they exactly fit the simulation results from the SimDriveLineTM model.

The simulation and experimental results for the upshift process are illustrated in Fig. 5.3 - Fig. 5.6 and the results of the downshift operation are demonstrated in Fig. 5.7 - Fig. 5.10. The frequency of data acquisition for both experimental and simulation tests are 1000 Hz . The angular velocities of the motor (ω_M) and output (ω_w) during the upshift and downshift operations are illustrated in Fig. 5.3 and Fig. 5.7. It can be observed that during the synchronization of the motor with the speed of the driveline in the target gear, the designed controller effectively maintained the output speed to such a point that the oscillation of the output speed at 511 RPM is suppressed in the simulation analysis, and in the experimental test, it remains less than 10%. It should be noted that, unlike the torque and inertia phases in controlling DCTs and ATs, in the proposed transmission, synchronization of the motor speed

and switching the brakes happen simultaneously as discussed in the beginning of this chapter.

In Fig. 5.1, disengagement of the off-going brake and engagement of the oncoming brakes start at $t = 16\text{ s}$ and $t = 26\text{ s}$ for the upshift and downshift operations, respectively. However, the synchronization of the motor starts later than $t = 16\text{ s}$ and $t = 26\text{ s}$ in Fig. 5.3 and Fig. 5.7. This delay corresponds to the time reserved for the preparation of the oncoming and off-going brakes. During this period, the friction surfaces of the oncoming brake have to come into contact and the friction surfaces of the off-going brake have to reach to the slip-stick point. By considering the time of preparation of the oncoming and off-going brakes in the shifting time, the upshift and downshift processes last respectively about 0.6 s and 0.8 s in the simulation, and they take about 0.8 s and 1 s in the experiments.

The angular velocities of the ring (ω_R) and the sun (ω_S) gears for the upshift and downshift operations are shown in Fig. 5.4 and Fig. 5.8. It can be seen that during the upshift process the sun gear is grounded and the ring gear is released and the opposite case holds for the downshift operation.

The variation of the gear ratio for the upshift and downshift processes are demonstrated in Fig. 5.5 and Fig 5.9, respectively. This variation can be used as criteria to measure the duration of the gear changing process.

The output torque for the upshift and downshift operations are illustrated in Fig. 5.6 and Fig. 5.10. It can be seen that the oscillation of the output torque during the gear changing process in the simulation is negligible and in the experimental test, it remains less than 15%. The oscillation of the output torque and output speed and the increase in the shifting time in the experimental test in comparison to simulation results probably come from unmodeled uncertainties in the dynamical model of the system and actuators, such as unmodeled uncertainties in the complex friction model of the internal gears, the variation of the viscosity of the transmission oil used for the experimental test with temperature, uncertainties in the position of the solenoid's plunger due to compression of the multi brake plates and deformation

5.2 SIMULATION AND EXPERIMENTAL RESULTS

of the band which result in the deviation of T_{BS} and T_{BR} from the desired values, and unmodeled uncertainties in the resistance of the solenoid actuators which comes from the variation of the temperature of the coil which causes uncertainness in the resulting force.

Transitions between slip and stick phases at the end of gear shifting operation in the experimental results are different from the theoretical results (i.e. the simulation results) in the upshift process in Figures 5.3-5.5 and the downshift in Figures 5.7-5.9. These differences are due to the consideration of friction torques in simulations in the form of Coulomb and viscous friction which is not an exact representative of the behavior of frictional torques of the brakes in the experimental testbed (Olsson et al., 1998; Berger, 2002).

The brakes frictional torque, the motor torque applied to both the computer model and the experimental setup, and the simulated output torque of the transmission are illustrated in Fig. 5.11 and Fig. 5.12 for the upshift and downshift operations, respectively. As illustrated in these figures, the additional motor torque required for the compensation of the slip friction on the brakes disappears at the end of gear shifting process when the oncoming brake comes to rest in the stick mode.

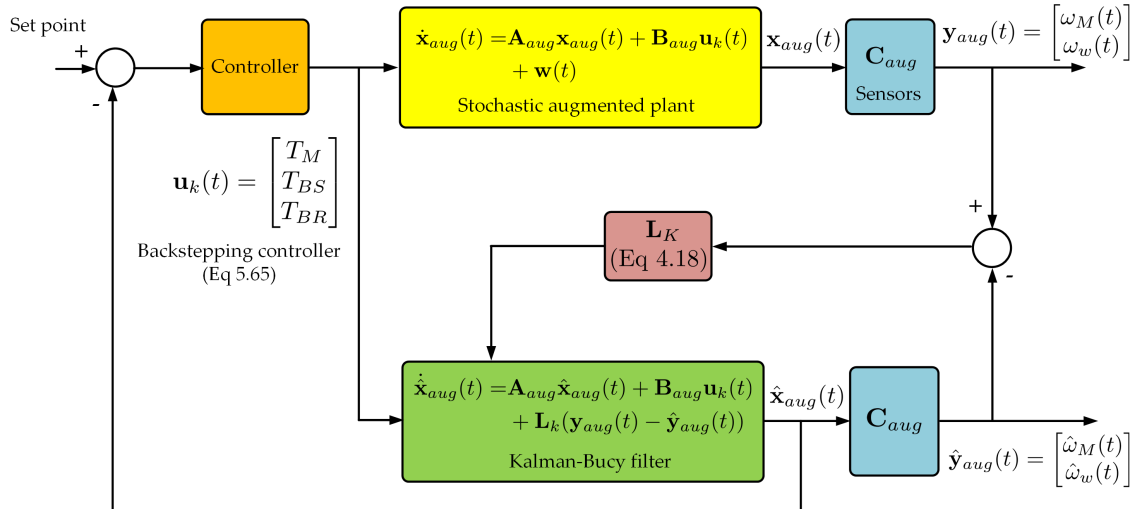
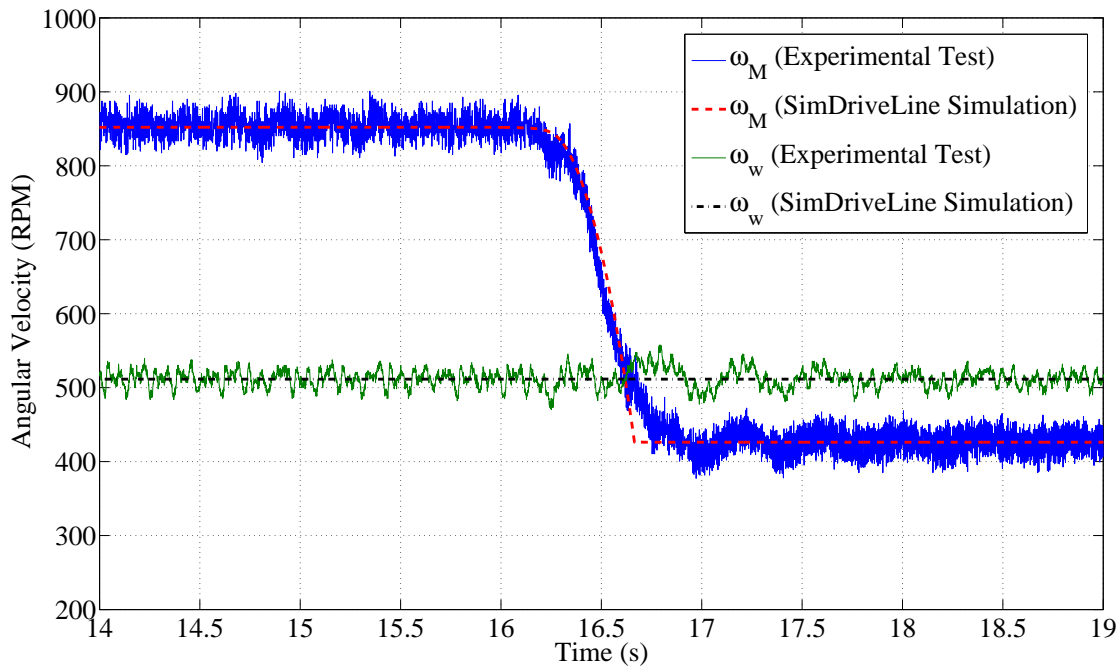
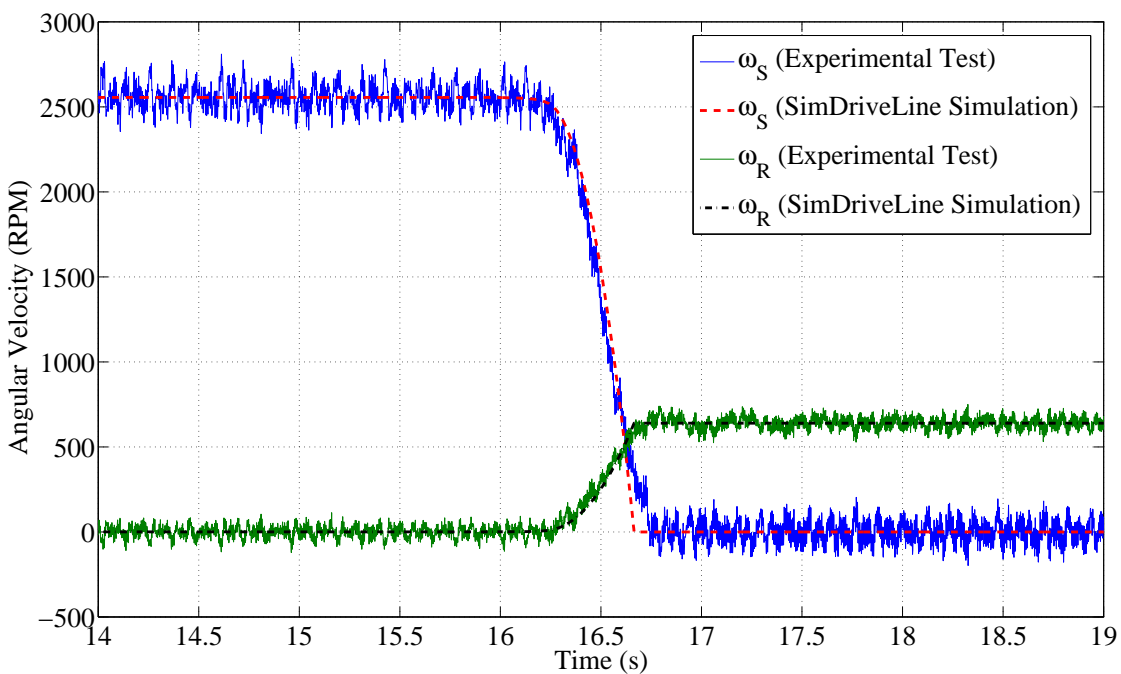


FIGURE 5.2. Block diagram of the observer-based backstepping controller

FIGURE 5.3. The motor (ω_M) and output (ω_w) speeds for the upshift operationFIGURE 5.4. The ring (ω_R) and sun (ω_S) speeds for the upshift operation

5.2 SIMULATION AND EXPERIMENTAL RESULTS

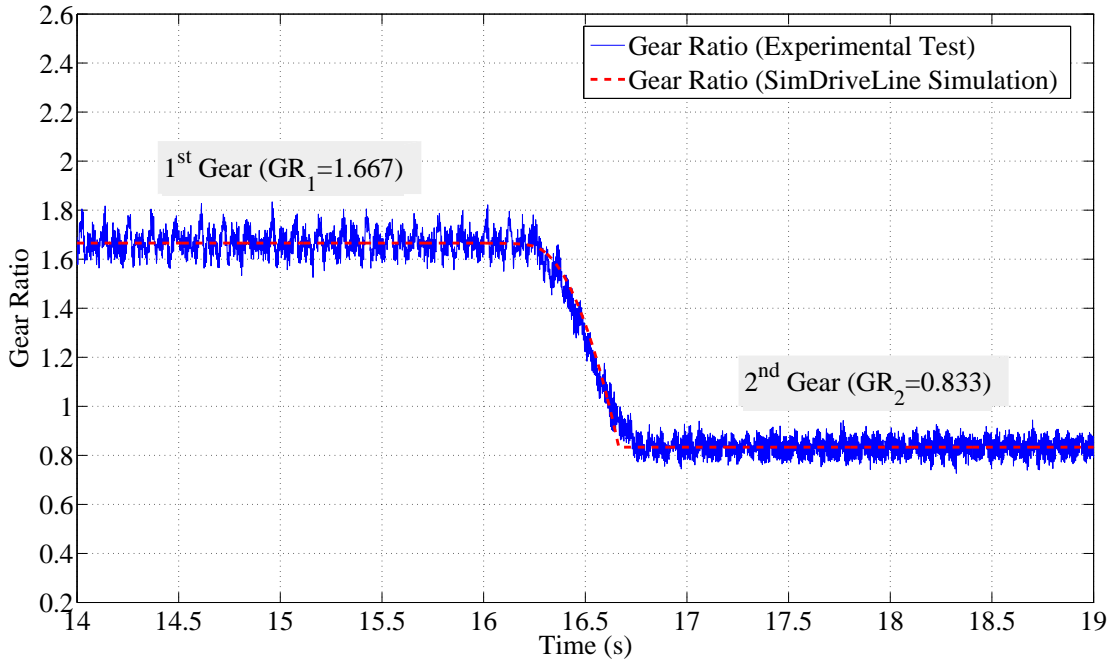


FIGURE 5.5. The variation of the gear ratio (GR) for the upshift operation

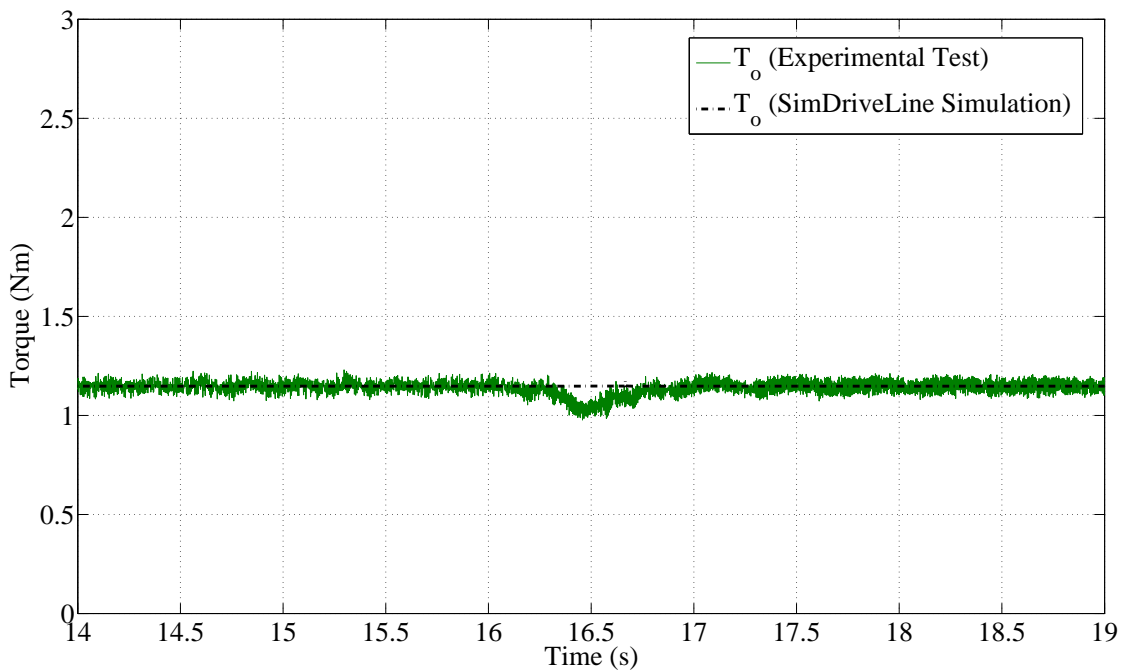
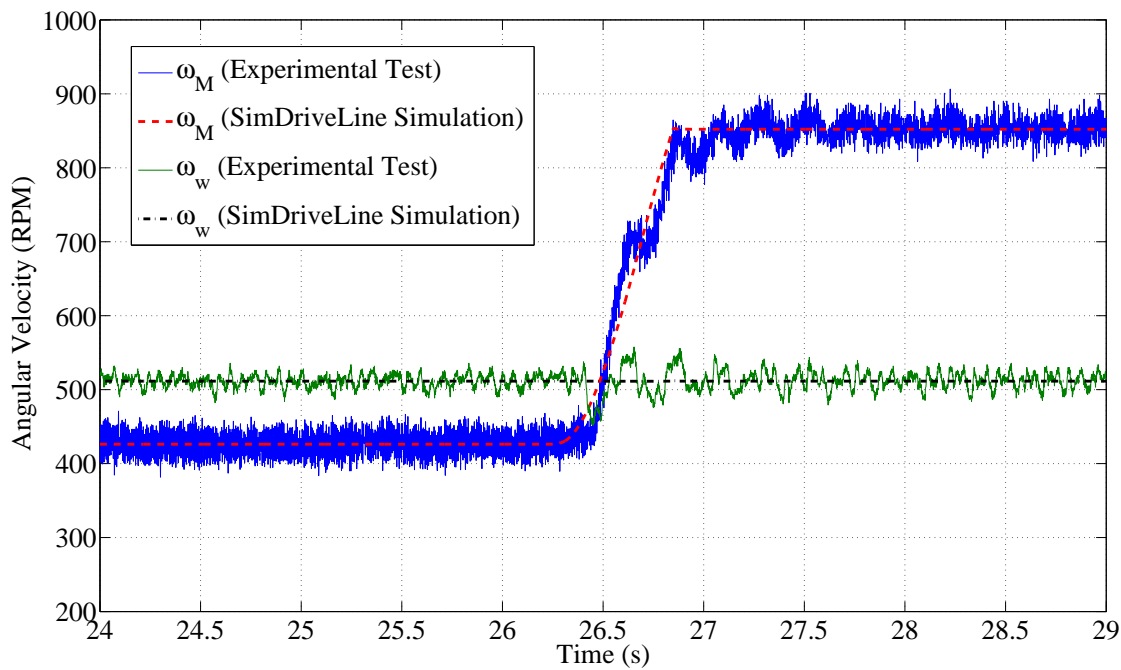
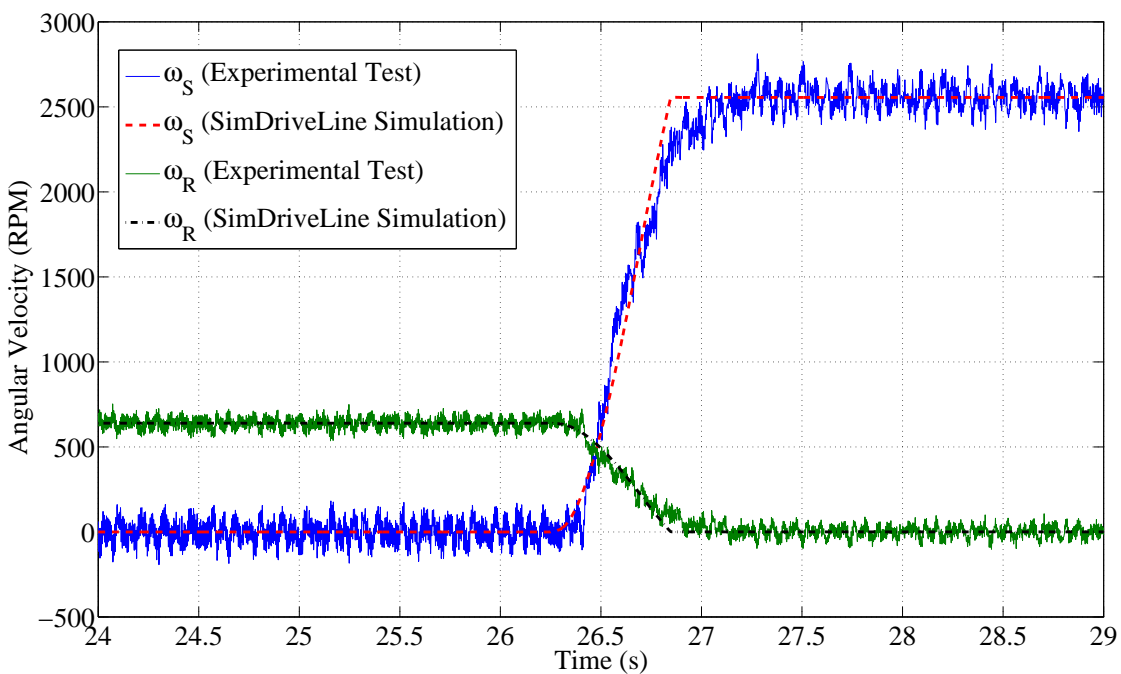


FIGURE 5.6. The output torque (T_o) for the upshift operation

FIGURE 5.7. The motor (ω_M) and output (ω_w) speeds for the downshift operationFIGURE 5.8. The ring (ω_R) and sun (ω_S) speeds for the downshift operation

5.2 SIMULATION AND EXPERIMENTAL RESULTS

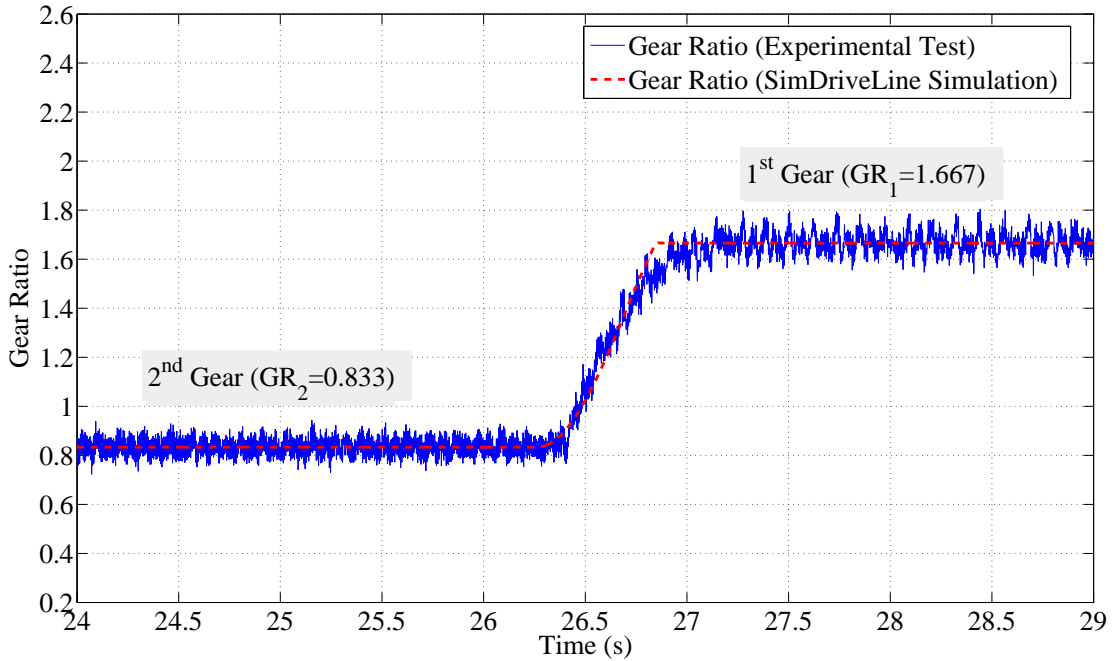


FIGURE 5.9. The variation of the gear ratio (GR) for the downshift operation

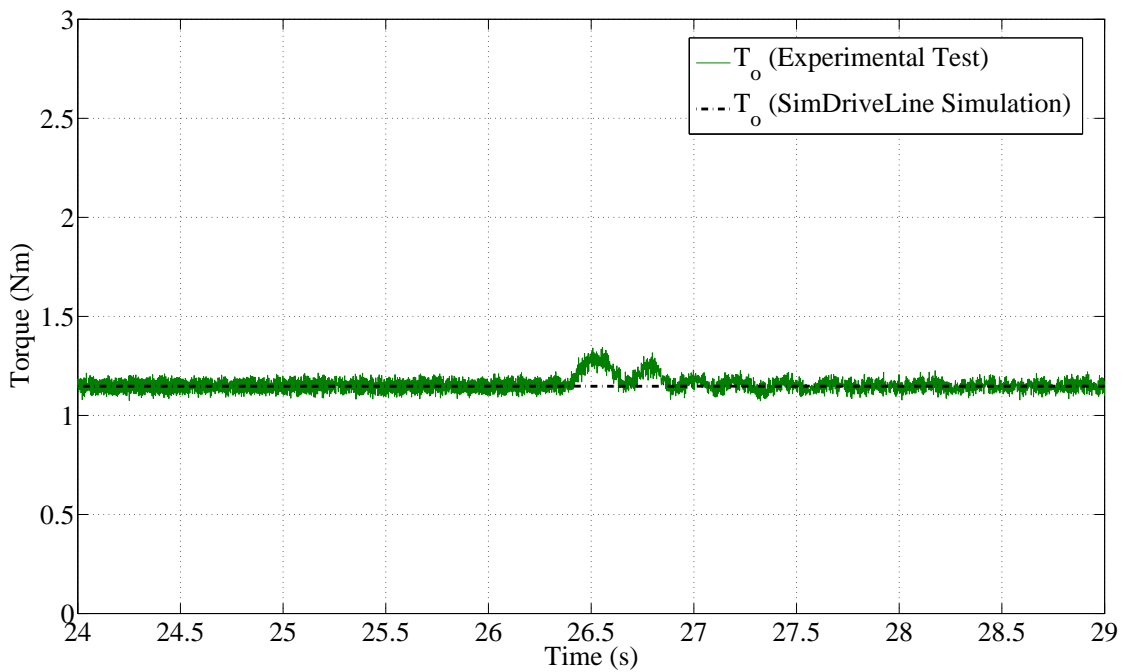


FIGURE 5.10. The output torque (T_o) for the downshift operation

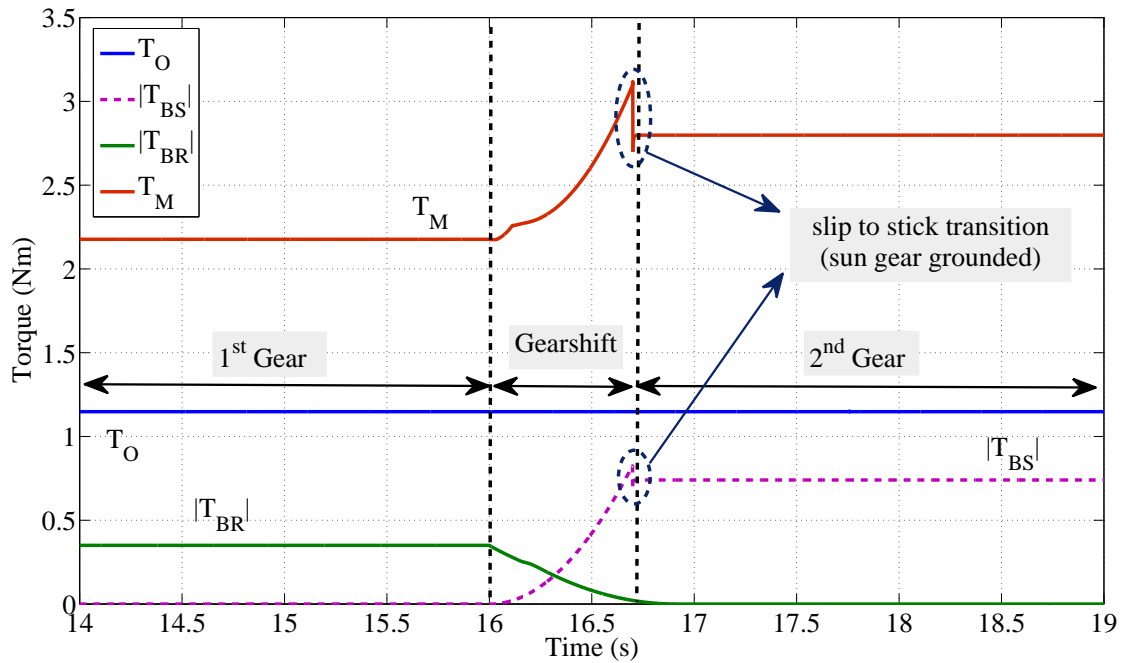


FIGURE 5.11. Simulated brake friction torque and motor torque (Upshift)

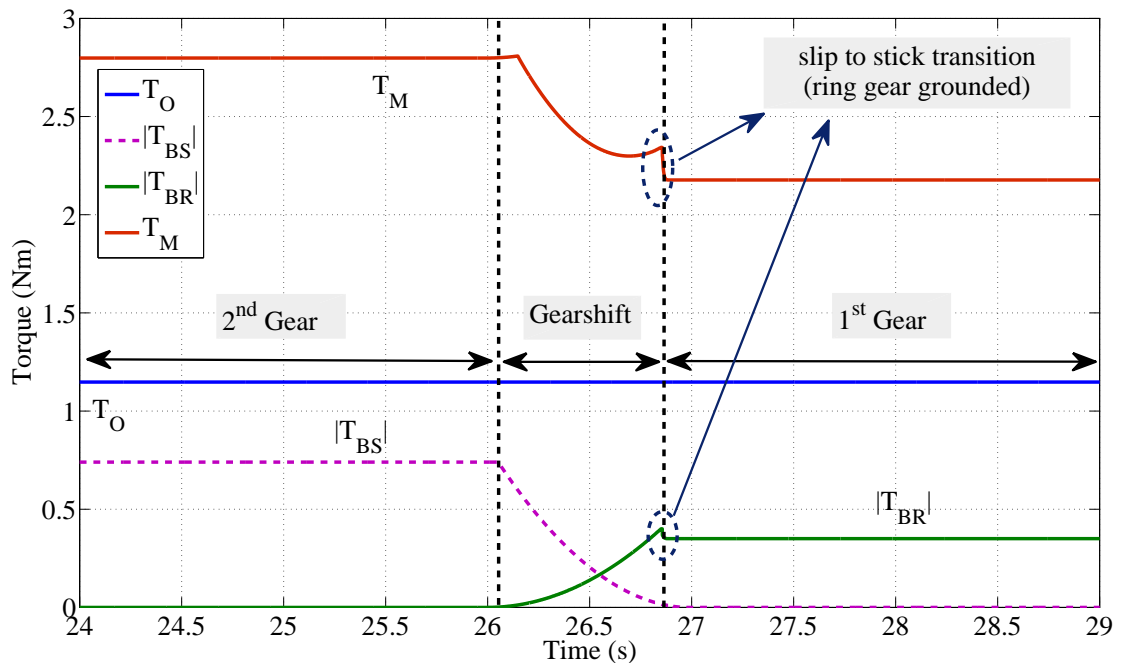


FIGURE 5.12. Simulated brake friction torque and motor torque (Downshift)

5.2 SIMULATION AND EXPERIMENTAL RESULTS

The effect of simulated engagement and disengagement intervals of the oncoming and off-going brakes from 0.1 s to 1.5 s ($0.1, 0.3, 0.6, 0.9, 1.2,$ and 1.5) on the shifting time and the energy dissipation for the upshift and downshift processes are illustrated in Fig. 5.13-5.18. It can be seen that increasing the engagement and disengagement intervals from 0.1 s to 1.5 s increases the shifting time from 0.18 s to 1.04 s for the upshift process and 0.46 s to 1.53 s for the downshift operation. The increases in the energy dissipation caused by the internal brakes of the transmission during the gear changing process are from 51.7 J to 96.23 J and from 18.8 J to 36.83 J for the upshift and downshift operations, respectively. This verifies that the smallest interval, i.e., the case with sudden engagement and disengagement of the oncoming and off-going brakes, corresponds to the minimum shifting time and minimum dissipated energy, as indicated by the results of the Pontryagin Minimum Principle.

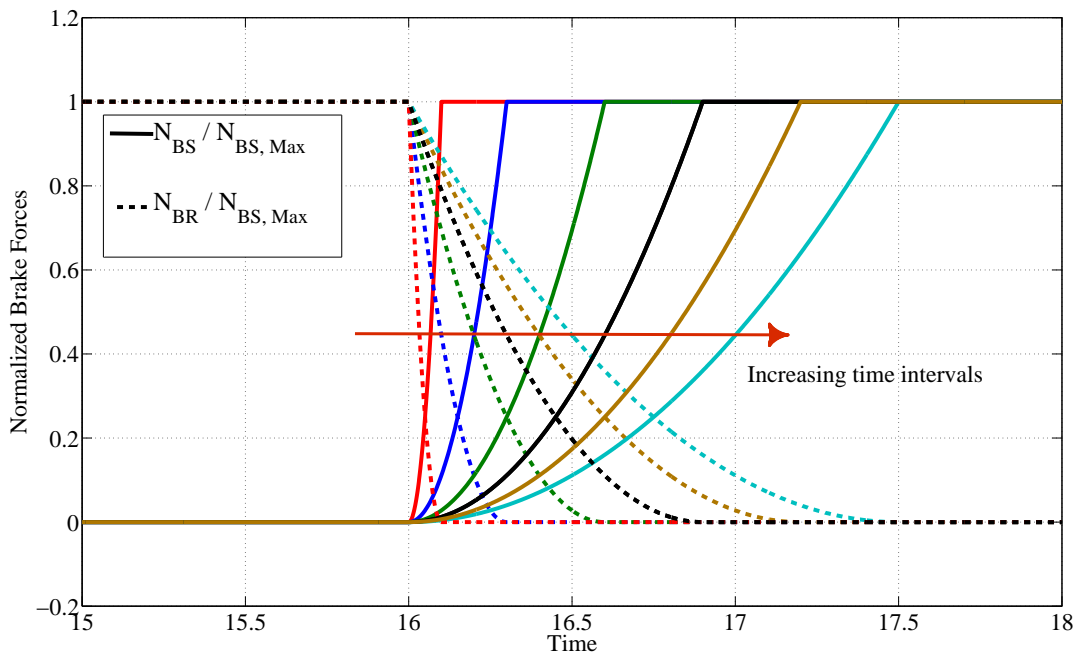


FIGURE 5.13. Normalized brake forces of the ring and sun during the upshift

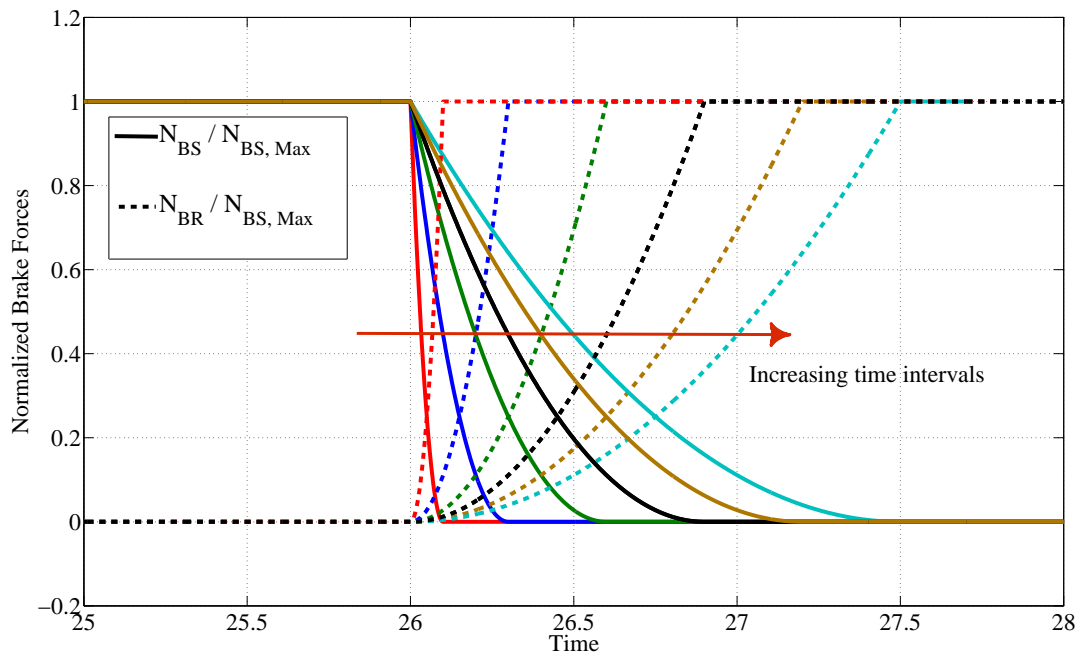


FIGURE 5.14. Normalized brake forces of the ring and sun during the downshift

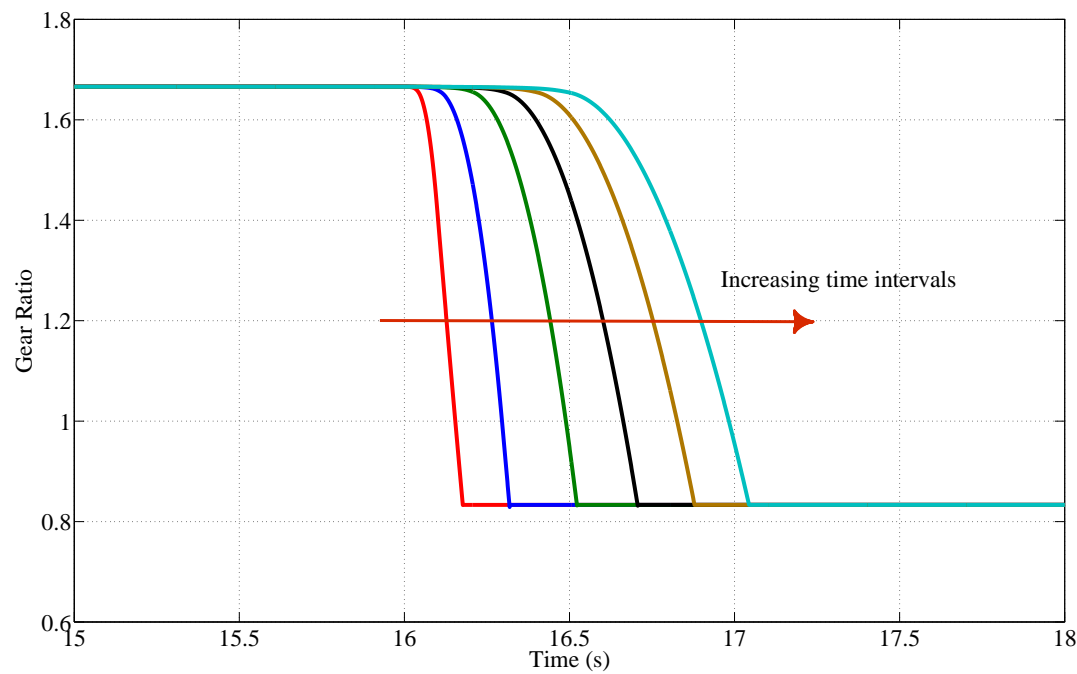


FIGURE 5.15. The variation of the gear ratio during the upshift

5.2 SIMULATION AND EXPERIMENTAL RESULTS

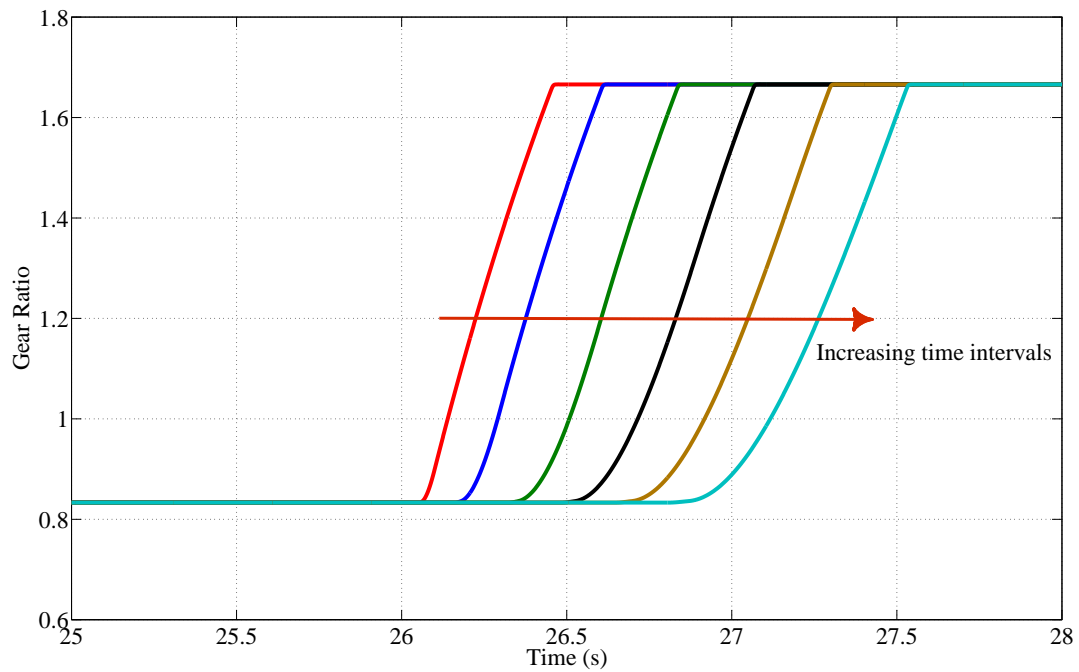


FIGURE 5.16. The variation of the gear ratio during the downshift

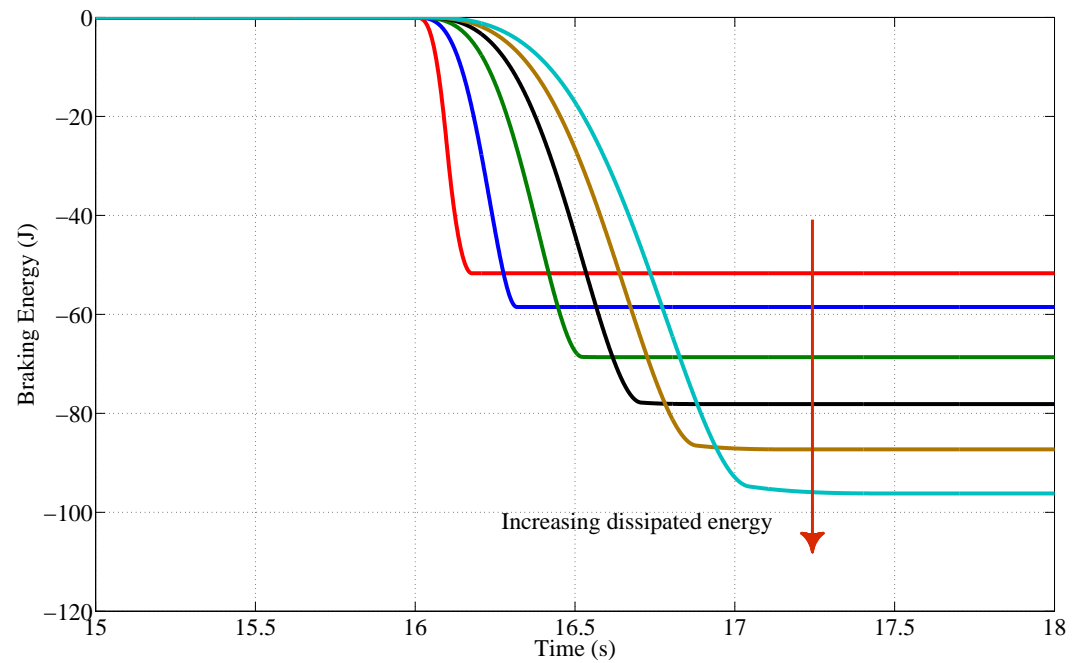


FIGURE 5.17. The braking energy during the upshift

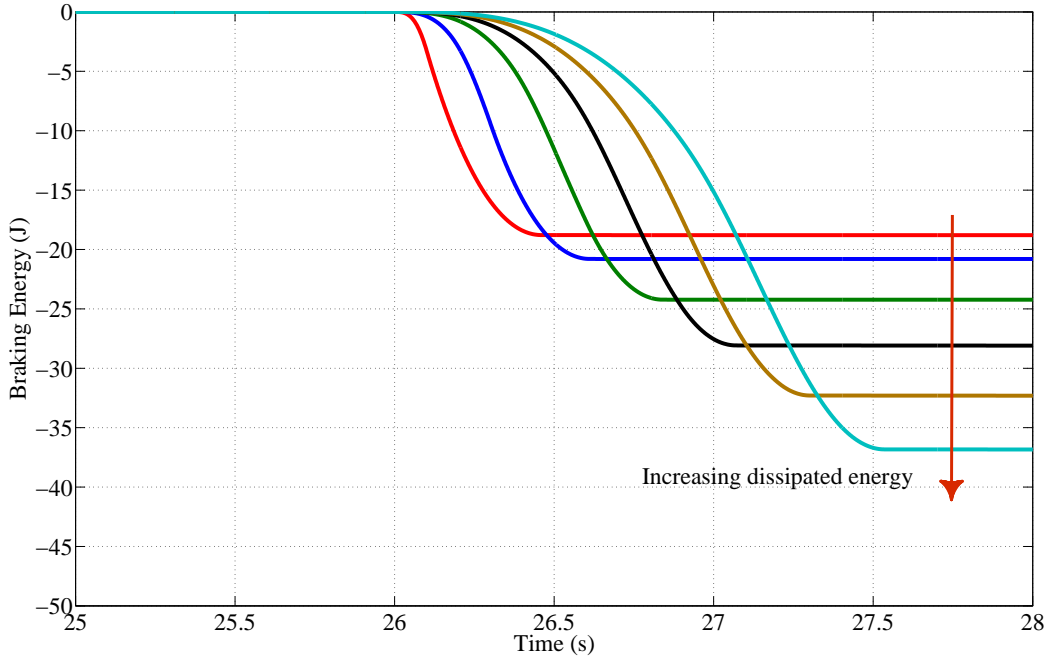


FIGURE 5.18. The braking energy during the downshift

In this chapter, the Pontryagin Minimum Principle is used to derive the optimal control law minimizing the shifting time and the energy dissipation during the gear changing process while keeping the output speed and output torque constant. The optimal control problem results in a bang-bang type control law for the oncoming and off-going brakes while the corresponding optimal trajectories for T_d and T_o maintain the output speed and output torque constant during the gear change. In order to provide a closed-loop controller based on the results of the Pontryagin Minimum Principle and due to the recursive dynamics of the powertrain the backstepping method is applied to design a controller that tracks the optimal trajectories while relaxing the abrupt changes in the control inputs to cope with the actuator limitations. Thereafter, the performance of the designed controller has been evaluated. The results indicate that the torque hole is almost eliminated in both experimental and simulation results while the oscillation of the output torque and output speed during the gear changing is negligible. While a completely seamless operation is shown to exist theoretically, due to uncertainties in the modeling of the system and actuators

5.2 SIMULATION AND EXPERIMENTAL RESULTS

in the experimental test rig, the output speed and output torque deviate from their desired values in amounts less than 10% and 15%, respectively.

Finally, the effect of engagement and disengagement intervals of the oncoming and off-going brakes is studied. Simulation results indicate that increasing the engagement and disengagement intervals of the oncoming and off-going brakes will increase the shifting time and the energy dissipation caused by the internal brakes of the transmission dramatically. The minimum shifting time and the energy dissipation corresponds to the sudden engagement and disengagement of the brakes as expected from the results of the Pontryagin Minimum Principle.

CHAPTER 6

Conclusions

In this chapter, the main contributions of this thesis are summarized in Section 6.1. Then, recommendations for future work are provided in Section 6.2.

6.1. Summary of Results and Contributions

- (i) This thesis proposes a novel two-speed transmission for electric vehicles called *dual brake transmission (DBT)* characterized by seamless gear shifts to enhance efficiency, drivability, and dynamic performance. The proposed system is a departure from conventional transmission developed for internal combustion engine vehicles (ICEVs) to innovative systems specifically designed for EVs. The mechanical design of conventional transmissions involves the use of clutches and torque converters to accommodate restrictions of internal combustion engines regarding speed controllability and range of operation. In contrast, the novel system developed for EVs is perpetually connected to the powertrain due to effective speed and torque controllability of electric motors as well as their wide range of efficient operation. In fact, the DBT system allows improving efficiency and drivability of the overall system by eliminating clutches and torque converters from the powertrain and replacing hydraulic actuators with electromechanical ones. Further, the kinematic analysis of the DBT system is provided to characterize the

CHAPTER 6. CONCLUSIONS

achievable gear ratios of the system based on the ratios of the planetary gear sets incorporated in the design of the DBT.

- (ii) A detailed dynamical model of the powertrain of an electric vehicle equipped with the DBT system is derived to investigate the responses of the system to control inputs and disturbances. To this end, various modeling techniques from classical and analytical dynamics are fused together. The Newtonian method of the classical dynamics is used to model the traction motor, flexible shafts, wheels, and vehicle. However, due to intricacies involved in determining constraint forces/torques of the transmission system and since the dynamics of the transmission as a whole is desired rather than the dynamics of gears as individual bodies, its dynamical model is provided by exploiting one of the principles of analytical dynamics, namely, the d'Alembert-Lagrange principle. Further, because the transmission system exhibits both discrete and continuous behaviour due to transitions between different gear ratios, its dynamical model is formulated in the framework of hybrid dynamical systems. The derived dynamical model is validated by means of the experimental testbed and simulation models. The results demonstrate a satisfactory agreement between the derived model and experimental/simulation analyses.
- (iii) A stochastic observer is developed to provide an accurate real-time monitoring of unmeasured states and disturbances for exploitation in the closed-loop feedback control system to enhance gear shifts. To achieve such a goal, the method of modeling unknown inputs as fictitious state variables of a dynamical system is combined with the Kalman-Bucy filter to provide a concurrent estimation of unmeasured states and the unknown input applied on the system. The observer estimates angular velocities of the off-going and on-coming gears and consequently the gear ratio, the input and output torques of the transmission, and the unknown torque exerted on the vehicle based on the speed measurements of the electric motor and

wheels which are commonly available in commercial vehicles. The performance of the designed observer is verified by a set of experiments and the estimation results are quantitatively compared to those of obtained from a deterministic Luenberger observer. It is observed that the KBF improves the accuracy of the estimation in comparison to DLO by alleviating the effect of measurement and process noises on the observation.

- (iv) An innovative gear shift strategy is developed for the DBT system in which the gear shift algorithm does not require to be distinctly separated into the torque and inertia phases of the conventional transmissions. For the DBT system, first, the gear shift control problem is formulated in such a way that the output torque and output speed of the transmission system are kept constant during the gear shift process. Then, based on this formulation, optimal gear shift problems are solved using the Pontryagin minimum principle (PMP) to minimize the characterized cost functional optimizing shifting time and energy dissipation during these operations. The proposed strategy is, in fact, an integrated gear shift technique in which the traction unit is controlled concurrently with the gear shift actuators. Further, in order to cope with the actuator limitations, a closed-loop controller using the Backstepping technique is designed to provide a stabilizing feedback law while ensuring stability and relaxing abrupt control commands from the optimal control law. The performance of the proposed gear shift strategy is validated by the experimental testbed designed and implemented for this purpose as well as a simulation model built in MATLAB/Simulink® using components of SimDriveLineTM library. The results confirm that the torque hole is almost eliminated in both experimental and simulation tests. In fact, a completely seamless operation is shown to exist theoretically, however due to uncertainties in the model of the system and actuators, the output speed and output torque deviate from their desired values in amounts less than 10% and 15%, respectively.

6.2. Recommendations for Future Work

(i) As expressed in Section 6.1, due to the presence of uncertainties in the models of the system and the actuators, the output torque and speed deviate from their desired values. This problem can be tackled by modeling the uncertainties of the system and actuators and designing a robust H_∞ controller to achieve desired performance and stability of the closed-loop system in the presence of modeling uncertainties and disturbances. To this end, unmodeled dynamics of the system and parameter uncertainties have to be characterized and corresponding weighting functions should be specified. Moreover, the disturbances imparted on the system should be modeled based on the information of their energy-density spectrum (frequency content). Then, the robust H_∞ controller $K(s)$ can be designed for the nominal plant $P(s)$ to achieve desired performance criteria stated as:

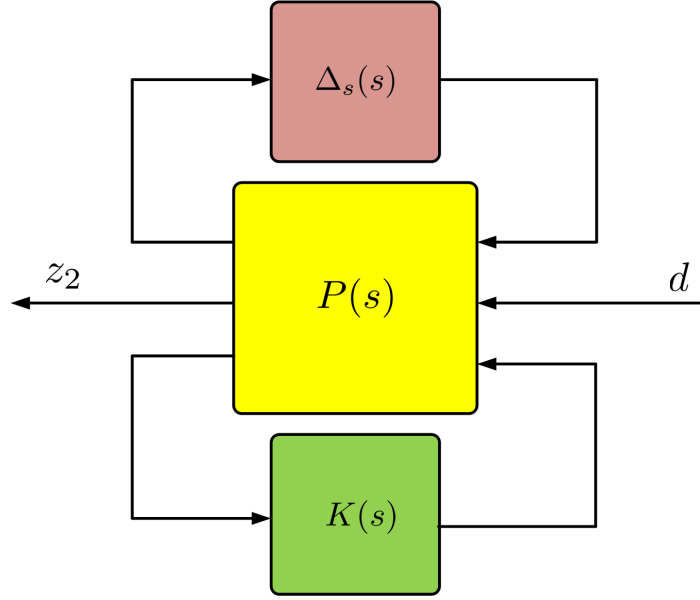
$$\|F_L F_U[P(s), \Delta_s(s)], K(s)\|_\infty < 1, \quad \forall \Delta_s(s) \in S, \|\Delta_s(S)\| < 1 \quad (6.1)$$

where F_L and F_U are the lower and upper linear fractional transformations (LFT), respectively, Δ_s is the dynamical perturbation, and S is the set of real-rational, proper, stable perturbations

$$S \triangleq \{\Delta_s(s) \in RH_\infty : \Delta_s(s_0) \in \Gamma, \forall s_0 \in \text{closed RHP}\}, \quad (6.2)$$

where Γ is the set of complex structured uncertainties. The LFT diagram of the system is shown in Fig. 6.1 (Boulet, 2014).

- (ii) Given the fact that the brakes' frictional torques of the DBT system have a direct impact on the gear shift quality, having accurate information of the imparted torque applied on the system by the brakes is necessary. However, friction is a highly complex phenomenon and its modeling is a challenging task. Moreover, relying on the force-torque model in the long-term may not be proper due to the wearing of the friction materials and the effect of temperature variations on the coefficient of friction. In order to tackle

FIGURE 6.1. Standard LFT diagram for H_∞ -optimal control design

this problem, the stochastic observer design in this thesis can be extended in such a way that the imparted torques of these brakes on the system be included in the estimation procedure. This not only improves the gear shift quality but is also beneficial for fault-detection of the brake actuators. Further, nonlinearities of the load applied to the vehicle such as road gradient variation, wind effect, and the braking torque applied by the driver can be further scrutinized while considering the effect of process and measurement noises.

- (iii) It should be noted that electrification of transportation is not limited to passenger cars. It basically encompasses motorcycles, passenger cars, delivery trucks, heavy duty truck, school buses, and etc. The technology developed in this thesis has been proven to work at the laboratory scale but needs to be scaled up to a working prototype on the above-mentioned vehicles to evaluate its performance and to investigate the effectiveness of the proposed observer-based controller.

CHAPTER 6. CONCLUSIONS

Furthermore, the design of electromechanical brakes could be further improved by considering lock mechanisms to fix the grounded components when the system is not in the gear shift process. Therefore, no extra power is required to prevent these grounded components from rotation, and hence, the lifetime of the actuators and the overall efficiency of the system will be improved.

Sizing of the transmission is one of the main challenges in the design of the DBT system for EVs. This is because of the limited available volume on the EV powertrain due to the considerable volume occupied by onboard batteries. Given the fact that most of the volume within the DBT system is occupied by the planetary gear sets, the design of gears will have the greatest impact on the transmission size. Increasing the number of planet gears in the planetary gear sets, gear profile (helical, spur), and gear face width are the parameters that can be used in order to decrease the overall diameter of the transmission in order to be retrofitted to any available volume. This topic can be studied as one of the most important avenues of future work.

Finally, using an appropriately designed multi-speed transmission for EVs could considerably improve the dynamic performance of the vehicle while maintaining or improving the overall efficiency of the system. As explained in Chapter 1, using multi-speed transmissions for EV powertrains boosts the available torque at low speeds for vehicle launching, acceleration, and hill climbing and increases the vehicle top speed by expanding the area under the tractive effort-speed curve. In fact, exploiting the multi-speed transmission will enrich the available combinations of torque and speed for a specific power and consequently provides an opportunity for the electric traction motor to operate within the highest efficiency region by appropriate selection of the gear ratios and gear shift schedule. Thus, gear ratio and gear shift schedule optimization problems can be scrutinized for efficiency

6.2 RECOMMENDATIONS FOR FUTURE WORK

and performance improvement for the electric vehicle powertrain equipped with the DBT system.

BIBLIOGRAPHY

- Alizadeh, H. V. and B. Boulet (2014). Robust control of synchromesh friction in an electric vehicle's clutchless automated manual transmission. In *IEEE Conference on Control Applications (CCA)*, pp. 611–616.
- Alizadeh, H. V., M. Helwa, and B. Boulet (2014). Constrained control of the synchromesh operating state in an electric vehicle's clutchless automated manual transmission. In *IEEE Conference on Control Applications (CCA)*, pp. 623–628.
- Alizadeh, H. V., M. S. R. Mousavi, and B. Boulet (2015). Synchromesh torque estimation in an electric vehicle's clutchless automated manual transmission using unknown input observer. In *IEEE Vehicle Power and Propulsion Conference (VPPC)*, pp. 1–5.
- Andrzejewski, R. and J. Awrejcewicz (2006). *Nonlinear dynamics of a wheeled vehicle*, Volume 10. Springer Science & Business Media.
- Angeles, J. (2002). *Fundamentals of robotic mechanical systems*, Volume 2. Springer.
- Angeles, J. (2013). Mech 577 optimum design, lecture notes. Deptrtment of Mechanical Engineering, McGill University.
- Armstrong-Hélouvry, B., P. Dupont, and C. C. De Wit (1994). A survey of models, analysis tools and compensation methods for the control of machines with friction. *Automatica, Elsevier* 30(7), 1083–1138.
- Asl, H. A., N. L. Azad, and J. McPhee (2012). Modeling torque converter characteristics in automatic drivelines: Lock-up clutch and engine braking simulation. In *ASME International Design Engineering Technical Conferences and Computers*

BIBLIOGRAPHY

- and Information in Engineering Conference*, pp. 359–367.
- Batchelor, G. K. (2000). *An introduction to fluid dynamics*. Cambridge university press.
- Benford, H. L. and M. B. Leising (1981). The lever analogy: A new tool in transmission analysis. Technical report, SAE Technical Paper.
- Berger, E. (2002). Friction modeling for dynamic system simulation. *Applied Mechanics Reviews, ASME* 55(6), 535–577.
- Berriri, M., P. Chevrel, and D. Lefebvre (2008). Active damping of automotive powertrain oscillations by a partial torque compensator. *Control Engineering Practice, Elsevier* 16(7), 874–883.
- Bishop, G. and G. Welch (2001). *An Introduction to the Kalman Filter*, SIGGRAPH 2001, Course 8. Department of Computer Science, University of North Carolina at Chapel Hill.
- Boldea, I. (2004). Linear electromagnetic actuators and their control: a review. *EPE Journal, Taylor & Francis* 14(1), 43–50.
- Boldea, I. (2013). *Linear electric machines, drives, and MAGLEVs handbook*. CRC Press.
- Boldea, I. and S. A. Nasar (1997). Linear electric actuators and generators. In *IEEE International Conference on Electric Machines and Drives*, pp. MA1–1.1–MA1–1.5.
- Boulet, B. (2003). Ecse-501a linear systems, lecture notes. Deptment of Electrical and Computer Engineering, McGill University.
- Boulet, B. (2014). Ecse 513 robust control systems, lecture notes. Deptment of Electrical and Computer Engineering, McGill University.
- Bowen, T. C. (2002, April 16). Electric continuously variable transmission. US Patent 6,371,878.
- Bundynas, R. and K. Nisbett (2009). *Shigley's Mechanical Engineering Design*. McGraw-Hill, New York.
- Cao, J.-Y., B.-G. Cao, and Z. Liu (2006). Driving resistance estimation based on unknown input observer. *Journal of Applied Sciences* 6(4), 888–891.

- Catenacci, M., E. Verdolini, V. Bosetti, and G. Fiorese (2013). Going electric: Expert survey on the future of battery technologies for electric vehicles. *Energy Policy, Elsevier* 61, 403–413.
- Cavallino, C. (2015, March 24). Two-speed transmission for electric vehicles. US Patent 8,984,976.
- Chen, T., D. Lee, and C.-K. Sung (1998). An experimental study on transmission efficiency of a rubber v-belt cvt. *Mechanism and machine theory, Elsevier* 33(4), 351–363.
- Chopra, V. (2014). *Design of innovative clutching mechanisms for hybrid automotive transmissions*. Ph. D. thesis, McGill University.
- Chopra, V., A. Smith, and J. Angeles (2013). Electromechanical clutch actuator: Design, analysis and experiments. Technical report, SAE Technical Paper.
- Ciesla, C. R. and M. J. Jennings (1995). A modular approach to powertrain modeling and shift quality analysis. Technical report, SAE Technical Paper.
- Coey, J. M. (2010). *Magnetism and magnetic materials*. Cambridge University Press.
- Crolla, D. (2009). *Automotive Engineering e-Mega Reference*. Butterworth-Heinemann.
- Deur, J., J. Petrić, J. Asgari, and D. Hrovat (2006). Recent advances in control-oriented modeling of automotive power train dynamics. *IEEE/ASME Transactions on Mechatronics* 11(5), 513–523.
- Ehsani, M., Y. Gao, and A. Emadi (2009). *Modern electric, hybrid electric, and fuel cell vehicles: fundamentals, theory, and design*. CRC press.
- Faid, S. (2015). A highly efficient two speed transmission for electric vehicles. In *Electric Vehicle Symposium & Exhibition 28, EVS28*, pp. 1–22.
- Farris, R. J. and M. Goldfarb (2011). Design of a multidisc electromechanical brake. *IEEE/ASME Transactions on Mechatronics* 16(6), 985–993.
- Fredriksson, J., H. Weiefors, and B. Egardt (2002). Powertrain control for active damping of driveline oscillations. *Vehicle System Dynamics, Taylor & Francis* 37(5), 359–376.

BIBLIOGRAPHY

- French, M. (1992). *Form, structure and mechanism*. Springer-Verlag.
- Furlani, E. P. (2001). *Permanent magnet and electromechanical devices: materials, analysis, and applications*. Academic Press.
- Gahagan, M., T. Yoshimura, and J. Vinci (2003). Technologies for modern manual transmission performance. Technical report, SAE Technical Paper.
- Galvagno, E., M. Velardocchia, and A. Vigliani (2011). Dynamic and kinematic model of a dual clutch transmission. *Mechanism and Machine Theory, Elsevier* 46(6), 794–805.
- Gao, B., H. Chen, Q. Liu, and H. Chu (2014). Position control of electric clutch actuator using a triple-step nonlinear method. *IEEE Transactions on Industrial Electronics*, 61(12), 6995–7003.
- Gao, B., Y. Lei, A. Ge, H. Chen, and K. Sanada (2011). Observer-based clutch disengagement control during gear shift process of automated manual transmission. *Vehicle System Dynamics, Taylor & Francis* 49(5), 685–701.
- Gao, B., Q. Liang, Y. Xiang, L. Guo, and H. Chen (2015). Gear ratio optimization and shift control of 2-speed i-amt in electric vehicle. *Mechanical Systems and Signal Processing, Elsevier* 50, 615–631.
- Ge, A., H. Jin, and Y. Lei (2000). Engine constant speed control in starting and shifting process of automated mechanical transmission (amt). In *FISITA World Automotive Congress, Seoul*.
- Ginsberg, J. H. (1998). *Advanced engineering dynamics*. Cambridge University Press.
- Glielmo, L., L. Iannelli, V. Vacca, and F. Vasca (2006). Gearshift control for automated manual transmissions. *IEEE/ASME Transactions on Mechatronics* 11(1), 17–26.
- Goebel, R., R. G. Sanfelice, and A. Teel (2009). Hybrid dynamical systems. *Control Systems, IEEE* 29(2), 28–93.
- Goebel, R., R. G. Sanfelice, and A. R. Teel (2012). *Hybrid Dynamical Systems: modeling, stability, and robustness*. Princeton University Press.

- Goetz, M. (2005). *Integrated powertrain control for twin clutch transmissions*. Ph. D. thesis, University of Leeds.
- Goldstein, H., C. Poole, and J. Safko (2001). *Classical Mechanics*, Volume 3. Addison-Wesley.
- Greenwood, D. T. (2006). *Advanced dynamics*. Cambridge University Press.
- Gunji, D. and H. Fujimoto (2013). Efficiency analysis of powertrain with toroidal continuously variable transmission for electric vehicles. In *39th Annual Conference of the IEEE Industrial Electronics Society, IECON*, pp. 6614–6619.
- Haj-Fraj, A. and F. Pfeiffer (1999). Dynamic modeling and analysis of automatic transmissions. In *IEEE/ASME International Conference on Advanced Intelligent Mechatronics*, pp. 1026–1031.
- Han, K. and Y. Yoon (2013). Clutch transmissible torque estimation for dry dual clutch transmission control. In *Proceedings of the FISITA 2012 World Automotive Congress, Springer*, pp. 449–456.
- He, W., N. Williard, C. Chen, and M. Pecht (2013). State of charge estimation for electric vehicle batteries using unscented kalman filtering. *Microelectronics Reliability*, Elsevier 53(6), 840–847.
- Hofman, T. and C. Dai (2010). Energy efficiency analysis and comparison of transmission technologies for an electric vehicle. In *IEEE Vehicle Power and Propulsion Conference (VPPC)*, pp. 1–6.
- Holmes, A. G. (2006, November 21). Planetary dual power path transmission with electric motors. US Patent 7,137,919.
- Hrovat, D. and W. Tobler (1991). Bond graph modeling of automotive power trains. *Journal of the Franklin Institute, Elsevier* 328(5), 623–662.
- Hu, X., R. Xiong, and B. Egardt (2014). Model-based dynamic power assessment of lithium-ion batteries considering different operating conditions. *IEEE Transactions on Industrial Informatics* 10(3), 1948–1959.
- Huang, K., M. L. Yan, Z. Wang, and D. D. Zhu (2012). Study on shift schedule of pure electric vehicles automatic transmission. In *Advanced Materials Research*,

BIBLIOGRAPHY

- Volume 591, pp. 1212–1216.
- Hubbard, G., K. Youcef-Toumi, et al. (1997). Modeling and simulation of a hybrid-electric vehicle drivetrain. In *IEEE American Control Conference*, Volume 1, pp. 636–640.
- Husain, I. (2011). *Electric and hybrid vehicles: design fundamentals*. CRC press.
- Hvolka, D. J., P. Hvolka, and V. Raffaj (2009, April 16). Direct drive electric shift two speed planetary gearbox. US Patent App. 12/386,310.
- Iqbal, S., F. Al-Bender, B. Pluymers, and W. Desmet (2014). Model for predicting drag torque in open multi-disks wet clutches. *ASME Journal of Fluids Engineering* 136(2), 021103–1–021103–11.
- Jeon, S. and M. Tomizuka (2007). Benefits of acceleration measurement in velocity estimation and motion control. *Control Engineering Practice*, Elsevier 15(3), 325–332.
- Jibin, H., P. Zengxiong, and W. Chao (2012). Experimental research on drag torque for single-plate wet clutch. *ASME Journal of Tribology* 134(1), 014502–1–014502–6.
- Jo, C., S. Hwang, and H. Kim (2010). Clamping-force control for electromechanical brake. *IEEE Transactions on Vehicular Technology* 59(7), 3205–3212.
- Jung, G., B. Cho, and K. Lee (2000). Dynamic analysis and closed-loop shifting control of ef-automatic transmission with proportional control solenoid valves. In *FISITA World Automotive Congress, Seoul, Korea*, pp. 12–15.
- Kadijk, G. and N. Ligterink (2012). Road load determination of passenger cars. *TNO report: TNO 10237*.
- Kahraman, A., D. Hilty, and A. Singh (2015). An experimental investigation of spin power losses of a planetary gear set. *Mechanism and Machine Theory*, Elsevier 86, 48–61.
- Kahraman, A., H. Ligata, K. Kienzle, and D. Zini (2004). A kinematics and power flow analysis methodology for automatic transmission planetary gear trains. *ASME Journal of Mechanical Design* 126(6), 1071–1081.
- Kailath, T. (1980). *Linear systems*, Volume 156. Prentice-Hall Englewood Cliffs, NJ.

- Khajepour, A., M. S. Fallah, and A. Goodarzi (2014). *Electric and Hybrid Vehicles: Technologies, Modeling and Control-A Mechatronic Approach*. John Wiley & Sons.
- Khalil, H. K. and J. Grizzle (1996). *Nonlinear systems*, Volume 3. Prentice hall New Jersey.
- Kim, D.-H., K.-S. Hong, and K. Yi (2006). Driving load estimation with the use of an estimated turbine torque. *JSME International Journal Series C Mechanical Systems, Machine Elements and Manufacturing* 49(1), 163–171.
- Kim, D. H., B. K. Shin, K. Yi, and K. I. Lee (2000). Vehicle driving load estimation for longitudinal motion control. In *Proceedings of FISITA World Automotive Congress, Seoul, Korea, Paper*, Number F2000G348.
- Kim, J., F. Park, Y. Park, and M. Shizuo (2002). Design and analysis of a spherical continuously variable transmission. *ASME Journal of Mechanical Design* 124(1), 21–29.
- Kim, J., S. Park, C. Seok, H. Song, D. Sung, C. Lim, and H. Kim (2003). Simulation of the shift force for a manual transmission. *Proceedings of the Institution of Mechanical Engineers, Part D: Journal of Automobile Engineering* 217(7), 573–581.
- Kim, N., S. Cha, and H. Peng (2011). Optimal control of hybrid electric vehicles based on pontryagin's minimum principle. *IEEE Transactions on Control Systems Technology* 19(5), 1279–1287.
- King, T. (1991). A fast electro-mechanical clutch element using a piezoelectric multilayer actuator. In *IEE Colloquium on Robot Actuators*, IET, pp. 1–4.
- Kirk, D. E. (2012). *Optimal control theory: an introduction*. Courier Corporation.
- Koser, M. (1985, February 5). Variable gear transmission system. US Patent 4,497,221.
- Kovacs, J. (2012). Mech 642 advanced dynamics, lecture notes. Department of Mechanical Engineering, McGill University.
- Kubur, M., A. Kahraman, D. Zini, and K. Kienzle (2004). Dynamic analysis of a multi-shaft helical gear transmission by finite elements: model and experiment. *ASME Journal of vibration and acoustics* 126(3), 398–406.

BIBLIOGRAPHY

- Kulkarni, M., T. Shim, and Y. Zhang (2007). Shift dynamics and control of dual-clutch transmissions. *Mechanism and Machine Theory*, Elsevier 42(2), 168–182.
- Lanczos, C. (1970). *The variational principles of mechanics*, Volume 4. Courier Corporation.
- Larminie, J. and J. Lowry (2004). *Electric vehicle technology explained*. John Wiley & Sons.
- Lazar, C., C. F. Caruntu, and A. E. Balau (2010). Modelling and predictive control of an electro-hydraulic actuated wet clutch for automatic transmission. In *IEEE International Symposium on Industrial Electronics (ISIE)*, pp. 256–261.
- Lewis, F. L., L. Xie, and D. Popa (2007). *Optimal and robust estimation: with an introduction to stochastic control theory*, Volume 29. CRC press.
- Li, X., W. Zhang, J. Li, M. Jiang, and Y. Zhang (2015). Analysis on synchronizer of manual transmission using finite element analysis. Technical report, SAE Technical Paper.
- Liang, Q., B. Z. Gao, and H. Chen (2012). Gear shifting control for pure electric vehicle with inverse-AMT. In *Applied Mechanics and Materials*, Trans Tech Publ, Volume 190, pp. 1286–1289.
- Lin, F. (2007). *Robust control design: an optimal control approach*, Volume 18. John Wiley & Sons.
- Liu, J. and H. Peng (2008). Modeling and control of a power-split hybrid vehicle. *IEEE Transactions on Control Systems Technology* 16(6), 1242–1251.
- Lucente, G., M. Montanari, and C. Rossi (2007). Modelling of an automated manual transmission system. *Mechatronics*, Elsevier 17(2), 73–91.
- Lukic, S. M., J. Cao, R. C. Bansal, F. Rodriguez, and A. Emadi (2008). Energy storage systems for automotive applications. *IEEE Transactions on Industrial electronics* 55(6), 2258–2267.
- Lukic, S. M., S. G. Wirasingha, F. Rodriguez, J. Cao, and A. Emadi (2006). Power management of an ultracapacitor/battery hybrid energy storage system in an hev. In *IEEE Vehicle Power and Propulsion Conference VPPC*, pp. 1–6.

- Lygeros, J. (2004). Lecture notes on hybrid systems. Citeseer.
- Lyshevski, S. E. (2008). *Electromechanical Systems and devices*. CRC Press.
- Mahajan, D. P., R. Narayanswamy, and S. Bavisetti (2012). High force density solenoid actuator for aerospace application. In *IEEE/ASME International Conference on Advanced Intelligent Mechatronics (AIM)*, pp. 1011–1016.
- Mashadi, B. and D. Crolla (2012). *Vehicle Powertrain Systems: Integration and Optimization*. John Wiley & Sons.
- Mashadi, B. and S. A. Emadi (2010). Dual-mode power-split transmission for hybrid electric vehicles. *IEEE Transactions on Vehicular Technology* 59(7), 3223–3232.
- Mason, S. J. (1953). *Feedback Theory: I. Some Properties of Signal Flow Graphs*. Massachusetts Institute of Technology, Research Laboratory of Electronics.
- Matsuoka, Y. and K. Kitada (2013, April 15). Electric vehicle power transmission apparatus. US Patent App. 14/380,001.
- Mi, C., M. A. Masrur, and D. W. Gao (2011). *Hybrid electric vehicles: principles and applications with practical perspectives*. John Wiley & Sons.
- Mori, H. and K. Morikawa (1995, July 25). Power transmission unit for electric vehicle. US Patent 5,435,794.
- Morozov, A., K. Humphries, T. Zou, S. Martins, and J. Angeles (2014). Design and optimization of a drivetrain with two-speed transmission for electric delivery step van. In *IEEE International Electric Vehicle Conference (IEVC)*, pp. 1–8.
- Moskwa, J. J., S. A. Munns, and Z. J. Rubin (1997). The development of vehicular powertrain system modeling methodologies: Philosophy and implementation. Technical report, SAE Technical Paper.
- Mousavi, M. S. R. and B. Boulet (2015). Dynamical modeling and optimal state estimation using kalman-bucy filter for a seamless two-speed transmission for electric vehicles. In *23th IEEE Mediterranean Conference on Control and Automation (MED)*, pp. 76–81.
- Mousavi, M. S. R. and B. Boulet (2016). Estimation of the state variables and unknown input of a two-speed electric vehicle driveline using fading-memory kalman

BIBLIOGRAPHY

- filter. *IEEE Transactions on Transportation Electrification*, 210–220.
- Mousavi, M. S. R., A. Pakniyat, and B. Boulet (2014). Dynamic modeling and controller design for a seamless two-speed transmission for electric vehicles. In *IEEE Conference on Control Applications (CCA)*, pp. 635–640.
- Mousavi, M. S. R., A. Pakniyat, T. Wang, and B. Boulet (2015). Seamless dual brake transmission for electric vehicles: Design, control and experiment. *Mechanism and Machine Theory*, Elsevier 94, 96–118.
- Munson, B. R., D. F. Young, and T. H. Okiishi (1990). *Fundamentals of fluid mechanics*, Volume 3. New York: Wiley.
- Naunheimer, H., B. Bertsche, J. Ryborz, and W. Novak (2010). *Automotive Transmissions: Fundamentals, Selection, Design and Application*. Springer Science & Business Media.
- Neelakantan, V. A., G. N. Washington, and N. K. Bucknor (2008). Model predictive control of a two stage actuation system using piezoelectric actuators for controllable industrial and automotive brakes and clutches. *Journal of Intelligent Material Systems and Structures* 19(7), 845–857.
- Ogata, K. (2009). *Modern control engineering*. Prentice Hall.
- Oh, J., J. Kim, and S. B. Choi (2013). Design of estimators for the output shaft torque of automated manual transmission systems. In *8th IEEE Conference on Industrial Electronics and Applications (ICIEA)*, pp. 1370–1375.
- Oh, J. J. and S. B. Choi (2015). Real-time estimation of transmitted torque on each clutch for ground vehicles with dual clutch transmission. *IEEE/ASME Transactions on Mechatronics* 20(1), 24–36.
- Oh, J. J., S. B. Choi, and J. Kim (2014). Driveline modeling and estimation of individual clutch torque during gear shifts for dual clutch transmission. *Mechatronics*, Elsevier 24(5), 449–463.
- Olsson, H., K. J. Åström, C. C. De Wit, M. Gafvert, and P. Lischinsky (1998). Friction models and friction compensation. *European journal of control*, Elsevier 4(3), 176–195.

- Ooyama, K., M. Imamura, and M. Kojima (1997, April 29). Transmission for electric vehicle. US Patent 5,623,851.
- Pahl, G., W. Beitz, J. Feldhusen, and K.-H. Grote (2007). *Engineering design: a systematic approach*. Springer-Verlag.
- Pakniyat, A. and P. E. Caines (2014a). The gear selection problem for electric vehicles: An optimal control formulation. In *Proceedings of the 13th International Conference on Control Automation Robotics & Vision ICARCV, IEEE, 2014*, pp. 1261–1266.
- Pakniyat, A. and P. E. Caines (2014b). On the relation between the minimum principle and dynamic programming for hybrid systems. In *53rd IEEE Conference on Decision and Control*, pp. 19–24.
- Pakniyat, A. and P. E. Caines (2015). Time optimal hybrid minimum principle and the gear changing problem for electric vehicles. In *Proceedings of the 5th IFAC Conference on Analysis and Design of Hybrid Systems, Atlanta, GA, USA, Elsevier*, Number 27, pp. 187–192.
- Pakniyat, A. and P. E. Caines (2016a). Hybrid optimal control of an electric vehicle with a dual-planetary transmission. *Nonlinear Analysis: Hybrid Systems*, DOI: 10.1016/j.nahs.2016.08.004., Elsevier.
- Pakniyat, A. and P. E. Caines (2016b). On the relation between the minimum principle and dynamic programming for classical and hybrid systems. *arXiv:1609.03158, accepted for publication in the IEEE Transactions on Automatic Control*.
- Panton, R. L. (2006). *Incompressible flow*. John Wiley & Sons.
- Pena-Alzola, R., R. Sebastian, J. Quesada, and A. Colmenar (2011). Review of flywheel based energy storage systems. In *International Conference on Power Engineering, Energy and Electrical Drives (POWERENG)*, pp. 1–6.
- Penaud, J. and D. Alazard (2010). Kinematic analysis of complex gear mechanisms. In *Proceedings of the World Congress on Engineering*, pp. 1134–1139.
- Pettersson, M. (1997). *Driveline modeling and control*. Ph. D. thesis, Department of Electrical Engineering, Linköping University.

BIBLIOGRAPHY

- Pfeiffer, F. and C. Glocker (1996). *Multibody dynamics with unilateral contacts*, Volume 9. John Wiley & Sons.
- Pfeiffer, F. and C. Glocker (2000). *Multibody dynamics with unilateral contacts*, Volume 421. Springer Science & Business Media.
- Radke, A. and Z. Gao (2006). A survey of state and disturbance observers for practitioners. In *IEEE American Control Conference*, pp. 5183–5188.
- Rahimi Mousavi, M. S. and B. Boulet (2014). Modeling, simulation and control of a seamless two-speed automated transmission for electric vehicles. In *IEEE American Control Conference (ACC)*, pp. 3826–3831.
- Rahimi Mousavi, M. S., A. Pakniyat, M. K. Helwa, and B. Boulet (2015). Observer-based backstepping controller design for gear shift control of a seamless clutchless two-speed transmission for electric vehicles. In *Vehicle Power and Propulsion Conference (VPPC)*, IEEE, pp. 1–6.
- Ramachandra, K. (2000). *Kalman filtering techniques for radar tracking*. CRC Press.
- Rosemeier, T., B.-R. Hohn, and C. Pelchen (2013, April 16). Transmission device. US Patent 8,419,579.
- Schrijver, E. and J. Van Dijk (2002). Disturbance observers for rigid mechanical systems: equivalence, stability, and design. *ASME Journal of Dynamic Systems, Measurement, and Control* 124(4), 539–548.
- Seetharaman, S., A. Kahraman, M. Moorhead, and T. Petry-Johnson (2009). Oil churning power losses of a gear pair: experiments and model validation. *ASME Journal of Tribology* 131(2), 022202–1–022202–10.
- Shaikh, M. S. and P. E. Caines (2007). On the hybrid optimal control problem: theory and algorithms. *IEEE Transactions on Automatic Control* 52(9), 1587–1603, Corrigendum: vol. 54, no. 6, pp. 1428, 2009.
- Shin, J., J. Kim, J. Choi, and S. Oh (2014). Design of 2-speed transmission for electric commercial vehicle. *International Journal of Automotive Technology, Springer* 15(1), 145–150.

- Simon, D. (2006). *Optimal state estimation: Kalman, H infinity, and nonlinear approaches*. John Wiley & Sons.
- Siriapuraju, K. B., V. Konduru, and P. Eswaramoorthy (2015). Detent profile optimization to improve shift quality of manual transmissions. Technical report, SAE Technical Paper.
- Söffker, D., T.-J. Yu, and P. C. Müller (1995). State estimation of dynamical systems with nonlinearities by using proportional-integral observer. *International Journal of Systems Science, Taylor & Francis* 26(9), 1571–1582.
- Sorniotti, A., T. Holdstock, G. L. Pilone, F. Viotto, S. Bertolotto, M. Everitt, R. J. Barnes, B. Stubbs, and M. Westby (2012). Analysis and simulation of the gearshift methodology for a novel two-speed transmission system for electric powertrains with a central motor. *Proceedings of the Institution of Mechanical Engineers, Part D: Journal of Automobile Engineering*, 915–929.
- Srivastava, N. and I. Haque (2008). Transient dynamics of metal v-belt cvt: Effects of band pack slip and friction characteristic. *Mechanism and Machine Theory, Elsevier* 43(4), 459–479.
- Srivastava, N. and I. Haque (2009a). Nonlinear dynamics of a friction-limited drive: Application to a chain continuously variable transmission (cvt) system. *Journal of Sound and Vibration, Elsevier* 321(1), 319–341.
- Srivastava, N. and I. Haque (2009b). A review on belt and chain continuously variable transmissions (cvt): Dynamics and control. *Mechanism and machine theory, Elsevier* 44(1), 19–41.
- Sun, F., X. Hu, Y. Zou, and S. Li (2011). Adaptive unscented kalman filtering for state of charge estimation of a lithium-ion battery for electric vehicles. *Energy, Elsevier* 36(5), 3531–3540.
- Tahmasebi, R., H. V. Alizadeh, S. Rahimi, and B. Boulet (2014). Robust H_∞ force control of a solenoid actuator using experimental data and finite element method. In *IEEE Conference on Control Applications (CCA)*, pp. 1172–1177.

BIBLIOGRAPHY

- Tanaka, H. (2003). Torque control of a double cavity half-toroidal cvt. *International journal of vehicle design, Inderscience Publishers* 32(3-4), 208–215.
- Taringoo, F. and P. E. Caines (2013). On the optimal control of impulsive hybrid systems on riemannian manifolds. *SIAM Journal on Control and Optimization* 51(4), 3127–3153.
- Tie, S. F. and C. W. Tan (2013). A review of energy sources and energy management system in electric vehicles. *Renewable and Sustainable Energy Reviews, Elsevier* 20, 82–102.
- Treder, M. and C. Woernle (2004). Simulation and experimental validation of the dynamic behavior of an electromechanically actuated multiple-disk clutch. *PAMM, Wiley Online Library* 4(1), 171–172.
- Tsai, M.-C., C.-C. Huang, and B.-J. Lin (2010). Kinematic analysis of planetary gear systems using block diagrams. *ASME Journal of Mechanical Design* 132(6), 065001.
- Ugarte, M. D., A. F. Militino, and A. T. Arnholt (2008). *Probability and Statistics* with R. CRC Press.
- Underhill, C. R. (1914). *Solenoids, electromagnets and electromagnetic windings*. D. Van Nostrand Company.
- Van Der Schaft, A. J. and J. M. Schumacher (2000). *An introduction to hybrid dynamical systems*, Volume 251. Springer-Verlag London.
- Vazquez, S., S. M. Lukic, E. Galvan, L. G. Franquelo, and J. M. Carrasco (2010). Energy storage systems for transport and grid applications. *IEEE Transactions on Industrial Electronics* 57(12), 3881–3895.
- Walker, P. D., S. A. Rahman, B. Zhu, and N. Zhang (2013). Modelling, simulations, and optimisation of electric vehicles for analysis of transmission ratio selection. *Advances in Mechanical Engineering* 5, 340435.
- Walker, P. D. and N. Zhang (2013). Modelling of dual clutch transmission equipped powertrains for shift transient simulations. *Mechanism and Machine Theory, Elsevier* 60, 47–59.

- Walker, P. D., N. Zhang, and R. Tamba (2011). Control of gear shifts in dual clutch transmission powertrains. *Mechanical Systems and Signal Processing, Elsevier* 25(6), 1923–1936.
- Weiss, H. (1998, September 29). Electric wheel drive for a utility vehicle. US Patent 5,813,488.
- Wenthen, D. W. (2013, August 27). Two-speed transaxle gearbox for electric vehicles. US Patent 8,517,882.
- Wojnarowski, J. and A. Lidwin (1975). The application of signal flow graphs—the kinematic analysis of planetary gear trains. *Mechanism and Machine Theory, Elsevier* 10(1), 17–31.
- Xiusheng, C., S. Yongdao, G. Qiang, and L. Xi (2011). Shift control for dry dual clutch transmission of pure electric vehicle. In *IEEE International Conference on Transportation, Mechanical, and Electrical Engineering (TMEE)*, pp. 854–857.
- Yi, K., B.-K. Shin, and K.-I. Lee (1999). Estimation of turbine torque using an adaptive nonlinear observer for closed-loop control of vehicle automatic transmissions. *KSME International Journal, Springer* 13(11), 783–790.
- Yi, K., B.-K. Shin, and K.-I. Lee (2000). Estimation of turbine torque of automatic transmissions using nonlinear observers. *ASME Journal of dynamic systems, measurement, and control* 122(2), 276–283.
- Yu, C.-H., C.-Y. Tseng, and C.-P. Wang (2012). Smooth gear-change control for EV clutchless automatic manual transmission. In *IEEE/ASME International Conference on Advanced Intelligent Mechatronics (AIM)*, pp. 971–976.
- Yuan, Y., G. Wu, X. He, Y. Song, and X. Zhang (2012). Electric vehicle drivetrain development in China. In *ASME/ISCIE 2012 International Symposium on Flexible Automation*, pp. 597–603.
- Yue, H., B. Wang, L. Yu, B. Gao, and H. Chen (2013). Modeling and simulation of an electric clutch actuator. In *Proceedings of the FISITA 2012 World Automotive Congress, Springer*, pp. 31–38.

BIBLIOGRAPHY

- Zhang, J., L. Chen, and G. Xi (2002). System dynamic modelling and adaptive optimal control for automatic clutch engagement of vehicles. *Proceedings of the Institution of Mechanical Engineers, Part D: Journal of Automobile Engineering* 216(12), 983–991.
- Zhang, M., F. Zhu, J. Shu, and C. Yin (2016, January 12). Two-speed transmission and electric vehicle. US Patent 9,234,565.
- Zhang, N., A. Crowther, D. Liu, and J. Jeyakumaran (2003). A finite element method for the dynamic analysis of automatic transmission gear shifting with a four-degree-of-freedom planetary gearset element. *Proceedings of the Institution of Mechanical Engineers, Part D: Journal of Automobile Engineering* 217(6), 461–473.
- Zhang, Z., C. Zuo, W. Hao, Y. Zuo, X. Zhao, and M. Zhang (2013). Three-speed transmission system for purely electric vehicles. *International Journal of Automotive Technology, Springer* 14(5), 773–778.
- Zhou, X., P. Walker, N. Zhang, B. Zhu, and J. Ruan (2014a). Numerical and experimental investigation of drag torque in a two-speed dual clutch transmission. *Mechanism and Machine Theory, Elsevier* 79, 46–63.
- Zhou, X., P. Walker, N. Zhang, B. Zhu, and J. Ruan (2014b). Study of power losses in a two-speed dual clutch transmission. Technical report, SAE Technical Paper.
- Zhu, B., N. Zhang, P. Walker, W. Zhan, X. Zhou, and J. Ruan (2013). Two-speed dct electric powertrain shifting control and rig testing. *Advances in Mechanical Engineering* 5, 1–10.
- Zhu, X., H. Zhang, J. Xi, J. Wang, and Z. Fang (2014). Optimal speed synchronization control for clutchless amt systems in electric vehicles with preview actions. In *IEEE American Control Conference (ACC)*, pp. 4611–4616.

APPENDIX A

APPENDIX A

In this appendix, assembly drawings of the DBT are provided to obtain a better insight into the current design and to provide an opportunity for further improvements.

A.1. Planetary Gear Sets and Their Interconnections

As explained in Chapter 2, planetary gear sets are the key components of the DBT design that allows transferring power from the traction motor to the driveline in different combinations of torque and speed. In this design, the planetary gear sets have interconnected sun and ring gears. Thus, in order to attain such a feature, as illustrated in Fig. A.1, the sun gears of the planetary gear sets **4** and **13** are linked together via the shaft **1** and the key **3**. This key is kept in its place using clamp **12**. Further, the ring gears are connected by means of shoulder screws **2** and nuts **15**. The spacers **8** are considered in-between the planetary gears to provide adequate space to yield independent rotations of carriers. Moreover, two sets of bearings **6** and **10** are placed on the shoulder screw **2** to support the radial load applied on the ring gears and washers **5**, **7**, **9**, **11** allow independent rotation of the inner rings of these bearings with respect their outer rings. The drum **14**, which stops the ring gear from rotating, is connected to the common ring gears via shoulder screws **2**. Figure A.2 illustrates the isometric exploded and collapsed views and Fig. A.3 compares the 3D CAD model and the implemented design of the DBT core structure.

APPENDIX A. APPENDIX A

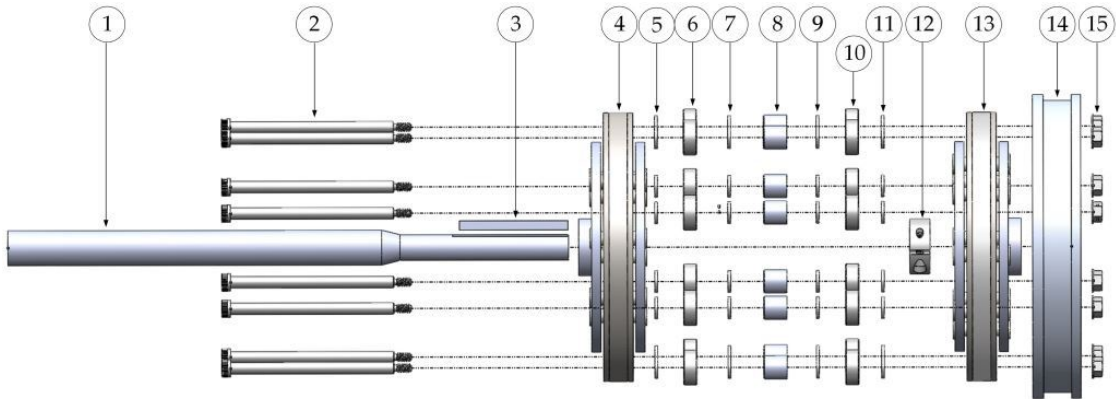


FIGURE A.1. Planetary gear sets and their interconnections

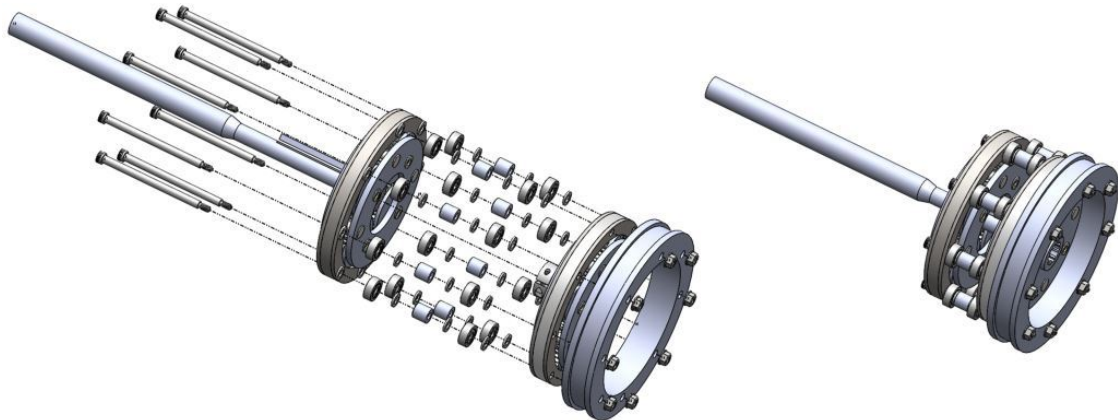


FIGURE A.2. Isometric exploded and collapsed views of the DBT core structure

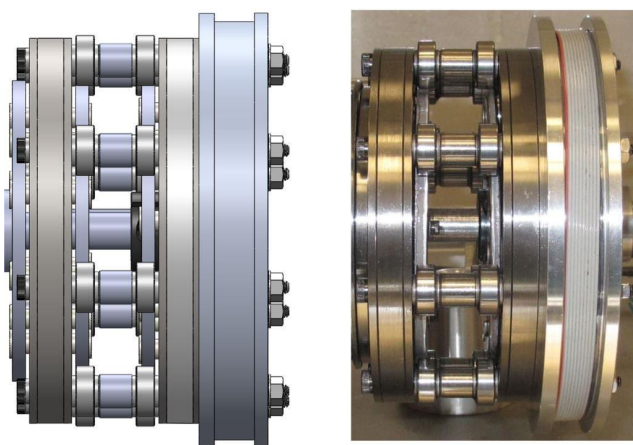


FIGURE A.3. 3D CAD model and implemented design of the DBT core structure

A.2. Bearings and Supports

As illustrated in Fig. A.4, the bearings sets **6** and **10** are placed inside the cylindrical tube **22** which is precisely machined to provide a transition fit between the bearings and the tube. The bearings **21** allow independent rotation of the sun shaft **1** with respect to the carrier of the planetary gear set **4**. The shaft adapter **19** adapts the size of the timing pulley **17** with the outer rings of bearings **21** and the set screws **20** hold the bearings inside the shaft adapter. In fact, the bearings **6**, **10**, and **21** align the gears inside the core structure of the DBT system and keep them coaxial with their axes of rotation. Moreover, the timing pulley **17** transfers the transmission output power and it is connected to the output carrier via screw **16** and nuts **18**. Figure A.5 illustrates the isometric exploded and collapsed views of these components.

The whole setup, as depicted in Fig. A.6, is established on the aluminium plate **23**. The stands **24** are bolted to this plate by bolts **25** and the threaded rods **28** adjust the height of the core structure of the DBT system by means of the clamp jaws **27** and **29** and nuts **26** underneath and on top of these jaws. Further, the sun shaft **1** is supported by the bearing **32** located on the stand **30** and tightened by bolts **31**. The stand **30** itself is established on the aluminium plate **23** by similar screws as of **31** as illustrated in Fig. A.6. Figure A.7 demonstrates the isometric and collapsed views of these components.

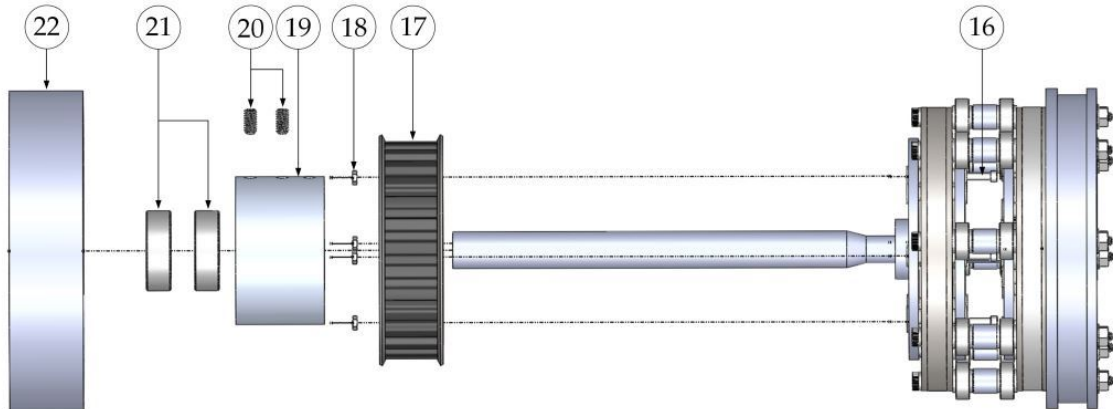


FIGURE A.4. Aligning bearings and output pulley of the DBT system

APPENDIX A. APPENDIX A

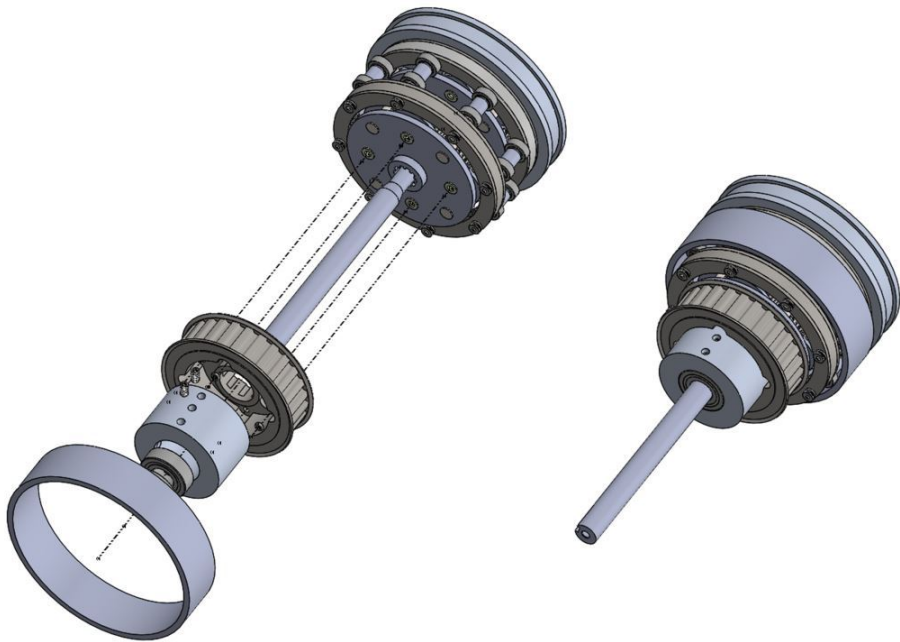


FIGURE A.5. Isometric exploded and collapsed views of aligning bearings and output pulley

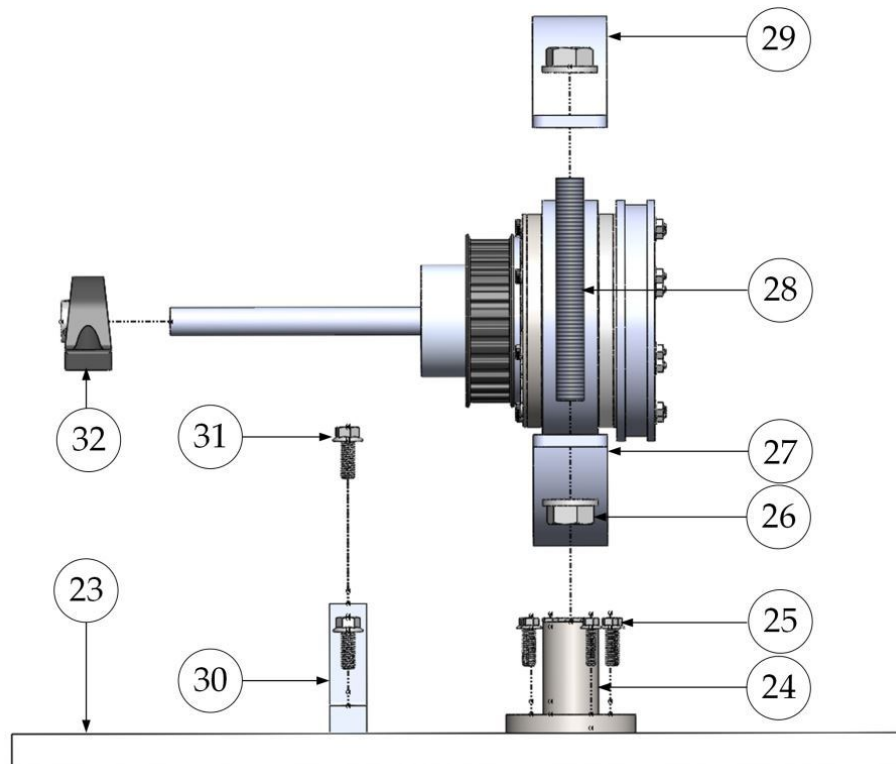


FIGURE A.6. Major supports of the DBT system

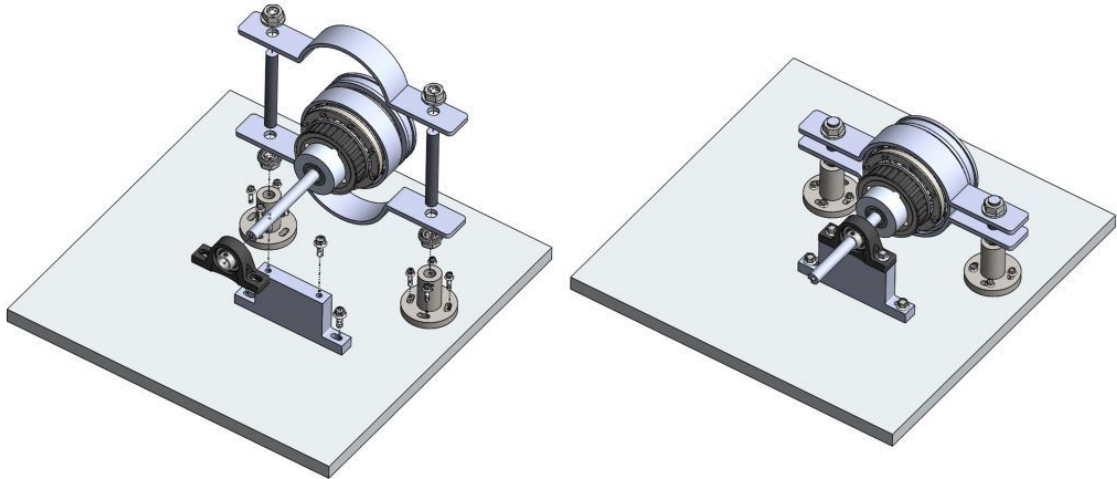


FIGURE A.7. Isometric exploded and collapsed views of the major supports of the DBT system

A.3. Motors and Brake Systems

As explained in Chapter 2, the brake system of the common sun gears is designed to be of the multi-plate type. The major components of this brake system, as illustrated in Fig. A.8, are the outer hub **36**, the inner hub **39**, a number of alternating friction and separator plates **44** and **45**, the apply-plate **46**, and the force actuator **50**. The outer hub **36** is placed on the stand **34** by means of the screws **37** and nuts **33**. The stand itself is fixed to the aluminium plate **23** by means of the bolts similar to that of **35** as illustrated in the figure. Further, the inner hub **39** is connected to the sun shaft **1** via the adaptor **40**, screws **38**, and the key **41**. The washer **42** and screw **43** hold the key in its place. The alternating friction and separator plates **44** and **45** are placed between the outer hub **36** and inner hub **39**. Moreover, The apply-plate **46** transfers the normal brake force from the actuator **50** to the brake plates. The apply-plate is connected to the force actuator **50** by means of the coupling **47**. This force actuator is fixed to the aluminium plate **23** using the stand **49** and nuts **48**. Figure A.9 illustrates the isometric exploded and collapsed views of the multi-plate brake mechanism for the sun gear.

APPENDIX A. APPENDIX A

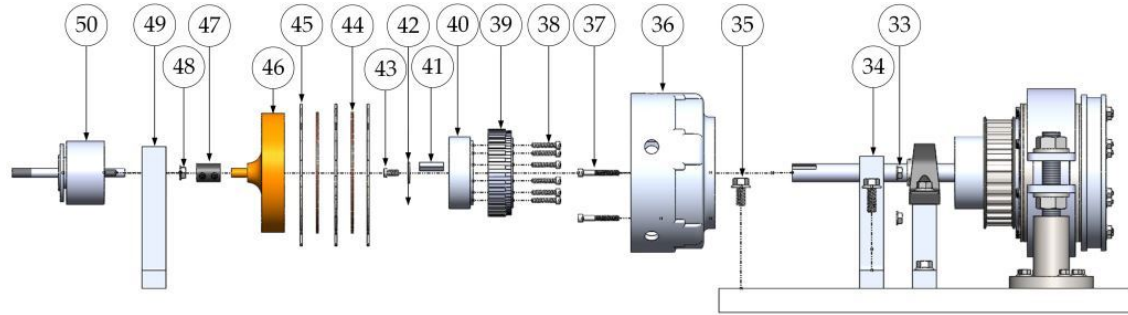


FIGURE A.8. Multi-plate brake mechanism for the common sun gears

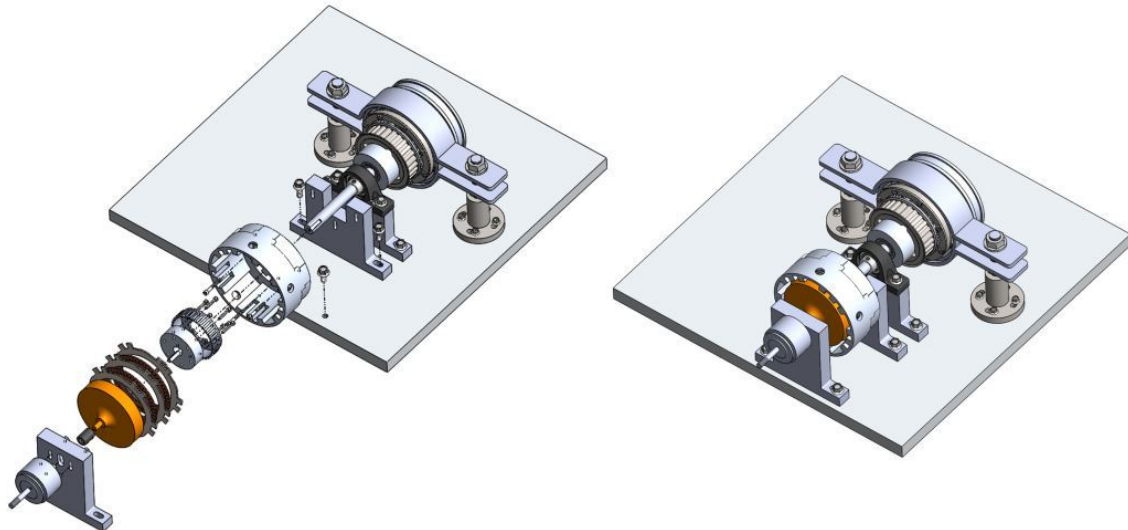


FIGURE A.9. Isometric exploded and collapsed views of the multi-plate brake mechanism

The installation procedure of the traction motor is shown in Fig. A.10. The traction motor **52** is connected to the input carrier of the planetary gear set **13** via the shaft adaptor **55**, the flexible coupling **56** and the splined shaft **58**. Further, the traction motor **52** is supported by the stand **53** via screws **51** and nuts **54**. The stand **53** is established on the aluminium plate **23** using screws **57**. Figure A.11 demonstrates the isometric exploded and collapsed views of the traction motor installation.

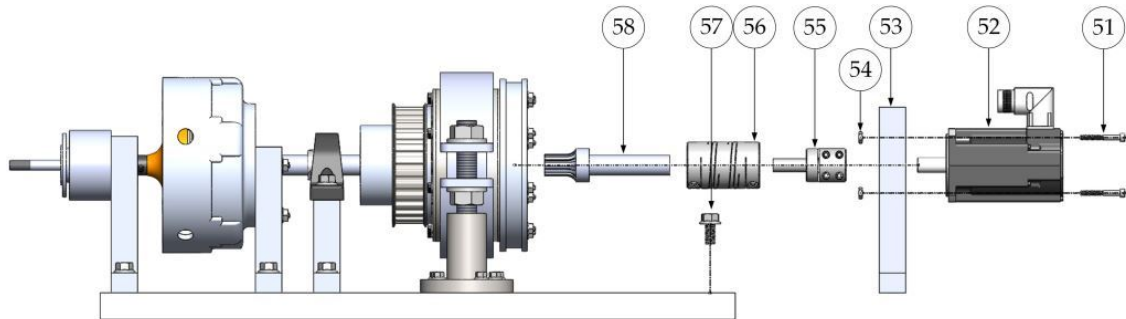


FIGURE A.10. Traction motor installation

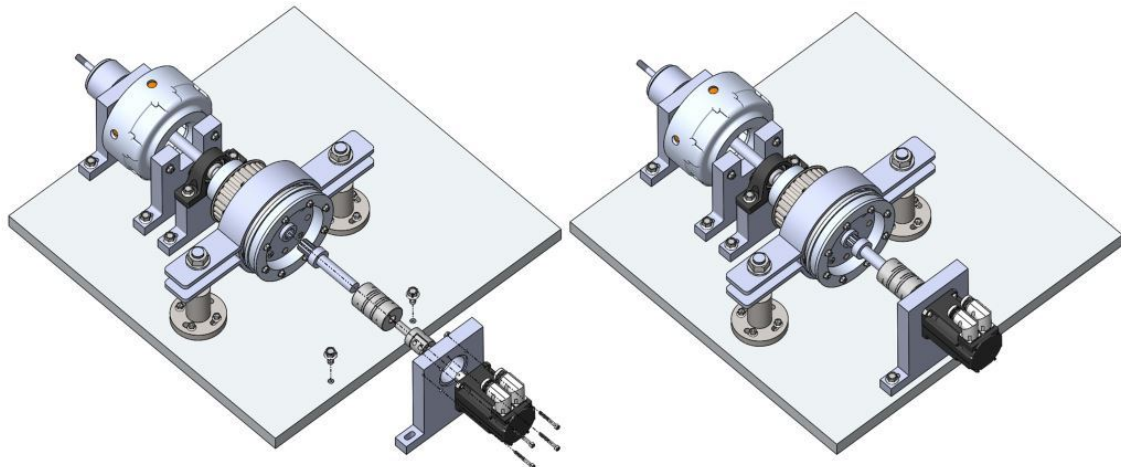


FIGURE A.11. Isometric exploded and collapsed views of the traction motor installation

The load motor installation is illustrated in Fig. A.12. The load motor **60** is connected to the timing pulley **64** via the shaft adaptor **63**. The timing pulley **64** will be connected to the timing pulley **17** by means of a timing belt. Similar to the traction motor **52**, the load motor **60** is supported by the stand **61** via screws **62** and nuts **59**. The stand **61** is secured on the aluminium plate **23** as illustrated in Fig. A.12. Figure A.13 illustrates the isometric exploded and collapsed views of the load motor installation.

APPENDIX A. APPENDIX A

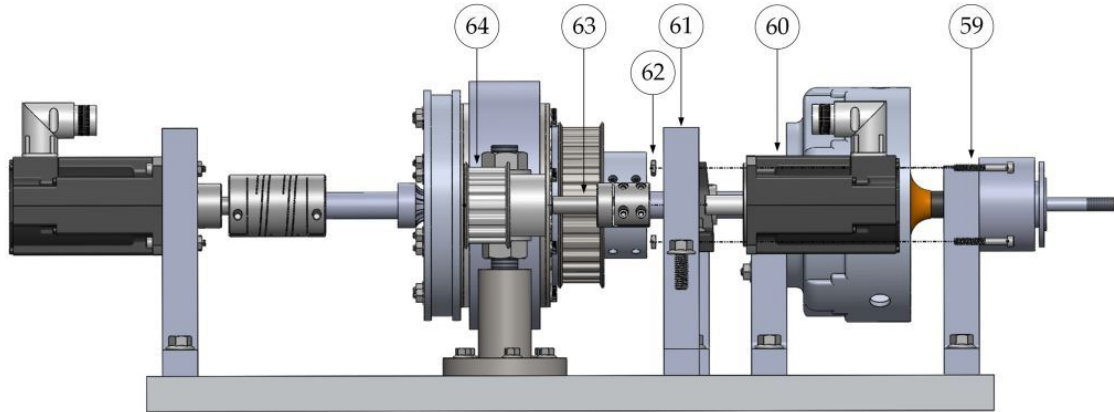


FIGURE A.12. Load motor installation

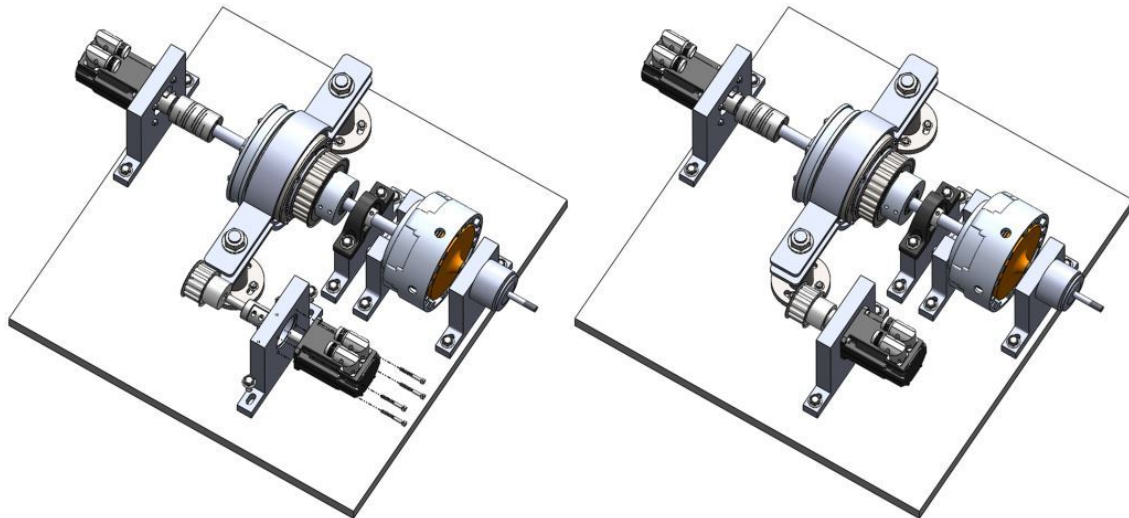


FIGURE A.13. Isometric exploded and collapsed views of the load motor installation

Finally, the installation of the force actuator of the ring brake is depicted in Fig. A.14. As it can be seen in this figure, the force actuator **68** is supported by the L shape stand **66** via nuts **65**. The stand **66** is fixed to the aluminium plate **23** using bolts **67**. The band of the brake will be warped about the drum **14** and pulled by the force actuator **68**. Figure A.15 illustrates the isometric exploded and collapsed views of the band brake force actuator installation.

A.4 FINAL 3D CAD MODEL AND IMPLEMENTED DESIGN

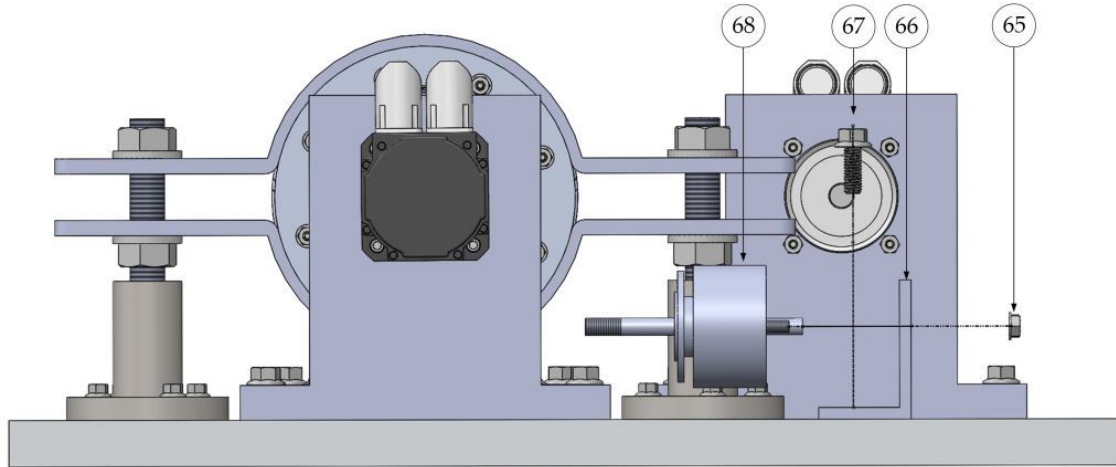


FIGURE A.14. Band brake force actuator installation

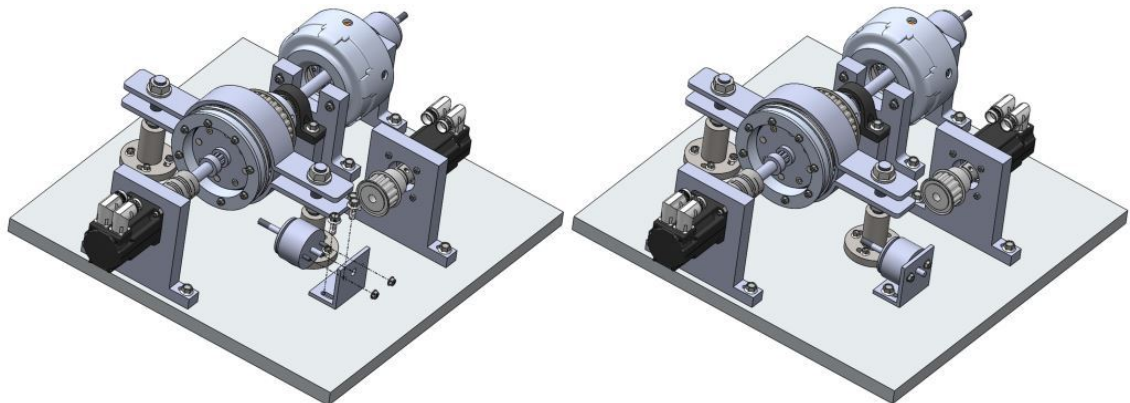


FIGURE A.15. Isometric exploded and collapsed views of the band brake force actuator installation

A.4. Final 3D CAD Model and Implemented Design

The isometric views of the final 3D CAD models and the implemented design are illustrated in Fig. A.16 and Fig. A.17 from different angles. As it can be seen from these figures, the implemented prototype satisfactorily matches with the 3D CAD model.

APPENDIX A. APPENDIX A

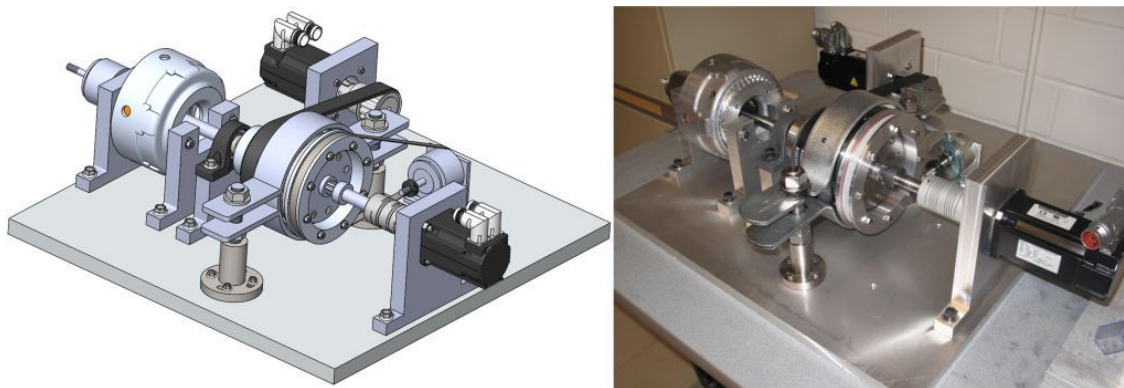


FIGURE A.16. 3D CAD model and the implemented prototype (front view)

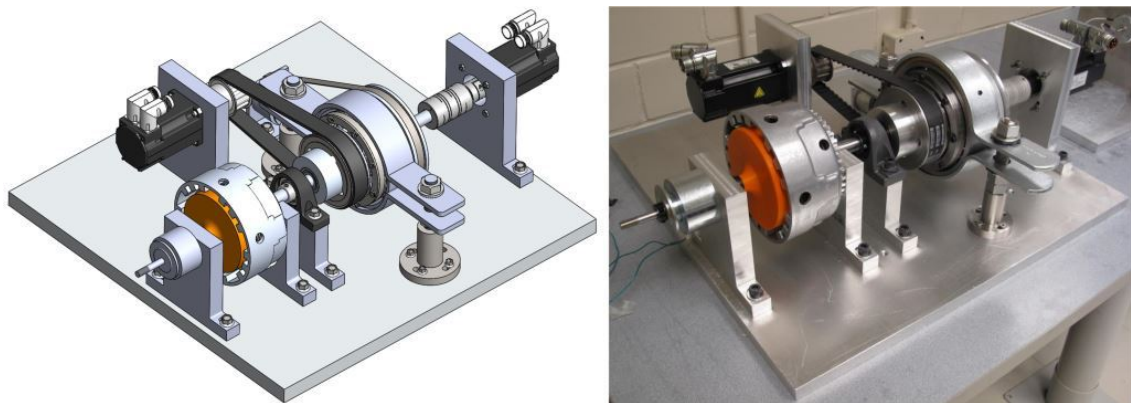


FIGURE A.17. 3D CAD model and the implemented prototype (rear view)

Document Log:

Manuscript Version 1

Typeset by $\mathcal{AM}\mathcal{S}$ -L^AT_EX — 24 January 2017

MIR SAMAN RAHIMI MOUSAVI

CENTRE FOR INTELLIGENT MACHINES, MCGILL UNIVERSITY, 3480 UNIVERSITY ST., MONTREAL (QUÉBEC), H3A 2A7, CANADA

E-mail address: saman@cim.mcgill.ca

Typeset by $\mathcal{AM}\mathcal{S}$ -L^AT_EX